# Extreme wave interaction with fixed and floating structures using hybrid coupling approach

Sithik Aliyar

# THÈSE DE DOCTORAT DE

L'ÉCOLE CENTRALE DE NANTES &
INDIAN INSTITUTE OF TECHNOLOGY MADRAS

ÉCOLE DOCTORALE N° 602
*Sciences pour l'Ingénieur*
Spécialité : *Mécanique des Milieux Fluides*

Par
**SITHIK ALIYAR**

# Extreme wave interaction with fixed and floating structures using hybrid coupling approach

**Thèse présentée et soutenue à l'Ecole Centrale de Nantes , le 10 Novembre 2022**
**Unité de recherche : UMR 6598, Laboratoire de recherche en Hydrodynamique, Energétique et Environnement Atmosphérique (LHEEA)**

## Rapporteurs avant soutenance :

Michel BENOIT Senior Researcher HDR, EDF, Chatou

Trilochan SAHOO Full Professor, Indian Institute of Technology Kharagpur (IITKGP), Inde

## Composition du Jury :

| | | |
|---|---|---|
| Président : | Pierre LUBIN | Professeur des universités, Université de Bordeaux |
| Examinateurs : | Arul JAYACHANDRAN S | Full professor, Indian Institute of Technology Madras (IITM), Inde |
| | NALLAYARASU S | Full professor, Indian Institute of Technology Madras (IITM), Inde |
| Dir. de thèse : | Pierre FERRANT | Professeur des universités, École Centrale de Nantes |
| Dir. de thèse : | Sriram VENKATACHALAM | Full professor, Indian Institute of Technology Madras (IITM), Inde |
| Co-encadrant : | Benjamin BOUSCASSE | Chargé de recherche, École Centrale de Nantes |


DEPARTMENT OF OCEAN ENGINEERING
INDIAN INSTITUTE OF TECHNOLOGY MADRAS
CHENNAI – 600036

# Extreme wave interaction with fixed and floating structures using hybrid coupling approach

*This thesis has been prepared in the framework of a Joint Doctoral Degree Programme between Indian Institute of Technology Madras and Ecole Centrale de Nantes*

*A Thesis*

*Submitted by*

**SITHIK ALIYAR**

*For the award of the degree*

*Of*

**DOCTOR OF PHILOSOPHY**

November 2022

*Dedicated to my beloved parents, brother, wife and Zara*

# THESIS CERTIFICATE

This is to undertake that the Thesis titled **EXTREME WAVE INTERACTION WITH FIXED AND FLOATING STRUCTURES USING HYBRID COUPLING APPROACH**, submitted by me to the Indian Institute of Technology Madras, for the award of **Doctor of Philosophy**, is a bona fide record of the research work done by me under the supervision of **Dr. V. Sriram and Prof. Pierre Ferrant**. The contents of this Thesis, in full or in parts, have not been submitted to any other Institute or University for the award of any degree or diploma.

**Chennai 600036** **Sithik Aliyar**

**Date: 10 November 2022**

**Dr. V. Sriram**
Research advisor
Associate Professor
Department of Ocean Engineering
Indian Institute of Technology Madras

**Prof. Pierre Ferrant**
Research advisor
Professor in Ocean Engineering
LHEEA Lab. - Centrale Nantes and CNRS

# ACKNOWLEDGEMENT

After completing my thesis on a five-year road filled with hit and miss, tears and laughter, I understand how many individuals helped and supported me to make this work possible, and I owe them a lot of gratitude.

First and foremost, I would like to thank the Almighty for his blessings during my study and in completing this thesis.

I give my sincere gratitude and respect to my supervisor Dr. V. Sriram. He has been the most active and competent research guide, often devoting hours to each issue I faced. Since 2013 when I first met him, he has been my life and career mentor and my most kind and helpful supervisor. Also to be mentioned, he helped with the funding and accompanied me on my first overseas trip to Hannover, Germany from India. Also, he was nice enough to put me up for the JDP opportunity with ECN and to help me all the way through till I got selected. His work ethic, curiosity in learning, and networking skills are all things that motivate me, and I intend to model these traits in my professional life.

I want to thank my other thesis director, Professor Pierre FERRANT. Prof. Pierre is the one who suggests this interesting topic and has maintained his faith in me over the years with few extensions. He is always able to offer helpful advice as the director and is incredibly supportive and motivating of my studies. Since he handled everything, from admission until the point of thesis submission, Thanks to him, I never had any administrative issues from ECN. I enjoyed spending time with him in Chennai during the GIAN course more than I did in Nantes. He kept in touch with me often during the terrifying initial covid period, which was a thoughtful gesture and he often offered me constant mental assurance.

I would also like to thank Dr. Benjamin BOUSCASSE, the main person I contacted almost daily during my PhD, for my famous "Doubt again" sessions. Benjamin is the senior researcher of the Chaire Hydrodynamique et Structure Marines CENTRALE NANTES - BUREAU VERITAS, a research project in which my work takes part, and the leader of our research team. I went from being a beginner in CFD to writing a thesis based on CFD, mainly thanks to all of his ranting, patience, and also definitely motivation. Many of his suggestions have been adopted and integrated into this thesis. I had a great time at the football games and the farewell party in his home with the famous "Mexican avocado dip," which was a pleasant memory to conclude the Nantes end.

My appreciation also extends to my other co-supervisor, Dr. Guillaume DUCROZET. He is the first person I go to when I'm having trouble with a theoretical question. He was always willing to lend a hand, and our conversations always added fresh perspective to my studies. He was especially helpful with the HOS wave models, which is really appreciated. He is the first person who reads my presentations and reads my articles. I truly valued his patience and time spent reading my manuscripts, which often had grammatical, spelling, and formatting issues. I

will admit that the papers are much better in quality as a result of his remarks.

I appreciate the constructive criticism and review that my doctoral committee members, Prof. S. Nallayarasu, Prof. Arul Jayachandran, and Dr. Deepak Kumar, provided. I also appreciate Dr. Guillaume Oger from Ecole Centrale Nantes and Prof. Antonio Souto-Iglesias from Universidad Politécnica de Madrid (UPM) for serving on the CSI Committee and helping to shape the thesis. I had the good fortune to interact with them frequently, which was vital since it gave my research a periodic course correction and outside perspective.

Also expressing my thanks to my colleagues. First, Youngmyung Choi, Youngjun Kim, and Théo Descamps who are all involved in the CN-BV project and OpenFOAM. They are the people I go to for particular OpenFOAM questions, and our conversations are always beneficial. Second, gratitude to Vineesh P. from IITM, was always there to help me with my coursework, experiments, and also sometimes personal matters. Additionally, I would like to thank Tommaso Zanelli, a fellow doctoral student who joined ECN at the same time as me and was a pleasant companion for my whole stay in Nantes.

Additionally, I would like to thank Dr. Sopheak SENG and the OpenFOAM team at Bureau Veritas. They provide me access to the well-validated CFD solver foamStar, which I can use in my thesis and which also acts as a reference of standard CFD solvers.

The financial support from MHRD India, IITM and the Chaire Hydrodynamique et Structure Marines CENTRALE NANTES are also thankfully acknowledged.

Finally, I would like to thank my parents from the bottom of my heart. Without their unwavering love and support, my thesis would not have been feasible. Last but not least, I want to thank my wife, Afrin Minsiya, for her enduring support throughout my PhD with travel, Covid hardship, and hearing my annoying progress speech all the time.

*Sithik Aliyar*
*November 2022*

# ABSTRACT

The present thesis aims to study the effectiveness and accuracy of the numerical solvers, *foamStar* and *foamStarSWENSE*, for wave structure interaction analysis of fixed and floating wind turbine substructures. The initial versions of solvers are developed by Bureau Veritas and ECN. The *foamStar* and *foamStarSWENSE* are OpenFOAM-based solvers which use the domain and the functional decomposition approach, respectively. The total field in the computational domain is divided into the incident and complementary field. The *foamStar* solves for the total flow fields, and *foamStarSWENSE* solves for the complementary (total minus incident) flow fields. These two solvers are independently coupled with HOS for wave generation.

The solvers are tested for three applications. The first and second applications presents the focusing wave interaction with fixed and moving cylinders respectively. In the third application, the *foamStar* and *foamStarSWENSE* solvers are used to simulate the interaction of regular and irregular waves with the OC3 Hywind SPAR type substructure. In the first application, along with non-breaking focusing wave, breaking focused wave investigations with the fixed cylinder is also studied. The 2D parametric studies for focused wave generation are carried out for both the solvers, and 3D wave interaction for different mesh types (coarse, medium, and fine) are investigated to understand the convergence for such transient type problems. The case's uncertainty is quantified using cross correlation approach and Richardson extrapolation technique, and validated with the experimental measurements. Also, the computational efficiency of both coupling techniques is compared, and recommendations for solver improvements are made. In the third application study, the moorings are modelled in two ways. One is by considering the mooring lines as a linear spring with defined spring stiffness, and another is by coupling the solvers with a lumped-mass dynamic mooring model (MoorDyn). MoorDyn, an open source model represents mooring line behaviour subject to axial elasticity, hydrodynamic forces, and vertical contact forces with the seabed. The intention is to develop a numerical tool to study the survivability of floating structures in extreme sea states. The coupled model developed in this thesis has been validated against the experiments carried out in the SOFTWIND project. The numerical model results of free surface elevation, floating body motions, and mooring tensions are compared with the experiments. The solvers' efficiency and accuracy for floating structure interaction are discussed and reported.

**Keywords**: *Numerical modelling; CFD; OpenFOAM; Floating bodies; SPAR; focusing wave; Richardson Extrapolation; SWENSE; Moorings; FOWT; MoorDyn; nonlinear wave structure interactions.*

# Table of Contents

# List of Acronyms

| | |
|---|---|
| BEM | Boundary Element Method. |
| CAD | Computer Aided Design. |
| CC | Cross Correlation. |
| CFD | Computational fluid dynamics. |
| CN | Crank–Nicolson method. |
| Co | Courant number. |
| CoG | Centre Of Gravity. |
| DD | Domain Decomposition. |
| DoF | Degree of Freedom. |
| FD | Functional Decomposition. |
| FNPT | Fully-nonlinear potential theory. |
| FOWT | Floating Offshore Wind Turbine. |
| FVM | Finite Volume Method. |
| HOS | Higher Order Spectral Method. |
| LS | Load Sensor for mooring. |
| MLPG | Meshless Local Petrov-Glerkin method. |
| NBR/BR | Non Breaking / Breaking. |
| NS | Navier-Stokes equations. |
| NWT | Numerical wave tank. |
| OWT | Offshore Wind Turbine. |
| PP | Pressure Probe. |
| PPSD | Points Per SPAR Diameter. |
| RANS | Reynolds Average Navier-Stokes equations. |
| Re | Reynolds number. |
| RK4 | Runge-Kutta $4^{th}$order method. |
| RMSE | Root Mean Squared Error. |
| RZ | Relaxation Zone. |
| SPAR | Single Point Anchor Reservoir. |
| SPH | Smoothed Particle Hydrodynamics. |
| STL | Stereolithography. |
| SWENSE | Spectral Wave Explicit Navier-Stokes equations. |
| TR | Time Reversal technique. |
| VoF | Volume of Fluid method. |
| WP | Wave Probe. |
| WSI | Wave Structure Interaction. |

# List of Notation

**Greek letters**

| | |
|---|---|
| $\alpha$ | Volume of Fluid (VoF) |
| $\chi$ | Total flow field |
| $\chi_C$ | Complementary flow field |
| $\chi_I$ | Incident flow field |
| $\epsilon$ | Absolute errors of the variable of interest |
| $\eta$ | Wave elevation |
| $\gamma$ | Diffusivity coefficient |
| $\Gamma_\phi$ | Diffusion coefficient |
| $\mu$ | Fluid dynamic viscosity |
| $\mu_a$ | Dynamic viscosity of air |
| $\mu_w$ | Dynamic viscosity of water |
| $\omega$ | Wave frequency, Specific dissipation |
| $\Phi$ | Wave velocity potential |
| $\phi$ | Flux at face $f$ |
| $\boldsymbol{\omega}$ | Angular velocity |
| $\boldsymbol{x} = (x, y, z)$ | Point vector in cartesian coordinates |
| $\psi$ | Incident wave stream function |
| $\rho$ | Fluid density |
| $\rho_a$ | density of air |
| $\rho_w$ | density of water |
| $\tau$ | Viscous stress tensor |
| $\varepsilon$ | Time delay |
| $\varsigma$ | Discrete time window representation |
| $\zeta$ | Computed solution in relaxation zone |

**Latin letters**

| | |
|---|---|
| $C_{a\times b}$ | Cross Correlation between $a$ and $b$ |
| $\boldsymbol{\theta}$ | Rotational motion |
| $\boldsymbol{a}_p, \boldsymbol{a}_q$ | Added mass forces on mooring line |
| $\boldsymbol{B}$ | Sea bed contact forces on mooring line |
| $\boldsymbol{C}$ | Internal damping forces on mooring line |

| | |
|---|---|
| $\boldsymbol{D}$ | Hydrodynamic forces on mooring line |
| $\boldsymbol{g}$ | Gravitational acceleration |
| $\boldsymbol{H}$ | Horizontal fairlead force |
| $\boldsymbol{H}_A$ | Horizontal anchor force |
| $\boldsymbol{I}_b$ | Mass moment of inertia of the body |
| $\boldsymbol{M}_b$ | Total torque acting on the body |
| $\boldsymbol{n}$ | Normal unit vector |
| $\boldsymbol{Q}$ | Forces acting on a rigid body |
| $\boldsymbol{q}$ | Translation motion |
| $\boldsymbol{r}_i$ | Node position vector |
| $\boldsymbol{T}$ | Cable tension |
| $\boldsymbol{u}$ | Fluid velocity |
| $\boldsymbol{u}_c$ | Complementary fluid velocity |
| $\boldsymbol{u}_f$ | Velocity at the cell face |
| $\boldsymbol{u}_I$ | Incident fluid velocity |
| $\boldsymbol{u}_r$ | Phase relative velocity |
| $\boldsymbol{V}$ | Vertical fairlead force |
| $\boldsymbol{V}_A$ | Vertical anchor force |
| $\boldsymbol{W}$ | Net buoyancy forces on mooring line |
| $A$ | Cable cross-sectional area |
| $a_N$ | Off-diagonal coefficient of discretized matrix |
| $a_P$ | Diagonal coefficient of discretized matrix |
| $C_{an}$ | Transverse added mass coefficient |
| $C_{at}$ | Tangential added mass coefficient |
| $C_{dn}$ | Transverse drag coefficient |
| $C_{dt}$ | Tangential drag coefficient |
| $d$ | diameter |
| $E$ | Young's modulus |
| $h$ | Vertical fairlead excursion |
| $h_g$ | Grid Spacing |
| $K$ | Stiffness matrix |
| $k$ | Wave number |
| $L$ | Unstretched line length in mooring |
| $l$ | Horizontal fairlead excursion |

| | |
|---|---|
| $m$ | Generalized mass |
| $p$ | Apparent order of convergence |
| $p_c$ | Complementary pressure |
| $p_d$ | Dynamic pressure |
| $p_I$ | Incident pressure |
| $p_I^*$ | Modified incident pressure |
| $q_f$ | Face properties |
| $r$ | Grid refinement ratio |
| $R_0$ | Inertial reference frame |
| $R_b$ | Body reference frame |
| $s$ | Unstretched distance from the anchor ($0 \leq s \leq L$ ) |
| $T_P$ | Peak period of irregular waves |
| $V$ | Cell volume |
| $w$ | Cable weight-per-unit length in fluid |
| $w_f$ | Weight function |
| $w_f^d$ | Dynamic weight function |
| h | Water depth |

# List of Figures

# List of Tables

Chapter 1

# INTRODUCTION

## 1.1 Offshore Wind Turbines (OWT)

The primary objective of the Paris agreement is to strengthen the global response to the threat of climate change by limiting global temperature rise to well below $2^oC$ above pre-industrial levels and pursuing efforts to limit temperature rise even further to $1.5^oC$ within this centuary (UNFCCC, 2015). Burning fossil fuels to meet energy demands releases large volumes of greenhouse gases (GHGs) such as $CO_2$, $CH_4$, $NO_2$, and other noxious gases into the atmosphere. GHGs absorb the heat emitted by the Earth as infrared radiation, trapping it near the Earth's surface and raising global temperatures. In 2018, GHGs emissions reached 58 GtCO2eq, the most in human history (Lamb et al., 2021). Among the total emissions, the energy sector accounted for 34%, followed by industry (24%), agriculture and forestry (21%), transportation (14%), and building operations (6%). The industry and building sectors indirectly contributed to emission growth by relying on energy production for power and heat, making energy production accounts for two-thirds of global greenhouse gas emissions (Lamb et al., 2021). GHGs emissions should be reduced by adopting renewables and other environmentally friendly energy sources to generate electricity on-site. According to International Renewable Energy Agency (IRENA) (IEA, 2019), renewable energy is on the rise and could contribute to 80% of world demand by 2050, up from only 25% in 2020. As seen in Figure 1.1, hydropower accounts for the largest share of renewable energies (40%), followed by solar and wind energy, both accounting for equal shares($27\% \approx 28\%$). Other renewables (5%) included bioenergy, geothermal and marine energy. Solar power and onshore wind have already proven to generate considerable amounts of electricity, and these sources of energy are already competitive with traditional sources of energy such as coal, gas, gasoline, and nuclear power. Solar and wind energy continued to be the most popular renewable energy sources in 2021, accounting for 88% of all net new renewable capacity additions.(IEA, 2019).

To meet the Paris agreements' target (UNFCCC, 2015), there is an indisputable need to create new technologies for green and renewable energy production. The success of this process lies in the diversification of the sources of energy production and Offshore wind appears to be an effective mean to help achieving these goals for several reasons. Offshore wind is a valuable renewable resource since it competes less with other land uses and has experienced less public opposition than onshore wind, while delivering a more consistent (less intermittent) energy supply. Offshore farms can also achieve better power densities by using taller and larger turbines with less size and noise pollution limits, allowing for a capacity factor of $40 - 50\%$ (Krey and

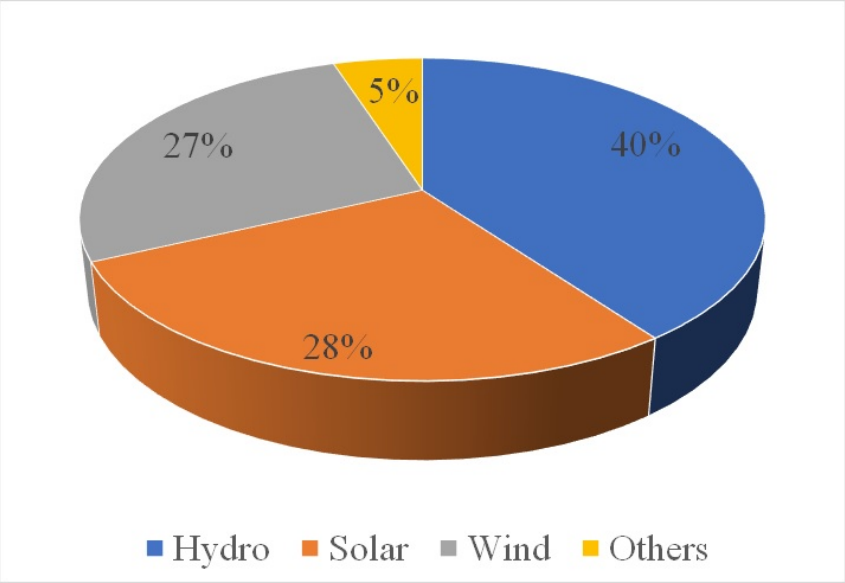


Figure 1.1 – Global renewable generation capacity by energy source, 2021 (IEA, 2019)

Clarke, 2011). Even though it represents only 0.3% of the global power production today, the expansion of offshore wind energy has become inevitable (Finance, 2019). Many offshore wind farms have been built since the first, "Windeby," was established in 1991, culminating in a total net installed capacity of 35.3 GW by the end of 2020, out of total wind energy capacity of 743 GW (GWEC, 2021). The United Kingdom, Germany, the Netherlands, Belgium, and Denmark are the top contributors, with 2.9 GW of offshore wind gross power capacity installed by 2020 as shown in Figure 1.2 (WindEurope, 2020). Furthermore, while nations with shallow sea depths have dominated the offshore wind market to date, lowering costs and increasing decarbonisation demands have prompted several governments to investigate the possibilities of floating offshore wind turbines. Full-scale prototypes of floating platforms for wind turbines are now being built, however they are still in the early stages of development. The International Energy Agency (NetZero, 2021) estimates that offshore wind has the potential to meet world's electricity demand 11 times over by 2040..

### 1.1.1 India in global energy market

India has the fourth-largest global energy consumption, after China, United States, and European Union. The IEA Stated Policies Scenario (STEPS) anticipates that India will surpass the European Union in 2030 to take third place in global consumption. In the STEPS, India will account for about a quarter of global energy demand growth from 2019 to 2040, making it the top country. But India is also the second-highest in the world in terms of renewable energy growth, after China. India's power system will be larger than the European Union's by 2040, and it will be the world's third largest in terms of electricity output; it will also have 30% more installed renewables capacity than the US by 2040 (India Energy Outlook, 2021).

India's total energy demand will steadily increase, reaching 2.8 times its current level by 2040

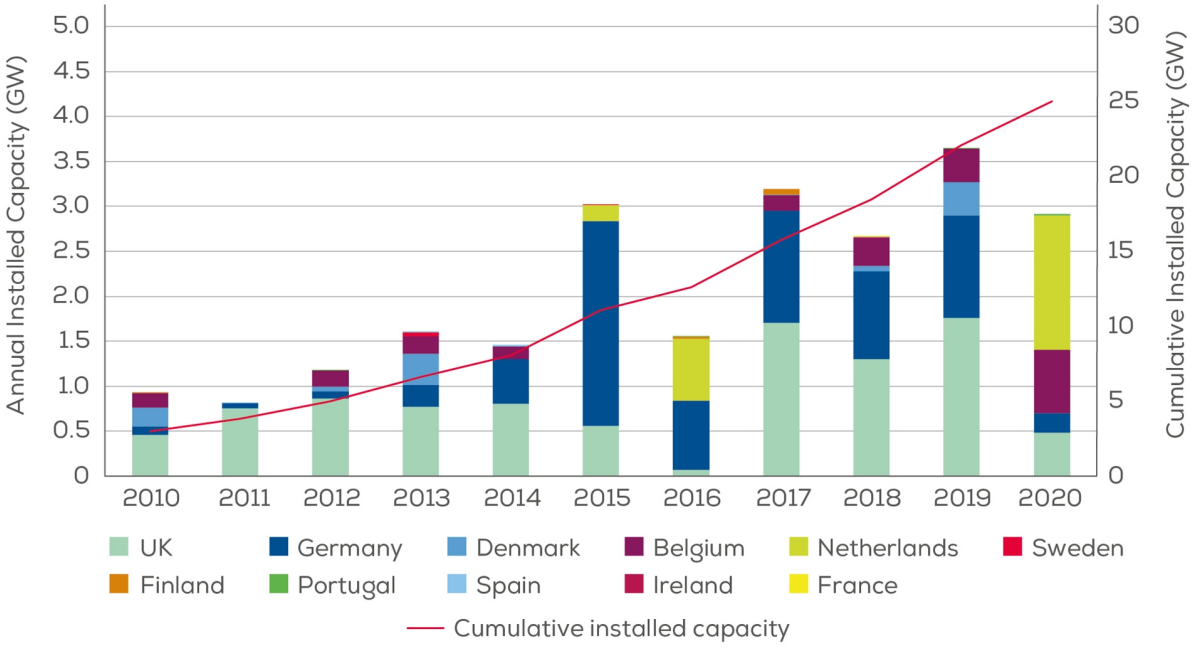


Figure 1.2 – Evolution of the total installed capacity of offshore wind in Europe for the past decade (WindEurope, 2020)

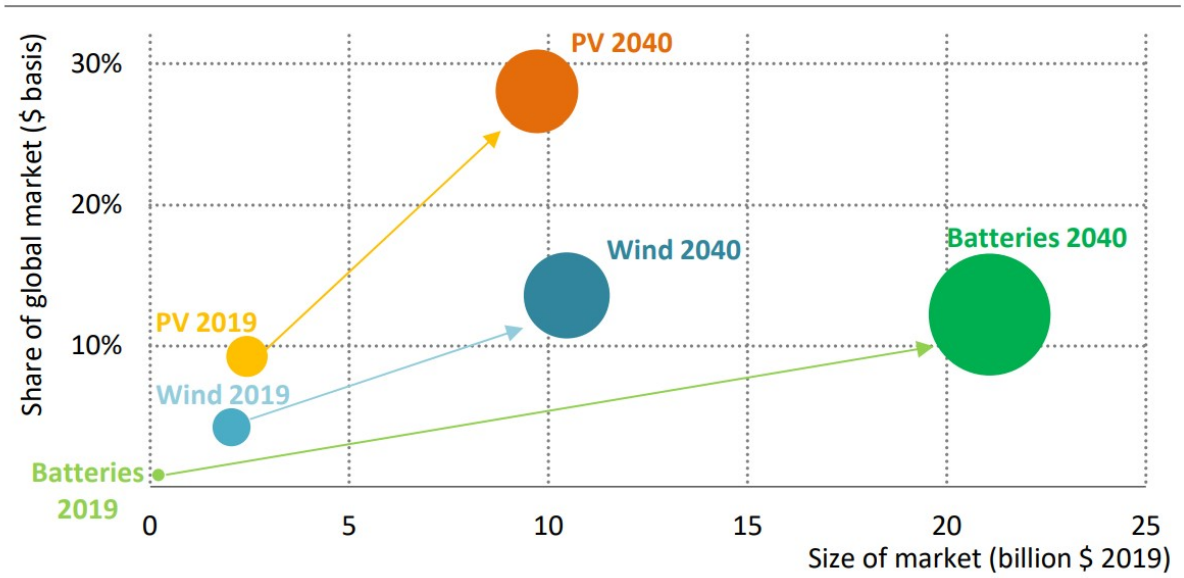


Figure 1.3 – India's market size and global share in clean energy technologies today and in the STEPS, 2040 (India Energy Outlook, 2021)

(414 GW). Coal, oil, and biomass supplied regularly more than 80% of India's overall energy needs. Coal has played a significant role in India's economic development while also contributing to air pollution and growing GHG emissions. Oil demand has more than doubled since 2000 as a result of growing vehicle ownership and road transport use. A lack of domestic resources means that India's dependence on crude oil imports has been steadily rising, reaching around 75% in 2019. Traditional biomass (predominantly fuelwood, but also animal waste and charcoal) was India's second largest energy source in 2000, accounting for roughly one-fourth of the primary energy mix. Overall, coal has an energetic share of 56% of today's generation (235 GW), natural gas and nuclear have an energetic share of less than 35 GW, and renewables are responsible for 137 GW. Among the renewables, Hydropower has a capacity of 49 GW, solar PV and wind has a capacity of 38 GW each, and other renewables have a capacity of 12 GW (India Energy Outlook, 2021).

The growing number of countries and organisations pledging to achieve net zero emissions reflects the growing feeling of urgency and escalating momentum surrounding clean energy transitions. By 2040, for each renewable sector, India will hold a significant portion of the worldwide market - roughly 10% for lithium-ion batteries, 15% for wind turbines, and 30% for solar PV (India Energy Outlook, 2021). STEPS predicts that by 2040, India's total capacity demand will be 1552 GW, with 1066 GW coming from renewables, according to the country's clean energy mission. By 2040, solar PV and wind will contribute for 88% of overall development. Furthermore, it is expected that the demand for wind energy will increase five fold above current available resources. Offshore wind has yet to take off in India, despite a potential of 10 GW to 20 GW, due to high capital costs, supply chain and infrastructure impediments. However, in the IVC (Indian Vision Case), with the industry gaining traction, offshore wind development will eventually increase, reaching 30 GW in 2040 (India Energy Outlook, 2021). As a result, academic and industrial research are essential for this clean energy mission, particularly in India's untapped offshore wind energy sector.

### 1.1.2 Offshore Wind Turbine substructures

Offshore windfarm support structures/foundations are typically more complex than onshore wind farms, posing more technical issues in design requirements to withstand the severe marine environment and persistent impact under large wave loads. Many offshore wind energy substructure ideas come from the decades-long development of the oil and gas industries. In general, the support structure of offshore wind turbines is used to classify them as, fixed OWT refers to a support structure that is bottom-mounted to the seabed and whose stability is controlled by a bottom fixed structure (monopile, jacket) and Floating OWT (FOWT) refers to a support structure that has no rigid connection with the seabed and whose stability is controlled by buoyancy and mooring (SPAR, TLP, Semi-Submersible). Some of the most popular offshore wind turbine foundations are given in Figure 1.4 and the brief descriptions of each type is discussed in this section. In Figure 1.5, the overall proportion of different substructure types for grid connected wind turbines until 2018 are presented.

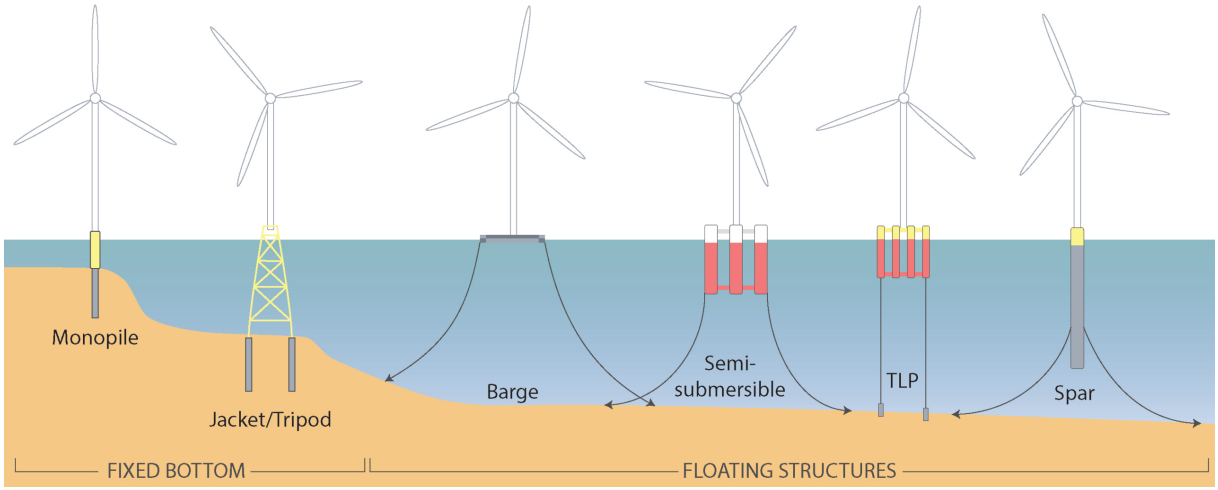


Figure 1.4 – Typical overview of offshore wind turbine substructures in industry (Focus, 2020)

#### 1.1.2.1 Bottom-mounted offshore wind turbine

The bottom-mounted wind turbine farms have been developed mainly in northern Europe and Asia (80% of the global market) and have increased by 30% per year over the last 10 years (IPCC). More than 80% of the grid connected offshore wind turbines are installed on monopiles (Figure 1.5). The monopile is the most widely adopted bottom fixed OWT because of its ease of production and installation. They consist of a steel tube section with a diameter of 4–6 m and a mass of up to 1000 tons that transfers the applied vertical and lateral loads into the seabed foundation. Horizontal earth pressures developed in the surrounding soil along the monopile immersed length resist cyclic lateral and moment loading arising from the waves and wind (Musial and Ram, 2010). It has the disadvantage of limited structural rigidity and damping due to its narrow shape hence limited to a shallow water depth of less than 30m.

The braced support structures (i.e. tripod and jacket/truss) are an alternatives to the monopile at deeper water because of their considerable structural stiffness. Tripods (Hildebrandt et al., 2013a) consist of a large-diameter central steel tubular section supported over its lower length by three braces. Jacket structures are lattice frames that are better suited to water depth of 20m-50m. Because the strut components offer less resistance to prevailing ocean waves and current flow than monopile, braced frame structures are particularly suitable for severe marine conditions. On the other hand, jackets are more expensive and require more maintenance than monopiles. Gravity-based structures (GBS), which can also be used to support offshore fixed turbines, are limited to moderate wave loads, while the manufacturing cost stays low due to the usage of concrete. But these bottom fixed structures have a limitation of water depth. As a result, the areas where these turbines can be installed are placed extremely close to the shorelines.

#### 1.1.2.2 Floating Offshore Wind Turbine (FOWT)

Moving from fixed foundations to floating structures is the option for taking advantage of the vast wind resource of seas in greater water depth. Ballasting, mooring, and buoyancy are

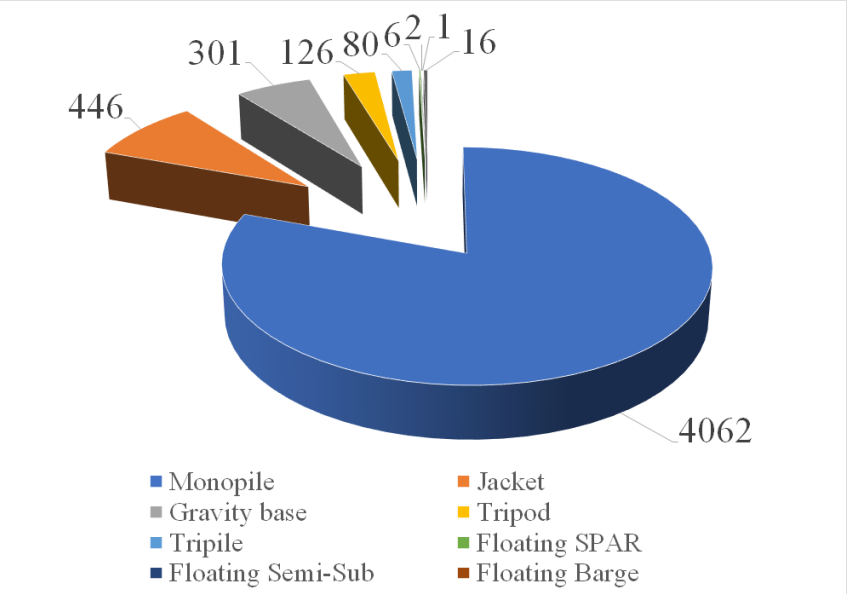


Figure 1.5 – Quantity share between substructure types for grid-connected wind turbines (Europe, 2018)

used to achieve floating stability in any FOWT structure. Floating wind turbines have clear advantages over their fixed equivalents like they are less sensitive to water depth, which expands the number of possible installation locations and the wind is more consistent, allowing for more precise control of energy generation. Finally, compared to bottom-fixed offshore wind turbines, the turbine can be constructed at the quayside and then towed to the location with conventional vessels, reducing installation time. This FOWT concept is based on a floating platform anchored to the ocean floor by mooring and connected to the land through an undersea cable. The major components of the FOWT are the wind turbine, floater and mooring. Only a few pilot projects have been deployed in the FOWT industry so far, although many advanced concepts have been reported in the literature. In any case, it has its drawbacks, including questionable engineering in the development (not enough FOWT to provide a clear picture of the optimum platform), interconnecting cables or chains that might disturb offshore ecosystems, and the need for extra heavy-duty cables to anchor floating platforms and to withstand the effects of wind and waves. A brief overview of some of the well-known floating substructures, including SPAR, Tension-Leg Platform, Semi-submersible, and Barge, is discussed in this subsection.

— **SPAR** : The vertical cylinder column with a large draft is regarded as SPAR. Ballasting is used to place a substantial mass at the bottom of the structure to lower the COG as much as possible. The buoyancy and mooring lines provide lateral stability. A Hywind design SPAR (Skaare et al., 2015) wind farm of five wind turbines (6 MW) has been installed and operational in Scotland since 2017.

— **Barge** : The barge has an extremely shallow draft, and its large waterplane area provides greater buoyancy and stability. FLOATGEN (Alexandre et al., 2018), a first 2MW prototype that has been deployed and is currently in service off the coast of France, is based on

the barge method.

— **TLP** : The TLP has excellent stability because of taut mooring lines that resist motions. Compared to other methods, this one offers the distinct benefit of being compact and having a lower structural mass. On the other hand, the platform installation can be complex due to the difficulty of installing high tension mooring lines to the bottom and the fact that it is naturally unstable when removed from its mooring system.

— **Semi-Submersible** : The buoyancy of semi-submersibles acts as a source of their stability. These platforms have the benefit of being relatively simple to set up. The floater can be towed to its destination or brought back to shore for repair or decommissioning, and the turbine can be placed on the quayside. It requires catenary mooring lines, which are less expensive than TLP platforms taut lines. Its most significant limitation is its complicated geometry, making fabrication more challenging.

All upcoming innovation (SpiderFLOAT (Dinius et al., 2022), OrthoSpar (Büttner et al., 2022), Hexafloat technology (Delahaye et al., 2019) and more) are now being investigated in order to make the offshore floating wind sector much more efficient in the future; nonetheless, these innovations will more or less fit into the above-listed floating categories. For a full overview of current technology in the FOWT, Castro-Santos and Diaz-Casas (2016) can be referred.

## 1.2 Current modeling techniques of OWT in Industry

For any concept of OWT, the engineering team has to design these structures to withstand metocean conditions throughout its lifetime. Finding an optimum solution that will provide survivability and efficiency at the lowest possible cost is crucial. Several engineering tools are developed based on simplified assumptions to study the multi-physics involved with OWT in a reasonable amount of time. This section briefs some of the techniques in modelling fixed and floating OWT.

### 1.2.1 Fixed OWT

Fixed offshore wind turbine substructure are frequently subjected to highly non-linear hydrodynamic loads from intermediate and shallow ocean conditions, including breaking waves. Extreme waves over the monopiles are inevitable during severe storms, when the strongest wave forces are expected. The IEC 61400-3 (2009) design code, among other handbooks, describes the current industry standard methodology for wave loads prediction on offshore wind support structures. Because the substructure environments are so similar in both instances, SACS (Bentley, 2018), SESAM (DNVGL, 2018) or any other oil and gas industry software tools can be used directly to design the substructure of OWT. But extreme or breaking waves are not represented in these similified model. As a result, more advanced approaches like CFD and reliability methodologies should be used and to understand the influence of extreme waves that cause the most damage to structures.

### 1.2.2 Floating OWT

For FOWT, aero-hydro-servo elastic solvers are often used to simulate the coupled behaviour of the turbine subject to wind and the floater motion due to waves and the elasticity of the overall structure. Thousands of design load cases (DLC) must be undertaken to test the FOWT's behaviour under various normal and extreme conditions. The system's design is thus validated or modified based on modelling results to verify design criteria such as motion, acceleration, mooring line tension, structural forces and moments, etc.

OpenFAST (Jonkman, 2013) is an aero-servo-hydro-elastic solver that optimises wind turbine design and lowers costs by simulating it in their environment. It is a partly nonlinear, multi-physics open-source tool for modelling the coupled dynamic response of wind turbines with modules like ElastoDyn, InflowWind, AeroDyn, ServoDyn, HydroDyn, and SubDyn.

— The structural dynamics module ElastoDyn is used to model the tower, platform, and rotor-nacelle assembly.

— The structural dynamics module SubDyn is used to model multi-member, bottom-supported substructures. Jackets, tripods, monopiles, and other non-floating lattice-type substructures for offshore wind turbines are supported by this module.

— The hydrodynamics module, HydroDyn, is used to calculate linear hydrodynamic forces on multi-member substructures. Regular waves, irregular waves from a JONSWAP or Pierson-Moskowitz spectrum, and irregular waves from a white noise spectrum may all be computed by HydroDyn. The hydrodynamic coefficients from linear diffraction and radiation problems computed with WAMIT or comparable programs must be provided to Hydrodyn.

— AeroDyn is a time-domain aerodynamics module that evaluates the aerodynamic loads on the blades and tower (lift, drag, and pitching moments).

— ServoDyn is OpenFAST's control and electrical drive dynamics module.

— InflowWind is an OpenFAST module for processing TurbSim's wind-inflow data. TurbSim is a turbulent-wind simulator that numerically simulates stochastic, full-field time series of three-component wind-speed vectors using a statistical model.

Other engineering tools capable of simulating the coupled dynamic response of wind turbines are HAWC2 (Horizontal Axis Wind turbine simulation Code 2nd generation, (Larsen and Hansen, 2007)) or DeepLines Wind (Le Cunff et al., 2013). They are primarily built on OpenFAST-like components. In simulations, aerodynamic loads, turbine and floater structural dynamics, active controller, hydrodynamic loads, and mooring line dynamics can all be included. The floating supports are defined using a hydrodynamic database generated by a diffraction/radiation code like WAMIT from the Massachusetts Institute of Technology (Lee and Newman, 2006) or ANSYS-AQWA (Ansys, 2013), which includes added mass and radiation damping matrices and first and second order wave loads. The empirical formulation of Morison can also be used to calculate wave loads (Morison et al., 1950).

### 1.2.3 Necessity for a CFD

Two theories widely used in offshore Oil and Gas sectors are applied in design solvers to estimate hydrodynamic load and behaviour of OWT based on the system's diameter to wavelength ratio ($D/\lambda$) and Keulegan–Carpenter (KC) number (Keulegan et al., 1958). One is the potential flow theory ($D/\lambda > 0.2$, KC $< 2.0$), which is applied when the oscillatory flow is too slow to allow the boundary layer to detach. The second is Morison empirical formula ($D/\lambda < 0.05$, KC 2 - 90), which is used when the oscillating flow is separated from the body's surface. The potential flow theory usually applied considers the solution of a boundary value problem for inviscid, incompressible flow about a rigid body. Using a panel method solution, this approach accounts for Froude-Krylov forces and diffraction effects for large volume structures. The resulting solution is frequency-dependent. Morison's equation is semi-empirical for calculating wave loads on slender structures. For a fixed cylindrical structure, it is equivalent to the potential flow solution when the wavelength to diameter ratio is large and viscous effects are negligible (Faltinsen, 1993). Morison's equation does not, however, account for diffraction effects. Due to the quadratic drag force and the formulation of relative velocities and accelerations, Morison's equation is solved in the time domain with frequency-independent coefficients. OrcaFlex software (Orcina, 2018), which specialises in analysing moored floating structures, mainly uses the Morison theory. A length, diameter, mass, inertia, and drag coefficient can be assigned to a line element at which the structure's geometry is modelled. Both these models can be efficient at a low computational cost, depending on the needed accuracy level. They are useful for anticipating OWT behaviour under 'operational' situations. For weakly nonlinear circumstances and simple geometries, they can also estimate higher-order loads. However, none of these approaches can account for violent nonlinear cases, rotational or turbulent effects that occurs in several situation, e.g. green water loading, breaking wave interaction, wave run up extreme wave interaction etc. To summarise the limitations of these theories:

— The OWT design can be near the limit of these theories validity range under specified wave characteristics and structure dimensions.

— In terms of the Morison formula, for simplicity and robustness, some assumptions or simplifications are usually adopted, such as employing one set of coefficients (drag and inertia) regardless of sea condition and identical for all members of similar diameter.

— Higher order wave loads are induced by irregular waves, which are known to be difficult to estimate using engineering methods when compared to experimental data. When using potential flow theory, they appear to be underestimated, while when using the Morison formula, they appear to be overestimated (Kvittem et al., 2012).

— Other basic assumptions of potential theory, such as irrotational flow, may limit the ability to reproduce realistic OWT behaviour in the presence of highly nonlinear waves.

— Investigation of the extreme sea state, including breaking waves, is not possible using the existing approximate software such as Ansys Aqua or similar time domain models

This demonstrates the necessity for a more advanced method of examining OWT hydrodynamics, such as Computational Fluid Dynamics (CFD). CFD simulations provide extensive

information on the pressure and velocity fields around the structure (for flow separation, Vortex Induced Vibration (VIV) studies), and highly nonlinear load distributions. It also includes viscous and turbulent effects in the fluid to replicate realistic flow behaviour like breaking and broken wave-structure interaction phenomena. However fine mesh elements are required to avoid excessive numerical dissipation during wave propagation and this comes at a higher computational costs than simpler models such as potential flow .

## 1.3 Numerical modeling using hybrid coupling approach

The numerical models for water wave applications have been generally classified based on the physics involved such as, FNPF (Fully Nonlinear Potential Flow models), CFD model (that solves Navier Stokes (NS)), NLSW (Nonlinear Shallow Water equations models), BT (Boussinesq-type models) and more. CFD and FNPF models are the most robust among the models for its wide range of applications. The scientific community has developed several FNPF-CFD coupled models over the years because of the model's robustness to different applications. In this subsection, each model is given a brief introduction before the coupling discussion.

### 1.3.1 CFD - Viscous flow models

The Reynolds-averaged Navier–Stokes equations (RANSE) is widely used in naval and offshore engineering applications, and it can be solved efficiently by breaking down velocities and viscosity into time-averaged and fluctuating components. This model can be solved by conventional Finite Volume Method (FVM) (Marshall et al., 1997), Finite Difference Method (FDM) (Chorin, 1968) or meshless particle-based methods (Lind et al., 2012; Rijas et al., 2019). Because the FVM satisfies the conservation laws even when the discretized mesh is relatively coarse, it is widely employed. In the context of Wave-Structure Interaction (WSI), air entrapment, viscous and turbulent effects mostly matter only in the close vicinity of the body. CFD models (Devolder et al., 2017; Kim et al., 2005a) can accurately capture the mentioned effects. The commercial viscous flow solvers using FVM used for naval applications are Simcenter STAR-CCM+ (Siemens, 2019) , FINE/Marine (NUMECA), ANSYS CFD (ANSYS, 2009). Commercial tools are robust, simple to use, and come with professional, effective support as part of the licencing. They consist of highly effective pre- and post-processing modules, meshing tools, and computer-aided design (CAD) software. However, the source codes are inaccessible, immutable, and occasionally referred to as a "black box." Additionally, licences might be expensive. The popular open-source code, Open-source Field Operation And Manipulation (OpenFOAM, OpenFOAM (2009)), is widely applied by researchers since the source code is completely transparent and simple to modify. Also, it has many integration strategies and solvers for a wide range of problems. In this thesis, OpenFOAM was mainly adopted in all simulations. However, CFD tools need a long computational domain to ensure adequate development of nonlinear wave propagation and to avoid boundary effects caused by waves interacting with any fixed or floating structures in the domain. Additionally, very fine mesh elements are needed to prevent excessive numerical

dissipation during wave propagation. Due to the considerable increases in computational costs caused by these factors, standard CFD methodologies are not practical for regular simulations of wave-structure interactions (Vandebeek et al., 2018; Yan et al., 2019; Ransley et al., 2020).

### 1.3.2 Potential flow models

When wave propagation over long distances or viscous effects around the structure can be ignored, FNPF models are routinely used to solve the problems. The FNPF models can be solved using the boundary element method (Grilli et al. (1989)), finite element technique (Wu and Hu (2004); Yan and Ma (2007); Sriram et al. (2006)), FDM (Engsig-Karup et al. (2009, 2012); Bihs et al. (2020)), FVM (Lin et al. (2021)), spectral element method (Engsig-Karup et al. (2016)), and high order spectral method (Ducrozet et al. (2012)). The commonly adopted potential flow commercial codes published are HydroStar (Chen, 2011) from Bureau Veritas, WAMIT (Lee and Newman, 2006), WADAM (Veritas, 1994) from DNV GL, ANSYS AQWA (Ansys, 2013). Also, there is an open-source code NEMOH (Babarit and Delhommeau, 2015) is available. In comparison to CFD models, these models have proved to require less computational effort at a given level of accuracy (Nematbakhsh et al., 2015). The FNPF models has less energy loss for long time simulations comparted to CFD. Düz et al. (2016) analyzed the capability of different potential models to couple with viscous solvers and concluded that none of them is superior to one other. However, when the flow separation and breaking happens, the irrotational flow assumption of the linearized potential theory might provide numerical difficulties in reproducing the realistic wave-structure interaction situation.

### 1.3.3 Coupling between the solvers

In recent years, a considerable effort has gone into developing near- and far-field coupled hybrid models that effectively cope with the shortcomings of both the CFD and the FNPF models. The goal is to use the CFD wave models near the body and the FNPF wave models far away from the body where viscous effects are minimal (indeed, the main objective of the FNPF model is wave generation). The scientific community has developed both meshless (Sriram et al., 2014b; Fourtakas et al., 2018; Yan and Ma, 2017) and mesh-based NS models (Campana and Lalli, 1992; Colicchio et al., 2006; Jacobsen et al., 2012) coupled with FNPF over the years. Refer to (Di Paolo et al., 2020; Sriram and Ma, 2021) for a detailed discussion of multiple hybrid coupled models developed for WSI problems. These FNPF-CFD coupling models can be classified as domain decomposition (DD) and functional decomposition (FD) strategies.

#### 1.3.3.1 Domain decomposition

The DD strategy divides the computational domain into parts and applies different mathematical models in each part. In most DD-based WSI problems, the computational domain is decomposed into a viscous inner sub-domain and a potential outer sub-domain. The information (velocity, pressure and surface elevation) will be transferred through either relaxation zones or a sharp interface. Jacobsen et al. (2012) introduced relaxation zones on coupling boundaries

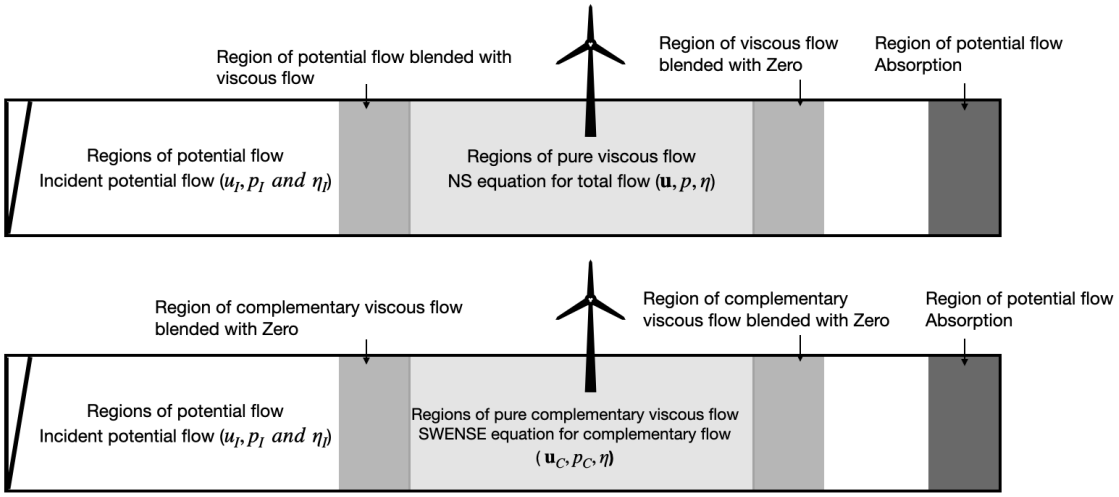


Figure 1.6 – Schematic representation of DD (top figure) and FD (bottom figure) coupling methods in numerical wave tank(NWT). $u, p, \eta$ represents velocity, pressure and surface elevation, respectively and subscript 'c' represents the complementary field variables

to gradually blend the information between the two models. In these zones, the weight function is applied for the smooth transition of flow quantities. Higuera et al. (2013) proposed a sharp interface instead of relaxation zones, which benefits the reduction in the computational domain, but there is a high chance of reflection reported. Also, based on how the information between the solvers is being transferred, it can be either one-way coupling (weak coupling) or two-way coupling (strong coupling). In one way coupling (for literature review, see Table 1.1), information is transferred only from the potential solver into the viscous solver, but in two way coupling (for literature review, see Table 1.1), the information is transferred in both ways, from potential to viscous and from viscous to potential solvers.The two-way coupling is advantageous since it allows for a significantly smaller computational region for the viscous solver. However, it necessitates an iterative process or an implicit approach between the two models on a shared interface, which might increase the computational costs. The advantage of one-way coupling is that no such iterations are needed, but it needs a longer viscous domain to avoid the reflection from outer boundaries. This approach is applicable only to the transient wave problems. *foamStar* (Choi et al., 2020), a DD-based one-way coupled solver developed by Bureau Veritas and Ecole Centrale Nantes with the background of interDymFoam from the OpenFOAM package, is one of the solvers used for the present investigation. Choi et al. (2018c); Kim (2021a) can be referred for developments and validations of the solver.

#### 1.3.3.2 Functional decomposition

The fundamental concept for the FD is Dommermuth (Dommermuth, 1993) proposal to use the Helmholtz decomposition to separate the velocity field into the rotational and irrotational parts to investigate the free surface flow. There are two categories under this decomposition,

based on whether the structure is considered in the potential solver or not. In the first category, the WSI problem is split into a potential component and a viscous part. The complete problem is initially solved by a potential solver, and then rectified by adding the viscous correction (Kim et al., 2005a,b; Edmund et al., 2013; Rosemurgy et al., 2016; Robaux and Benoit, 2021). One drawback of this strategy is that the potential solver must first solve the entire problem before applying viscosity correction. As a result, challenges such as higher-order waves, stability issues in the steep waves and breaking induced by presence of structure with complex interactions are still constraints in this classification. Recently, Robaux (2020) recently published a thorough description of nonlinear waves interactions with a horizontal cylinder with a rectangular cross section employing potential solver, CFD solver, and HPC-OpenFOAM coupled DD and FD based solver. In comparison to the full CFD simulation, both coupling approaches, in particular the FD-based approach, need a minimal amount of computational time while providing an accurate representation of the loads and associated hydrodynamic coefficients. In the second category, the total unknown ($\chi$) is decomposed into the incident part ($\chi_I$) and the complementary part ($\chi_C$). Only the incident flow is modelled in the incident part (Wave only), leaving all the interaction with structure calculated by the viscous solver as the complementary part. The common name among researchers for this classification is SWENSE (Spectral Wave Explicit Navier Stokes Equations), proposed by (Ferrant et al., 2002) and actively developed by (Gentaz, 2004; Luquet et al., 2003; Li et al., 2018; Kim, 2021a). The NS equation modified into the SWENSE is solved to yield the complementary fields ($\chi_C$). The advantage of this method is that the wave models directly provide incident wave solutions, minimising the problem's complexity and cost. For a detailed derivation of single-phase and two-phase SWENSE, refer to (Luquet et al., 2007) and (Li et al., 2018) respectively. The applications in single-phase SWENSE over the years can be read in (Luquet et al., 2007; Monroy et al., 2010). The proposed two-phase SWENSE method (Li et al., 2021b) is implemented on top of *foamStar* and is called as *foamStarSWENSE*, and the only difference is that in this solver, the NS equations in *foamStar* are replaced by SWENSE. Recent developments of *foamStarSWENSE* such as efficient regular and irregular wave generation in the solver and higher-order forces estimation on a vertical cylinder and buoy can be read at Choi (2019); Kim (2021b); Li et al. (2018).

### 1.3.4 Summary and coupling of two flows

To outline, Figure 1.6 represents the numerical wave tank (NWT) with the potential and the CFD model along with the relaxation zones. The top figure represents the DD one way coupling, and the bottom represents the FD approach. The potential solution is blended into the CFD domain through the inlet relaxation zone in the DD, and the blended properties are carried forward inside the CFD domain by solving the NS equation. The CFD solution is blended to zero/incident wave characteristics based on one/two way coupling in the outlet relaxation zone. In the FD, potential solutions are available across the domain; therefore, incident potential solutions are interpolated across the SWENSE grid and processed at each instant. Inside the computational domain, only complementary fields are solved using SWENSE, and

waves diffracted/radiated from the body are suppressed in the relaxation zones. Table 1.1 can be referred for summary of literature for DD and FD based solvers (inspired from Choi et al. (2017a)).

### 1.3.5 Modeling of Floating structures with CFD

In general, any problem in CFD implies the use of a grid or mesh to replace a continuous problem domain with a finite field. This model works flawlessly when the problem does not involve any solid body motion in the computational domain. However, many offshore engineering applications require solid body motion in the computational domain, which has a consequence on the fluid flow. Sliding interface, overset mesh adaptation, and mesh morphing are the three different ways dynamic mesh motion operates in OpenFOAM. A sliding interface allows one or more internal subdomains to translate or rotate relative to a static background mesh domain, with the interface between the domains sliding relative to each other. The main disadvantage of sliding interfaces is that they are only appropriate for single DoF motions. A complex motion can be simulated using a mesh overset technique, but it may prove very computationally expensive mainly due to the mesh refinement and adaptation, the remapping, and the re-computation. This is not necessary if the mesh is only deformed and the mesh's topology remains unchanged. Pinguet (2021) has extended the application of overset meshes in wave structure interaction problems by investigating the hydrodynamic response of the NREL-designed DeepCWind semi-submersible FOWT. Mesh morphing is the most commonly used method in CFD floating body simulations. The method deforms meshes into new meshes by updating the node positions near the floating body while preserving the shape of the target floating body. Because only the nodal positions are updated, the necessary computation time is shorter than that of the sliding interface and overset mesh methods. However, in the case of large deformations, solutions may diverge due to the skewness of the mesh, and meshes that have been optimized for a generated wave signal may also get impacted. Windt et al. (2018) concluded that while run time is longer, the accuracy of the overset mesh is equivalent to that of the mesh morphing approach. When the body motion exceeds the mesh morphing strategy's maximum level of stability, it is advised to employ the overset method. Assuming that the amplitude of the floating body motion is relatively small in the studies carried out during this Ph.D, the mesh morphing deformation method is adopted. A few recent literature on floating structures in CFD with morphing techniques are :

Benitz et al. (2014) compares results from a CFD model using OpenFOAM for the DeepCwind semi-submersible concept with potential flow theory and the Morison equation using the Hydrodyn module from FAST. The thesis employed a loosely coupled Fluid-Structure Interactions (FSI) solver derived from OpenFOAM to simulate the DeepCWind floater. However, the motion predictions were inadequate when compared to experimental data. Bruinsma et al. (2018) worked on the DeepCWind platform's wave-induced motions and free decay tests. For wave generation and absorption, they employed waves2foam (Jacobsen, 2017), and they also provided a quasi-static mooring approach that was implemented in waves2foam. The results are compared with those of experiments and the need for a stabilizing method for FSI simulation

| Previous research | Decomposition | Coupling way | Numerical model | |
|---|---|---|---|---|
| | | | Potential | NS |
| Guignard et al. (1999) | DD | One | BEM | FVM |
| Lachaume et al. (2003b), Grilli et al. (2004) | DD | One | BEM | FVM |
| Christensen et al. (2009) | DD | One | $\phi_I$ | FVM |
| Jacobsen et al. (2012) | DD | One | $\phi_I$ | FVM |
| Hildebrandt et al. (2013b) | DD | One | FEM | FVM |
| Higuera et al. (2013) | DD | One | $\phi_I$ | FVM |
| Paulsen et al. (2014a) | DD | One | FDM | FVM |
| Düz et al. (2016) | DD | One | FDM | FVM |
| Monroy et al. (2016), Choi (2019) | | | | |
| Kim (2021b) (*foamStar*) | DD | One | $\phi_I$, HOS | FVM |
| Agarwal et al. (2021b) | DD | One | FEM | MLPG |
| Robaux and Benoit (2021) | DD | One | HPC | FVM |
| Tahara et al. (1992) | DD | Two | BEM | FVM |
| Campana and Lalli (1992) | DD | Two | BEM | FVM |
| Campana et al. (1995) | DD | Two | BEM | FVM |
| Chen and Lee (1999) | DD | Two | BEM | FVM |
| Guillerm (2001) | DD | *Two* | Poincaré | *FDM* |
| Iafrati and Campana (2003) | DD | Two | BEM | FVM |
| Colicchio et al. (2006) | DD | Two | BEM | FVM |
| Hamilton and Yeung (2011) | DD | Two | Shell func | FVM |
| Sriram et al. (2014b) | DD | Two | FEM | IMLPG |
| Fredriksen (2015) | DD | Two | HPC | FVM |
| Lu et al. (2016) | DD | Two | FVM | FVM |
| Siddiqui (2017) | DD | Two | HPC | FVM |
| Verbrugghe et al. (2018) | DD | Two | FDM | SPH |
| Choi (2019) | DD | Two | Poincaré | FVM |
| Landesman (2022) | DD | Two | BEM | FVM |
| Kim et al. (2005a) | FD I | One | BEM | FVM |
| Kim et al. (2005b) | FD I | One | $\phi_I$ | FVM |
| Edmund et al. (2013) | FD I | Two | BEM | FVM |
| Rosemurgy et al. (2016) | FD I | Two | BEM | FVM |
| Robaux and Benoit (2021) | FD I | One | HPC | FVM |
| Ferrant et al. (2002) | FD II | One | $\phi_I$ | FDM |
| Gentaz (2004) | FD II | One | $\phi_I$ | FVM |
| Luquet et al. (2007) | FD II | One | $\phi_I$ | FVM |
| Vukčević et al. (2016) | FD II | One | $\phi_I$ | FVM |
| Li et al. (2018), Kim (2021b) (*foamStarSWENSE*) | FD II | One | HOS | FVM |

Table 1.1 – Summary of research on the coupling of potential/viscous flows updated from (Choi, 2019); BEM (Boundary Element Method), FVM (Finite Volume Method), HOS (Higher Order Spectral method), $\phi_I$ represents incident velocity potential for potential solvers based on analytical wave theories

is emphasized. The simplified mooring concept showed good effectiveness. Other literature used to investigate the DeepCWind floater using OpenFOAM can be read at Rivera Arreba (2017), Zhou et al. (2019), Dunbar et al. (2015). Burmester et al. (2020) examined the surge motion of the DeepCWind platform with 3 DoF using the software ReFRESCO (Vaz et al., 2009). Wang et al. (2019b) used ReFRESCO to calculate the same floater's pitch decay motion. Huang et al. (2021) and Cheng et al. (2019) evaluated the same DeepCwind floater with the naoeFOAMSJTU model (Wang et al., 2019a).

Quallen and Xing (2016) used CFD to analyse the aerodynamics of the turbine and the hydrodynamic flow around the Spar type FOWT. They also created and used a generalised quasi-static crowfoot mooring line model for the OC3-Hywind FOWT system (Quallen et al., 2013). Beyer et al. (2015) used a coupling method between CFD and the Multibody software SIMPACK, a commercial aero-servo-hydro-elastic simulation tool, to model a Spar and barge type FOWT. In one part of the present thesis study, OC3 Hywind-based SPAR was hydrodynamically assessed with the DD and FD coupling (Section 1.3.3) and validated the models using the experimental results.

#### 1.3.5.1 Mooring

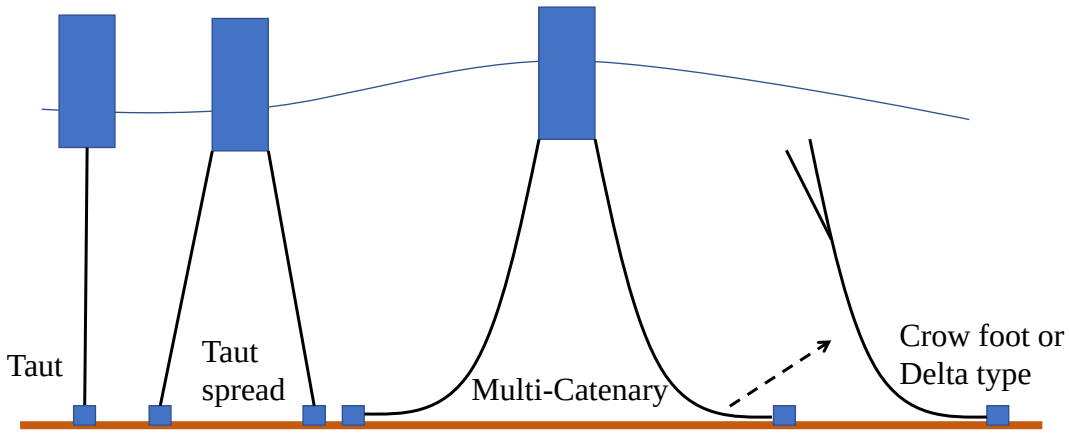


Figure 1.7 – Typical Mooring line configurations

Some of the typical offshore mooring configurations for station keeping of floating bodies in various sea states are shown in Figure 1.7. According to whether the line is pretensioned, stretched tightly, or hangs loosely, they are often categorised as taut or slack/catenary. In a catenary line, the horizontal restoring force for the floating structure is provided by the weight of the chain links or clump weights. Wire or synthetic ropes make up a taut-line system, which is typically quite pretensioned and as a result they are highly rigid in both the horizontal and vertical directions. If the taut mooring is directly attached to the sea floor, they can greatly reduce the vertical motions of the floating structure. Multiple catenary moorings are typically offered in places to lessen the horizontal movements of floating structure. The mooring lines used for Statoil's pilot Hywind FOWT are called crow-foot lines (last configuration in Figure

1.7), in which a catenary line is attached to the bottom and then splits into two distinct fairlead connections at the platform. The crowfoot mooring system contributes to the reduction of platform yaw by extending the mooring line's effective moment arm. As the platform yaws and one connection line starts to slacken, the arm of the crowfoot is currently switched from one fairlead connection to the other. In this study, the crowfoot mooring model (Quallen et al., 2013) is adopted and validated for OC3 Hywind-based SPAR.

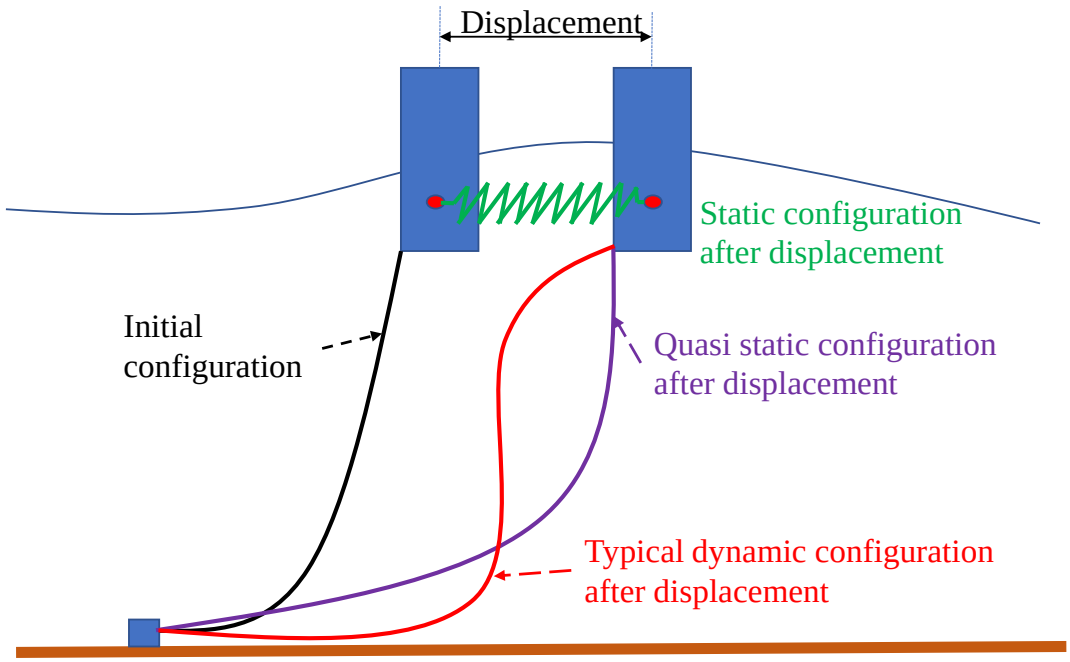


Figure 1.8 – Differnce between the static, quasi-static and dynamic mooring models, similar to (Vickers, 2012)

Different model types, with varied levels of complexity, can be used to mathematically describe the behaviour of the mooring system with interactions between the variables, parameters, and environmental inputs. Three forms of model types generally used are static, quasi-static, and dynamic mooring models with their typical representation shown in the Figure 1.8, they are briefly discussed in following subsections.

— **Static mooring model** : Static analysis is often used in preliminary design to compute the static response of moored vessels (Karnoski and Palo, 1988). By displacing the floating structure through prescribed distances and calculating the static restoring load, the static analysis also provides relationships between the displacement and the restoring force of the mooring line in terms of stiffness. The static analysis method is exceptionally quick and reliable for most systems and the typical spring-based static mooring method, as depicted in Figure 1.8 is used in the current study for both linear and rotational motions, and the findings are validated with experimental results (Refer Chapter 5).

— **Quasi static mooring model** : The offshore sector has a tradition of designing the mooring system through quasi-static analysis, justified by the low responsiveness of the

large masses involved and the corresponding low induced velocities. This approach ignores the dynamic effects on the mooring system and the motion dependence of mass, damping, and fluid acceleration on the system. Also these models derive the mooring line shape and tension from the catenary formulations, based on the assumption that the line is in static equilibrium in each time step, that inertia effects can be neglected and that the line profile is reasonably well described by the catenary equations. ANSYS AQWA (Ansys, 2013), MAP++ (Masciola et al., 2013), MoorPy (Hall et al., 2021), FLEXCOM (Kenny, 2016) are some of the software packages available for Quasi static mooring models. In operational conditions, this assumption might be sufficient (Thomsen et al., 2017), but it underestimates line tensions in extreme conditions, mostly due to the exclusion of hydrodynamic drag and inertial effects on mooring lines. Also, in deep waters, a mooring line's response may be delayed, causing it to violate the catenary profile assumptions of a quasi-static model (Vickers, 2012). Additionally, for some floating structures that react quickly to motions, a scenario similar to that shown in Figure 1.8 may arise, in which the top of the line follows the floater motion, but there is a delayed response further down the line, violating the catenary profile assumptions of a quasi-static model. The different graphs of computed displacements and tensions in Yang et al. (2012) show the significant potential differences between the predicted outputs from a quasi-static and a dynamic mooring models.

— **Dynamic mooring model** : The mooring line dynamics are formulated using Newton's second law (of motion), which states that motions are caused by forces acting on the body, similar to most mechanical systems. The solution to these equations must often be found by either linearizing the model or using numerical methods to approximation the governing nonlinear differential equations. The mooring line is discretized spatially to generate a set of ordinary differential equations (ODEs), which are then discretized in time and solved using an integration algorithm to get the numerical approximations. A static analysis solution is frequently the starting point for a dynamic simulation, which then evolves through time. Masciola et al. (2014) compared different spatial discretization techniques like finite differences and finite element methods (FEMs) with lumped mass method, while examining the features of the various models and weighing the benefits of each. The lumped mass approach has a significant benefit over other approaches. This method involves lumping of all the effects of mass, external forces and internal reactions at a finite number of nodes connected by massless springs. A set of discrete equations of motion is generated by applying the equations of dynamic equilibrium and continuity (stress/strain) to each mass (For detailed discussion refer Section 2.1.4.3.3). This method is shown to have the advantage of a strictly diagonal mass matrix, eliminating the requirement of added computation for matrix inversion such as in other spatial discretization techniques. MDD (Dewey, 1999), SEAWAY (Journee and Adegeest, 2003), OrcaFlex (Randolph and Quiggin, 2009), Moody (Ferri and Palm, 2015), and MoorDyn (Hall, 2015) are some of the mooring dynamics models developed in recent years. Compared to other models, MoorDyn is an open-source lumped-mass mooring line model, developed at the University of

Victoria, Canada, that supports arbitrary line interconnections, clump weights and floats, and different line properties. The model accounts for internal axial stiffness and damping forces, weight and buoyancy forces, hydrodynamic forces from Morison's equation, and vertical spring-damper forces from contact with the seabed.

For detailed review of the mooring models, Davidson and Ringwood (2017) can be referred. The one goal of the present study aims to implement a static and lumped mass based dynamic mooring model (MoorDyn) into *foamStar* and *foamStarSWENSE* to carry out a complete hydrodynamic coupled analysis of moored floating structures mimicking the model test in NWT.

## 1.4 Motivation

The motivation of the present thesis is to create a cutting-edge numerical simulation software for wave-structure interactions, particularly exploring different possibilities of coupling fluids, structures and mooring lines. *foamStar* (Choi et al., 2018a) is one such solver which is based on the one-way DD strategy and it is a two-phase viscous CFD solver built from the open-source CFD package *OpenFOAM*. *foamStarSWENSE* is another solver based on two-phase SWENSE method (Li et al., 2021b) with FD strategy and it is implemented on top of *foamStar*. The only difference between *foamStarSWENSE* and *foamStar* is that SWENSE is used in place of the NS equations in *foamStar*. Both the *foamStar* and *foamStarSWENSE* solvers are used in this thesis.

Despite the coupling of a single-phase potential solver with a two-phase viscous solver has already been documented in the literature, it was mainly used for domain decomposition rather than functional decomposition. Li et al. (2021b) created a two-phase model with the objective of using coarse mesh for incident wave propagation to reduce the computational cost. Yet, the developed model was validated on a limited number of applications such as wave generation and propagation (Choi, 2019; Li et al., 2021b; Kim, 2021b), higher order forces over the cylinder in regular waves (Li et al., 2021b) and seakeeping analysis of a ship with forward speed in waves (Kim, 2021b).

New applications are examined in this thesis to evaluate the efficiency and robustness of the coupling methods proposed, such as focusing waves impact over fixed and moving cylinders, and wave interaction with floating body. In order to simulate the moored floating body interaction, an open source mooring solver is coupled with the CFD. These applications are tested with both the DD and FD solvers, and a meaningful comparison is given, as well as suggestions for improvements is provided.

## 1.5 Objective and Scope of the thesis

The aim of the thesis is to evaluate the performance of two different coupling procedure in CFD (based on DD and FD) to simulate complex interactions between fixed, moving and floating bodies in extreme waves.

**Scope :**

The following is the scope of the study, with the research question investigating the extreme wave-structure interaction using DD and FD approaches:

- Application of the developed model to handle regular and irregular sea state, non-breaking and breaking focused waves.
- Development and improvement of the coupled (potential + viscous) numerical solvers to handle the extreme waves with fixed and moving structures.
- Investigation on the domain decomposition and functional decomposition approaches and its efficiency for wave interactions with floating structures.
- Inclusion of mooring models in the numerical solvers for solving moored floating structures and their validation with experiments.

## 1.6 Contribution of the present work

The present thesis aims at addressing the following question: the performance of the domain decomposition and functional decomposition approach for wave-structure interactions, particularly for dealing with extreme events. The contributions made in this work are summarised in the following section. The thesis is split into three parts. The first and second part focused on studies involving cylinder resembling monopile foundation, whereas the third part is based on applications involving substructure of FOWT.

The DD-based solver *foamStar* and FD-based solver *foamStarSWENSE* addresses the focused waves interactions with the fixed and moving cylinder. Additionally, the aspect of computational efficiency is also highlighted. The experimental details used for comparison in the first and second part of the investigation are taken from Saincher et al. (2022).

— **Non-breaking focused wave interaction with fixed cylinder**: HOS, *foamStar*, and *foamStarSWENSE* are used to test the generation and propagation of non-linear focusing waves in a numerical wave tank (NWT). Mesh and time step requirements, variable start times, relaxation zone length, and vertical cell requirement are all addressed in parametric research. For the waves from the experiment and the numerical solvers, a deterministic analysis using cross correlation is undertaken to assess the quality of the waves generated in both solvers.

Different mesh configurations with proper refinement ratios are discussed for non-breaking focusing wave interactions with the cylinder. Richardson extrapolation is presented to examine the convergence in temporal problem. Surface elevation, pressure, and force are compared between solvers and the experiment.

— **Breaking focused wave interaction with fixed cylinder**: The *foamStarSWENSE* solver does not yet support breaking waves from the incident field. Hence only *foamStar* is used for the investigation in this case. The parametric studies indicated in the preceding application that a 2D NWT is constructed in the foamStar. Similar parametric studies as

discussed above were carried out. The focused breaking wave interaction with the cylinder is then addressed and validated using pressure and force acting over the cylinder with the experiment. The potential of the *foamStar* model to address the breaking wave phenomena is demonstrated in this application.

— **Non-breaking focused wave interaction with moving cylinder**: The interaction of a moving cylinder with a focusing wave is investigated. A cylinder is towed with a velocity against the wave propagation directions to represent a uniform current in the laboratory. The cylinder movement is addressed at two different speeds (0.33 m/s and 0.75 m/s). The cylinder is carefully placed to interact precisely with the focusing wave in both time and space as in experiments. The *foamStar* and *foamStarSWENSE* solvers are used to test both situations. The physical understanding of flow situations is discussed in depth, and the experimental measurements are used to validate parameters such as force, pressure over the cylinder, and wave probe. A convergence study based on the Richardson extrapolation approach is proposed, similar to the previous application.

Regular and irregular wave interaction with SPAR type moored substructure of FOWT is examined in the third part, employing DD-based solver *foamStar* and FD-based solver *foamStarSWENSE*.

— **Wave interaction on SPAR type FOWT**: The *foamStar* and *foamStarSWENSE* solver is applied to simulate the interaction of sea waves with OC3 Hywind SPAR FOWT. The intention is to develop a numerical tool that allows the study of the survivability of floating structures in extreme sea states. In this study, the moorings are modelled in two ways. One is by considering the mooring lines as a linear spring with defined spring stiffness, and another is by coupling the solver (*foamStar*/*foamStarSWENSE*) with a lumped-mass mooring dynamics model (MoorDyn). MoorDyn represents the mooring line behaviour subject to axial elasticity, hydrodynamic forces, and vertical contact forces with the seabed. The stiffness based approach and coupled model has been validated against the experiments carried out as part of the SOFTWIND project (Arnal et al., 2019). The numerical model results of free surface elevation, floating body motions, and mooring tensions are compared with the experimental measurements.

## 1.7 Thesis outline

This thesis is organized as follows:

— Chapter 1: This chapter provides fundamentals about fixed and floating OWT. It also provides basic idea about the different numerical couplings. The chapter also includes a summary of identified challenges and open questions, subsequently defining the objective and scope of this thesis.

— Chapter 2: It is divided into two sections. The first section presents the mathematical formulation for the Navier Stokes (NS) flow model and the SWENSE model. The governing equations of the two flow models are reviewed, and their boundary conditions are discussed.

It is followed by introducing the regular and irregular wave theories, as well as HOS based incident wave kinematics used in this thesis. Finally, the Tian wave breaking model for the realization of the extreme event is reviewed. The second section of this chapter discusses the implementation of 6 DOF rigid body motion as well as the various mooring configurations used in this investigation. At the end of this chapter, the entire flow chart of the *foamStar* and *foamStarSWENSE* solvers is presented

— Chapter 3: There are two parts to this chapter. The first part addresses interactions of non-breaking focusing waves with a fixed cylinder, while the second section discusses interactions of breaking focusing waves with a fixed cylinder. The parametric investigations for each cases are covered in detail in each section along with the validation.

— Chapter 4: This chapter is split into two sections. The first section discusses the non-breaking focusing wave interactions with a moving cylinder travelling at a speed of 0.33 m/s, while the second section discusses a speed of 0.75 m/s. The parametric investigations for each cases are covered in detail, and validated with the experiments. The convergence study for both the cases are provided in AppendixA.

— Chapter 5: This chapter describes the SPAR type FOWT modelling technique in the CFD solver. The validation of the floating body mesh is discussed first, followed by the hydrostatics of the mesh. In the 3D solver, appropriate mesh and time configuration are chosen for mesh generation based on 2D regular and irregular wave propagation. This chapter also discusses the two different types of mooring systems (stiffness matrix and dynamic mooring) and their effectiveness. In both *foamStar* and *foamStarSWENSE*, the SPAR interaction with regular and irregular waves is compared to the experiment in terms of motions and mooring tension.

— Chapter 6: This chapter summarizes the contributions and conclusions of this thesis. Encountered limitations throughout this work are addressed, and possible directions for future research are presented.

Chapter 2

# GOVERNING EQUATIONS AND NUMERICAL MODELS

This chapter provides a comprehensive overview of the governing equations and numerical techniques used in this thesis. A typical two-phase computational domain in a numerical wave tank (NWT) with potential and viscous flow partition is shown in Figure 2.1. The free surface wave propagation and a body is shown floating in a viscous fluid (CFD) domain having five boundary conditions: inlet, outlet, bottom, top, and the body itself. Relaxation zones (inlet and outlet zones) are close to the outside boundaries of the viscous domain, where a solution from the potential flow domain is progressively forced using a spatially varied weight function. The solution is exactly the target solution (at the outlet zone, the target can either be blended to the potential solution or blended to zero, but at inlet, target indicates the potential solution) at the boundary, and then the forcing decreases until there is no forcing at the end of the relaxation zone, at which point the computational domain is said to be a 'pure CFD solution'. It can also be said in terms of weight function, which is one at the outer boundary, and zero at the viscous zone boundary. Inside the viscous domain, the two-phase Navier-Stokes equations simulation is solved in two ways in this study. A incompressible two-phase NS flow model is used in one, while the SWENSE approach is used in the other.

In the present work, the viscous zone is also used to examine both fixed and floating structures. The floating structure follows Newton's Law and based on the motion, the CFD mesh must be morphed using the Laplacian equation at each timestep. Also, mooring must be provided to prevent the floating structure from drifting away. This mooring can be described using a straightforward static spring model or a dynamic formulation using Newton's law. Overall, the governing equations for each NS/SWENSE method are first addressed, and then the governing equations for potential solvers, rigid body motion, mesh morphing, and discussion of mooring are presented. The numerical formulations for the equations presented, along with a description of the coupling process between the models, are presented in the following part of the chapter. At the end of this chapter, the complete algorithm used by the solvers *foamStar* and *foamStarSWENSE* to handle any wave-structure interaction problem is presented.

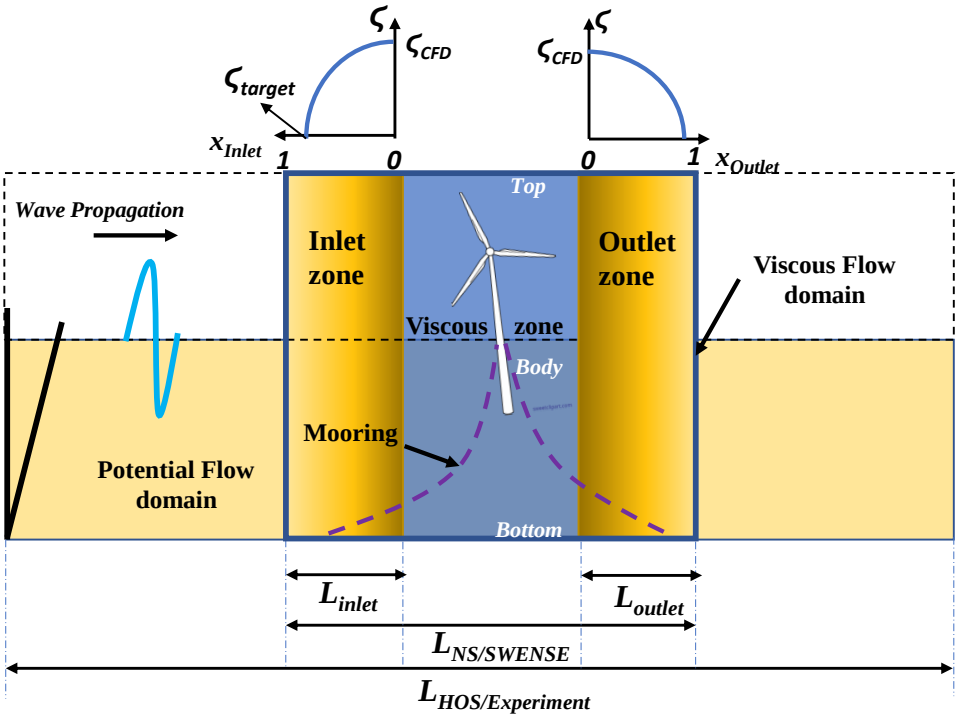


Figure 2.1 – Illustration of the computational domain description of the problem with general boundaries and relaxation zones

## 2.1 Mathematical models

### 2.1.1 Incompressible two phase flow model

This section discusses the description of incompressible two-phase Newtonian flow and its mathematical model. The first part describes the conservation equation of mass and momentum and its numerical framework, and the second part of the section describes different interface capturing techniques, detailing the VoF technique.

#### 2.1.1.1 Governing equations

The most prevalent fluids encountered in marine applications are water and air. If it is treated as a single phase, the Navier-Stokes equation, which was established in 1830, is sufficient to describe their behaviour.The fundamental assumptions behind these equations are:

— Fluid is a continuum, defining macroscopic properties (density, pressure and bulk velocity) at infinitesimal volume

— Fluid is isotropic, symmetric and Newtonian. Hence the stress tensor $T_{ij}$ is linearly proportional to the strain-rate tensor

— Fluid flow can be described through conservation laws. Also, fluid is considered isothermal, and the influence of the effect of temperature is not considered. Hence only mass and momentum conservation will be considered.

Mass conservation or continuity equation (Eqn. (2.1)) and momentum equation (Eqn. (2.2)) of a typical flow model for incompressible two-phase Newtonian flow is given as (Jasak, 1996) :

$$\nabla \cdot \boldsymbol{u} = 0 \tag{2.1}$$

$$\frac{\partial(\rho \mathbf{u})}{\partial t} + \nabla \cdot (\rho \boldsymbol{u}\boldsymbol{u}^{\boldsymbol{T}}) = -\nabla p_d + \nabla \cdot (\mu(\nabla \boldsymbol{u} + \nabla \mathbf{u}^T)) - (\boldsymbol{g} \cdot \boldsymbol{x})\Delta\rho \tag{2.2}$$

where $\boldsymbol{u}, \boldsymbol{x}$ and $\mathbf{g}= [0, 0, -g]^T$ are the fluid velocity, position and gravitational acceleration vector, respectively. The dynamic pressure $p_d = p - \rho \boldsymbol{g} \cdot \boldsymbol{x}$ is as introduced in Rusche (2003).

The density in the case of an offshore engineering application remains constant, (which means that it is incompressible): the density of water ($\rho_w \approx 1000 kg/m^3$) and the density of air ($\rho_a \approx 1 kg/m^3$). The surface tension is considered negligible in this thesis. The linear dynamic viscosity of water and air is $\mu_w = 10^{-3} Ns/m^2$ and $\mu_a = 10^{-5} Ns/m^2$ respectively.

#### 2.1.1.2 Volume of Fluid method (VoF)

In this thesis, VoF interface capturing technique (Hirt and Nichols, 1981) with an interface compression method is applied due to its mass conservation property. This VoF is likely the most extensively used and applied in offshore and marine applications for free-surface flows. An indicator scalar function $\alpha$ is used to represent the fractional volume of a cell ($V_{cell}$) occupied by the fluid $V_{fluid}$,

$$\alpha = \frac{V_{fluid}}{V_{cell}} \tag{2.3}$$

where

$$\alpha = \begin{cases} 1, & \text{if } V_{fluid} = V_{cell} \\ 0, & \text{if } V_{fluid} = 0 \\ 0 < \alpha < 1 & \text{if } V_{fluid} < V_{cell} \end{cases} \tag{2.4}$$

This method requires significantly less computing storage and power than other methods (Marker-and-cell or MAC Scheme (Harlow and Welch, 1965), Level set methods (Osher and Fedkiw, 2001) etc.) since it only requires one variable instead of a large number of particles to capture the interface. If the volume fraction has a value of 0, it is air, and if it has a value of 1, it is water, as stated in the Eqn.(2.3). If the value is between 0 and 1, the cells that store that value are in the interface or free surface. For an incompressible flow field, the following equation depicts the evolution of the volume fraction:

$$\frac{\partial \alpha}{\partial t} + \nabla.(\alpha \boldsymbol{u}) = 0 \tag{2.5}$$

$$\begin{cases} \rho = \rho_w \alpha + \rho_a(1 - \alpha) \\ \mu = \mu_w \alpha + \mu_a(1 - \alpha) \end{cases} \tag{2.6}$$

In this system, properties appearing in the conservation equation are determined by the

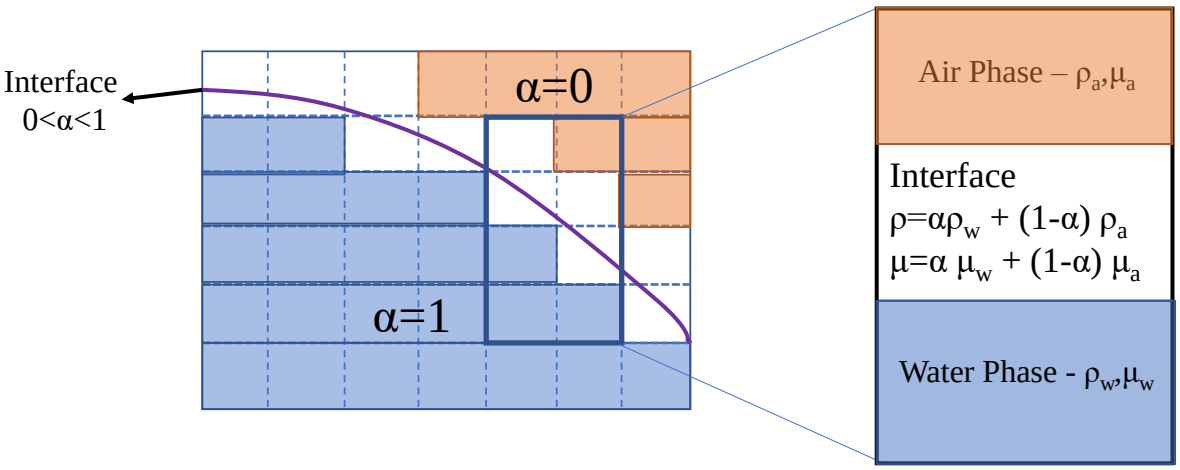


Figure 2.2 – Schematic view of the interfacial region in the VoF method and the properties in each cell in the two phase flow

distribution of phases in each control volume depending on the $\alpha$ fraction. When the volume fraction is known, the expression in Eqn.(2.6) is used to calculate fluid parameters such as density and viscosity at the interface. The water phase is denoted by the subscript '$w$,' while the air phase is denoted by the subscript '$a$.' For clarity, the mentioned interface parameters are presented in Figure 2.2.

Even modest inaccuracies in the volume fraction would result in huge errors due to the high-density ratio between water and air ($\approx 1000$). Also, standard differencing schemes applied to Eqn.(2.3) introduces too much numerical diffusion and smears the step profile of the interface over several cells. In order to avoid such issues, in the present approach, an additional convective term derived from the weighted average of individual phase velocities is incorporated into the VoF equation to ensure the smoothness of the volume fraction and reconstruction of the interface. The modified VoF equation is derived using the following two individual equations of the water and air phases.

$$\frac{\partial \alpha}{\partial t} + \nabla.(\alpha \boldsymbol{u}_w) = 0 \tag{2.7}$$

$$\frac{\partial (1-\alpha)}{\partial t} + \nabla.((1-\alpha)\boldsymbol{u}_a)) = 0 \tag{2.8}$$

In the above equations subscripts $w$ and $a$ denote the water and gas phases respectively. Above equations are rearranged in terms of the air and water phase velocities as follows:

$$\frac{\partial \alpha}{\partial t} + \nabla.((\alpha \boldsymbol{u}_w) + \alpha(\boldsymbol{u}_w \alpha) - \alpha(\boldsymbol{u}_w \alpha)) + \nabla.(\alpha(1-\alpha)\boldsymbol{u}_a - \alpha(1-\alpha)\boldsymbol{u}_a) = 0 \tag{2.9}$$

$$\frac{\partial \alpha}{\partial t} + \nabla.(\alpha\{\alpha \boldsymbol{u}_w + (1-\alpha)\boldsymbol{u}_a\}) + \nabla.((\boldsymbol{u}_w - \boldsymbol{u}_a)\alpha(1-\alpha)) = 0 \tag{2.10}$$

In the Eq.No (2.10), $\boldsymbol{u}_w - \boldsymbol{u}_a$ can be defined as $\boldsymbol{u}_r$ and is commonly referred as the compression

term which is a phase relative velocity and vanishes at individual phases (Berberović et al., 2009). This velocity is used to maintain sharp interface and minimize smearing. The final modified VoF equation adopted in the present study is :

$$\frac{\partial \alpha}{\partial t} + \nabla.(\alpha \boldsymbol{u}) + \nabla.(\boldsymbol{u}_r \alpha(1-\alpha)) = 0 \tag{2.11}$$

The third term is added artificially to reduce the numerical diffusion and it plays a role only in the interface. Also the velocity in the interface region is evaluated with the weighted average of the velocity between the two phases as:

$$\boldsymbol{u} = \alpha \boldsymbol{u}_w + (1-\alpha)\boldsymbol{u}_a \tag{2.12}$$

To avoid non-physical behaviour, the phase function must remain bounded between 0 and 1. The numerical discretization of Eqn (2.11) requires careful manipulations to ensure that this phase function field is valid and restricted. This is as a result of the interface's high gradients in the field.

#### 2.1.1.3 Physical boundary conditions

Every CFD problem is defined by the initial and boundary conditions. It is usual to impose boundary conditions at the physical boundary when designing a computational grid for any partial different equation (PDE) problems. The Dirichlet type, the Neumann type, and the combination of two conditions are the three mathematical types of boundary conditions commonly adopted. Specific values are imposed on the boundary to scalar or vector fields (usually velocity in CFD problems) in a Dirichlet condition, whereas the gradient of the field normal to the boundary is imposed in a Neumann condition (usually dynamic pressure, $p_d$). The mixed type boundary condition is defined as a function of the field values at the boundary and their derivatives. The velocity, dynamic pressure, and phase fraction boundary conditions for the typical boundaries defined in Figure 2.1 are briefed below.

— **Velocity** : The boundary values for the velocity are explicitly known, thanks to the relaxation zones and the relaxation scheme. The top boundary represents an open-air boundary condition with constant total pressure in the computational domain. A no-slip boundary condition is enforced on the body surface for the structure/body in the computational domain, making the fluid velocity equal to the body velocity ($\boldsymbol{u} = \boldsymbol{u}_b$). In some circumstances, if the wave is generated at a shallow depth, the bottom boundary will be specified as a slip boundary condition.

— **Dynamic pressure** : The boundary condition for the dynamic pressure applied in the form of Neumann BC can be determined from the dot product of the momentum equation (Eqn.(2.2)) with the surface unit normal vector ($\mathbf{n}$) for all borders where the Dirichlet velocity B.C. is applied. Kim (2021b) can be referred for detailed discussion over this condition.

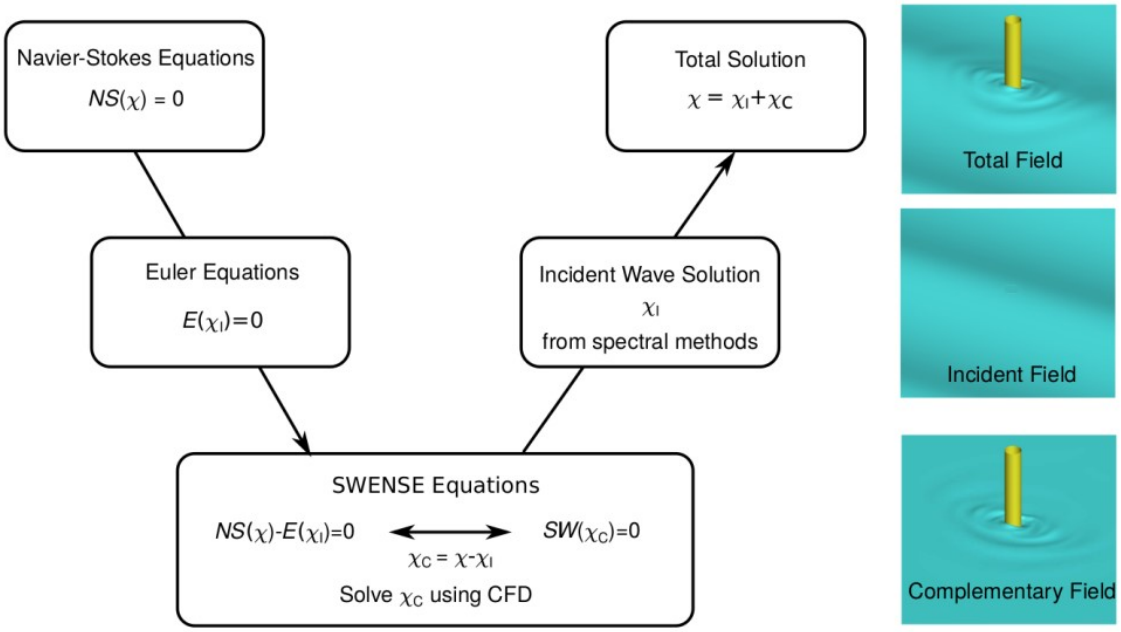


Figure 2.3 – SWENSE decomposition of the functional quantities of the total flow into incident and complementary parts (Li et al., 2021b)

— **Phase fraction** : The fluid velocity passively transports the phase-fraction. As a result, no explicit boundary criteria for the body and wall boundaries are necessary. The boundary values for the wave boundary conditions are explicitly applied at the inlet and outlet using the incident wave elevation.

### 2.1.2 SWENSE model

Ferrant et al. (2002) introduced the Spectral Wave Explicit Navier-Stokes Equations (SWENSE) formulation, which is a special version of the Navier-Stokes equations. The SWENSE formulation assumes that,

$$\chi = \chi_I + \chi_C \tag{2.13}$$

The primary variables (pressure,velocity and free surface elevation) of the flow $\chi$ is divided into incident part $\chi_I$ and a complementary part $\chi_C$. The SWENSE method defines these variables in the respective fields as,

1. Total field ($\chi$): It represents the real flow in the computational domain, final solution of the wave-structure interaction problem. The flow is governed by incompressible Navier-Stokes equation
2. Incident field($\chi_I$): This part represents the propagation of incident waves in the computational domain without structures. Also the flow is assumed to be irrotational and viscosity of fluid is neglected, so that this part is solved by potential flow theory with dedicated non linear spectral wave models. This flow is governed by the incompressible Euler equations.

3. Complementary field ($\chi_C$): This part represents the difference between the total field and the incident field ($\chi_C = \chi - \chi_I$). This field is generated due to the structures and the viscosity of the fluid. The complementary variables are governed by the Spectral Wave Explicit Navier-Stokes Equations (SWENSE), which will be discussed in the next section.

Figure 2.3 shows the SWENSE decomposition of the total flow's functional quantities into incident and complementary components. The total flow field considering wave-structure interaction is depicted in the first row of the figure. The single phase free-surface incident solution of the incompressible Euler equation is represented in the second row. The complementary wave field and the SWENSE, which characterise the viscosity and structure's influence on the wave field, are represented in the third row. Li et al. (2021b) performed functional decomposition on both velocity and pressure in a two-phase flow solution and used a non-decomposed VoF phase fraction for free surface tracking. Also he attempted the Ghost Fluid Method(GFM) along with the conservative and non-conservative forms of the SWENSE. Choi (2019) developed Li's method by combining non-conservative SWENSE with GFM and the Level Set (LS) phase indicator function. The conservative form of the SWENSE formulation from Li (2018) PhD thesis is addressed in the following section, as it is the formulation used in the present work.

#### 2.1.2.1 Two-phase SWENSE

Li et al. (2021b) derived the two-phase SWENSE approach by maintaining the two fundamental requirements of SWENSE. First, the ability to employ coarser mesh for incident wave propagation must be preserved, and second, in pure incident wave propagation scenarios, the source terms in the SWENSE momentum equation must be equal to zero. There will be no complementary velocity or pressure generated. As a result, regardless of the CFD mesh, the entire velocity field equals the incident potential wave solution. A brief derivation of the two-phase SWENSE model is presented below,

**Two-phase Navier-Stokes equations :** The two-phase NS equation in non conservative form are recalled as,

$$\nabla \cdot \boldsymbol{u} = 0 \tag{2.14}$$

$$\frac{\partial \boldsymbol{u}}{\partial t} + \boldsymbol{u}\nabla\boldsymbol{u} = -\frac{\nabla p}{\rho} + \boldsymbol{g} + \frac{\nabla \cdot (\mu(\nabla \boldsymbol{u} + \nabla \boldsymbol{u}^T))}{\rho} \tag{2.15}$$

Because the hydrostatic part's incident pressure will be subtracted later, the total pressure is employed instead of dynamic pressure.

**Direct extension of Euler equations :** Incident wave fields must be extended throughout the computational domain to support the two-phase flow (Li et al., 2021b). One of the benefits of coupling with spectral approaches in the potential flow models (described in the next section) is that it can be directly extended without any discontinuities. Following this expansion, the

Euler equation is valid across the total computational domain, as recalled as,

$$\nabla \boldsymbol{u}_I = 0 \tag{2.16}$$

$$\frac{\partial \boldsymbol{u}_I}{\partial t} + \boldsymbol{u}_I \cdot \nabla \boldsymbol{u}_I = -\frac{\nabla p_I}{\rho_I} + \boldsymbol{g} \tag{2.17}$$

**SWENSE :** Applying the functional decomposition procedure ($\chi = \chi_I + \chi_C$) in the above equations and subtracting the Euler equations (Eqn.(2.17)) from NS equation (Eqn.(2.15)) results in the following SWENSE equations,

$$\nabla . \boldsymbol{u}_c = 0$$

$$\frac{\partial \boldsymbol{u}_c}{\partial t} + \boldsymbol{u}_c \cdot \nabla \boldsymbol{u}_c + \boldsymbol{u}_c \cdot \nabla \boldsymbol{u}_I + \boldsymbol{u}_I \cdot \nabla \boldsymbol{u}_c = -\frac{\nabla p_c}{\rho} + \frac{\nabla \cdot (\mu(\nabla \boldsymbol{u}_c + \nabla \boldsymbol{u}_c^T))}{\rho} + \underline{\frac{\nabla p_I}{\rho_I} - \frac{\nabla p_I}{\rho}} + \underline{\frac{2\nabla \boldsymbol{u}_I \cdot \nabla \mu}{\rho}} \tag{2.18}$$

Comparing the momentum equations of SWENSE in single (Ferrant et al., 2002) and multi phase ( Eqn.(2.18)), there are two extra terms (extra viscous term and extra pressure term) that is underlined arised. The additional viscous term may exist in the interface because of the viscosity gradient. There are two reasons for this additional viscous term could be dropped. One, it fails to meet the SWENSE condition by not making the source term equal to zero in the pure incident wave situation. Second, the viscous term's interface gradient is significantly less than the pressure and gravity contributions, thus it does not need to be adequately resolved. Two-phase CFD simulations frequently do not require meshes that capture the free surface boundary layer for traditional marine and offshore applications.

The extra pressure term gets canceled in single phase equation($\rho_I = \rho_w = \rho$). In multi phase case, extended density for incident field makes the term non zero in the air phase. Assuming density ratio of water and air as 1000,

$$\frac{\nabla p_I}{\rho_I} - \frac{\nabla p_I}{\rho} = \frac{\nabla p_I}{\rho_w} - \frac{\nabla p_I}{\rho_a} = \frac{1}{1000}\frac{\nabla p_I}{\rho_a} - \frac{\nabla p_I}{\rho_a} = -\frac{999 \nabla p_I}{1000 \rho_a} \tag{2.19}$$

This non zero value makes the governing SWENSE momentum equation less interesting as extra source term (against the idea of SWENSE) and the value is so large (1000 times the acceleration of the water particle), that the simulation may become unstable. Hence direct extension of the incident field in the air is unsuitable for the two -phase SWENSE method. To overcome this, modified Euler equation is proposed in (Li et al., 2021b).

**Modified Euler equation :** It is proposed to modify the Euler equations to use the density according to the actual free surface position, in order to cancel the underlined source terms in

Eqn.(2.18). Modified incident pressure $p_I^*$ is introduced as,

$$p_I^* = \rho \frac{p_I}{\rho_I} \tag{2.20}$$

where $\rho$ is the density field in the two-phase flow, and $\rho_I$ density of incident waves (water). Using this modified pressure in the Euler equation Eqn.(2.17) and simplifying the equation,

$$\frac{\partial \boldsymbol{u}_I}{\partial t} + \boldsymbol{u}_I \cdot \nabla \boldsymbol{u}_I = -\frac{\nabla p_I^*}{\rho} + \frac{p_I}{\rho_I}\frac{\nabla \rho}{\rho} + \boldsymbol{g} \tag{2.21}$$

From the RHS of the equation, it can be understood that the gradient of the density is zero in both the phases (air and water) and non-zero only on the interface. Also, solutions of the original Euler equations ($\boldsymbol{u}_I$ and $p_I$) still satisfy the modified Euler equation. The denominator of the pressure gradient term is in accordance with the two-phase NS equations, which also overcomes the mismatched density in developing SWENSE equation.

**Conservative two-phase SWENSE:** The conservative two-phase SWENSE can be obtained in a similar procedure. However, an additional step is necessary to transform the modified Euler equations as,

$$\rho(\frac{\partial \boldsymbol{u}_I}{\partial t} + \boldsymbol{u}_I \cdot \nabla \boldsymbol{u}_I) = \nabla p_I^* + \frac{p_I}{\rho_I}\nabla \rho + \boldsymbol{\rho g} \tag{2.22}$$

Conservative form of NS equation, multiplying the density on both sides,

$$\frac{\partial \rho \boldsymbol{u}}{\partial t} + \nabla \cdot (\rho \boldsymbol{u}\boldsymbol{u}) = -\nabla p + \rho g + \nabla \cdot (\mu(\nabla \boldsymbol{u} + \nabla \boldsymbol{u}^T)) \tag{2.23}$$

Subtracting the above Euler equation from the conservative NS equation and applying the notion of SWENSE($\chi_C = \chi - \chi_I$) results in following equation (after simplification),

$$\frac{\partial \rho \boldsymbol{u}_c}{\partial t} + \nabla \cdot (\rho \boldsymbol{u}\boldsymbol{u}_c) + \rho \boldsymbol{u}_c \nabla \cdot \boldsymbol{u}_I = -\nabla p_c + \nabla \cdot (\mu(\nabla \boldsymbol{u} + \nabla \boldsymbol{u}^T)) + \frac{p_I}{\rho_I}\nabla \rho \tag{2.24}$$

For detailed derivation Li et al. (2021b) can be referred. The VoF convection scheme applied to the SWENSE formulation is identical to the two phase flow model, and no functional decomposition is applied to the phase-fraction ($\alpha$) field. The total velocity may not satisfy the continuity equation due to the interpolation inaccuracy of incident velocity($\nabla \cdot \boldsymbol{u}_c = -\nabla \cdot \boldsymbol{u}_I$). Previous studies on SWENSE remarked that the divergence of the reconstructed incident wave velocity field is not zero (Vukčević et al., 2016; Li et al., 2021b). This minor imperfection may cause VoF to be unbounded in the computational domain. Hence the VoF domain is not decomposed in SWENSE formulation. The transport equation of VoF is read as,

$$\frac{\partial \alpha}{\partial t} + \boldsymbol{u}.\nabla \alpha + \nabla.(\boldsymbol{u}_r \alpha(1-\alpha)) = 0 \tag{2.25}$$

where $\boldsymbol{u} = \boldsymbol{u}_I + \boldsymbol{u}_c$ is the total velocity solution reconstructed by SWENSE ideology.

#### 2.1.2.2 SWENSE model boundary conditions

— **Phase fraction** ($\alpha$): The VoF boundary condition is identical to the two-phase flow model since no functional decomposition is applied to the phase-function field. The boundary values are explicitly applied using the known wave elevation at the inlet and outlet for wave boundary conditions. The zero Neumann boundary condition is used when the boundary values are unknown for other boundaries.

— **Complementary velocity** ($\boldsymbol{u}_c$): With the functional decomposition, the no-slip or free-slip boundary condition is applied to the bodies and walls. The no-slip boundary condition with a boundary velocity $\boldsymbol{u}_b$, reads as follows $\boldsymbol{u}_c = \boldsymbol{u}_b - \boldsymbol{u}_I$

— **Complementary pressure** ($p_c$): From the pressure boundary condition and the pressure functional decomposition, the complementary pressure boundary condition can be found and it read as.

$$\frac{\partial p_c}{\partial n} = -\frac{D(\rho \boldsymbol{u}_b)}{Dt} \cdot \boldsymbol{n} + \boldsymbol{n} \cdot \nabla \cdot (\mu(\nabla \boldsymbol{u}_b + \nabla \boldsymbol{u}_b^T)) + \rho \boldsymbol{g} \cdot \boldsymbol{n} - \frac{\partial p_I^*}{\partial n} \quad \text{for } x \in \partial\Omega_B \tag{2.26}$$

where $\boldsymbol{u}_b$ represents boundary velocity, $p_I^*$ represents the incident pressure. The material derivative ($D/Dt$) of the momentum at the boundary point is the first term on the right-hand side. The second term, which is considered to be very small, is the surface normal gradient of the shear stress. The surface normal gradient of incident pressure is the fourth term. The discussion over this condition may be found in Kim (2021b).

### 2.1.3 Potential flow model (Wave theories)

For accurate wave-structure interaction simulations, the quality of the generated waves is important. Although the incident waves propagation problem is no longer handled by the CFD solvers (both with DD and FD), external solvers are still required to solve it. These external solvers should be more accurate and efficient in computing incident waves than the viscous CFD solvers to increase overall efficiency. The incident waves were derived using spectral wave models and its brief background is presented in this section. The potential theory and the general principle of spectral methods are presented in the first half. Second, the stream-function wave theory is introduced to model unidirectional regular waves. Finally, the Higher-Order Spectral (HOS) method for irregular is briefly discussed.

#### 2.1.3.1 Potential theory and spectral methods

The incident wave generation is based on the potential theory approach. With the assumption of an ideal fluid and irrotational flow, it is possible to define a velocity potential ($\Phi$) as,

$$\boldsymbol{u}_I = \nabla \Phi \tag{2.27}$$

Then the incident wave potential satisfies Laplace's equation in the fluid domain ($\Omega$)

$$\Delta\Phi = 0 \quad \boldsymbol{x} \in \Omega \tag{2.28}$$

The non linear kinematic and dynamic free surface boundary conditions for incident waves are given as,

$$\frac{\partial \eta_I}{\partial t} + \frac{\partial \Phi}{\partial x}\frac{\partial \eta_I}{\partial x} + \frac{\partial \Phi}{\partial y}\frac{\partial \eta_I}{\partial y} + \frac{\partial \Phi}{\partial z} = 0 \quad at\ z = \eta_I(\boldsymbol{x}, t) \tag{2.29}$$

$$\frac{\partial \Phi}{\partial t} + \frac{1}{2}(\nabla\Phi)^2 + gz = 0 \quad at\ z = \eta_I(\boldsymbol{x}, t) \tag{2.30}$$

where $x$ and $y$ are horizontal coordinate, $t$ is time. The flat bottom condition is given as,

$$\frac{\partial \Phi}{\partial z} = 0\ at\ z = -h \tag{2.31}$$

where $h$ is water depth. In the present work, spectral methods are used to solve the potential and surface elevation.

#### 2.1.3.2 Regular waves: Stream function wave theory

The open-source CN-Stream model (the library is published with GNU General public license and can be downloaded from the URL `https://github.com/LHEEA/CN-Stream`) is used to describe nonlinear regular waves propagating over a flat bottom. It is based on the stream function theory (Rienecker and Fenton, 1981) that allows an efficient and accurate solution of regular wave trains up to the breaking wave limit. The model assumes periodic boundary conditions and solves the propagation in a moving frame, making the problem steady. Spatial discretization is achieved thanks to a spectral method that decomposes the unknowns (free surface elevation and velocity potential) on a set of basis functions (given below) that satisfy intrinsically Laplace equation (Eqn.(2.28)) as well as the bottom boundary condition (Eqn.(2.31)).

$$\eta_I(x)e^{-iwt} = \left[\frac{a_0}{2} + \sum_{n=1}^{N_2} a_n cos(k_n x)\right] e^{-i\omega t} \tag{2.32}$$

$$\psi(x,z)e^{-iwt} = \left[b_0 z + \sum_{n=1}^{N_1} b_n \frac{sinh(k_n(z+h))}{cosh(k_n h)}\right] e^{-i\omega t} \tag{2.33}$$

where $a_n$ and $b_n$ are the modal amplitudes of the free surface elevation and stream function respectively. $k_n$ is the wave number of the $n^{th}$ Fourier component. The integers $N_1$ and $N_2$ are the number of truncated Fourier series modes used to evaluated the stream function and elevation. Based on the algorithm suggested by Ducrozet et al. (2019) optimal number of modes are automatically selected.

#### 2.1.3.3 Irregular waves: Higher Order Spectral method

Stream function methodology is limited to regular waves. In order to address another type of uni or multidirectional wave, corresponding to irregular sea states, with the objective of an

accurate and computationally efficient numerical model, the High-Order Spectral (HOS) method (Dommermuth et al., 1988; West et al., 1987) has been adopted. This numerical approach relies on a pseudo-spectral discretization scheme that exhibits a high (exponential) convergence rate and that allows the use of Fast Fourier Transforms, which ensures high efficiency.

The original HOS method (Dommermuth et al., 1988; West et al., 1987) was dedicated to the time evolution of an initially prescribed wave field in an open domain with periodic boundary conditions. The present study intends to replicate experiments carried out in a wave tank where the waves are generated thanks to a wavemaker in a finite-size domain. Then, in this work, a dedicated Numerical Wave Tank (NWT) based on HOS is used (Ducrozet et al., 2012). This open-source solver named HOS-NWT has been developed at LHEEA Lab, (Ecole Centrale Nantes (ECN)) and now constitutes the central element for the digital twin of the ECN wave tank facility. The geometry is the exact physical one, including perfectly reflective sidewalls. The initial conditions are fluid at rest and the waves are generated thanks to a wavemaker. For a direct comparison with experiments, the exact same wavemaker motion is used in the numerical and the physical wave tank. In addition, a numerical absorbing zone mimics the physical beach located close to the wall opposite to the wavemaker to prevent wave reflection. This NWT has been applied and validated on different wave configurations of various levels of complexity (Ducrozet et al., 2012, 2016b; Michel et al., 2020; Canard et al., 2020).

The modal amplitudes are numerically evaluated to satisfy the free surface boundary conditions. They can be used to reconstruct the wave field (velocity and pressure through Bernoulli's equation (Eqn.(2.30)) at required locations (Section 2.2.3.1).

Vorticity and viscosity effects are naturally ignored in non-linear potential flow models like the HOS-NWT model. The efficiency of the wave model is substantially increased by these irrotational and inviscid assumptions. These assumptions, on the other hand, exclude the use of potential flow solvers for relatively high vorticity phenomena like breaking waves, which are common in design seastates. To address this constraint, a numerical breaking model must be proposed, which can account for the impact of breaking wave events on the potential model. The energy from the breaking waves is released in free-surface fragmentation, vorticity, and turbulence when the waves break. The Tian-Barthelemy wave breaking model, which uses Tian's eddy viscosity model and Barthelemy's breaking criterion (Tian et al., 2012; Barthelemy et al., 2018), is used in the LHEEA lab's in-house version of open-source HOS solvers. The breaking onset criteria are used to predict the breaking event prior to the wave breaking, and the wave profile is used to estimate the amount of dissipation. Definitions and recommended values for the model can be found in Seiffert et al. (2017); Seiffert and Ducrozet (2018); Tian et al. (2012); Hasan et al. (2019).

### 2.1.4 Floating body

The governing equations for rigid body motions and their implementation (mesh morphing) are briefly described in this section. Following that are the comprehensive governing equations

for the different mooring models used in the study and their validation.

#### 2.1.4.1 Rigid body motions

Numerous reputable textbooks have derived and addressed the equations of motion for a floating body with six degrees of freedom (Fossen, 1999, 2011; Faltinsen, 1993), however the reference coordinate system may change depending on the situation (SNAME, 1950; Jensen, 2001). Therefore it is important to define the frame of reference in which the governing equations are valid. There are two reference frames used in the present study, the inertial ($R_0$) and the body reference frame ($R_b$) (refer Figure 2.4). Newton's second law may be used directly in the inertial reference frame without introducing any fictitious forces like centrifugal or Coriolis forces. The body-fixed reference frame is fixed on the floating body, and its origin coincides with the centre of gravity (COG). It may rotate or accelerate according to the motion of the body. All the frames are based on Cartesian systems and defined according to the right-hand rule. The inertial reference frame's origin is positioned at the center of the domain at the still water level in the free surface.

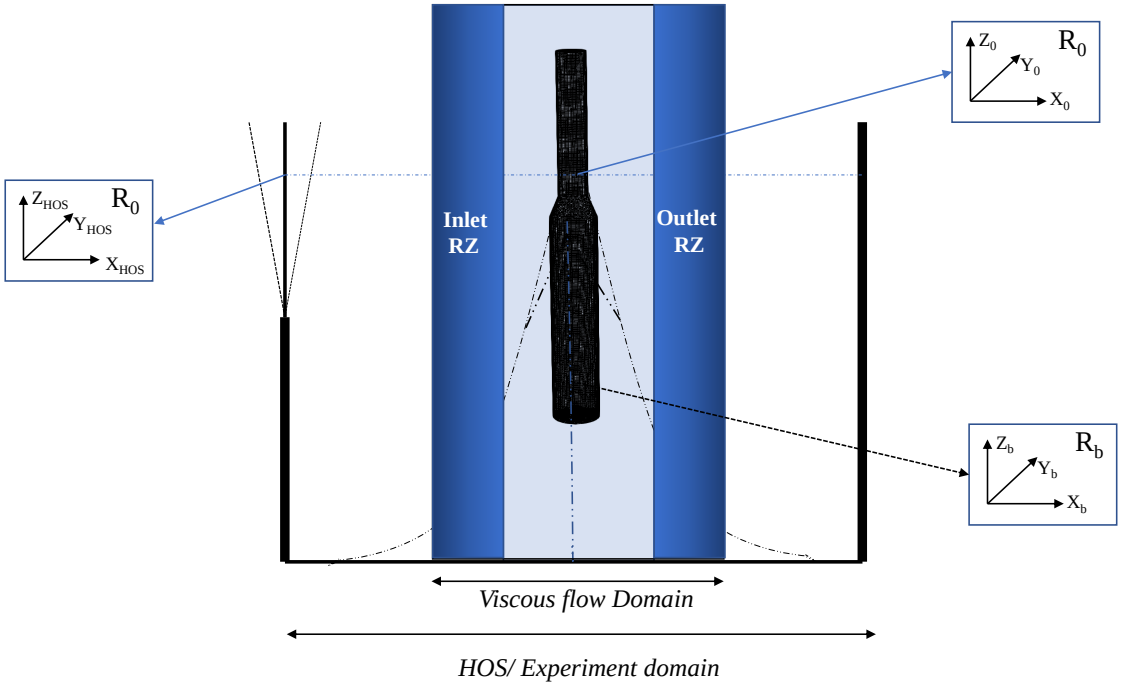


Figure 2.4 – The Inertial referential frame $R_0$ and the body-fixed frame $R_b$ in computational domain with different origin

The present work follows the definition of Seng (2012). Three translations and three rotations make up the 6DoF system. Surge, sway, and heave are translational motions along the axes $X_0, Y_0, Z_0$ in $R_0$ frame, and yaw, pitch, and roll are rotations defined with the Euler intrisic angles with zyx convention.It is important to emphasize that these 6DoF motions can be thought of as the position of the body-fixed reference frame relatively to the inertial reference frame.

The equations of translational motion are expressed as follows in $R_b$:

$$[m]\ \ddot{\boldsymbol{q}} = \boldsymbol{Q}_e + \boldsymbol{Q}_v + \boldsymbol{Q}_c \tag{2.34}$$

Where $m$ is the generalized mass of the body; $\boldsymbol{q}$ represents the translation motion and the acceleration when with double dot ; $\boldsymbol{Q}_e$ represents the external forces which is mainly composed of the fluid force ($\boldsymbol{Q}_{e,fluid}$), the mooring ($\boldsymbol{Q}_{e,M}$) and gravitational ($\boldsymbol{Q}_{e,g}$) forces ; $\boldsymbol{Q}_v$ and $\boldsymbol{Q}_c$ are the quadratic velocity forces (Coriolis/centrifugal forces) and constraint forces respectively. Among all the forces, the fluid force is evaluated as the surface integration of pressure and viscous stress over the body surface as given in the Eqn. (2.35). Here, $\boldsymbol{n}$ is a unit surface normal vector pointing inside the body. Since $\boldsymbol{\tau}$ is the viscous stress tensor calculated at the body surface and $p$ is the total fluid pressure, both hydrostatic and hydrodynamic forces are taken into account in the integral. For the evaluation of the mooring force ($\boldsymbol{Q}_{e,M}$), Section 2.1.4.3 can be referred.

$$\boldsymbol{Q}_{e,fluid} = \int_{body} (p\boldsymbol{n} - \boldsymbol{\tau} \cdot \boldsymbol{n})\ dS \tag{2.35}$$

For rotational motions, it is natural to solve in the body fixed coordinate system ($R_b$), which is defined to align with the principal axis of inertia which gives a constant inertia matrix for solid bodies. The equation's vectorial form is given as,

$$\boldsymbol{I}_b\ \dot{\boldsymbol{\omega}} + \boldsymbol{\omega} \times (\boldsymbol{I}_b\ \boldsymbol{\omega}) = \boldsymbol{M}_b \tag{2.36}$$

where $\boldsymbol{\omega}$ represents the angular velocity with respect to $R_b$ with the dot indicating time derivative. $\boldsymbol{M}_b$ denotes total torque about COG expressed in $R_b$. $\boldsymbol{I}_b$ represents mass moment of inertia in the form of diagonal matrix. The total torque acting on the body is given by,

$$\boldsymbol{M}_b = \boldsymbol{M}_{e,fluid} + \boldsymbol{M}_{e,M} + \boldsymbol{M}_c \tag{2.37}$$

where $\boldsymbol{M}_c$ represents the constraint moments. Since origin of $R_b$ coincides with the COG, the torque from gravitational force does not contribute. For the evaluation of mooring generated torque ($\boldsymbol{M}_{e,M}$), refer Section 2.1.4.3. The torque induced by the fluid forces ($\boldsymbol{M}_{e,fluid}$) is,

$$\boldsymbol{M}_{e,fluid} = \int_{body} (\boldsymbol{q} - \boldsymbol{q}_{COG})(p\ \boldsymbol{n} + \boldsymbol{\tau} \cdot \boldsymbol{n})\ dS \tag{2.38}$$

where $\boldsymbol{q}_{COG}$ is the location of COG in $R_0$.

#### 2.1.4.2 Mesh morphing

Different morphing techniques can be applied within the finite volume framework (Jasak and Tuković, 2010) like spring analogy, pseudo-solid, laplacian smoothing, algebraic interpolation, solid body motion, etc. The mesh update strategy is based on the laplacian mesh smoothing technique in the present work and the mesh motion of the computational domain is calculated by solving the cell center Laplace smoothing equation (Jasak and Tukovic, 2006). The Laplacian

equation is given as,

$$\nabla \cdot (\gamma(r)\nabla \boldsymbol{x}) = 0; \quad \gamma(r) = \frac{1}{r^2} \tag{2.39}$$

where $\boldsymbol{x}$ is the point displacement field and $\gamma$ is the diffusivity coefficient. $r$ is the distance to the moving boundary. Several choices for $\gamma$ are presented in Löhner and Yang (1996); Jasak and Tuković (2010). In the present work, the inverse quadratic distance relation has been chosen as the coefficient will be significant, and the gradient will be small, yielding a small relative displacement for the points close to the moving boundary, preserving the cells' quality near the moving boundaries (Jasak and Tukovic, 2006).

#### 2.1.4.3 Mooring system

The present work aims to implement a static and dynamic mooring model (MoorDyn (Hall, 2015)) into *foamStar* and *foamStarSWENSE* to conduct a fully coupled analysis of moored floating structures replicating the model test in NWT. Along with static and dynamic mooring models, a quasi-static model is also briefly discussed in this subsection.

**2.1.4.3.1 Static mooring model: Stiffness Matrix** The external mooring used to control the motions in six DoF is simplified as the linear spring model with stiffness matrix $[K]$. The restoring force is given as,

$$[\boldsymbol{Q}_{e,M}] = [K] * [\boldsymbol{q}^T \boldsymbol{\theta}^T] \tag{2.40}$$

where $\boldsymbol{Q}_{e,M}$ represents external force and moment from mooring, and $\delta q$ represents the change in motion (along the six DoF). The coefficients of the stiffness matrix for the floating body may be computed by determining the restoring force for a specific displacement in a in a pull-out test. This force is added to the right-hand side of the equation of motion (Eqn. (2.34)) that can be interpreted as attaching a spring to the body's center of gravity. The working procedure of the stiffness matrix method inside the *foamStar* algorithm is depicted in the general flowchart shown in the Figure 2.16.

**2.1.4.3.2 Quasi-Static mooring model** The MSQS (Multi Segmented Quasi Static) model is a development of a single line element theory that combines many different catenary cables at common connecting points. By taking into account the typical mooring line loads and nonlinear geometric restoring for catenary and taut mooring systems, this simple model enables a reliable, first-pass evaluation of a mooring system. MAP++ (Masciola et al., 2013), MoorPy (Hall et al., 2021) and AQWA (Ansys, 2013) are some of the mooring models that follows MSQS theory. It should be noted that AQWA also can do dynamic mooring analysis. This section presents a brief description of this MSQS, since the mooring models are compared later in the Chapter for validation. Terminologies and symbols used in this section are taken from the MAP++ theory manual and intended to help readers understand it and should not be confused with any symbols used in this thesis.

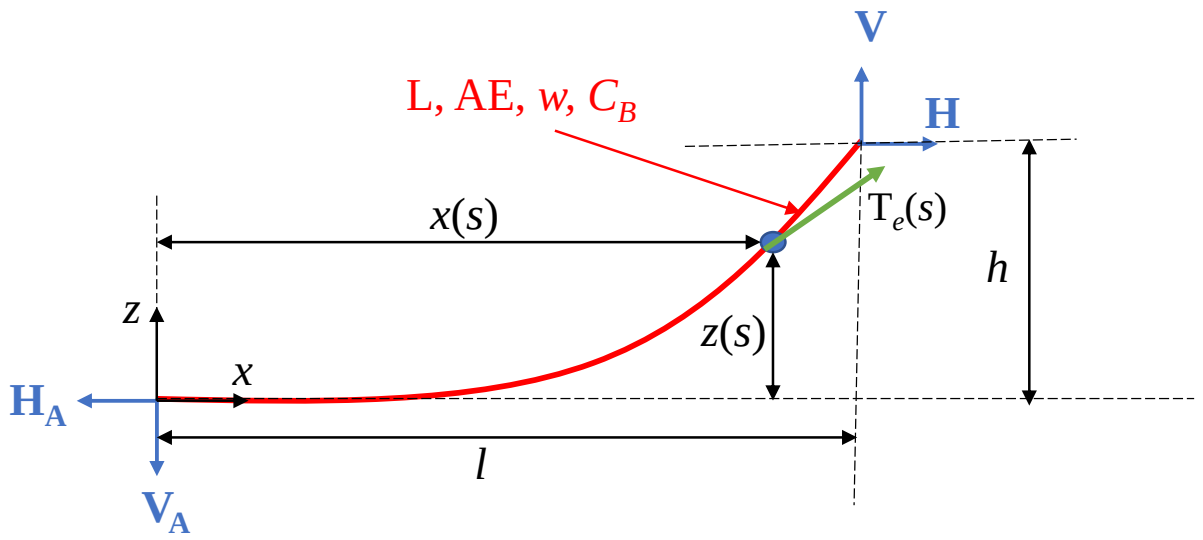


Figure 2.5 – Definition of the entities in a single-line mooring line relative to the local xz axis (Masciola et al., 2013)

Two distinct sets of equations must be solved for this system to function. The first is the continuous nonlinear catenary algebraic equations, and the second is the force balance equation. Given a set of line properties, the line geometry may be represented as a function of the forces exerted at the line's end as,

$$x(s) = \frac{H}{w}\left\{\ln\left[\frac{V_A + ws}{H} + \sqrt{1+\left(\frac{V_A+ws}{H}\right)^2}\right] - \ln\left[\frac{V_A}{H} + \sqrt{1+\left(\frac{V_A}{H}\right)^2}\right]\right\} + \frac{Hs}{EA} \tag{2.41}$$

$$z(s) = \frac{H}{w}\left[\sqrt{1+\left(\frac{V_A+ws}{H}\right)^2} - \sqrt{1+\left(\frac{V_A}{H}\right)^2}\right] + \frac{1}{EA}\left(V_A s + \frac{ws^2}{2}\right) \tag{2.42}$$

where $x$ and $z$ are coordinates relative to local frame (Figure 2.5). The fairlead excursion dimensions ($l$ and $h$) are the known entity but the force parameters $H$ and $V$ are needed in practice. Here, these forces are determined by simultaneously solving the following two equations.

$$l = \frac{H}{w}\left[\ln\left(\frac{V}{H} + \sqrt{1+\left(\frac{V}{H}\right)^2}\right) - \ln\left(\frac{V-wL}{H} + \sqrt{1+\left(\frac{V-wL}{H}\right)^2}\right)\right] + \frac{HL}{EA} \tag{2.43}$$

$$h = \frac{H}{w}\left[\sqrt{1+\left(\frac{V}{H}\right)^2} - \sqrt{1+\left(\frac{V-wL}{H}\right)^2}\right] + \frac{1}{EA}\left(VL - \frac{wL^2}{2}\right) \tag{2.44}$$

These element level forces at fairlead ($H$, $V$ ) and anchor ($H_A$, $V_A$) are transformed from the local frame into the global coordinate system, and the force contribution at each element's anchor

and fairlead is added to the corresponding node attached. Based on the force balance equation, the node position is updated and as an outcome, the element forces must be recalculated and the process continues.

Hence, this process requires two distinct sets of equations to be solved simultaneously to achieve the static cable configuration. The first set of equations is the force-balance relationships in three directions for each node; the second set of equations is the two catenary functions (Eqn. (2.43) and Eqn. (2.44)). For detailed evaluation of the MSQS theory, Masciola et al. (2013) can be referred.

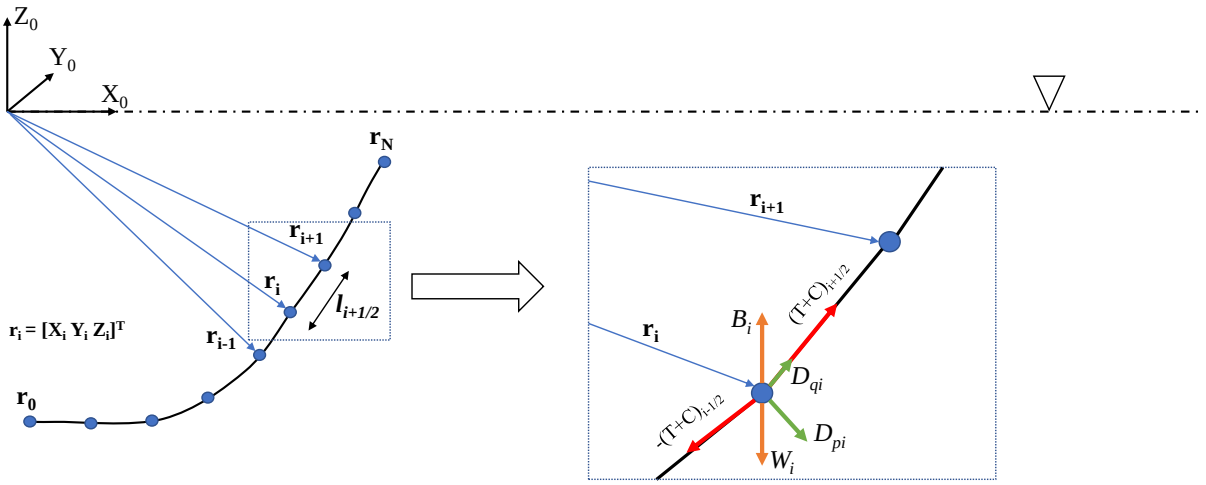


Figure 2.6 – Mooring line discretization in MoorDyn with a representation of internal and external forces in inertial reference frame $R_0$ (Hall and Goupee, 2015)

**2.1.4.3.3 Dynamic mooring model: MoorDyn** The dynamic mooring solver MoorDyn (Hall, 2015) is a lumped-mass mooring model that lumps all the effects of mass, external forces, and inertial reactions at a finite number of nodes, along the mooring line connected by massless spring as shown in the Figure 2.6. The version of MoorDyn used in this work was v1.01.03C. It follows the right-handed inertial reference frame defined with the z-axis being measured positive up from the water plane (See Figure 5.4). The location of each node $i$ is defined by the position vector $\boldsymbol{r}_i$ which includes $[X_i, Y_i, Z_i]$ components of the vector. The equation of motion for each node $i$ is written as follows in the inertial reference frame $R_0$:

$$(M_i + \boldsymbol{a}_{pi} + \boldsymbol{a}_{qi})\ddot{\boldsymbol{r}}_i = \boldsymbol{T}_i + \boldsymbol{C}_i + \boldsymbol{W}_i + \boldsymbol{B}_i + \boldsymbol{D}_{pi} + \boldsymbol{D}_{qi} \tag{2.45}$$

where $m_i$ is the mass matrix for node $i$. The mass of the mooring cable is discretized into point masses at each node by allotting each node half the combined mass of the two neighboring cable segments.

The mooring line is represented as a cylinder of diameter $d$, unstretched length L, and density $\rho$. For a mooring line with $N$ segments connecting $N+1$ nodes, the unstretched length of each line segment is $l_0 = L/N$. The forces acting on the nodes are divided into internal and external

forces. The internal forces include net buoyancy ($\boldsymbol{W}_i$), tension ($\boldsymbol{T}_i$) and internal damping ($\boldsymbol{C}_i$) forces. The external forces contain transverse and tangential hydrodynamic forces ($\boldsymbol{D}_{pi}$ and $\boldsymbol{D}_{qi}$) based on Morison's equation, added mass force ($\boldsymbol{a}_{pi}$ and $\boldsymbol{a}_{qi}$) and the seabed contact force ($\boldsymbol{B}_i$). The tension, $\boldsymbol{T}_{i+1/2}$ in any line segment is calculated as,

$$\boldsymbol{T}_{i+1/2} = \begin{cases} E\frac{\pi}{4}d^2\left(\frac{l}{l_0}-1\right) & \text{if } l > l_0 \\ 0 & \text{if } l \leq l_0 \end{cases} \tag{2.46}$$

Where $E$ is Young's modulus. The calculations assume that line tensions are always positive $l > l_0$ (compression line forces are not allowed). By multiplying a unit vector directed along a line segment, the above equation can be rewritten in vector form as

$$\boldsymbol{T}_{i+(1/2)} = \begin{cases} E\frac{\pi}{4}d^2\left(\frac{||\boldsymbol{r}_{i+1}-\boldsymbol{r}_i||}{l_0}-1\right)\left(\frac{\boldsymbol{r}_{i+1}-\boldsymbol{r}_i}{||\boldsymbol{r}_{i+1}-\boldsymbol{r}_i||}\right) & \text{if } ||\boldsymbol{r}_{i+1}-\boldsymbol{r}_i|| > l_0 \\ 0 & \text{if } ||\boldsymbol{r}_{i+1}-\boldsymbol{r}_i|| \leq l_0 \end{cases} \tag{2.47}$$

The net buoyancy ($\boldsymbol{W}_i$) at node $i$ assuming the force is evenly divided among two connecting nodes is described in vector form as follows:

$$\boldsymbol{W}_i = \hat{\boldsymbol{e}}_z \frac{\boldsymbol{W}_{i-\frac{1}{2}} + \boldsymbol{W}_{i+\frac{1}{2}}}{2} \tag{2.48}$$

where where $\hat{\boldsymbol{e}}_z$ is a unit vector in the positive z direction and,

$$\boldsymbol{W}_i = \frac{\pi}{4}d^2 l(\rho_w - \rho)g \tag{2.49}$$

where $\rho_w$ is the density of water and $\rho$ is the density of the mooring line. In order to improve numerically stability, a numerical internal damping force is included:

$$\boldsymbol{C}_{i+(1/2)} = C_{inter}\frac{\pi}{4}d^2\dot{\epsilon}_{i+(1/2)}\left(\frac{\boldsymbol{r}_{i+1}-\boldsymbol{r}_i}{||\boldsymbol{r}_{i+1}-\boldsymbol{r}_i||}\right) \tag{2.50}$$

where $C_{inter}$ is the numerical internal damping coefficient and $\dot{\epsilon}_{i+1/2}$ is the strain rate of the segment, '$i+(1/2)$'. The linear spring damper model is activated only when the node interacts with the sea bottom ($z_{bot}$) and it is given as:

$$\boldsymbol{B}_i = dl[(z_{bot}-z_i)k_b - \dot{z}_i c_b]\hat{\boldsymbol{e}}_z \tag{2.51}$$

where $k_b$ is the seabed stiffness coefficient, and $c_b$ is the seabed damping coefficient.

The drag and added mass are calculated at each node $i$ based on Morison's equation. The direction of a line passing between two adjacent nodes is approximated by the tangential direction $\hat{\boldsymbol{q}}_i$ (Figure 2.6) :

$$\hat{\boldsymbol{q}}_i = \frac{\boldsymbol{r}_{i+1}-\boldsymbol{r}_i}{||\boldsymbol{r}_{i+1}-\boldsymbol{r}_i||} \tag{2.52}$$

Transverse and tangential drag forces are calculated using the transverse drag coefficient $C_{dn}$, and the tangential drag coefficient,$C_{dt}$ respectively. Similarly, transverse and tangential added mass forces are calculated using the transverse added mass coefficient $C_{an}$, and the tangential added mass coefficient,$C_{at}$ respectively. Both forces are computed as follows:

$$\boldsymbol{D}_{pi} = \frac{1}{2}\rho_w C_{dn} dl \;||\; (\ddot{\boldsymbol{r}} \cdot \hat{\boldsymbol{q}}_i)\hat{\boldsymbol{q}}_i - \ddot{\boldsymbol{r}} \;||\; [(\ddot{\boldsymbol{r}} \cdot \hat{\boldsymbol{q}}_i)\hat{\boldsymbol{q}}_i - \ddot{\boldsymbol{r}}] \tag{2.53}$$

$$\boldsymbol{D}_{qi} = \frac{1}{2}\rho_w C_{dt} dl \;||\; (-\ddot{\boldsymbol{r}} \cdot \hat{\boldsymbol{q}}_i)\hat{\boldsymbol{q}}_i \;||\; [(-\ddot{\boldsymbol{r}} \cdot \hat{\boldsymbol{q}}_i)\hat{\boldsymbol{q}}_i] \tag{2.54}$$

$$\boldsymbol{a}_{pi}\ddot{\boldsymbol{r}}_i = \rho_w C_{an} \frac{\pi}{4} d^2 l[(\ddot{\boldsymbol{r}} \cdot \hat{\boldsymbol{q}}_i)\hat{\boldsymbol{q}}_i - \dot{\boldsymbol{r}}_i] \tag{2.55}$$

$$\boldsymbol{a}_{qi}\ddot{\boldsymbol{r}}_i = \rho_w C_{at} \frac{\pi}{4} d^2 l(-\ddot{\boldsymbol{r}} \cdot \hat{\boldsymbol{q}}_i)\hat{\boldsymbol{q}}_i \tag{2.56}$$

The second-order system of ordinary differential equations presented in Eqn.(2.45) can be reduced to a system of first-order differential equations, and then solved using a second-order Runge-Kutta integration scheme with a constant time step.

#### 2.1.4.4 Validation of MoorDyn with other mooring models

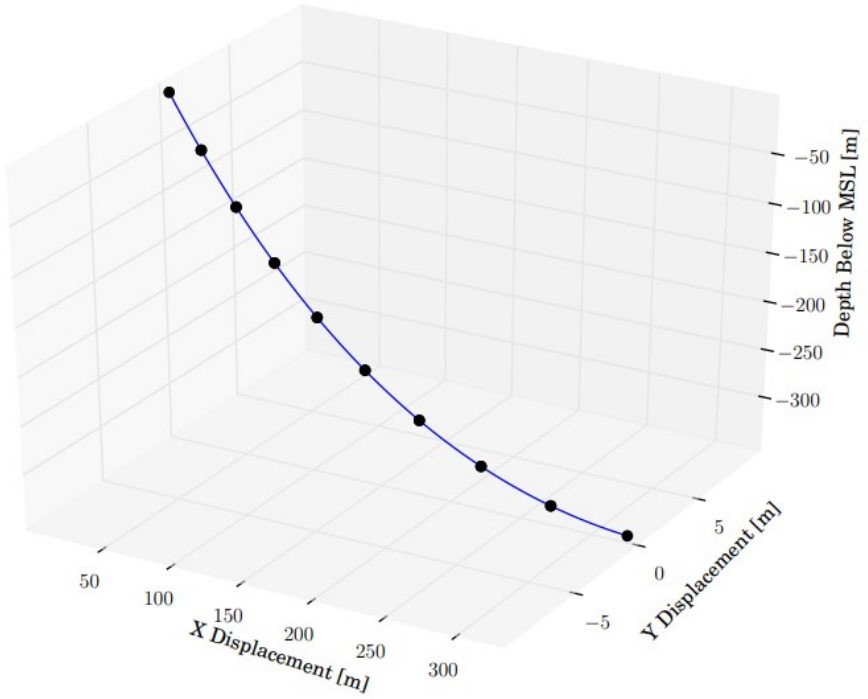


Figure 2.7 – Multi segmented single catenary mooring line for validation study

The solution for the dynamic mooring solver (MoorDyn) is based on a three-step process. First, it generates a Quasi Static model based on the input conditions. Second, to allow the

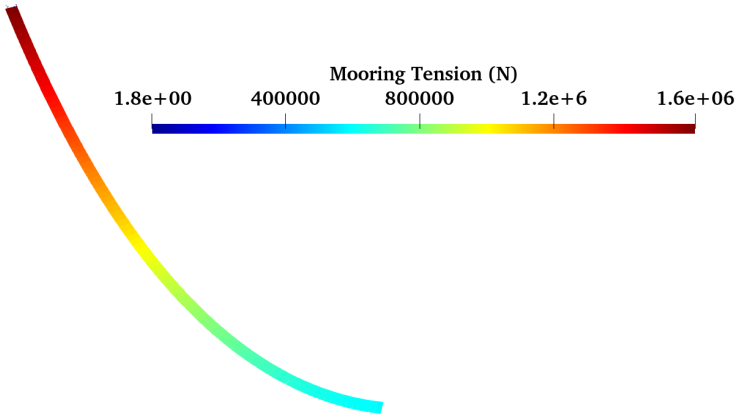


Figure 2.8 – Mooring tension observed in MoorDyn model for the multi segmented single catenary mooring

system to achieve the initial equilibrium, dynamic relaxation will be carried out, which includes dynamic drag and acceleration forces. Finally, tension at each fairlead as well as the motion (position, velocity, and acceleration) of each node at each time step will be evaluated. The MoorDyn standalone solver is validated for correctness in this subsection with different mooring models (MoorPy (Hall et al., 2021), MAP (Masciola, 2018), and AQWA (Ansys, 2013)) for application of single catenary and single delta lines. The first validation problem is a single, homogeneous cable suspended between two points as shown in the Figure 2.7. The line properties are:

— Axial stiffness : 9.817 × 1010 N

— Unstretched line length : 500 m

— Horizontal fairlead excursion : 325 m

— Vertical fairlead excursion : -350 m

— Cable weight-per-unit length in fluid : 292.8 N/m

The mooring line's tension across the mooring line is verified using the standalone Moordyn model, as illustrated in the Figure 2.8. Since all the details are not explicitly available, certain parameters are assumed and hence there is a little variation in the results observed, but the overall agreement was good as shown in Figure 2.9. In the figure, 'Analytical' indicates determining the pretensions using simple catenary equations (Refer Section 2.1.4.3.2). Besides using the MSQS MAP++ model, Moorpy and AQWA were also involved in this validation. The observed total tension between AQWA and MAP is slightly higher than the theoretical tension, although MoorPy and MoorDyn predictions are relatively close. The overall disagreement is less than 0.5%, indicating that the MoorDyn setup is effective for the task at hand.

The single delta line is the subject of the second validation, as it is one part of the mooring configuration used in the floating SPAR interaction study in Chapter 5. Figure 2.10 can be used to look up the nomenclature of the single delta line considered. A steel mooring element having

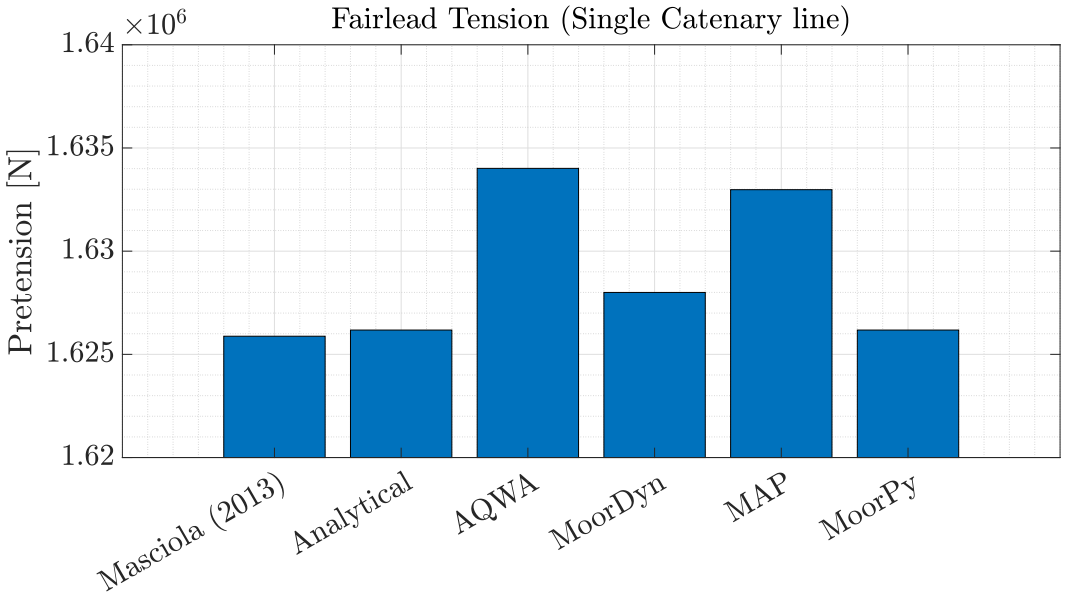


Figure 2.9 – Comparison of maximum fairlead tension of single Catenary line for different mooring models

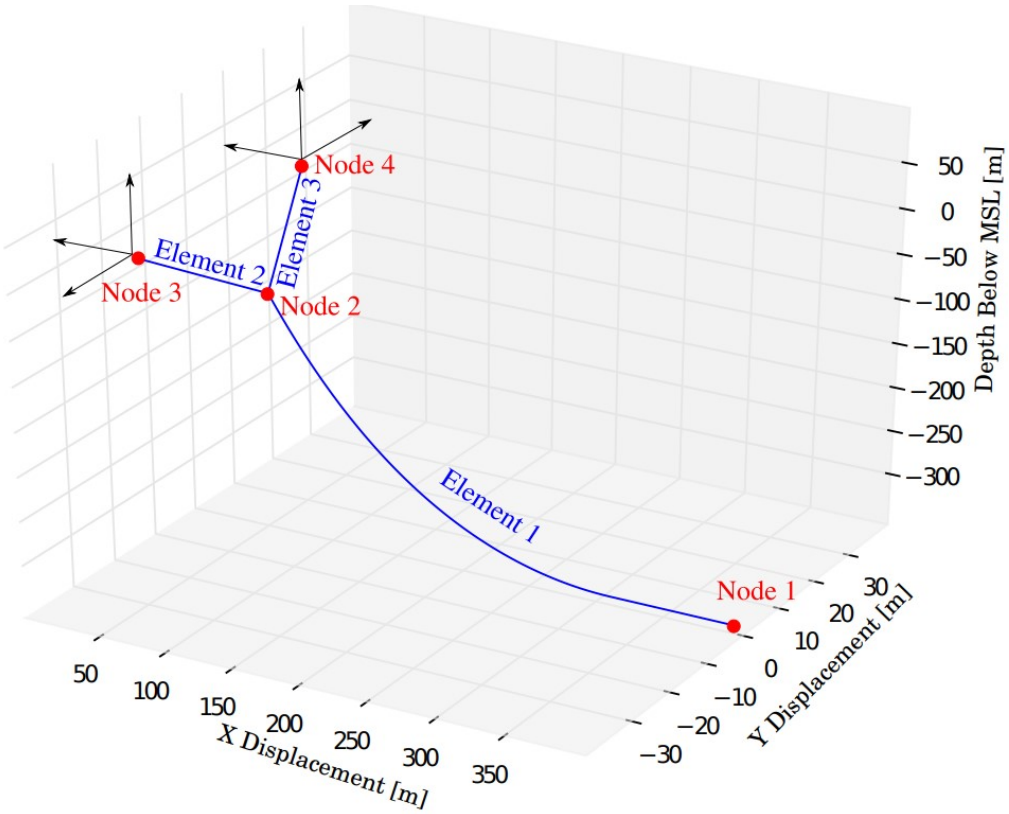


Figure 2.10 – Multi segmented single delta line mooring for validation study (Masciola et al., 2013)

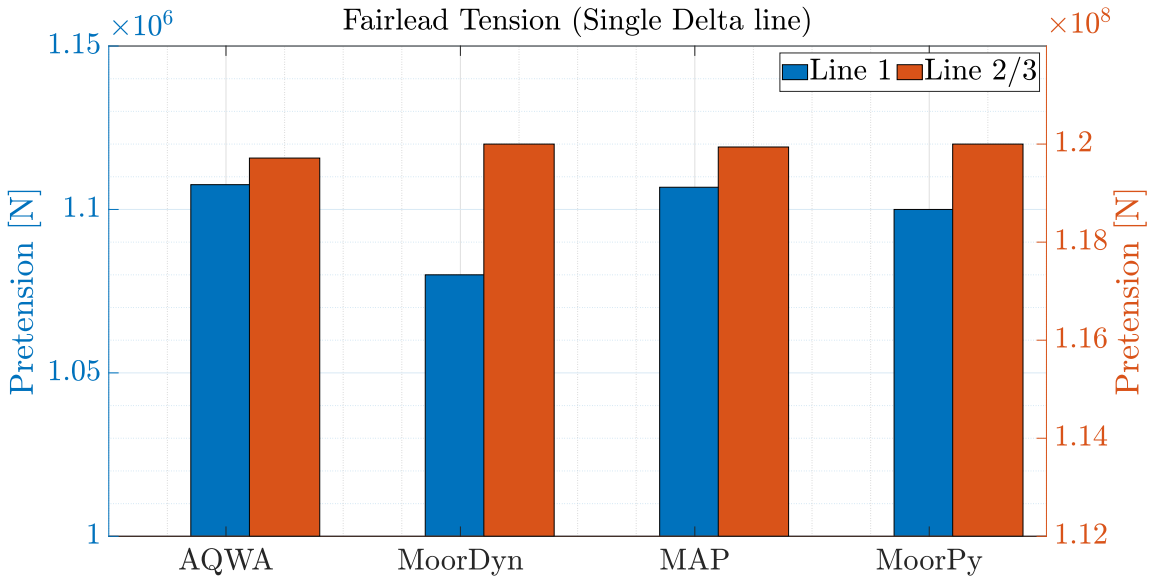


Figure 2.11 – Comparison of maximum fairlead tension of single delta line for different mooring models

a diameter of 0.25m and a mass density of 320 kg/m is defined as Line 1 (Element 1). It is connected to nylon lines of Line 2 and 3 (Elements 2 and 3) with diameters of 0.3m and mass densities of 100 kg/m and has an unstretched length of 450 m. This delta line introduces the connecting node between the lines, the position of which will be iterated by the solvers, and the accuracy of the pretension is dependent on the final node position. The static pretension comparison between the solvers for the case is as shown in Figure 2.11. Since Lines 2 and 3 are symmetric, the figure shows a single bar representing both lines. For Line 2/3, the difference between the models is quite small, but for Line 1, the difference is nearly 2% of the pretension between the models. It is found that the original iteration of the connection node position displaces into a new position, resulting in the line tension differences. The dynamics assumed by MoorDyn could also be a concern. However, because the error is minimal, the MoorDyn model is agreed upon for its robustness to be used for further investigation.

### 2.1.5 Moving cylinder implementation in *foamStar/ foamStarSWENSE*

The implementation of the motion of a rigid body with constant forward speed is achieved by applying constant velocity to the entire domain ($\boldsymbol{u}_{domain}$) with respect to the Inertial reference frame ($R_0$). Then, boundary conditions are modified to impose other boundaries will have zero moving velocity, and only the body inside the domain moves with forward speed ($\boldsymbol{u}_{body}$=$\boldsymbol{u}_{domain}$). The schematic representation of the body movement with the different boundary conditions are shown in Figure 2.12. This choice of representation of the moving body has the advantage of avoiding mesh morphing and its limitations, as detailed in Section 1.3.5. This approach allows slip or no slip to side or bottom boundaries while maintaining incident wave velocity (obtained via HOS-NWT) for the inlet boundary and relaxation in the outlet. In the SWENSE formulation, the

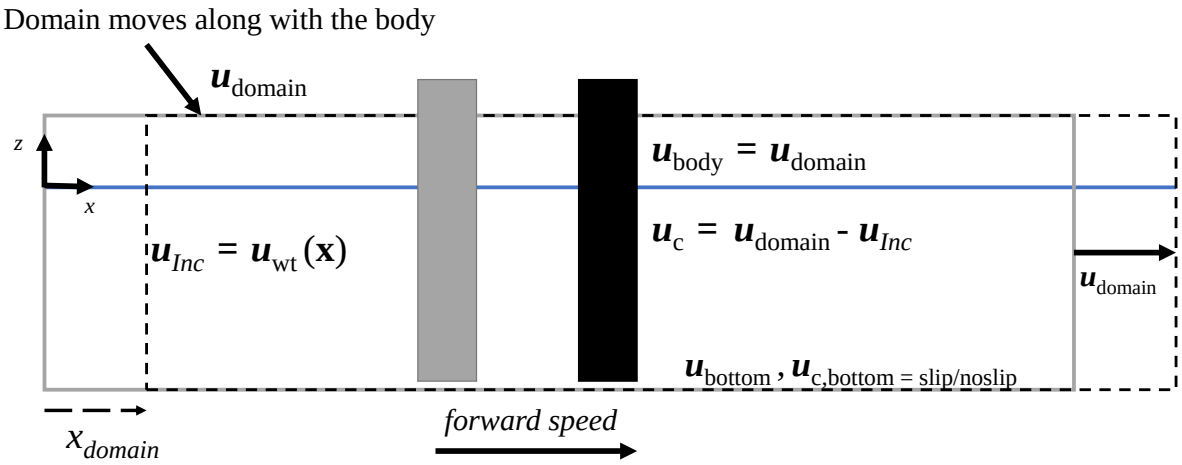


Figure 2.12 – Schematic representation of cylinder moving with forward speed implementation in the NWT. Both DD and FD way of imposing boundary conditions are shown with primitive variables $\boldsymbol{u}$ and $\boldsymbol{u}_c$.

domain velocity provided will be added to the formulation, such as $\boldsymbol{u}_c = \boldsymbol{u}_{frame} - \boldsymbol{u}_{Inc}$. Two body boundary conditions are introduced based on the above technique known as *movingWallVelocity* and *movingWallSwenseVelocity* to execute this formulation with any forward speed problem inside foamStar and foamStarSWENSE solver.

### 2.1.6 Error Estimation

The accuracy of numerical results depends upon the discretization of the governing equations. Grid generation and the simulation setup, therefore plays a critical role and need to follow established strategies that ensure sufficiently accurate results. The first part of this section introduces the quantitative determination of coefficients based on the cross correlation analysis of time series. The second part of the section introduces and discusses concepts of error estimation based on systematic grid refinement .

#### 2.1.6.1 Cross correlation

In the validation study in the coming chapters, error analysis based on cross-correlation is adopted to compare the numerically simulated results with experiment or reference results. The cross correlation between time series corresponding to the reference time series and one other simulated time series, which offers a correlation factor $C$ as a function of a time-lag $\tau$, was used for the deterministic comparison. The maximum correlation factor value and its related time-lag can be regarded as the shape and amplitude correspondence of the two time series, as well as an estimate of the time shift between them, respectively. A variant of the correlation function was calculated by sliding the simulated time window over a reference time window as

$$C_{a\times b}(\varepsilon) = \int_{-\infty}^{+\infty} \varsigma_a(t)\ \varsigma_b(t+\varepsilon)dt \tag{2.57}$$

where $\varsigma_a(t)$ and $\varsigma_b(t)$ represent the discrete-time series for the reference and simulated time windows, respectively and $\varepsilon$ denotes the time delay. The time range for the integration in the equation is maintained the same, and if the child sampling frequency is of a different sampling frequency, then a cubic interpolation is carried out to match the parent sampling frequency. The advantage of the proposed technique is that besides measuring the similarity between the signals, it can also measure the time shift between them. In the present case, the cross-correlated time series is normalized with an autocorrelation coefficient at zero lag, such as

$$\overline{C_{a\times b}(\varepsilon)} = \frac{C_{a\times b}(\varepsilon)}{\sqrt{C_{aa}(0)C_{aa}(0)}} \tag{2.58}$$

where $C_{a\times b}(\varepsilon)$ represents the covariance of two real continuous time series of, say, reference signal and any of the numerical time series. and $C_{aa}$ is the sample variance of $\varsigma_a(t)$, the reference signal. In other words the covariance is normalised by auto-correlation values with respect to $\varsigma_a$ at zero time lag. The time series are perfectly matched when the maximum cross correlation value is one. The difference in value from one, on the other hand, represents the quantification of inaccuracy.

#### 2.1.6.2 Uncertainty analysis - Richardson extrapolation

The numerical results of CFD methods depends upon the spatial and temporal discretization. In transient 3D problems (such as focused wave interacting with a cylinder), the number of unknowns is a function of the grid spacing to the power of four. At the same time, the error is typically a function of the grid spacing to the power of one or two, depending on the order of the approximation schemes (Oberhagemann, 2017). Insufficient grid resolution or poor quality grids may lead to inaccurate results or give wrong tendencies. Even with very fine discretizations, one may still not obtain sufficiently converged, i. e. grid-independent, results, mainly due to the asymptotic accuracy. Beyond a certain level of refinement, further reduction of the discretization error will not be worth the additional computational effort. In the present work, the Richardson extrapolation, a widely accepted approach for uncertainty and error estimation of steady or quasi-steady problems, was applied for this transient problem.

In numerical analysis, the literature shows that there are different procedures to verify and validate the accuracy of the simulations. A laymen approach is to compare the results of simulations with experimental results, and consider that the simulations are valid if they resemble the experiments. A second approach is to use numerical convergence. The procedure is typically performed by refining the mesh until the solution no longer varies and normally a peak magnitude or error over an entire duration will be used to check convergence. Finally, some authors combine numerical convergence and validation with experimental results. In this study, grid convergence was evaluated based on the Richardson extrapolation (Richardson and Gaunt, 1927) method along with validation against experiments and discussion of its uncertainty.

The Richardson extrapolation method, also known as '$h^2$ extrapolation', is a method for obtaining a higher-order estimate of the continuum value (value at zero grid spacing) from a series of lower-order discrete values. Based on (Roache, 1997), any quantity from a numerical

simulation is expressed as:

$$\nu = \nu_{exact} + g_1 h_g + g_2 h_g^2 + g_3 h_g^3 + ... \tag{2.59}$$

where $h_g$ is the grid spacing and $g_i$ are the functions defined in the continuum and thus are independent of the grid spacing. $\nu_{exact}$ is the continuum value at zero grid spacing. Let the mesh types coarse, medium and fine be represented as 1, 2 and 3 respectively.

Let the grid refinement ratio $r$ be written as,

$$r_{1-2} = \frac{h_{g1}}{h_{g2}}, r_{2-3} = \frac{h_{g2}}{h_{g3}} \tag{2.60}$$

Without considering the absence of an odd power in Eqn. (2.59) may be rewritten and generalized to $p^{th}$ order methods as:

$$\nu_{exact} \approx \nu_3 + \frac{\nu_2 - \nu_3}{r^p - 1} \tag{2.61}$$

The apparent order of the method and absolute error can be calculated as

$$p = \frac{1}{\ln(r)} \left| \ln \left| \frac{\epsilon_{32}}{\epsilon_{21}} \right| + q(p) \right| \tag{2.62}$$

where $\epsilon_{32} = \nu_3 - \nu_2$, $\epsilon_{21} = \nu_2 - \nu_1$ are the absolute errors of the variable of interest $\nu$ obtained with the three different meshes and the function $q(p)$ is defined as

$$q(p) = \ln \left( \frac{(r_{2-3})^p - s}{(r_{1-2})^p - s} \right) \tag{2.63}$$

where s is the parameter related to monotonic or oscillatory behaviour of the solution (Roache, 1997) as the grid is refined and it is calculated as,

$$s = \frac{\epsilon_{32}/\epsilon_{21}}{|\epsilon_{32}/\epsilon_{21}|} \tag{2.64}$$

As can be seen, Eq.(2.62) and Eq.(2.63) must be solved iteratively. Once the preceding values are obtained, the extrapolated value of the solution can be obtained as

$$\nu_{ext}^{2-3} = \frac{(r_{2-3}^p)\nu_3 - \nu_2}{(r_{2-3}^p) - 1} \tag{2.65}$$

This extrapolated solution ($\nu_{ext}$) will be shown in the thesis, that demonstrates the use of this technique to verify the grid refinement's convergence and establish the procedure for the evaluation of convergence in the spatio-temporal problem.

## 2.2 Numerical formulations

The Finite Difference Method (FDM), Finite Element Method (FEM), Finite Volume Method (FVM), Boundary Element Method (BEM), Meshfree methods (SPH, MLPG,..) are some of the numerical methods to solve the partial differential equations discussed in section 2.1.1.1 and

2.1.2.1. Each approach has its own set of benefits and drawbacks, and the method chosen will be determined by factors such as mathematical background, workgroup history, available code capabilities, and so on. As a result, our primary focus will be on applying the cell-centered Finite Volume Method to solve the governing equations ((Jasak, 1996; Ferziger and Perić, 1999) can be referred for detail descriptions). The discretization of the governing equations and the interpolation schemes used in the numerical solvers are briefly presented in the first part of the section followed by the OpenFOAM implementation of the two-phase flow and SWENSE models.

### 2.2.1 General Finite Volume discretization

For generic NS equation,

$$\underbrace{\frac{\partial \rho\phi}{\partial t}}_{I} + \underbrace{\nabla.(\rho \boldsymbol{u}\phi)}_{II} = \underbrace{\nabla.(\Gamma_\phi \nabla\phi)}_{III} + \underbrace{S_\phi(\phi)}_{IV} \tag{2.66}$$

where $\Gamma_\phi$ is the diffusion coefficient. The term (I) temporal rate of change of variable $\phi$. The term (II) represents the convection of $\phi$ due to the velocity vector, and the term (III) represents the diffusion rate of $\phi$ across the domain. The source term (IV) includes all the force quantities like pressure, gravity, and surface tension forces. Also, note that the equation is second order, hence the order of discretization should be equal to or higher than the second-order to achieve acceptable accuracy.

Integrating the equation (2.66) over the control volume $V_p$ at P (Figure 2.13a) over the time interval , $t$ to $t+\nabla t$ is given as,

$$\int_t^{t+\nabla t} \left[ \int_{V_p} \frac{\partial \rho\phi}{\partial t} dV + \int_{V_p} \nabla\cdot(\rho \boldsymbol{u}\phi) dV - \int_{V_p} \nabla\cdot(\rho\Gamma_\phi \nabla\phi) dV \right] dt = \int_t^{t+\nabla t} \left[ \int_{V_p} S_\phi(\phi) dV \right] dt \tag{2.67}$$

The discretization of equation (2.67) will now be examined term by term.

#### 2.2.1.1 Convective term

$$\int_{V_p} \nabla \cdot (\rho \boldsymbol{u}\phi) dV = \sum_f \boldsymbol{S} \cdot (\rho \boldsymbol{u}\phi)_f = \sum_f F\phi_f \tag{2.68}$$

where F in the equation 2.68 represents the mass flux through the face, $F = \boldsymbol{S}(\rho \boldsymbol{u})_f$. In order to solve this convective term, the face value of the variables, especially $\phi$, are calculated from the values in the cell centres, which is obtained using the convection differencing schemes like Central Differencing (CD), Upwind Differencing (UD), Total Variation Diminishing (TVD) etc. According to the central differencing (CD) scheme, linear variation of $\phi$ is assumed between P and N and face value (Figure 2.13b) is interpolated from the following rule,

$$\phi_f = f_x \phi_P + (1 - f_x)\phi_N \tag{2.69}$$

The interpolation factor $f_x$ is defined as the ratio of the distances between $\boldsymbol{fN}$ and $\boldsymbol{PN}$ .

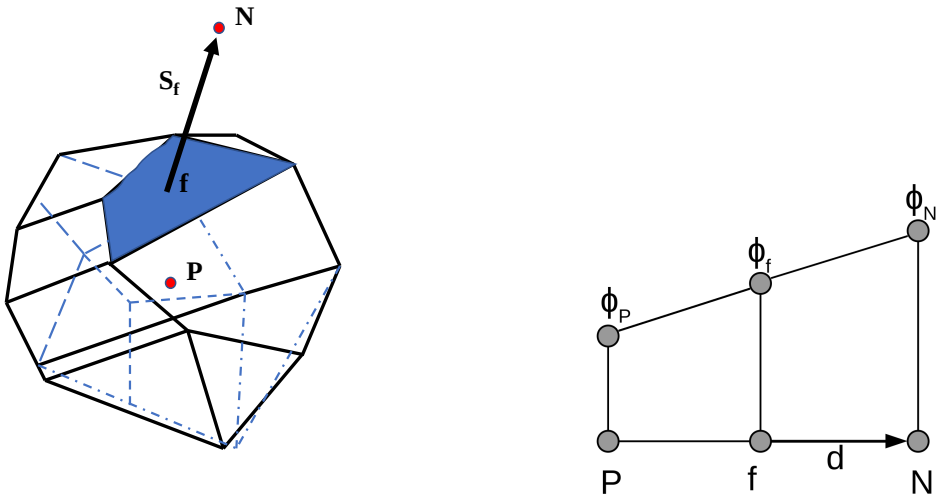


*(a)* Typical control volume *(b)* Typical interpolation depiction

Figure 2.13 – Schematic for the control volume (P) with neighbour (N) and illustration of interpolation for face value from the cell centre on a non orthogonal mesh

Although this method is second-order accuracy yet, the boundness of the solution is no longer possible (Ferziger and Perić, 1999). The Upwind Differencing scheme (Eqn. (2.70)), which is based on the direction of flow, can provide the boundness, but this method is first-order accurate.

$$\phi_f = \begin{cases} \phi_p & \phi_f \geq 0 \\ \phi_N & \phi_f < 0 \end{cases} \tag{2.70}$$

The blending differencing (BD) combines the advantage of both the methods by linearly combining both the methods (Eqn.(2.71)). The blending factor ($0 \geq \gamma \leq 1$) determines weightage between the schemes.

$$\phi_f = (1-\gamma)(\phi_f)_{UD} + \gamma(\phi_f)_{CD} \tag{2.71}$$

#### 2.2.1.2 Diffusion term

The diffusion term will be discretized similar to the previous subsection. Under the assumptions of linear variation of $\phi$ from the Eqn.(2.67), it follows

$$\int_{V_p} \nabla \cdot (\rho\Gamma_\phi \nabla\phi) dV = \sum_f \boldsymbol{S} \cdot (\rho\Gamma_\phi \nabla\phi)_f = \sum_f (\rho\Gamma_\phi)_f \boldsymbol{S}_f (\nabla\phi)_f \tag{2.72}$$

From the Figure 2.13b, if the distance vector $\boldsymbol{d}$ and $\boldsymbol{S}_f$ are parallel and in line, then the mesh is orthogonal, and the following expression can be used to discretise the term $\boldsymbol{S}_f(\nabla\phi)_f$,

$$\boldsymbol{S}_f \cdot (\nabla\phi)_f = |\boldsymbol{S}_f| \left( \frac{\phi_N - \phi_P}{|\boldsymbol{d}|} \right) \tag{2.73}$$

An alternative method of estimating the face gradient is to interpolate the gradients at the cell centre towards the face as mentioned in the Eqn.(2.74), with $f_x$ being the same as mentioned

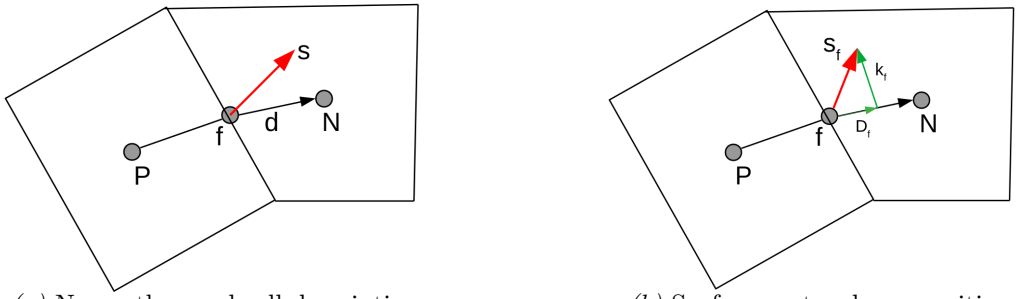


*(a)* Non-orthogonal cell description *(b)* Surface vector decomposition

Figure 2.14 – Schematic for the interpolation for face value on a non orthogonal mesh

in the convection scheme.

$$\boldsymbol{S}_f \cdot (\nabla\phi)_f = \boldsymbol{S}_f \cdot (f_x(\nabla\phi)_P + (1 - f_x)(\nabla\phi)_N) \tag{2.74}$$

Although both methods are second-order accurate, this method is still similar to that of the central differencing scheme mentioned earlier (CD). Also, Eqn. (2.74) uses a larger computational molecule to obtain the gradient of the cell centre of neighbour cells, increasing the computation by multifold, which in turn cannot be used for non-orthogonal mesh. Jasak (1996) examined various compositions for non-orthogonal components, and recommended to split the term into two parts, one for orthogonal parts and the other for non-orthogonal parts.

$$\boldsymbol{S}_f(\nabla\phi)_f = \boldsymbol{D}_f \cdot (\nabla\phi)_f + \boldsymbol{k}_f(\nabla\phi)_f \tag{2.75}$$

The vector $\boldsymbol{D}_f$ denotes the orthogonal component connecting the centres of the control volume, limiting the less accurate method only to the non-orthogonal part, as shown in Figure 2.14b. The minimum correction, orthogonal correction and over-relaxed approach are some decomposition techniques to estimate the non-orthogonal part. The non-orthogonal correction potentially creates unboundedness, particularly if mesh non-orthogonality is large. If the preservation of boundedness is more important than accuracy, the non-orthogonal correction has to be limited or completely discarded, thus violating the accuracy of the discretisation. The final form of diffusion term is the same for all the three approaches as given in Eqn.(2.76). The face interpolate is calculated as mentioned in Eqn.(2.74).

$$\boldsymbol{S}_f(\nabla\phi)_f = |\boldsymbol{D}_f| \quad \frac{\phi_N - \phi_P}{|\boldsymbol{d}|} + \boldsymbol{k}_f(\nabla\phi)_f \tag{2.76}$$

#### 2.2.1.3 Source term

All partial differential equation terms that cannot be expressed in terms of convection, diffusion, or temporal terms will be treated as source terms. This term can be hence the representative function of $\phi$. Considering the general comments given by Patankar (1980) in order to discretize the source term, it is assumed as a linear function of $\phi$,

$$\int_{V_p} S_\phi(\phi) dV = \int_{V_p} (S_u + S_p\phi) dV = S_u V_p + S_p V_p \phi_p \tag{2.77}$$

The term $S_u$ will be treated explicitly and depends on the sign of $S_p$, it will be treated implicitly (if $S_p < 0$), or it will be treated explicitly (if $S_p > 0$). Treating it implicitly increases the diagonal dominance of the system matrix.

#### 2.2.1.4 Semi discretized form of transport equations

Using Eqns (2.68), (2.72) and 2.77 and assuming that the control volumes does not change with the time, semi discretized form of the transport equation is given as,

$$\int_t^{t+\nabla t} \left[ \left( \frac{\partial(\rho\phi)}{\partial t} \right)_P V_P + \sum_f F\phi_f - \sum_f (\rho\Gamma_\phi)_f \boldsymbol{S} \cdot (\nabla\phi)_f \right] dt = \int_t^{t+\nabla t} \Big( S_u V_P + S_P V_P \phi_P \Big) dt \tag{2.78}$$

#### 2.2.1.5 Temporal discretisation

The time derivatives in the Eqn.(2.78) can be calculated directly as

$$\left( \frac{\partial \rho\phi}{\partial t} \right)_P = \frac{\rho_P^n \phi_P^n - \rho_P^0 \phi_P^0}{\Delta t} \tag{2.79}$$

$$\int_t^{t+\Delta t} \phi(t) = \frac{1}{2} \Big( \phi^0 + \phi^n \Big) \Delta t \tag{2.80}$$

where

$$\phi^n = \phi(t + \Delta t); \quad \phi^0 = \phi(t) \tag{2.81}$$

Assuming that the density and diffusivity do not change in time and using the above Eqns, **Crank Nicholson** form of temporal discretization is derived. It is second-order accurate, and it is unconditionally stable but does not guarantee the boundness of the solution (Patankar, 1980). As described earlier, boundness can be obtained if the equation is discretized to first-order temporal accuracy. Several temporal discretization methods have developed several temporal discretization methods by neglecting the variation of face values of $\phi$ and $\nabla\phi$ in time. The new form of the equation, first-order accurate in time is given in the Eqn. (2.83), and a choice has to be made to determine the face values of $\phi$ and $\nabla\phi$.

$$\begin{aligned} \frac{\rho_P \phi_P^n - \rho_P \phi_P^0}{\Delta t} V_P + \frac{1}{2} \sum_f F\phi_f^n - \frac{1}{2} (\rho(\Gamma_\phi)_f) \boldsymbol{S} \cdot (\nabla\phi)_f^n \\ + \frac{1}{2} \sum_f F\phi_f^0 - \frac{1}{2} (\rho(\Gamma_\phi)_f) \boldsymbol{S} \cdot (\nabla\phi)_f^0 \\ = S_u V_P + \frac{1}{2} S_P V_P \phi_P^n + \frac{1}{2} S_P V_P \phi_P^0 \end{aligned} \tag{2.82}$$

$$\frac{\rho_P\phi_P^n - \rho_P\phi_P^0}{\Delta t}V_P + \sum_f F\phi_f - (\rho(\Gamma_\phi)_f)\boldsymbol{S}\cdot(\nabla\phi)_f = S_uV_P + S_PV_P\phi_P \tag{2.83}$$

In **explicit discretisation**, face values are determined from the old-time field Eqn. (2.84), and the only unknown will be the $\phi$, and it can be calculated directly using Eqn. (2.85)) instead of solving system of equations as in the Crank Nicholson method. However, if the Courant number is larger than unity, then the system becomes unstable even for steady-state problems.

$$\phi_f = f_x\phi_P^0 + (1-f_x)\phi_N^0 \tag{2.84}$$

$$\phi_P^n = \phi_P^0 + \frac{\Delta t}{\rho_P V_P}\left[\sum_f F\phi_f - \sum_f (\rho(\Gamma_\phi)_f)\boldsymbol{S}.(\nabla\phi)_f + S_uV_P + S_PV_P\phi_P^0\right] \tag{2.85}$$

The **Euler implicit method** expresses the face value in terms of new time-level Eqn. (2.86)) cell values creating the system of equations. The coupling is much stronger, and the system is stable even if the Courant number limit is violated and guarantees boundness. Although, this method is still first-order accurate.

$$\phi_f = f_x\phi_P^n + (1-f_x)\phi_N^n \tag{2.86}$$

Another accurate second-order scheme, but still neglecting the variation of face values in time, is **Backward differencing scheme** which uses three time level. It is achieved using Taylor series expansion for the 'second old time level ($\phi^{00}$)' . The final form of discretized equation in the backward differencing is given in the Eqn. (2.87), but still, it lacks boundness (Jasak, 1996).

$$\frac{\frac{3}{2}\rho_P\phi^n - 2\rho_P\phi^0 + \frac{1}{2}\rho_P\phi^{00}}{\Delta t}V_P + \sum_f F\phi_f - \sum_f (\rho(\Gamma_\phi)_f)\boldsymbol{S}\cdot(\nabla\phi)_f = S_uV_P + S_PV_P\phi_P^n \tag{2.87}$$

#### 2.2.1.6 System of linear equations and convergence

Any form of discretisation equation for the generic transport equation leads to a linear algebraic equation for each control volume in the form,

$$a_P\phi_P^n + \sum_N a_N\phi_N^n = R_P \tag{2.88}$$

where $a_P$ and $a_N$ are the coefficients associated with the faces of control volumes P and its neighbours N. The term $R_P$ denotes the explicit contributions from boundary conditions (to be discussed in the next section) and source terms. In order to obtain the solution of $\phi_P$ in the entire domain for the new time step, the linear algebraic equation can be written in matrix form,

$$[A][\phi] = [B] \tag{2.89}$$

In the above expression, $[A]$ will be a square matrix with diagonal elements represented as $a_P$ and off-diagonal elements contributions are from $a_N$. The vectors $[\phi]$ contain the value of $\phi$ at each cell centre, and $[B]$ contains all the explicitly discretized terms. The matrix is solved iteratively until a residual tolerance is achieved. The general convergence rate of the iterative method depends on the coefficients of system matrix $[A]$. The Conjugate Gradient method (CG) proposed by Hestenes and Stiefel (1952) guarantees that the exact solution will be obtained in the number of iterations lesser than or equal to the number of equations in the system. The convergence rate also can be improved by preconditioning the matrix. The Incomplete Cholesky preconditioned Conjugate Gradient (ICCG) solver will be used for symmetric matrices (Jacobs, 1986). The adopted solver for asymmetric matrices is the Bi-CGSTAB (biconjugate gradient stabilized method) by Van der Vorst (1992).

#### 2.2.1.7 Numerical solution

There are four unknowns (the three velocity components and the pressure) and four equations (three momentum and one continuity equation), however the pressure term in the continuity equation is missing. Combining equations with one another and allowing that unknowns assessed should fulfil both equations is one of the interesting methods in numerical solutions for CFD problems.

**2.2.1.7.1 Pressure Velocity algorithm** In order to derive the pressure equation, a semi-discretized form of the momentum equation is obtained using Eqn. (2.88):

$$a_P \boldsymbol{u}_P = \boldsymbol{H}(\boldsymbol{u}) - \nabla p \tag{2.90}$$

The term $\boldsymbol{H}(\boldsymbol{u})$ consists of two parts: "transport part" which includes matrix of coefficients for all neighbour cells multiplied by corresponding velocities and the "source part" composed of source terms of the transient terms and all other source terms apart from pressure gradient. Keeping the velocity $\boldsymbol{u}_P$, the velocity on the cell centre, on LHS,

$$\boldsymbol{u}_P = \frac{\boldsymbol{H}(\boldsymbol{u})}{a_P} - \frac{\nabla p}{a_P} \tag{2.91}$$

The velocity at the cell face can be interpolated and obtained as,

$$\boldsymbol{u}_f = \left(\frac{\boldsymbol{H}(\boldsymbol{u})}{a_P}\right)_f - \left(\frac{1}{a_P}\right)_f (\nabla p)_f \tag{2.92}$$

The discrete incompressible continuity equation is expressed as,

$$\sum_f \boldsymbol{S}_f \boldsymbol{u}_f = 0 \tag{2.93}$$

Using the equations (2.92) and (2.93), the following form of the pressure equation is obtained.

$$\nabla \cdot \left( \frac{1}{a_P} \nabla p \right) = \sum_f \boldsymbol{S}_f \left( \frac{\boldsymbol{H}(\boldsymbol{u})}{a_P} \right)_f \tag{2.94}$$

The final form of the discretized incompressible Navier-Stokes equations is :

$$a_P \boldsymbol{u}_P = \boldsymbol{H}(\boldsymbol{u}) - \sum_f \boldsymbol{S}_f (p)_f \tag{2.95}$$

$$\sum_f \boldsymbol{S}_f \left[ \left( \frac{1}{a_P} \right) (\nabla p)_f \right] = \sum_f \boldsymbol{S}_f \left( \frac{\boldsymbol{H}(\boldsymbol{u})}{a_P} \right)_f \tag{2.96}$$

The face fluxes $F_f$ are computed using $\boldsymbol{u}_f$ from Eqn. (2.92) and these face fluxes are guaranteed to be conservative by satisfying Eqn. (2.93)

$$F_f = \boldsymbol{S}_f \cdot \boldsymbol{u}_f = \boldsymbol{S}_f \cdot \left[ \left( \frac{\boldsymbol{H}(\boldsymbol{u})}{a_P} \right)_f - \left( \frac{1}{a_P} \right) (\nabla p)_f \right] \tag{2.97}$$

Eqns. (2.95) and (2.96) demonstrate the linear relationship between velocity and pressure and vice versa. This inter equation coupling necessitates specific treatment; PISO and SIMPLE are some popular ways of dealing with it.

**2.2.1.7.2 PISO** Pressure implicit with Splitting of Operators (PISO) has been originally proposed by Issa (1986) for transient flow type of problems. This algorithm is computationally cheap compared to Semi Implicit Pressure Linked Equation (SIMPLE) as there are only three equations to be solved every iteration, but in another algorithm (to be discussed next), it is four equations. For the incompressible equations derived (2.95) and (2.96), PISO algorithm can be describes in following stages.

**Momentum predictor:** To solve the momentum equation (2.95), pressure term is unknown. The pressure field from the previous time step is used to solve the momentum equation obtaining the solution in the form of a new velocity field (approximate).

**Pressure correction:** Using the velocity field, $\boldsymbol{H}(\boldsymbol{u})$ can be formulated, and the pressure Poisson equation 2.94 is solved to obtain the corrected pressure field across the domain.

**Velocity correction:** The velocity field should also be corrected as a consequence of the new pressure distribution, and it is carried out explicitly by solving Eqn. (2.91). By looking at the equation (2.91), the error arises from two terms, either $\boldsymbol{H}(\boldsymbol{u})$ or from the pressure. This PISO algorithm assumes that the whole velocity error only comes from the pressure term. Because non-linear coupling is less important than Pressure Velocity coupling, coefficients $\boldsymbol{H}(\boldsymbol{u})$ will be changed only in the next momentum predictor.

**2.2.1.7.3 SIMPLE** The Semi Implicit Pressure Linked Equation (SIMPLE) formulated by Patankar (1980) is widely used for steady-state problems. The discretized momentum and pressure correction equations are solved implicitly, and the velocity correction is solved explicitly,

making it a 'Semi Implicit method'. Since the SIMPLE algorithm is being used for solving the steady-state type of problems, relaxation factors are used to improve the diagonal dominance of the system matrix as there is no transient term. This method can be described in the following stages.

**Momentum predictor:** Solve the under-relaxed momentum equation (2.95), with initial guessed pressure. The solution will be obtained in the form of a new velocity field (approximate), different from the guessed velocity field.

**Pressure correction:** Using the velocity field, $\boldsymbol{H}(\boldsymbol{u})$ can be formulated, and the pressure Poisson equation (Eqn. 2.94) is solved to obtain the corrected pressure field across the domain. Also, calculate the conservative fluxes from (Eqn. (2.97)). Update the pressure and velocity with appropriate under-relaxation.

**Velocity correction:** The velocity field should be corrected explicitly by solving Eqn. (2.91). Solve the other transport variables if available in the equation. To improve the convergence, all other variables are also under-relaxed in an implicit manner.

**Convergence check:** From the obtained pressure and velocity field, verify that the solution is converged with the tolerance needed. Else, use these variables in the momentum predictor equation (instead of $\boldsymbol{H}(\boldsymbol{u})$ - that the difference from PISO) and continue solving until the convergence is obtained.

**2.2.1.7.4 PIMPLE** The advantage of the PISO loop is solving the transient problem with less computational time but has a limitation of Courant number ($Co < 1$) to maintain stability. However, the SIMPLE algorithm developed for steady-state simulation has no time step limitations. Combining the advantages of PISO and SIMPLE - segregated iterative approach, PIMPLE is developed (Patankar and Spalding, 1983). The PIMPLE algorithm comprises two loops- with the inner loop solving the pressure velocity coupling like PISO, and the outer loop follows the SIMPLE algorithm's idea to deal with velocity and free surface position $\alpha$ coupling. $Co$ can be much larger than 1 and no under-relaxation is required for a stable solution. This allows for larger time steps, but the computational effort for each time step is larger than with PISO.

### 2.2.2 *foamStar* and *foamStarSWENSE*

The previous finite volume descriptions are applied to the specific DD and FD solvers, *foamStar* and *foamStarSWENSE*, accordingly, in this section, along with a illustration of their solution algorithm. Recalling, foamStar is based on the open-source solver, interDymFoam (of OpenFOAM), which is used to solve the multiphase problem by coupling the Navier-Stokes equations with a Volume of Fluid (VoF) method. foamStarSWENSE is a derived version of foamStar with the only difference of solving SWENSE equations instead of NS.

#### 2.2.2.1 Finite volume discretization - *foamStar*

The numerical discretization of the governing equations for the two-phase incompressible flow model used in foamStar is presented in this section. The momentum equation's finite volume representation is as follows:

$$\frac{\partial(V\rho\boldsymbol{u})_P}{\partial t} + \sum_f^N((\rho\boldsymbol{\phi})_f\boldsymbol{u}_f) - \sum_f^N(\mu_f\boldsymbol{S}_f\cdot(\nabla\boldsymbol{u}_f)) - \nabla\boldsymbol{u}\cdot\nabla\mu V_P = -\nabla p_d V_P - (\boldsymbol{g}\cdot\boldsymbol{x})\nabla\rho V_P \quad (2.98)$$

The algebraic VoF convection equation with the artificial compression term is represented in finite volume representation as,

$$\frac{\partial(V\alpha)_P}{\partial t} + \sum_f^N(\boldsymbol{\phi}\alpha)_f + \sum_f^N(\boldsymbol{\phi}_{r,f}\alpha_f(1-\alpha_f)) = 0 \quad (2.99)$$

The subscript $P$ denotes the averaged properties of the owner cell, while $N$ denotes the averaged properties of the neighbour cells. The face averaged properties acquired by a cells to face interpolation are denoted by $(...)_f$. $\phi_f = \boldsymbol{u}_f\cdot\boldsymbol{S}_f$ represents the velocity face flux at face $f$; $\boldsymbol{u}_{r,f}$ is the flux of the relative velocity (ref Section 2.1.1.2). The mass flux $((\rho\phi)_f)$ can be computed from the VoF flux $((\phi\alpha)_f)$ using Eqn. (2.100), and this mass flux formulation couples Eqn. (2.98) and Eqn/ (2.99)

$$(\rho\phi)_f = (\phi\alpha)_f(\rho_{water} - \rho_{air}) + \phi_f\rho_{air} \quad (2.100)$$

Assuming a arbitrary time integration scheme is applied to Eqn.(2.98), and using the similar discretization as in section 2.2.1.7, momentum equation is given as,

$$\text{UEqn} : \pm\, a_P\boldsymbol{u}_P - \boldsymbol{H}(\boldsymbol{u}) = \nabla p_d V_P + (\boldsymbol{g}\cdot\boldsymbol{x})\nabla\rho V_P \quad (2.101)$$

The velocity $\boldsymbol{u}_P$ from the LHS of Eqn.(2.101) must satisfy the continuity condition. Applying the continuity equation to $\boldsymbol{u}_P$ yields pressure equation as

$$\nabla\cdot\boldsymbol{u}_P = \nabla\cdot\left[\frac{\boldsymbol{H}(\boldsymbol{u})}{a_P} - \frac{1}{a_P}[-\nabla p_{d,P}V_P - (\boldsymbol{g}\cdot\boldsymbol{x})\nabla\rho_P V_P]\right] = 0 \quad (2.102)$$

$$\text{pEqn} : \sum_f^N\left[\left(\frac{1}{a_P}\nabla p_d\right)_f\right]\cdot\boldsymbol{S}_f = \sum_f^N\left[\frac{\boldsymbol{H}(\boldsymbol{u})}{a_P} - \frac{1}{a_P}(\boldsymbol{g}\cdot\boldsymbol{x})\nabla\rho_P V_P\right]_f\cdot\boldsymbol{S}_f \quad (2.103)$$

The Poisson equation in the pressure equation is used to obtain the dynamic pressure. Using the computed dynamic pressure, the velocity and flux are corrected using following equation.

$$\begin{aligned}\boldsymbol{u}_P &= \left[\frac{\boldsymbol{H}(\boldsymbol{u})}{a_P} - \frac{1}{a_P}(\boldsymbol{g}\cdot\boldsymbol{x})\nabla\rho_P V_P\right] - \left[\frac{V_P}{a_P}\nabla p_{d,P}\right] \\ \phi_f &= \left[\frac{\boldsymbol{H}(\boldsymbol{u})}{a_P} - \frac{1}{a_P}(\boldsymbol{g}\cdot\boldsymbol{x})\nabla\rho_P V_P\right]_f\cdot\boldsymbol{S}_f - \left[\frac{V_P}{a_P}\nabla p_{d,P}\right]_f\cdot\boldsymbol{S}_f\end{aligned} \quad (2.104)$$

With UEqn (Eqn.(2.98)), pEqn (Eqn.(2.101)) and the correction equation (Eqn.(2.104)), nonlinear iteration is solved to estimate the corrected dynamic pressure and velocity.

#### 2.2.2.2 Finite volume discretization - *foamStarSWENSE*

The finite volume (FV) representation of the SWENSE formulation is presented in this section. The VoF convection equation is identical to the one used in the *foamStar*, hence it is not discussed here. SWENSE's momentum equation (Eqn. 2.24) is discretized as follows in Finite Volume representation:

$$\frac{\partial(V\rho\boldsymbol{u}_c)_P}{\partial t}+\sum_f^N((\rho\phi)_f\boldsymbol{u}_{c,f})-\sum_f^N(\mu_f\boldsymbol{S}_f\cdot(\nabla\boldsymbol{u}_{c,f}))-\nabla\boldsymbol{u}_{c,P}\cdot\nabla\mu_P V_P+\rho\boldsymbol{u}_{c,P}\cdot\nabla\boldsymbol{u}_{I,P}V_P-\frac{p_{I,P}}{\rho_w}\nabla\rho_P V_P \tag{2.105}$$

The subscripts and variables are identical to those defined in the previous section. Using the similar discretization as in section 2.2.1.7 and also similar to the previous section, the complementary velocity equation ($U_C$ Eqn) can be rewritten as given in Eqn. (2.106). $a_{c,P}$ represents the diagonal components of SWENSE momentum equation ($U_C$ Eqn) and $\boldsymbol{H}_c$ includes all the off-diagonal and source terms of the system.

$$U_C \text{ Eqn} : a_{c,P}\boldsymbol{u}_{c,P}-\boldsymbol{H}_c=-\left[\nabla p_{c,P}V_P+\frac{p_{I,P}}{\rho_w}\nabla\rho_P V_P\right] \tag{2.106}$$

$$\nabla\cdot\boldsymbol{u}_{c,P}=\nabla\cdot\left[\frac{\boldsymbol{H_C}}{a_{c,P}}-\frac{1}{pmba_{c,P}}[\nabla p_{c,P}V_P+\frac{p_{I,P}}{\rho_w}\nabla\rho_P V_P]\right]=0 \tag{2.107}$$

The following complementary pressure equation is obtained by substituting this velocity (Eqn. (2.106)) into the continuity equation (Eqn. (2.107)):

$$p_C \text{ Eqn} : \sum_f^N\left[\left(\frac{1}{\boldsymbol{a}_{c,P}}\nabla p_{c,P}\right)_f\right]\cdot\boldsymbol{S}_f=\sum_f^N\left[\frac{\boldsymbol{H}_c}{a_{c,P}}-\frac{1}{\boldsymbol{a}_{c,P}}\frac{p_{I,P}}{\rho_w}\nabla\rho_P V_P\right]_f\cdot\boldsymbol{S}_f \tag{2.108}$$

The complementary pressure equation is a Poisson equation that allows the complementary pressure to be calculated. Following the computation of the complementary pressure, the complementary velocity and fluid flux are corrected, as shown in Eqns. (2.108)

$$\begin{aligned}\boldsymbol{u}_c&=\left[\frac{\boldsymbol{H}_c}{\boldsymbol{a}_{c,P}}-\frac{1}{\boldsymbol{a}_{c,P}}\frac{p_{I,P}}{\rho_w}\nabla\rho_P V_P\right]-\left[\frac{V_P}{\boldsymbol{a}_{c,P}}\nabla p_{c,P}\right]\\ \phi_f&=\phi_{I,f}+\left[\frac{\boldsymbol{H}_c}{\boldsymbol{a}_{c,P}}-\frac{1}{\boldsymbol{a}_{c,P}}\frac{p_{I,P}}{\rho_w}\nabla\rho_P V_P\right]_f\cdot\boldsymbol{S}_f-\left[\frac{V_P}{\boldsymbol{a}_{c,P}}\nabla p_{c,P}\right]_f\cdot\boldsymbol{S}_f\end{aligned} \tag{2.109}$$

Therefore, the complementary pressure and the complementary velocity are strongly coupled within the non-linear iterations between Eqn.(2.106), Eqn.(2.108) and Eqn.(2.109).

#### 2.2.2.3 Discretization schemes and solutions

The OpenFOAM discretization schemes applied in the current *foamStar* and *foamStar-SWENSE* simulations are described in this section. The divergence term in finite volume format

| Item | Equation | fvScheme | Scheme |
|---|---|---|---|
| Gradient | $\nabla q$ | grad (q) | cellLimited Gauss linear 1.0 |
| S.N. gradient | $\boldsymbol{n} \cdot (\nabla q)_f$ | snGrad | corrected 0.5 |
| VoF convention | $\nabla \cdot (\boldsymbol{u}\alpha)$ | div (phi,alpha) | Gauss vanLeer + MULES limiter |
| VoF relative flux | $\nabla \cdot (\boldsymbol{u}_r\alpha(1-\alpha))$ | div(phirb,alpha) | Gauss linear |
| Mom. convection | $\nabla \cdot (\rho\boldsymbol{u}\boldsymbol{u})$ | div (rhoPhi, $U$ ) | Gauss linear UpwindV grad(U) |
| Mom. convection | $\nabla \cdot (\rho\boldsymbol{u}\boldsymbol{u}_c)$ | div (rhoPhi, Uc) | Gauss linear UpwindV grad($\boldsymbol{u}_c$) |
| Mom Laplacian | $\nabla \cdot (\mu\nabla (\mathbf{u}))$ | Laplacian | Gauss linear corrected 0.5 |
| Pressure Laplacian | $\nabla \cdot (\frac{1}{qp}\nabla(p))$ | Laplacian | Gauss linear corrected 0.5 |

Table 2.1 – Spatial discretization schemes

is $\sum_f^N((\rho\phi)_f\boldsymbol{u}_f)$, while in OpenFOAM format is $div(rhoPhi, U)$. This is a typical example of OpenFOAM nomenclature with finite volume discretization.

OpenFOAM has several spatial discretization schemes; however, only a few have been extensively confirmed. The OpenFOAM community regularly uses most of the spatial discretization techniques employed in this thesis. The spatial discretization strategies for each term of the governing equations often employed in simulations are summarised in Table 2.1. $q_f$ is a cell to face interpolated quantity, while $q$ is an arbitrary cell averaged quantity. The "*cellLimited*" technique in the Table constrains the cells-to-face interpolated value based on the owner and neighbour cell information. The surface normal gradient is S.N, and the "*corrected*" indicates non-orthogonal correction. The VoF transportation divergence scheme employs the *Van-Leer* scheme (Van Leer, 1979) and the OpenFOAM internal limiter MULES (Multidimensional Universal Limiter for Explicit Solver) (Zalesak, 1979). MULES uses the Flux-Corrected Transport scheme, which is dependent on information from neighbouring cells, and it adjusts the scheme's correctness and VoF boundness. The convection term of the momentum equation is discretized in this thesis using a second-order upwind technique with the V-option designated *linearUpwindV*. The V-option is an additional option for the discretization of a vector field. The flow limiters are calculated separately for each vector component when using the V option. Choi (2019) can be referred for the stability of the V-option.

For an unsteady problem in OpenFOAM, time integration schemes (ddtSchemes) can be chosen from Implicit Euler (Euler), Crank-Nicolson (CN), and second-order backward differential formula (BDF2). The Euler scheme is stable, although each time step does have a considerable amount of energy dissipation. The CN scheme is a second-order implicit scheme with an off-centring coefficient that allows for fine-tuning of numerical damping and stability. In this present thesis, both Euler and CN scheme with off-centring 0.95 is tested.

This part skips the selection of a linear systems solver for each variable as the standard OpenFOAM schemes and solver is adopted. The tolerance level employed in this thesis is $10^{-7}$. The number of non-linear iterations used by the PIMPLE algorithm is defined by the PIMPLE settings in OpenFOAM (fvSolutions). This thesis uses eight to ten outer iterations and two to four inner iterations (PISO). In this thesis, one to two non-orthogonal corrector iterations are used. Relaxation factors (not to be confused with relaxation zones) are frequently employed to

increase the stability of simulations. However, all relaxation factors are set to one to reduce the impact of computational coefficients on simulations and focus more on the numerical schemes themselves.

#### 2.2.2.4 Solver boundary conditions

The mathematical formulation of the two-phase flow model's boundary conditions, as well as the SWENSE formulation, were previously discussed. The numerical and physical properties of each variable at the boundary are described in this section. Table 2.2 summarizes the boundary conditions in OpenFOAM notations for all variables.

| | **Body/Wall** | **Inlet & Oulet** | **Open** |
|---|---|---|---|
| $\boldsymbol{u}$ | movingWallVelocity/ slip | waveVelocity | pressureInletOutletVelocity |
| $\boldsymbol{u}_c$ | movingWallSwenseVelocity | zero vector | pressureInletOutletVelocity |
| $\alpha$ | zeroGradient | waveAlpha | inletOutlet |
| $p_d$ | fixedFluxPressure | zeroGradient | totalPressure |
| $p_c$ | fixedFluxPressure | zeroGradient | totalPressure |

Table 2.2 – Boundary conditions for all variables

- **Body/Wall boundary**
  - **movingWallVelocity**: The solid body's surface is regarded impermeable. The fluid velocity is made equal to the body surface velocity when the no-slip condition is assumed. The no-slip body boundary condition with/without body motion is covered by the *movingWallVelocity* boundary condition.
  - **slip** : The slip boundary condition in OpenFOAM applies the free-slip boundary condition
  - **movingWallSwenseVelocity**: To deal with the SWENSE body boundary condition ($\boldsymbol{u}_{body} - \boldsymbol{u}_I$), a new boundary condition named *movingWallSwenseVelocity* is introduced.
  - **zeroGradient**: The phase fraction gradient at the wall/body interface is considered to be zero, implying that the surface normal gradient of $\rho$ is zero everywhere.
  - **fixedFluxPressure**: When the boundary does not move, OpenFOAM recommends using the *fixedFluxPressure* pressure boundary condition. The fluid flux, which is specified with the velocity boundary condition, adjusts the dynamic pressure gradient with the *fixedFluxPressure* boundary condition (Kim, 2021b).
- **Inlet/Outlet**: Due to the relaxation scheme, the inlet and outlet boundaries are considered to have an undisturbed wave field. As a result, using inlet and outlet boundary conditions can be thought of as an explicit relaxation with a weight of 1.0.
  - **waveVelocity** : The overall velocity at the inlet and outlet boundaries is the same as the incident wave velocity. Like the overall velocity, the incident wave elevation defines the VoF field at the boundary.

- **zeroGradient** : Despite the incident dynamic pressure being known, the dynamic pressure is subjected to the *zeroGradient* boundary condition.
- The complementary flow in the SWENSE model is gradually reduced in the relaxation zone, and it must disappear at the inlet and outlet boundaries. As a result, for the complementary velocity, zero velocity is used, and for the complementary pressure, *zeroGradient* is used. The same *waveAlpha* boundary condition is used because the VoF field is not decomposed.

■ **Open boundary condition**: The top boundary of the computational domain is frequently stated as an open-air boundary condition in most naval applications.

- Because the incident flow components are reduced at the top boundary, the total and complementary velocity boundary conditions are the same.
- For pressure, an approximation introduced at this boundary is that the total pressure $p$ is constant and equal to the atmospheric pressure ($p = p_0 - 0.5\rho|\boldsymbol{u}|^2$). The reference pressure $p_0$ is set to zero.
- The zero normal gradient is imposed when the flow at the boundary is inflow. The cell-center velocity is imposed on the boundary when it comes to outflow. This boundary condition is known as *pressureInletOutletVelocity* in OpenFOAM notation.
- The VoF uses the inletOutlet boundary condition, which normally works the same as *zeroGradient* However, it switches to *fixedValue* if the velocity vector next to the boundary aims inside the domain.

### 2.2.3 Wave generation and absorption

Recalling, FNPF-CFD coupling models are classified based on domain decomposition (DD) and functional decomposition (FD) strategies. The DD strategy divides the computational domain into parts and applies different mathematical models in each part. In most DD-based WSI problems, the computational domain is decomposed into a viscous inner sub-domain and potential outer sub-domain. The wave information (velocity, pressure and surface elevation) will be transferred through either a sharp interface or relaxation zones. Higuera et al. (2013) proposed a sharp interface instead of relaxation zones, hence advantageous of the reduction in the computational domain, but there is a high chance of reflection reported. Jacobsen et al. (2012) introduced relaxation zones on coupling boundaries to gradually blend the information between the two models (Engsig-Karup et al., 2007; Seng, 2012). There are two types of relaxation methods available in general. One method is implicit blending, in which the target equations are inserted into the governing equations (Kim et al., 2012; Vukčević et al., 2016). Many researchers have used implicit blending and found it to be effective. Another relaxation method is the explicit blending approach, which directly blends the computed solution with the desired solution after solving the governing equation. This thesis employs explicit blending, which is discussed below.

The simplest way of wave generation in one way DD (*foamStar*) is to impose wave velocity and free surface elevation from potential wave models at the inlet of the CFD domain. As

mentioned, *foamStar* adopts the wave generation and absorption method based on an explicit scheme that relaxes the computed solution towards a given target flow field (Jacobsen et al., 2012; Seng, 2012; Mayer et al., 1998; Engsig-Karup, 2006; Choi et al., 2018b), and the scheme requires a weight function that varies between 0 and 1 in the relaxation zone (see Figure 2.1). After solving the governing equations, the computed solution ($\zeta$) is relaxed with the target (incident wave) solution ($\zeta_{target}$) as follows:

$$\zeta = w_f \zeta_{target} + (1 - w_f)\zeta_{CFD} \tag{2.110}$$

where $\zeta$ is either the velocity field($\mathbf{u}$) or the VoF field ($\alpha$), $w$ is the weight function, and $\zeta_{target}$ will be the given target flow field usually set to be either the incident wavefield or calm-water. Two common choices of weight function are the polynomial weight function (Mayer et al., 1998; Engsig-Karup, 2006; Choi et al., 2018b) and the exponential weight function (Jacobsen et al., 2012; Seng, 2012; Choi et al., 2018b). The present study adopts the explicit relaxation scheme using polynomial weight function given as,

$$w_f(x) = -2x^3 + 3x^2 \tag{2.111}$$

here $x \in [0, 1]$, is the normalised coordinate inside the relaxation zone. The above technique can be applied to the wave absorption zone and if the target values ($\zeta_{target}$) are set to no waves, the entire wavefield is damped, and if the target values are set to incident waves, then the scattered waves are damped.

Another addition to the *foamStar* library was the dynamic weight function given as,

$$w_f^d = 1 - (1 - w_f)^{|\mathbf{u}-\mathbf{u}_{target}|\Delta t/\Delta x} \tag{2.112}$$

The relaxation weight is calculated using this dynamic weight function depending on the difference between the target and computed solution. Choi (2019) observed that the static exponential weight function preserved wave amplitude the best, while the dynamic weight function resulted in the least amount of wave reflection. In the present work, static polynomial weight function is adopted based on suggestions given in Kim (2021b).

Similar relaxation zones are also presented in the FD approach *foamStarSWENSE* with $\zeta$ denoting the complementary variable. The generation of waves in the SWENSE method does not define specific zones for wave generation. It imposes the incident wave solution explicitly in the entire computational domain and solves the disturbances of the incident waves as a complementary correction. The spectral wave models used for wave generation is either based on the stream function theory (Fenton, 2014; Ducrozet et al., 2019) for regular wave propagation and the High-Order Spectral methods -*HOS* (Ducrozet et al., 2012, 2016a) for complex sea states. They have been demonstrated as accurate and efficient in several literature. The advantage of using spectral wave models (HOS-NWT) helps the SWENSE method adjust the zone of the incident wave above the free surface also, such that the same functional decomposition can be used in the entire CFD computational domain (Li et al., 2018).

#### 2.2.3.1 Reconstruction of irregular waves in the CFD domain (Grid2Grid)

For both the DD and FD strategies, incident waves generated from HOS are solved independently, not alongside with *foamStar* and *foamStarSWENSE*. The results of the incident waves from HOS computations are stored for further use. The pseudo-spectral formalism permits the storage of modal coefficients of the quantities of interest that can be reconstructed with a linear combination of basis functions. The *foamStar* and *foamStarSWENSE* solvers shall use these modal coefficients to reconstruct the incident wave information on their mesh. The modal amplitudes are first transformed onto uniformly spaced discretized points by IFFT, and then a B-spline interpolation scheme is used to interpolate into the solver's mesh. This interpolation is needed as HOS simulation used fewer points per peak wavelength than required for CFD solvers. One of the consequences of the interpolated velocity field is that it has a large divergence, which breaks the boundness of the VoF field and causes instability problems, especially in the *foamStarSWENSE* (Li et al., 2021b). This instability can be avoided by using interpolation with the zero-padding technique, i.e. introducing additional zero amplitudes modes at the end of the spectrum, adding extra spatial points, and making the HOS grid finer at the post-processing stage. With this method, the incident velocity divergence after interpolation is drastically reduced. The interpolation method mentioned above is made available to the public in an open-source wrapper program named Grid2Grid (Choi et al., 2017b). Further details on the Grid2Grid interpolation scheme and its application method are presented in the Grid2Grid manual.

### 2.2.4 Solution algorithm

The key steps of the implementation of the above procedures are summarized for both the DD and FD solvers in this section.

#### 2.2.4.1 *foamStar*

The *foamStar* algorithm between each time step is as follows.

— Wave generation and absorption in the relaxation zone are updated based on the weight function Eqn.(2.110)

— The fluid equations (Eqn.(2.98), (2.101), (2.104)) and VoF ($\alpha$) equation Eqn.(2.5) are solved in PIMPLE algorithms (SIMPLE+PISO supplied with OpenFOAM)

— The body motion (floating body) is solved (Eqn.(2.34),(2.36)) along with mooring equations (Section 2.1.4.3) and the computational mesh is updated accordingly (Eqn.(2.39))

— After solving for VoF ($\alpha$), it is relaxed in the relaxation zone to impose the target values. Thus, the fluid velocity is also relaxed in the relaxation zone at the end of PISO

— If there is a turbulence model, it will be solved at the last step in the algorithm.

Figure 2.16 explains the detailed implementation of the mentioned algorithm in the two-phase solver *foamStar*.

#### 2.2.4.2 *foamStarSWENSE*

The structure of the *foamStarSWENSE* solver solves the subsequent algorithm in its conservative form (Section 2.1.2.1) between each time step.

— At the beginning of the time step, the incident wave properties $\boldsymbol{u}_I$ and $p_I$ are updated from potential wave solvers and mapped on the CFD mesh. The total velocity is reconstructed with $\boldsymbol{u} = \boldsymbol{u}_I + \boldsymbol{u}_c$

— Initiating PIMPLE, the body motion (floating body) is solved (Eqn.(2.34),(2.36)) first along with mooring equations (Section 2.1.4.3) and the computational mesh is updated accordingly (Eqn.(2.39))

— The VoF field (Eqn.(2.25)) is solved and the modified incident wave pressure is updated with new density and viscosity field Eqn.(2.6).

— In the PISO loop, the complementary velocity field is solved from Eqn.(2.106) first (the momentum prediction step). Secondly, the complementary pressure is solved (Eqn.(2.108)). The pressure field corrects the flux of the complementary velocity (Eqn.(2.109)). After the correction, the flux is used to reconstruct the complementary velocity field at the cell centre.

— The solution is then blended to the target values in the relaxation zones to attenuate the complementary waves in the far-field (Eqn.(2.110)).

— In the PIMPLE loop, outer nonlinear iterations are made to achieve convergence of the VoF, the velocity, and the pressure before moving to the next time-step.

### 2.2.5 *foamStar/foamStarSWENSE*-MoorDyn coupling

MoorDyn is coupled to the *foamStar/foamStarSWENSE* solver in two way coupling approach where the information between the solvers is passed at each time step, and each solver will influence the solutions of the other. The core functions in MoorDyn are compiled into a shared library to use the dynamic loading of the functions inside the *foamStar/foamStarSWENSE*. Generally, there are two ways of coupling between the solvers that can be adopted (Beazley et al., 2001; Lee et al., 2021), tight and loose coupling. Each solver is solved separately in the loose coupling, and some variables are exchanged between the solvers. Also, it can adopt different time step sizes for each solver. However, in the tight coupling, both the solvers save all the variables and data in the common coupled solver, and each solver composes its own governing equation. The present work has adopted the loose coupling between the *foamStar/foamStarSWENSE* and MoorDyn. The coupling procedure follows three phases: initialization, information sharing, and closing.

**Initialization phase**: Before the time loop begins, the solvers are being set up, and the mooring system is created. An initialization function is then called calculating its initial conditions based on body position specified by the equation of the motion.

**Information sharing phase**: As time progress, *foamStar/foamStarSWENSE* transfers the six degrees of freedom displacement $(\boldsymbol{q}, \boldsymbol{\theta})$, velocities $(\dot{q}, \omega)$, and current timestep size into the

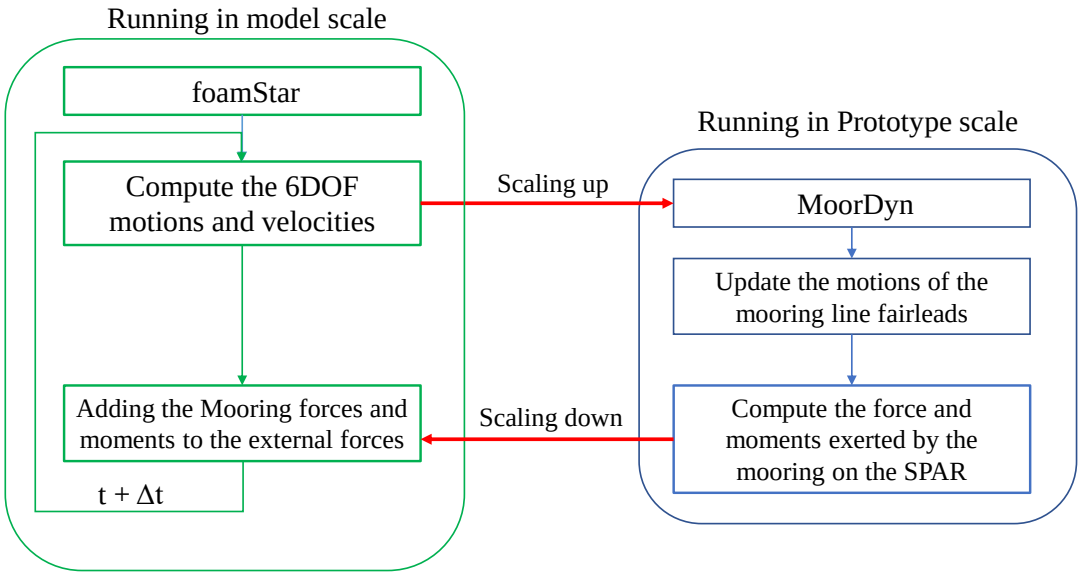


Figure 2.15 – Flow chart of the short algorithm between the *foamStar* (in model scale) and MoorDyn library (in prototype scale). hydrodynamic

MoorDyn. MoorDyn calculates the fairleads' position, velocities, and accelerations based on the input. Along with that, the mooring system tensile load and restoring forces are calculated and shared with the *foamStar/foamStarSWENSE* as one of the external forces $[\boldsymbol{Q}_{e,M}]$. Then the *foamStar/foamStarSWENSE* calculates the platform motions, accelerations etc., and the loop continues till the last time step.

**Closing phase**: The last stage releases the variables and memories used to calculate the tensile load of the mooring system after the end of calculations.

It should be noted that *foamStar/foamStarSWENSE* uses a body reference system ($R_b$) for its governing equation, and MoorDyn uses an inertial frame of reference ($R_0$) for its governing equation. Hence, body displacements and velocities are transferred to the inertial reference frame at each timestep and mooring tension to the body reference frame. The detailed framework of the coupling procedure is shown in the Figure 2.16.

Although MoorDyn is simple in concept, its practical implementation can be difficult, as it is sensitive to the input parameters chosen, causing numerical instability (Paduano et al., 2020). Similar instability is observed in the present study when working with the mooring properties on experimental model values. However, using the prototype values shows that numerical instability can be avoided. Hence the mooring properties used in the experiment are modified to prototype values using Froude and Cauchy scaling. The final updated system of coupling considered is as shown in Figure 2.15, wherein the mooring analysis will be carried out in prototype conditions for motions and velocities and the computed forces are scaled-down and coupled with the CFD.

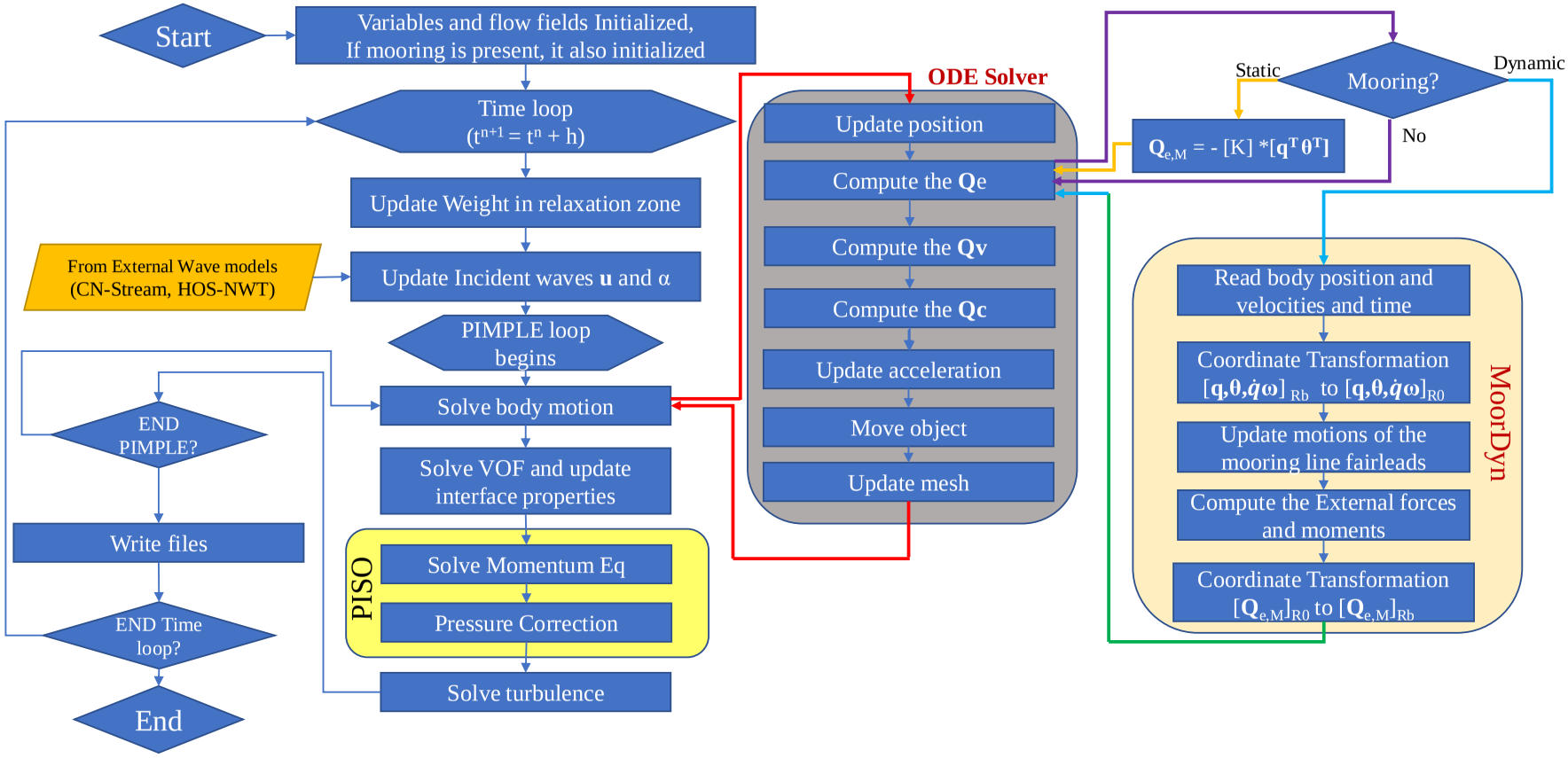


Figure 2.16 – Computational algorithm of coupling between the potential theory wave models, *foamStar*, and MoorDyn solver

Chapter 3

# FOCUSING WAVE INTERACTION WITH FIXED CYLINDER

Since offshore renewable energy became widely exploited in the last few decades, scientists and engineers have been paying more and more attention to offshore monopiles as a crucial foundation concept. Offshore monopiles (i.e. hollow cylinders) are frequently exposed to the harsh ocean environment and typically have a significantly larger diameter than other pile foundations. The advancement of numerical techniques has recently been used to solve such a complex interaction with the cylinders (Sriram et al., 2021c; Toedter et al., 2021; Zeng et al., 2021; Kamath et al., 2016). Although simple regular and irregular waves over the cylinder have been studied for a long time, steep or extreme waves interactions with cylinders is still a topic of active research. The focusing wave is widely recognized as one way of representing the extreme waves at sea, that can be generated easily in both experimental and numerical studies. The linear and second-order wave theories often used in routine design may not be sufficient for a reliable assessment since focusing waves sometimes entail considerable nonlinearity. The interaction between a fixed cylinder and NBR and BR focused waves, which has received much attention recently (Sriram et al., 2021c; Agarwal et al., 2021a) was chosen to validate the numerical models in this chapter. There are two parts to this chapter, (a) The NBR focused wave interaction with the fixed cylinder, and (b) BR focused wave interaction with the fixed cylinder. This chapter presents a first verification and validation (V&V) of *foamstar* and *foamstarSWENSE* in the case of a fixed structure subjected to focused waves. This part consequently does not include the mooring or rigid motion modules. However, it presents an inter comparison and conclusion on the respective efficiency of both approaches.

The overall structure of the chapter is as follows. First, the experimental setup and details are discussed, followed by NBR and BR focusing wave generation and validation. The NBR focusing wave interaction with the cylinder is detailed and validated in the next part of the following section, and the interaction of the BR focusing wave with the cylinder is presented in the last section. Also, the comparative discussion summarises and compares the efficiency of each coupling approach and improvements needed are discussed.

## 3.1 Experimental set-up

The experiments performed in the Schneiderberg wave flume at Leibniz University of Hannover, Germany, by Sriram et al. (2021a) are used for the present study. Both NBR and BR

focused waves interaction with the cylinder are examined during the experiment. The laboratory measurements on focusing wave interactions with a fixed and moving cylinder have been released for a comparative study between different numerical models (Agarwal et al., 2021a; Sriram et al., 2021c). The tank has dimensions of 110 m, 2.2 m, and 2 m as length, width and depth, respectively. The flume was filled with fresh water to a depth of 0.7m. The cylinder of interest is made of aluminium and has a diameter of 0.22 m, a length of 1.025 m with a 12 mm wall thickness, which represents a scaled-down model of a monopile that corresponds to the Alpha Ventus wind farm in the North Sea, off the coast of Germany. The variations in free-surface elevation along the tank are measured using seven resistance type wave gauges (WP1-7). The probe WP1 was placed close to the wavemaker ($x = 5.327$ m from HOS origin in $R_0$ frame), three-wave gauges (WP2-4) were placed at $x \approx 18$ m from the wavemaker. Similarly from HOS origin in $R_0$ frame (Section 2.1.4.1), the three other wave gauges (WP5- 7) are centred around the cylinder ($x = 25$ m) with WP5 placed at $x = 24.445$ m, WP6 at $x = 25$ m and WP7 at $x = 25.625$ m respectively. The probes position in $R_0$ frame with respect to the CFD origin are at $-0.445$ m (WP5), parallel to the origin (WP6), and 0.625 m from the origin (WP7). Typical representation of the probes and the experimental domain is shown in the Figure 3.1. Details about the location of wave gauges are also given in Table 3.1.

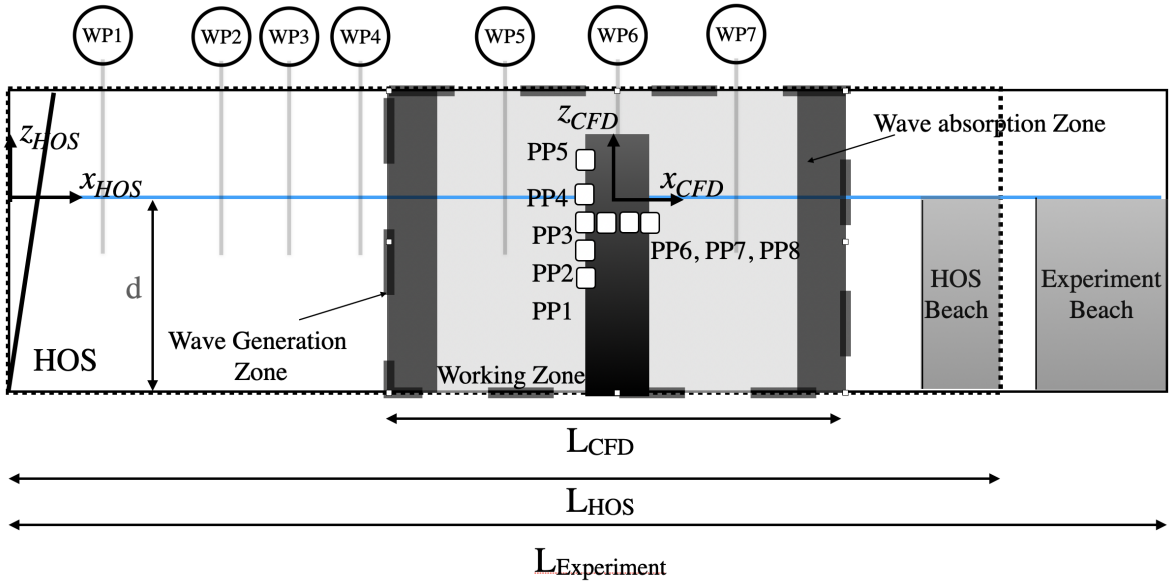


Figure 3.1 – Typical representation of the experiment, HOS-NWT and of CFD zone along with the description of wave probes (WP) and pressure sensors (PP) (not drawn to scale)

Eight pressure transducers were placed across the surface of the cylinder to monitor the time-varying and impulsive pressures caused by the waves (Table 3.2). PP1 is the lowest and is situated at a distance of 0.415 m from the bottom of the flume, with PP1-5 being positioned at 0°, encountering the incident waves at constant vertical spacing's of 0.1m. The final three transducers (PP6-8) are positioned at the same level as PP3 (0.615 m from the flume bottom) but are orientated in circumference at 20°, 90° and 180° around the cylinder. A force sensor positioned at the cylinder's top bearing and tightly fastened to the steel frame in the flume

| Wave probe | X from HOS origin in $R_0$ frame (m) | Y from HOS origin in $R_0$ frame (m) |
|---|---|---|
| **WP1** | 4.975 | 0.015 |
| **WP2** | 13.928 | 0.015 |
| **WP3** | 14.178 | 0.015 |
| **WP4** | 14.428 | 0.015 |
| **WP5** | 24.31 | 0.275 |
| **WP6** | 24.88 | 0.275 |
| **WP7** | 25.585 | 0.275 |

Table 3.1 – Details about the wave gauge locations in Experiment

was used to measure the total horizontal inline force acting on the cylinder. In order to capture the highly short-term pressures and loads generated by steep waves on the structure, the wave elevation was recorded at 100 Hz, while the pressure and inline force were captured at 9600 Hz.

| Pressure probe | Vertical location (m) | Angular Position ($^o$) |
|---|---|---|
| **PP1** | 0.415 | 0 |
| **PP2** | 0.515 | 0 |
| **PP3** | 0.615 | 0 |
| **PP4** | 0.715 | 0 |
| **PP5** | 0.815 | 0 |
| **PP6** | 0.615 | 20 |
| **PP7** | 0.615 | 90 |
| **PP8** | 0.615 | 180 |

Table 3.2 – Pressure sensor locations on the cylinder

| Case | $f_c$ (Hz) | $\Delta f/f_c$ | $f_1$ (Hz) | $t_f$ | N | $G_a$ |
|---|---|---|---|---|---|---|
| NBR focusing wave | 0.68 | 1 | 0.34 | 38.0 | 32 | 0.002 |

Note: $f_c$, center frequency; $\Delta f$ , frequency bandwidth; $t_f$, focusing time; N, number of wave packets; $G_a$, amplitude gain parameter

Table 3.3 – Tested wave packet characteristics

The experimental results in this Chapter (NBR and BR focusing wave) correspond to the wave characteristics, as shown in Table 3.3, which have been generated based on the second-order wavemaker theory (Sriram et al., 2015). A superposition of 32 (N) wave packets with constant steepness ($S = a_i k_i$ where $i \in [1 : \mathrm{N}]$, S is determined from $S = \pi G_a$, where $G_a$ is the amplitude gain parameter) generate the focused wave. The wave packet frequencies ranges from $f_1 = 0.34$ Hz to $f_n = 1.02$ Hz with the center frequency ($f_c$ ) and bandwidth ($\Delta f$ ) is $f_c = \Delta f = 0.68$ Hz. Accordingly, in intermediate depth ($k_c d = 1.453$), the focused wave spectrum is broad-banded. The second-order wavemaker theory was used to prescribe the wavemaker motion to restrict the generation of spurious waves. The amplitude gain parameter was adjusted to $Ga = 0.003$ for

generating breaking focused waves.

## 3.2 Verification and validation of focusing wave only simulation

The primary requirement for any WSI simulation is an accurate wavefield reproduction. The HOS wave generation and propagation of both NBR and BR focusing waves are discussed in this section's first part. Then NBR focusing waves generation with validation in *foamStar*, and *foamStarSWENSE* is presented in the second part. The third part of the section discusses the BR focusing wave generation and propagation in *foamStar*. The SWENSE approach's investigation for the breaking wave model necessitates a full reevaluation of its formulation. Therefore only *foamStar* is being evaluated for breaking wave scenarios.

### 3.2.1 HOS-NWT : Wave reproduction using Time Reversal

In the HOS-NWT, waves can be generated with user-defined amplitude, phase, frequency, and propagation angle for monochromatic regular waves and user-defined spectrum and wave characteristics for irregular waves. HOS-NWT can also generate waves using the experiment's recorded wave maker motions. Although the latter would be ideal for the current situation, the wave maker motion was instead generated using the Time Reversal (TR)technique in order to reduce the uncertainties related to experimental generation. The accurate reproduction of the incident wavefield is achieved thanks to the TR methodology applied to the reproduction of waves in water tanks (Chabchoub and Fink, 2014; Ducrozet et al., 2016b, 2020). The method's main idea is to make use of the time-symmetry of the physical laws of conservative systems, such as wave propagation. The TR method results in a simple way to reproduce any temporal free-surface profile at an arbitrary location in a wave tank.

This two-step procedure uses a target free surface elevation $\eta_t(t)$ that one wants to reproduce. In the present configuration, the wave-only experimental measurement of the wave gauge at the focusing location was used. The first step uses this temporal elevation to generate the wavefield in the tank, which was measured at the target location $x_t$. The measured signal $\eta_m(t)$ is time-reversed and generated in the same wave tank during a second step. Due to the time-invariance of the governing equations, it is expected that the target free-surface elevation $\eta_t(t)$ was reproduced at the target location $x_t$. This is validated for the NBR and BR focusing waves in HOS-NWT and is presented after the numerical setup adopted is discussed in the following subsections.

#### 3.2.1.1 Numerical setup

The computational domain for HOS was made similar to the experimental tank dimensions, with a 0.7 m water depth (Section 3.1). Only the length of the domain was reduced to 50 m (in the experiment, it is 110 m) as the focusing point is set to nearly 25 m, and a longer domain is not necessary. The wave absorption in the HOS-NWT is provided by a numerical beach that prevents the reflection from the opposite wall. The study's wave probes (WP) are identical to those of the wave flume mentioned in the experimental setup (Table 3.1). Regarding HOS

parameters, $N_x$ is the number of points in the domain that controls the spatial discretization of the HOS-NWT. The $N_x$ is linked to the maximum wavenumber in the spectral method as ($k_{max}$). In an irregular non-breaking sea state, the ratio ($k_{max}/k_p$) has a typical range of 20-30. In the present study, the ratio is maintained at 25, and the order of non-linearity of HOS is fixed to 5. The wave is generated by loading wave paddle motion from the TR study as input of HOS-NWT for a direct comparison to experiments, and the Tian model is used to account for the BR wave case. Definitions and recommended values for the breaking model are similar to values given in Seiffert et al. (2017); Seiffert and Ducrozet (2018); Tian et al. (2012). This 'classical' choice of parameters should ensure an accurate description of the wave field evolution in HOS-NWT. A constant phase shift observed in the experiment is 0.14 s (Sriram et al., 2021c). This may be attributed to the trigger at use for the recording during experiments that possibly experienced such a small time delay, and this shift is corrected in the numerical results. The results for NBR and BR focusing waves are presented one after each other in the following subsections.

#### 3.2.1.2 HOS validation : NBR focusing wave

Figure 3.2 shows the results of the TR validation technique for HOS-NWT using wave probe WP6 (the focusing point) in comparison to the experiment (Figure 3.2a, and Figure 3.2b zooms in near the focusing time window). The accuracy of the methodology is fulfilled, but some minor discrepancies were observed which can be attributed to the probe vibrations after impact in this configuration. Cross correlation analysis of the results from the experiments and the HOS probes WP5, WP6, and WP7 is used to quantify this. It has been found that there is some difference between the HOS and experimental results; the average observed coefficient value is 0.991. As HOS input is the feeder to the DD and FD-based solvers, this difference will also be visible in waves generated inside the CFD. Nevertheless, this difference is not too significant to be concerning, which could result from experimental uncertainty (Sriram et al., 2015). This NBR focusing wave generated with nonlinear potential flow solver will be used into the *foamStar* and *foamStarSWENSE* solvers for their wave requirements.

#### 3.2.1.3 HOS validation : BR focusing wave

The location of the WP 6 probe, which is 25 m from the HOS origin in the $R_0$ frame, is the focusing point of breaking in the spatial domain. Additionally, in the temporal domain, the HOS time window's focusing time would be nearly 38.2 s. The wave elevation comparison at wave probe WP1 near the paddle and WP5 to WP7 near the cylinder location are shown in Figures 3.3b to 3.3d. Figure 3.3a shows overall excellent agreement, except in the two peak troughs surrounding the largest wave. The probe WP5 reveals a little difference between the experiment's maximum amplitude and HOS at the focusing point, as well as changes beyond the focusing event. Cross-correlation analysis is used to quantify this, and the resultant coefficient is 0.988 when compared to the experiment's result. Figure 3.3c indicates very good agreement of the focused wave profile, including the preceding and following troughs. As expected, some discrepancies are observed after the focused breaking wave passes, which may be attributed to

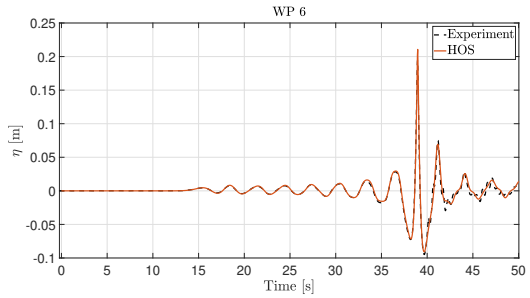


*(a)* Wave probe comparison- complete time window

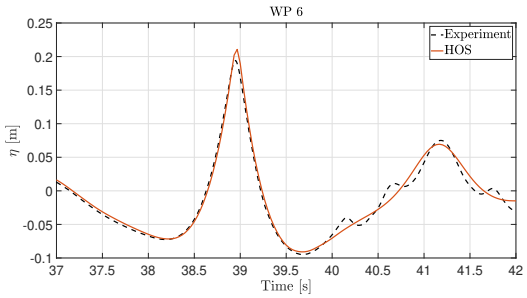


*(b)* Wave probe comparison- At focusing time

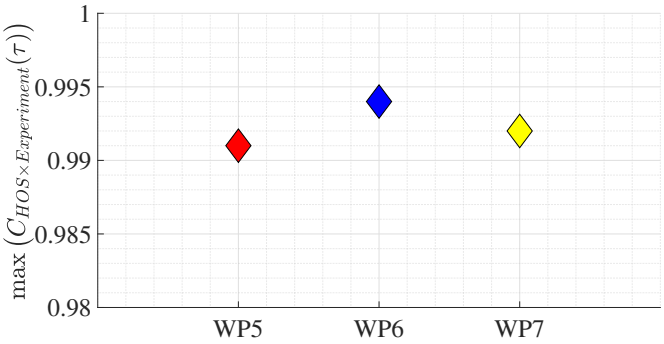


*(c)* Cross Correlation between HOS vs Experiment for probes WP5, WP6 and WP7

Figure 3.2 – Validation of Time Reversal(TR) principle of focusing wave generation with Experimental results

| **Items** | **Value** |
|---|---|
| Depth, d (m) | 0.700 |
| Diameter of cylinder (D)(m) | 0.22 m |
| 2D CFD NWT(m) length X depth | 2.75 X 1.4 |
| Freesurface refinement zone depth(m) | 0.44 |

Table 3.4 – Physical properties for numerical computations

the breaking model that does not simulate the whole complexity of breaking waves and also the vibration of wave gauges (high-frequency waves observed after t=40 s) which could not be avoided in experiment. This is also proven by the correlation coefficient of 0.99 and the WP7 probe, which is almost 0.988. These outcome ensures an nearly accurate and efficient solution to the breaking wave problem from the potential solver, and this HOS wave's surface elevation and velocity will be provided at the inlet zone of the *foamStar* solver for its wave generation.

### 3.2.2 Numerical setup for foamStar/foamStarSWENSE

The validation of the wave generation and propagation simulations in CFD was carried out in a $2D$ NWT to determine the most appropriate parameters for the solvers. Here the CFD represents both the *foamStar* and *foamStarSWENSE* solvers. The two dimensional CFD domain was 2.75 m ×1.4 m (length × height) to maintain the similar domain for the next wave-structure interaction study.The *foamStar* solver, which simulates the wave system, needs fine meshes to

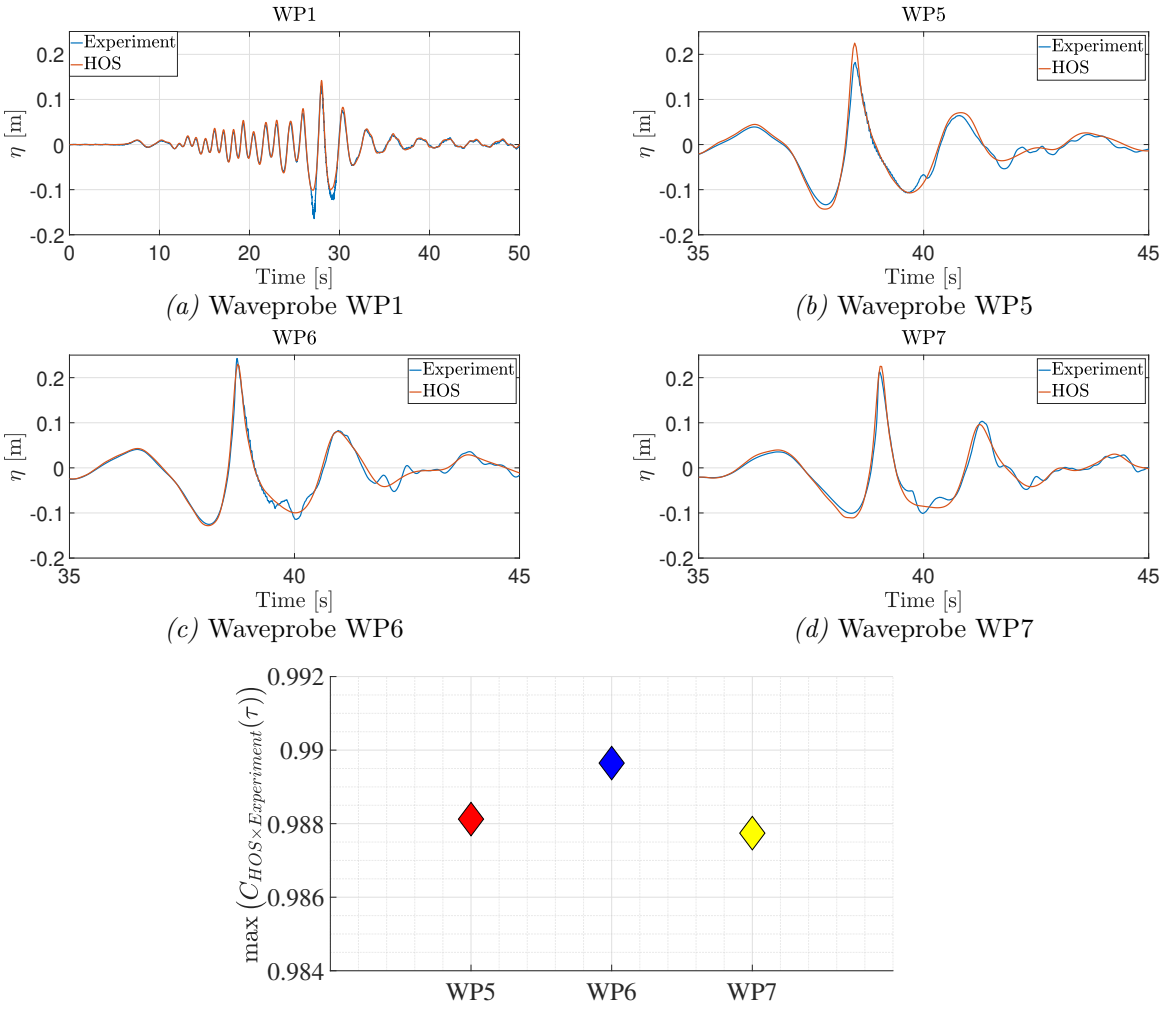


*(a)* Waveprobe WP1

*(b)* Waveprobe WP5

*(c)* Waveprobe WP6

*(d)* Waveprobe WP7

*(e)* Cross Correlation between HOS vs Experiment for probes WP5, WP6 and WP7

Figure 3.3 – Comparison of time series of the wave profile at near the paddle (WP1) and near the focusing point (WP5,WP6,WP7) along with cross correlation comparison with experiment

propagate the wave accurately. Instead, incident wave propagation in the *foamStarSWENSE* solver is much easier as wave models explicitly give incident waves (Section 2.2.3.1). This incident focusing wave modelling is intentionally designed to test the stability and accuracy of the solvers. Since both solvers are relying on HOS for wave generation, the HOS wave is validated first (previous section, Section 3.2.1), followed by a discussion of other parameters that are required for both the solvers in this section. Other domain parameters are shown in Table 3.4 and the typical computational domain are shown in Figure 3.4. The figure shows that in the coupling section, the focusing wave is generated in HOS-NWT and is coupled with CFD NWT using *Grid2Grid* (Section 2.2.3.1).Similar setup of WP5 to WP7 as studied in HOS validation is maintained in both the solvers here (Figure 3.4). The CFD computed focusing wave, and other parameters were compared and validated using these wave gauge measurements. Each inlet, outlet relaxation zone, and free surface (FS) refinement zone will be addressed in their respective sections.

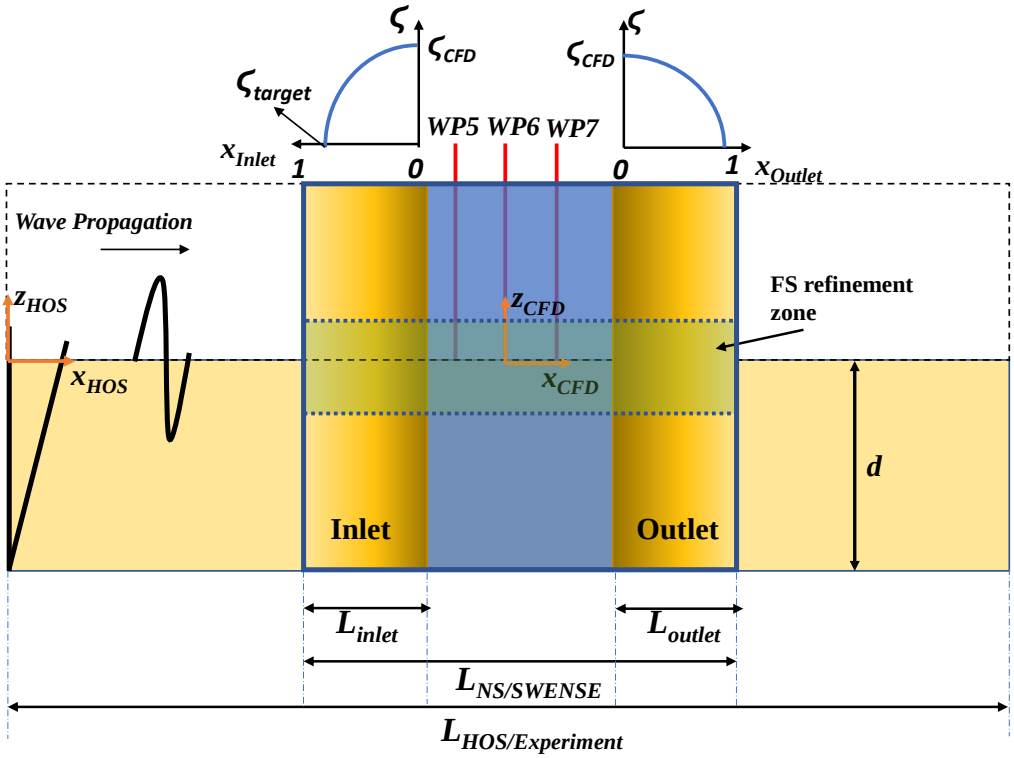


Figure 3.4 – 2D NWT computational domain for parametric studies with representation of HOS and CFD (NS and SWENSE), $d$ represents the water depth

### 3.2.3 Non breaking focusing wave modeling

In order to assure accurate wave propagation in the CFD domain (*foamStar* and *foamStar-SWENSE*) and to obtain excellent interaction with the structure later, the NBR focusing wave will be examined for various CFD parameters in this section. The parameters investigated in the present section are as follows:

— Influence of mesh size and time step on wave propagation

— Influence of different HOS initiation time

— Influence of relaxation zonal length

— Influence of cell ratio between free surface zones and outer zones (Figure 3.4)

Recalling the wave characteristics, the wave considered for validation is a unidirectional focusing wave group consisting of 32 wave components and the frequencies of the wave components range from $f_l = 0.34$ Hz to $f_u = 1.02$ Hz. In the present work, based on transient zero-crossing wave period (T) measured for this focusing wave study (as 2.08 s) and maximum amplitude height ($\eta_{max}$) as 0.21 m, the transient wavelength is evaluated using linear dispersion relation. This transient wave length and maximum height values will be in the following parametric studies.

#### 3.2.3.1 Influence of mesh size and time step

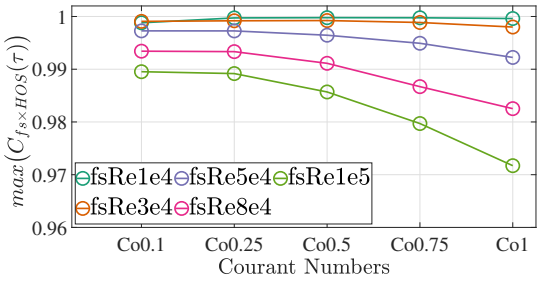


*(a)* For different Re and Co : *foamStar*

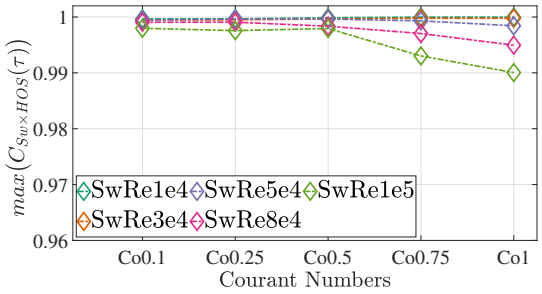


*(b)* For different Re and Co : *foamStarSWENSE*

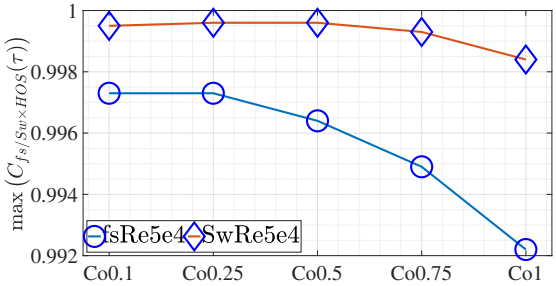


*(c)* For same Re at different Co : *foamStar* and *foamStarSWENSE*

Figure 3.5 – Comparison of focusing wave generated in *foamStar* and *foamStarSWENSE* with HOS wave for different cell based Reynolds numbers and Courant numbers (Re and Co)

The computational meshes and time steps were examined to understand their influence on the focusing wave generation. Mesh parameters are identified in terms of lateral spacing $\Delta x$, vertical spacing in the free surface zone $\Delta z$ and time step $\Delta t$. With the analytic wave fluid velocities, representative cell-based Courant numbers (Co) and cell-based Reynolds numbers ($Re_\Delta$) (Choi, 2019) can be defined as

$$Co = \sqrt{Co_x^2 + Co_z^2}, \quad Re_\Delta = \sqrt{Re_{\Delta x}^2 + Re_{\Delta z}^2}$$

where

$$Co_x = \frac{u_{wave}\Delta t}{\Delta x}, Co_z = \frac{w_{wave}\Delta t}{\Delta z}, Re_{\Delta x} = \frac{u_{wave}\Delta x}{\nu}, Re_{\Delta z} = \frac{w_{wave}\Delta z}{\nu}$$

$u_{wave}$ and $w_{wave}$ are the maximum horizontal and vertical velocity, in this case at the focusing point it is 1.4 m.s$^{-1}$ and 0.5 m.s$^{-1}$ respectively which is taken from HOS-NWT output. The test matrix for this study is given in Table 3.5. The aspect ratio of one was maintained for all the cases and varied the cell size from Re 1.13 $10^4$ to 1.13 $10^5$. For each $Re$, different $Co$ are tested for both the *foamStar* and *foamStarSWENSE* solver. The solver's wave probe at the focusing location is compared to the reference signal which is the HOS-NWT, at the same location using cross correlation (Eqn. (2.57)), and the outcome is shown in Figure 3.5a and Figure 3.5b for *foamStar* and *foamStarSWENSE* respectively. The comparison in Section 3.2.1 shows that there are slight differences between HOS and experiment results that led to the decision to use HOS-NWT as a reference set of results. Another reason is that the HOS wave is what the solvers

| **TestCase Name** | **Cell Reynolds number ($Re$)** | **Cell Courant number ($Co$)** | **Number of cells per transient ($\lambda$)** |
|---|---|---|---|
| fsRe1e5,SwRe1e5 | 1.13 $10^5$ | 1 0.75 0.5 0.25 0.1 | 30 |
| fsRe8e4,SwRe8e4 | 8.52 $10^4$ | 1 0.75 0.5 0.25 0.1 | 40 |
| fsRe5e4, SwRe5e4 | 5.68 $10^4$ | 1 0.75 0.5 0.25 0.1 | 60 |
| fsRe3e4, SwRe3e4 | 2.84 $10^4$ | 1 0.75 0.5 0.25 0.1 | 120 |
| fsRe1e4, SwRe1e4 | 1.13 $10^4$ | 1 0.75 0.5 0.25 0.1 | 300 |

Table 3.5 – Mesh and time discretization based on cell based $Re$ and $Co$ for the convergence tests. fs stands for *foamStar* and Sw stands for *foamStarSWENSE*

*foamStar*/*foamStarSWENSE* are taking as an incident wave, and hence it will be appropriate to use that as a reference wave other than experiment results for this parametric study. Thus, HOS-NWT is chosen as a reference result for cross correlation comparison for this study and other parametric investigations in this section. The first figure illustrates the *foamStar* cross correlation with HOS, and in almost all the cases, the efficiency of *foamStar* increases when refining the mesh and downsizing the $Co$. The highest accuracy is observed for mesh fsRe3e4 and fsRe1e4 in the order of $0.99 - 0.995$. The second figure highlights the *foamStarSWENSE* correlation with HOS for different Re and Co. A coarser mesh in the *foamStarSWENSE* (SwRe8e4, SwRe1e5) even has a good accuracy ($0.995 - 0.998$), matching with the finest mesh coefficient results in the *foamStar*. This is also proven in Figure 3.5c, that temporal variation for the same mesh configuration between *foamStar* and *foamStarSWENSE* shows that the SWENSE solver achieved similar good accuracy for all the temporal variation. In contrast, *foamStar* solver proves to be less accurate even with the highest refined timestep of Co 0.1. For a finer mesh, *foamStarSWENSE* converges towards the same value, even for a small timestep. These cases prove the essential advantage of the SWENSE method, i.e., allowing the use of coarse mesh to simulate incident waves: *foamStarSWENSE* solver can use a grid $2-4$ times coarser than that of *foamStar* (in each dimension) to achieve the same accuracy for the application of incident waves. The less accurate results seen for fsRe1e5 at a Co of 1 appear to have a 40% amplitude loss at the focusing point, but it appears to fit neatly with the wave in the total duration time (total simulation time 5 s), therefore takes the value of 0.97. Given the facts, mesh Re5e4 to Re1e4 for cell-based Co less than 0.25 achieves an accuracy better than 0.99 in both solvers and will be studied further in the WSI investigation in the presence of structure (Section 3.3.1).

#### 3.2.3.2 Influence of HOS initiation time

The duration of the wave recorded in the reference experiment is 85 s, with the focusing time at 39 s (see Figure 3.2b). However, because the WSI's residual effects beyond the focusing time are of limited interest in this investigation, the HOS duration was set to 50 s. Simulating this long duration in CFD would be computationally very costly as the time step requirement is also very fine to capture the focusing wave. It should be noted that focused waves are localized in time, and energetic frequency components are only in the zone of interest after a specific time. Since the CFD domain is small, it is interesting to optimize the initiation time only for the

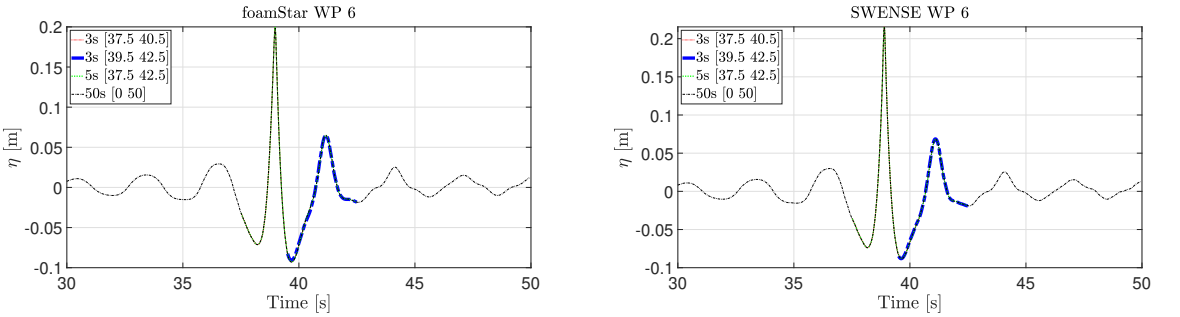


*(a)* Different initiation time : *foamStar* *(b)* Different initiation time : *foamStarSWENSE*

Figure 3.6 – Comparison between focusing wave generated in the *foamStar* and *foamStarSWENSE* domain for different HOS initiation time

focusing time. Because of the coupling advantage, the simulation can be adjusted to start at a random time in the HOS time scale rather than at 0 because that will be the first timestep in the CFD to initialise the domain. To understand its influence, four test cases were considered

— Case 1 - 3 s simulation starting at 37.5 s to 40.54 s

— Case 2 - 3 s simulation starting at 39.5 s to 42.5 s

— Case 3 - 5 s simulation starting at 37.5 s to 42.5 s

— Case 4 - 50 s simulation starting at 0 s

The wave probe at the focusing location WP6 is compared for these four test cases, and the results are illustrated in Figure 3.6a for the *foamStar* solver and in Figure 3.6b for the *foamStarSWENSE* solver. To understand the time influence at the scale of numerical duration itself, the vertical and horizontal axes are preserved as dimensionalized ones. Similarly, vertical scale non-dimensioning is also difficult in each case since peaks also vary for different cases. The results show that the simulation duration has no significant effect, whether it be 50 s, 5 s, or 3 s. But since it is a localised wave, it is important to generate the wave before the focusing point; hence we cannot start the simulation too late (Case 2). Also, no phase difference was observed in any case tested in the two solvers. Based on the findings, a 5 s simulation with a start time of 37.5 s was chosen for the 3D interaction study, saving a significant amount of computational time. Despite the fact that initiating the wave in between will cause some initial instability in the presence of structure, this must be carefully eliminated from the simulation to prevent the error from propagating inside the solution.

#### 3.2.3.3 Influence of relaxation zone

The inlet relaxation zone blends the velocity and VoF field into the CFD domain from the HOS domain and also absorbs the reflected/scattered waves coming from the body. As described earlier, the philosophy of generating waves is different in *foamStarSWENSE*; subsequently, only the *foamStar* solver was studied for this parameter. Choi et al. (2018c) suggested the length of the inlet ($L_{Inlet}$) zone should be 1-1.5 times the wavelength in the case of regular/irregular waves. This yields $30-40\%$ of the cells in the relaxation zone, which increases the computational

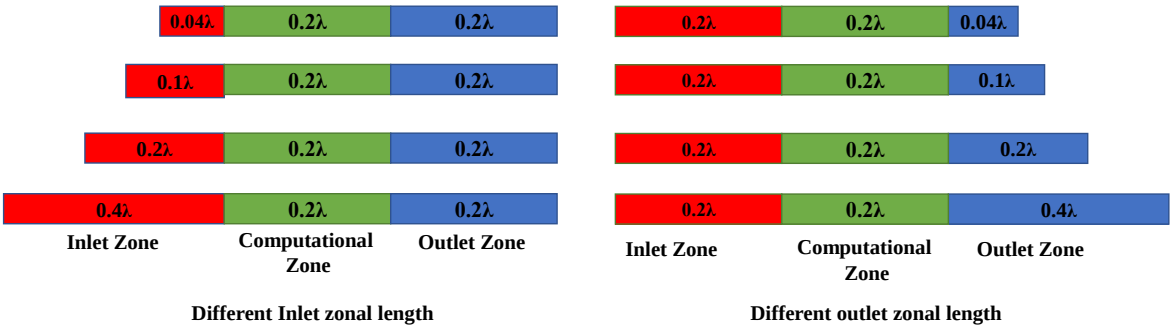


Figure 3.7 – Computational domain for inlet and outlet relaxation zones for different lengths based on $\lambda$ (Transient wave length calculated based on transient wave period T)

cost. If $L_{Inlet}$ can be reduced, it lessens the number of cells and reduces the computational cost. For the interaction between a focusing wave and a given structure, a localized wave group of relatively short time duration will pass through. It is expected that the reflections from the structure will not affect the focusing wave. Hence, the only objective of the inlet zone is to blend the focusing wave properly. A study on different $L_{Inlet}$ keeping the length of the CFD domain and outlet zone constant was carried out (see Figure 3.7). The $L_{Inlet}$ was measured in terms of transient wave length ($\lambda$) calculated based on the transient wave period $T$, varying from $0.04\lambda$ to $0.4\lambda$. The wave probe WP6 comparison for these different cases is shown in Figure 3.8a. As in the work of Hildebrandt and Sriram (2014), throughout the study, the time was normalized by the transient zero up crossing wave period ($T$) measured at the focusing point, while the wave elevations were normalized by the maximum wave amplitude recorded ($\eta_{max}$) at WP6. It can be observed that there is only a marginal influence of less than 0.5% variation in amplitude when the inlet length is $0.04\lambda$, and no other discrepancy was observed.

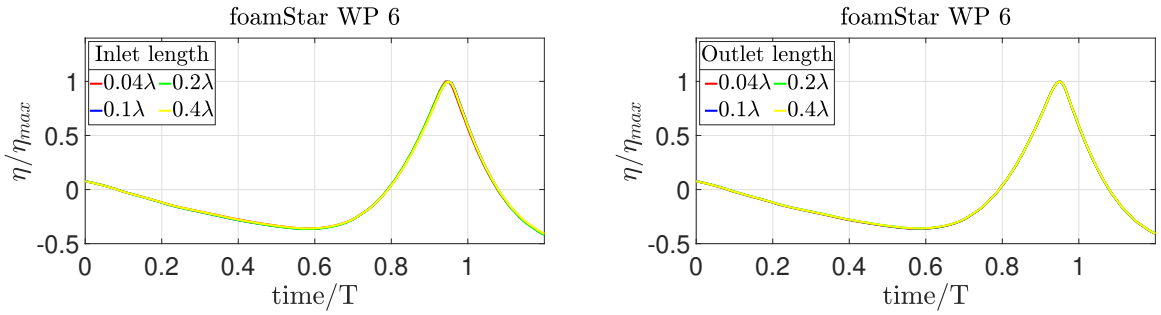


*(a)* For different Inlet zones

*(b)* For different Outlet Zones

Figure 3.8 – Comparison between focusing wave generated in the *foamStar* for different relaxation zone length

The purpose of the outlet relaxation zone is to absorb the incident or scatter waves from the body. Similar to the previous study, $L_{Inlet}$ and length of the CFD domain were retained while $L_{Outlet}$ was changed from $0.04\lambda$ to $0.4\lambda$ (Figure 3.7). The results shown in Figure 3.8b prove

that there is no significant deviation in amplitude and phase and also that there is no reflection. When comparing computation costs, $0.2\lambda$ costs five times less than $0.4\lambda$, and interestingly, $0.04\lambda$ takes ten times less time to compute than $0.4\lambda$ for the same accuracy. Hence, short $L_{Inlet}$ and $L_{Outlet}$ of $0.04\lambda$ will be used for the subsequent interaction studies, reducing the computational time further.

#### 3.2.3.4 Influence of cells outside the FS zone

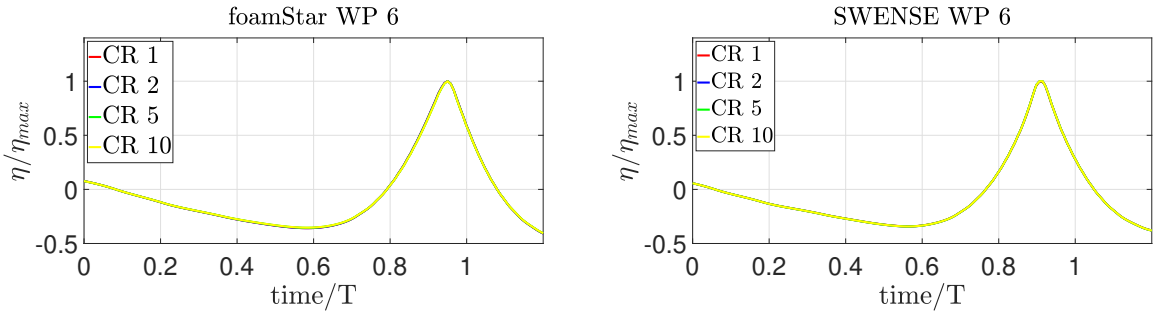


*(a)* Different CR across domain - *foamStar* *(b)* Different CR across domain - *SWENSE*

Figure 3.9 – Comparison between focusing wave generated in the *foamStar* and *foamStar-SWENSE* for different cell size ratio between the zones

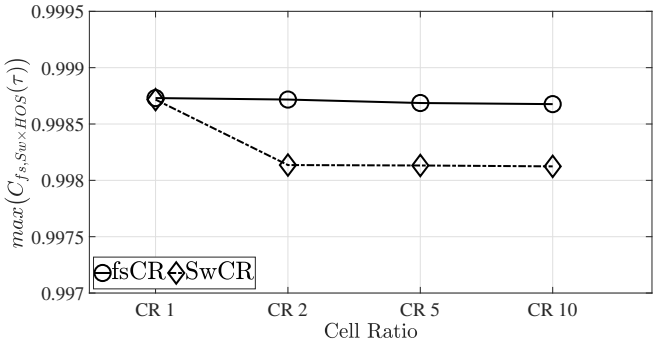


Figure 3.10 – Cross Correlation between numerical wave based different CR setup and HOS for *foamStar* and *foamStarSWENSE* solvers

By altering the cell size at outer zones distant from the free surface zone, the final parametric study aims to investigate the influence of cell size above and below the free surface on wave generation (Figure 3.4). For this the Cell size ratio (CR) was set as,

$$CR = \frac{\Delta x_{Out}}{\Delta x_{FS}}$$

where FS represents the free surface zone and Out represents the outer zone. Since the aspect ratio in this study is maintained as 1, cell size in the two directions are the same. For the requirement of a 3D interaction study at a later stage, four test cases with CR ratios of 1,2,5, and 10 were examined. Based on the size of cells in the free surface zone, the width of outer cells

was modified as per CR. Like the earlier studies, the wave probe WP6 at the focusing location was chosen to investigate the wave variation for both solvers. Figure 3.9a and Figure 3.9b show that there is almost no influence on cell variation above and below the free surface. The results are also correlated with HOS and the outcome is depicted in Figure 3.10. The solution is more accurate at CR1 than in other situations, but the variation is too small to be a concern. As a result, it is important to highlight that the CR variation is kept between 2 to 10, depending on the mesh type used for the future interaction study (Section 3.3.1). In any case, it has been proved that this will have no effect or influence over the wave propagation in the present case.

### 3.2.4 Breaking focusing wave modeling

When the focusing wave train approaches the breaking point, the fluid particle velocity exceeds the wave crest velocity, leading to wave breaking. The computed free surface profile during wave propagation at different time instants near the focusing time is presented in Figure 3.11, along with wave probe locations WP5 to WP7. As the waves propagate from where fluid particle velocity exceeds wave crest velocity, the prominent wave crest becomes almost vertical, which denotes the onset of wave breaking, as seen in first row in Figure 3.11 . The wave breaking is embarked by the small water jet at the wave crest, and the profile of the wave crest becomes highly deformed and asymmetric, with an over-turning motion induced by the wave crest (Figure 3) passing the WP6. The overturning wave crest breaks with an air pocket covering (third and fourth row of Figure 3.11), referred to as the splash-up phenomenon just before WP7, and generates another small jet of water in the downstream direction (last row of Figure 3.11) on WP7. The results for the wave breaking profile are consistent with Kamath et al. (2016); Aggarwal et al. (2020). Also, a typical wave profile with velocity variation at the breaking time instant is shown in Figure 3.12. The investigation makes it evident that only on WP5 can consistent results be obtained until a non-breaking focusing wave can be seen, whereas, in other probes, a two or three free surface may be visible after focusing time, raising doubts about the correctness of the wave probe results. So, in this section, parametric studies are conducted using probe WP5.

HOS initiation time and cells outside the FS zone produce results similar to those of the NBR-focused wave case in regard to all previous parametric analyses. As a result, these parametric studies are not replicated. This section discusses only studies of spatial and temporal requirements and relaxation zones. They are provided despite behaving similarly to the prior section as their analysis is based on WP5 rather than WP6, as in the previous section. It should be noted that only the *foamStar* solver is investigated in this section because *foamStarSWENSE* is not yet able to analyse the breaking wave interaction.

#### 3.2.4.1 Influence of mesh size and time step

This parametric study is similar to study carried out in Section 3.2.3.1, but here to reproduce the BR focusing wave in the CFD zone. Additionally, a more thorough spatial description is investigated in order to correctly comprehend the parameters for breaking wave propagation in

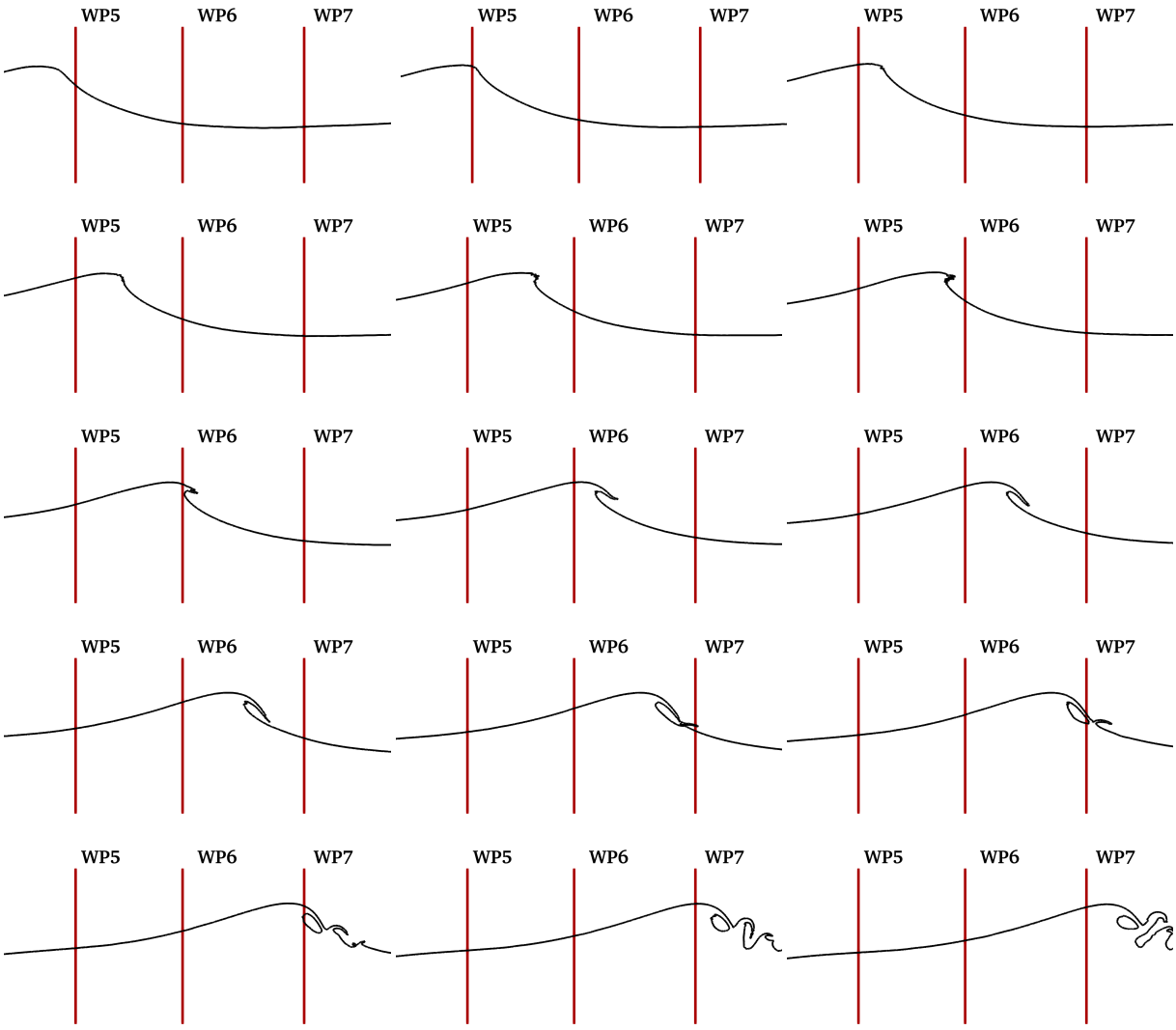


Figure 3.11 – Computed wave profile during the focused breaking wave propagation at different time instants around the breaking point

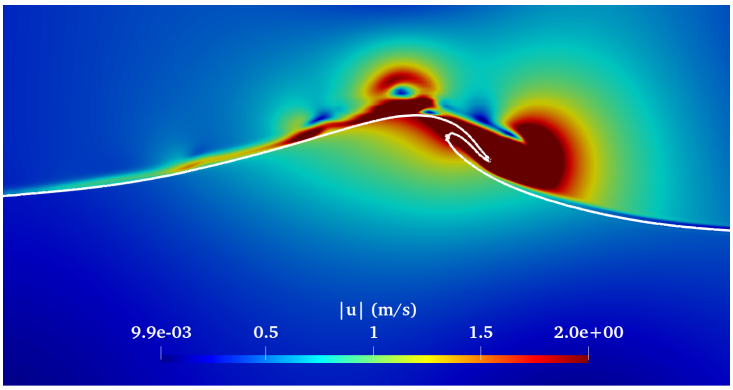


Figure 3.12 – Typical 2D focused breaking wave generated in the *foamStar* with velocity representation

| **TestCase Name** | **Cell Reynolds number ($Re$)** | **Cell Courant number ($Co$)** | **Number of cells per transient ($\lambda$)** |
|---|---|---|---|
| fsRe2e6 | 2.96 $10^6$ | 1 0.75 0.5 0.25 0.1 | 32 |
| fsRe1e6 | 1.48 $10^6$ | 1 0.75 0.5 0.25 0.1 | 64 |
| fsRe7e5 | 7.41 $10^5$ | 1 0.75 0.5 0.25 0.1 | 128 |
| fsRe3e5 | 3.7 $10^5$ | 1 0.75 0.5 0.25 0.1 | 256 |
| fsRe1e5 | 1.85 $10^5$ | 1 0.75 0.5 0.25 0.1 | 338 |
| fsRe9e4 | 9.26 $10^4$ | 1 0.75 0.5 0.25 0.1 | 1350 |

Table 3.6 – Mesh and time discretization based on cell based $Re$ and $Co$ for the focused breaking wave convergence tests. fs stands for *foamStar*

CFD. The simulations use a two-dimensional rectangular computational domain, and the waves travel from inlet to outlet. As a general rule, NS solvers need fine meshes to propagate the waves accurately. Thirty combinations of mesh size and the time step are tried (see Table 3.6) in terms of lateral spacing $\Delta x$, vertical spacing in the free surface zone $\Delta z$ and time step $\Delta t$. The aspect ratio of cells in the free surface zone is maintained at 1. The number of cells per wavelength ($\Delta x/\lambda_C$) is varied from 32 to 1350 (six Re numbers), and for each case, five different Co are being tested. Representative cell-based Courant number can be defined by using analytic wave velocities as mentioned in the Section 3.2.3.1.

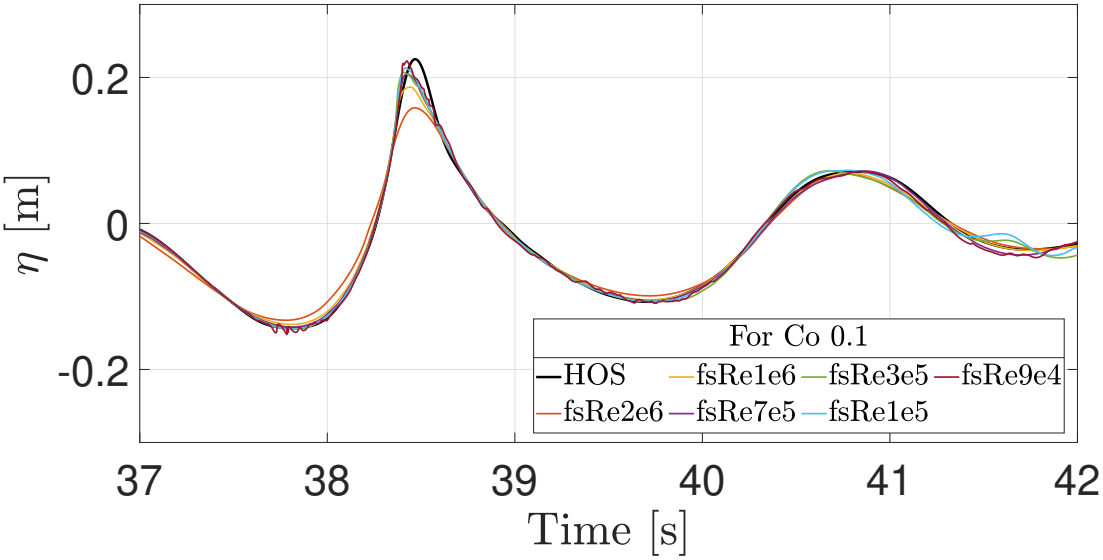


Figure 3.13 – Typical comparison of time series of the wave profile at (WP5) for test cases fsRe2e6 to fsRe9e4 with Co 0.1

Figure 3.13 plots the time series of surface elevation for the typical combinations of test cases from fsRe2e6 to fsRe9e4 mesh types for Co 0.1. HOS wave probe results are used as a reference results for validating *foamStar* solutions for the reasons quoted in Section 3.2.1.3. Figure 3.14a represents the maximum of the cross correlation coefficient as a function of Co for different mesh sizes (fsRe2e6 to fsRe9e4). Figure 3.14b illustrates the zoomed window to observe the minor

changes in the previous figure. The figure shows that accuracy increases by refining the mesh and downsizing the Courant number for almost all the cases. The coarse mesh types (fsRe2e6 and fsRe9e4) showed good convergence when moving from Co 1 to Co 0.1, from 0.58 to 0.88 and 0.74 to 0.95, respectively. Attaining one (a perfect case) looks computationally expensive, seeing from the case of fsM6. Even the most refined mesh and finest time step (fsRe9e4 at Co 0.1) would reach an accuracy of only 0.995. Hence fsRe3e5 at Co0.1 proves to be economical in terms of spatial and temporal resolution with an accuracy of more than 0.99 and hence chosen for the 3D breaking wave-structure interaction study (Section 3.3.2).

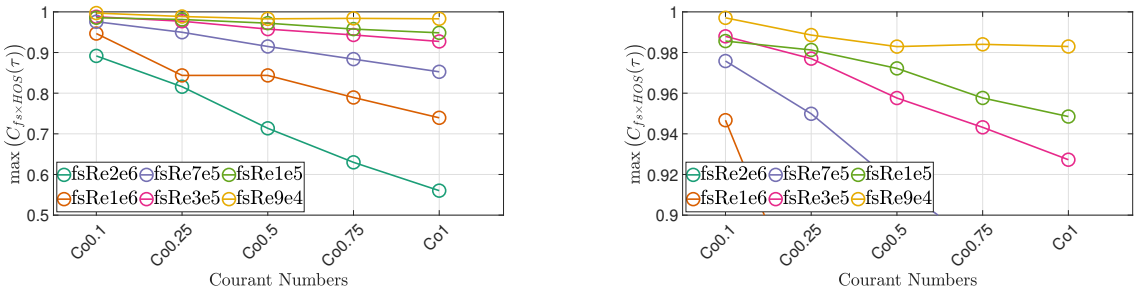


*(a)* Cross Correlation Coefficient for WP5

*(b)* Zoomed window of Figure 3.14a

Figure 3.14 – Comparison of Cross correlation coefficient for the wave generated in the *foamStar* with HOS wave for different mesh types and Courant number

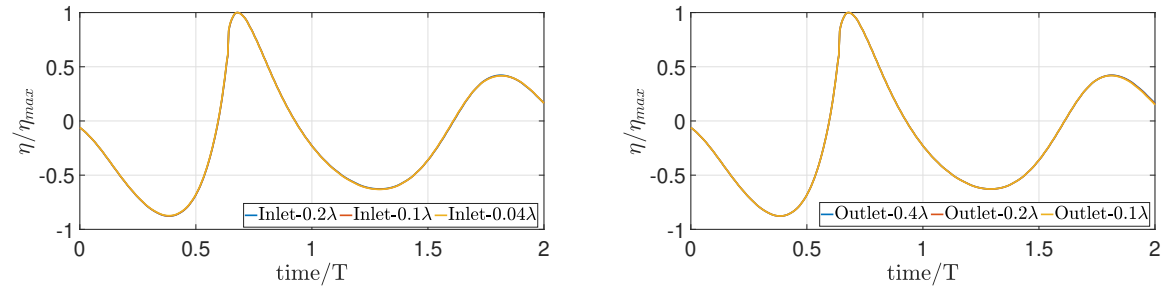


*(a)* Different Inlet zonal length




*(b)* Different Outlet zonal length

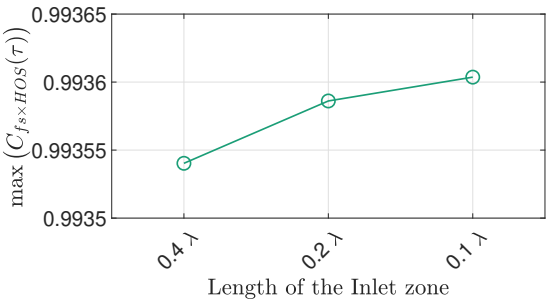


*(c)* Different Inlet zonal length

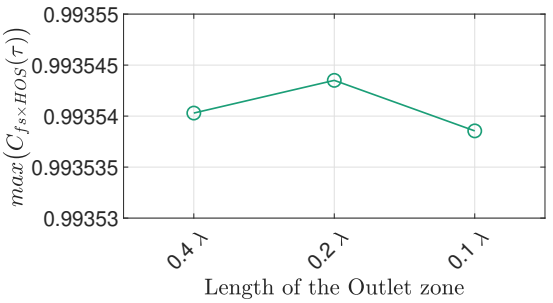


*(d)* Different Outlet zonal length

Figure 3.15 – Comparison between focusing wave generated in the *foamStar* for different relaxation zone length

#### 3.2.4.2 Influence of relaxation zone

This part can be seen as a continuation of Section 3.2.3.3 and is tested for similar variables, except, in this case, the wave is a BR focusing wave. A study on different $L_{Inlet}$ keeping the length of the CFD domain and outlet zone constant is carried out on the medium refined mesh. The $L_{Inlet}$ is measured in terms of transient wave length ($\lambda$), varying from $0.1\lambda, 0.2\lambda, 0.4\lambda$. Typical representation of these zone with the domain can be seen in Figure 3.7. The surface elevation comparison at wave probe WP5 for these different cases is shown in Figure 3.15a. It is readily apparent qualitatively that there is no apparent visual difference between the test cases as shown in the Figure 3.15a. The same coefficient and range of fourth or fifth decimal variation in the cross-correlation results (Figure 3.15c) demonstrate that this insignificant difference between test results and HOS data for WP5 is negligible to be a concern.

Similar to the previous study, promptly retaining $L_{Inlet}$ and length of the CFD domain and changing $L_{Outlet}$ from $0.1\lambda$ to $0.4\lambda$ has been carried out. The results as shown in Figure 3.15b and 3.15d proves that there is no significant deviation in amplitude and phase and also that there is no reflection observed. Hence, shorter $L_{Inlet}$ and $L_{Outlet}$ of $0.1\lambda$ will be used for 3D breaking wave-structure interaction study (Section 3.3.2).

## 3.3 Focusing wave interaction with fixed cylinder

The previously validated unidirectional focusing waves (NBR and BR) are now studied during their interaction with a fixed cylinder. Pressure across the cylinder and induced force are also compared with experimental findings for both solvers, in addition to comparing the wave elevation. The NBR focusing wave interaction with the cylinder is covered in the first part of the section, and the BR focusing wave interaction with the cylinder is covered in the second part.

### 3.3.1 Non breaking focusing wave interaction with cylinder

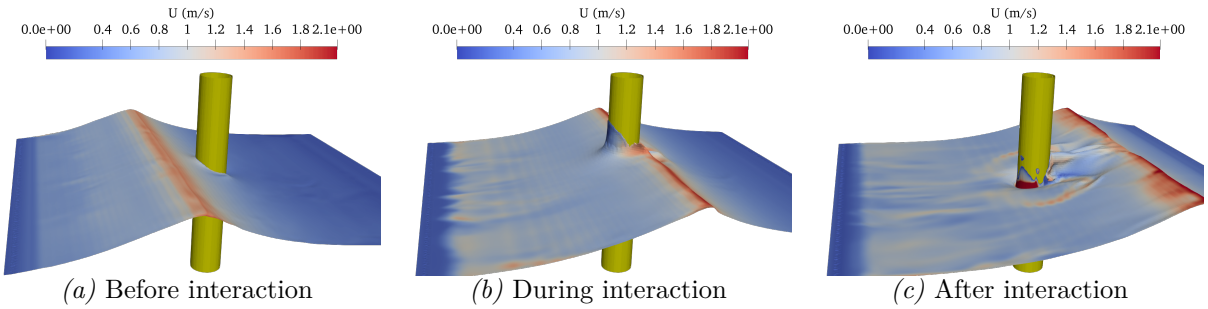


*(a)* Before interaction *(b)* During interaction *(c)* After interaction

Figure 3.16 – Typical interaction of focusing wave on the fixed cylinder and its velocity description over the flow field

Focused wave-structure interaction as a three-dimensional simulation is performed with a vertical circular cylinder in a NWT. The interaction modifies the kinematics and the flow field around the cylinder as shown in Figure 3.16. The figure shows the free surface with velocity

magnitude when the focused wave interacts with the cylinder for different time instants for a typical case. First, the focused wave crest interacts with the cylinder causing a rise of water level in front of the cylinder. Thus velocity around the cylinder increases in the vicinity of the cylinder. Second, the focused wave impacts the cylinder, resulting in increased water levels on both sides of the cylinder.Small water jets aligned with the backside of the cylinder in the wave direction are formed on the downstream side by the collision of separated wavefronts that were formed behind the cylinder.

#### 3.3.1.1 Numerical set up

The CFD domain is placed inside the HOS domain (same domain length as in section 3.1), where viscous effects play a significant role near the structures. The diameter of the cylinder (D) is 0.22 m. The length of the CFD domain was set at 2.75 m (12D -including $0.04\lambda$ for the inlet zone and $0.04\lambda$ for the outlet zone, see section 3.1). The width and water depth of the CFD domain are the same as those of the experimental domain, with the only difference being the air zone above FS of 0.7 m. Note that here, CFD represents both the NS and SWENSE domain. The overall computational domain is shown in Figure 3.1.

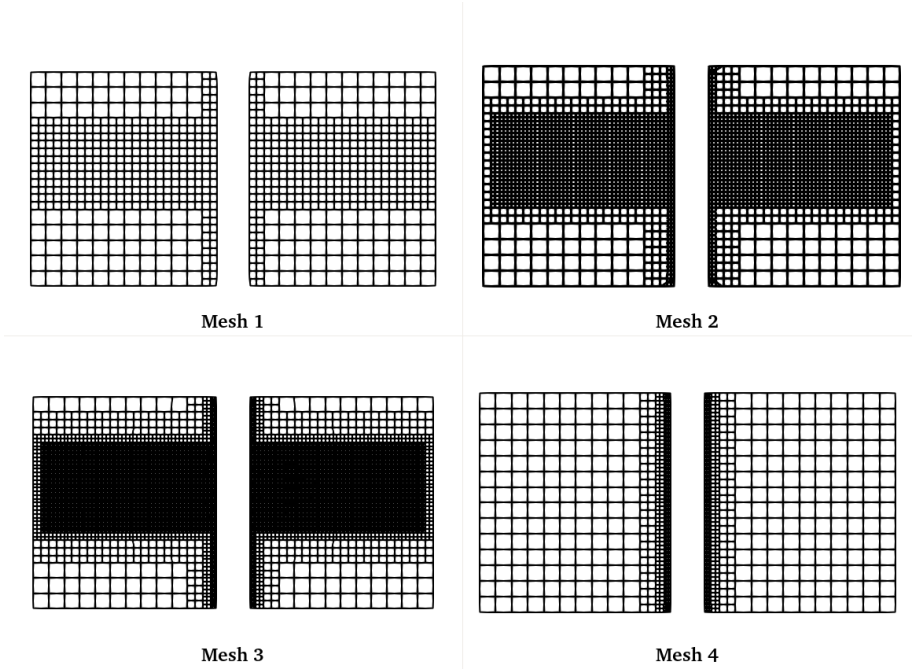


Figure 3.17 – Mesh configuration of three levels Coarse, medium and fine mesh with refinement ratio of 2 for each case and Mesh 4 without free surface refinement to investigate the performance of SWENSE

Finally, to perform a convergence study, three different mesh configurations with different discretization levels were generated using the OpenFOAM utility SnappyHexMesh. The grids were generated as an unstructured mesh but control was established over the mesh growth with a refinement ratio ($r$ - refer Section 2.1.6.2) of 2 . The refinement ratio is nothing more than a comparison of the average spacing between grids 1 and 2. The free surface zone was similar to the

Table 3.7 – Test Matrix and its nomenclature for fixed cylinder interaction with NBR focusing wave

| **Mesh** | **TimeStep (s)** | **Co** | **TestCase (Nomenclature)** |
|---|---|---|---|
| Mesh 1 (M1) | 0.0001,0.001, 0.01 | 0.003,0.03,0.3 | *foamStar*- fsCo0.3M1.. *foamStarSWENSE* -SwCo0.3M1.. |
| Mesh 2 (M2) | 0.0001,0.001, 0.01 | 0.007, 0.07, 0.7 | *foamStar*- fsCo0.7M2.. *foamStarSWENSE* -SwCo0.7M2.. |
| Mesh 3 (M3) | 0.0001,0.001, 0.01 | 0.01. 0.1, 1 | *foamStar*- fsCo0.1M3.. *foamStarSWENSE* -SwCo0.1M3 |
| Mesh 4 (M4) | 0.001, 0.01 | 0.1,1 | *foamStar*- fsCo0.1M4.. *foamStarSWENSE* -SwCo0.1M4 |

results from the parametric studies with three configurations chosen (Re5e4, Re3e4 and Re1e4). The presence of cylinder alters these configurations sightly, while maintaining them at the same level of refinement. These configurations will be represented by Mesh 1 (M1), Mesh 2 (M2) and Mesh 3 (M3) hereafter. An illustration of all these configurations is given in Figure 3.17. In summary, Mesh 1 (coarse mesh) has 31,248 elements, Mesh 2 (medium mesh) has 226,072 elements, and Mesh 3 (fine mesh) has 1,751,736 elements. An additional mesh Mesh 4 (based on Re1e5) was made similar to Mesh 3 but without any free surface refinement to investigate the advantage of the SWENSE methodology. The grid size parameter $h$ (refer Section 2.1.6.2) for each mesh case is 40 mm, 20 mm, and 10 mm, and their corresponding grid refinement ratio is 2. The CR ratio is maintained at 2,5,10 for each mesh type respectively (From section 3.2.3.4). In this problem, the discretization for parallel simulations is maintained at 1 CPU for every 30000 cells for exact comparison in computational cost between the solvers in last section (Section 3.3.1.3). All the simulations are run with the same residual tolerances and schemes and simulations were carried out using the cluster (supercomputer LIGER, at Centrale Nantes, France). In particular, most of the in-house codes are OpenMP or MPI paralleled. Considering the variation in the number of CPUs (Np) for different test cases, in an attempt to compare the solvers and mesh types, a CPU effort defined as (Agarwal et al., 2021a) $\frac{T_{CPU}\dot{N}p}{T_{SIM}}$ was used. $T_{CPU}$ is the overall execution time for the simulation and $T_{SIM}$ represents the duration of the simulation. The $Np$ for mesh types M1,M2,M3 and M4 are $1, 8, 58, 1$ respectively. In this way, the computational cost is comparable between the test cases and solvers in order to understand the solver efficiency.

Unlike the previous parametric studies (See 3.2.3.1) that used cell-based Co, three unique time steps of 0.01 s, 0.001 s, and 0.0001 s were investigated for each mesh to investigate the influence of temporal variation in each solver based on physical Co. This time, however, the timesteps chosen are based on the outcome of cell-based Co with values below 0.25. As mentioned, 'Co' in this study is the physical Courant number assessed based on the maximum velocity of the wave and minimum cell size in the mesh. More details about the test matrix are presented in Table 3.7. The *foamStar* and *foamStarSWENSE* solvers were tested for each combination of mesh type and Courant number, and the results are reviewed in the following sections.

#### 3.3.1.2 Results and discussion

This section is split into three parts. The first part compares different mesh combinations with the finest mesh and its verification in order to propose a temporal problem convergence technique. The second part compares experimental results with different mesh type combinations. The final subsection compares the computational efficiency of the two solvers.

**3.3.1.2.1 Validation with finest mesh combination - fsCo0.01M3** In order to investigate the changes in the free surface, pressure and force during the interaction, the numerical results for different cases are examined. This subsection is divided into two parts. The first part focuses on *foamStar*, and the following part is for *foamStarSWENSE* solver. In each part, along with wave elevation, pressure and force and its correlation along with grid convergence are also discussed. Assuming that the finest mesh M3 with the smallest Co (fsCo0.01M3) tends to be the most accurate, it is considered a reference case for the cross-correlation study with other mesh types, and the accuracy of the assumption is validated in the following subsection.

**3.3.1.2.1.1 foamStar** The numerical representation of NBR focusing wave impacts over the fixed cylinder is presented in the Figure 3.18. The figures are snapped from the simulation at different time instants around the focusing time (38.6 s to 39.2 s), when the crest of the incident wave passes the cylinder. The free surface represents the position of the free surface, which is reconstructed by 0.5 contour of VoF field ($\alpha = 0.5$). In all the figures the wave travels from the left to the right. the wave reaches its maximum amplitude at the focusing location, shown as the run up over the cylinder at 3.18d and its trough at 3.18f.

The numerically captured free surface elevation probe readings are shown in Figure 3.20. Note that only three wave gauges WP5, WP6 and WP7, fall within the computational domain and hence are presented . The wavefront before the focusing point, at the focusing point and after the focusing point is measured by the WP5, WP6 and WP7 probes respectively (See Figure 3.19). For reference purposes, the HOS wave generated in HOS-NWT and experimental results are also shown. Note that HOS evaluation is without the structure, but the experiment and CFD results here are with the structure. Most of the mesh types replicate the focused wave profile precisely, while slight numerical damping is observed only in M1 and M4. The reason is that coarser free surface meshes are unable to capture the smaller wavelengths in the wave and leading to slight phase shift across the mesh types. The scattered wave from the cylinder along with incident wave recorded in WP7 shows certain inefficiency of some test cases to capture the leeward wave accurately. It appears that only the finer mesh M3 with the finest time step captures all flow field characteristics with high accuracy. This is proven in the cross correlation relation presented between the finest mesh configuration fsCo0.01M3 and other mesh types in Figure 3.20d. When the cross correlation of each wave probe reading is taken, it appears that the differences between the wave probes readings are almost identical. Consequently, the mean of all the coefficients was selected for the sake of concision. It should be noted that the *foamStarSWENSE* evaluation in the following section follows a similar procedure. The plot's X-axis is the computational cost, and it can be seen that the finer mesh has a higher computational

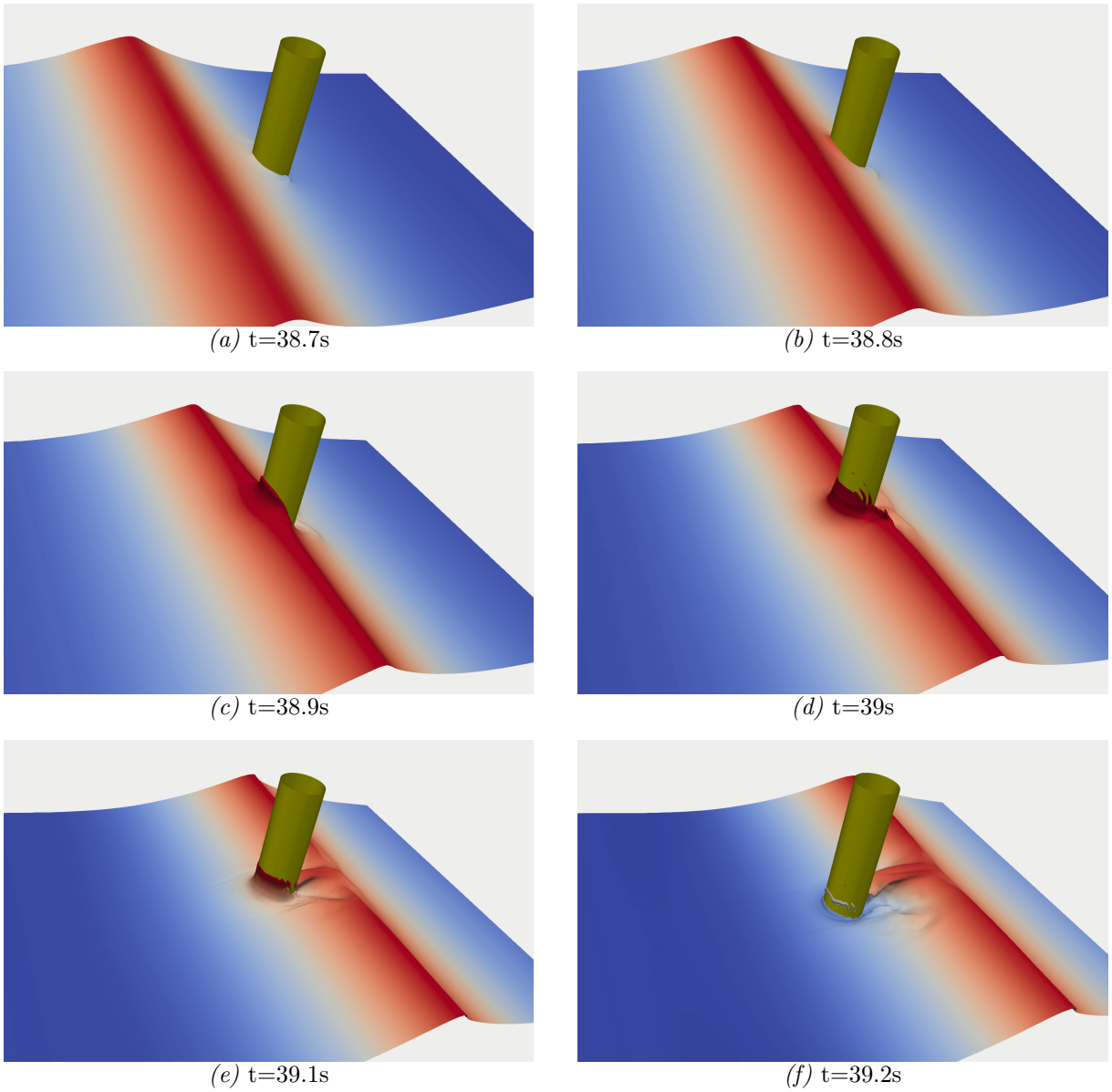

*(a)* t=38.7s *(b)* t=38.8s *(c)* t=38.9s *(d)* t=39s *(e)* t=39.1s *(f)* t=39.2s

Figure 3.18 – Free surface near the fixed cylinder in NBR focusing waves

cost than the coarser ones. The cross correlation number may appear considerably closer to one because the simulation length taken into account for the comparison is not the peak point but rather the whole duration of simulation. The meshes M1, M2 and M3 with coarser time steps have a similar accuracy of approximately 0.991 but reducing the Co improves their respective accuracies. The increase in accuracy from M1 to M2 is higher than from M2 to M3, showing that the solution is nearly converged. The mesh type M4 corresponds poorly to the focused wave because fewer cells are in the free surface refinement region. The one-way DD coupling is proven to be able to create a good approximation even with the coarsest mesh (fsCo0.1M4) approaching the accuracy of fsCo0.3M1, fsCo0.7M2, and fsCo1M3 by little temporal refining, as shown by the mesh's ability to reach 0.99 with a medium time step. Even yet, the findings from the mesh types listed are hardly accurate. As already mentioned, the only purpose of this

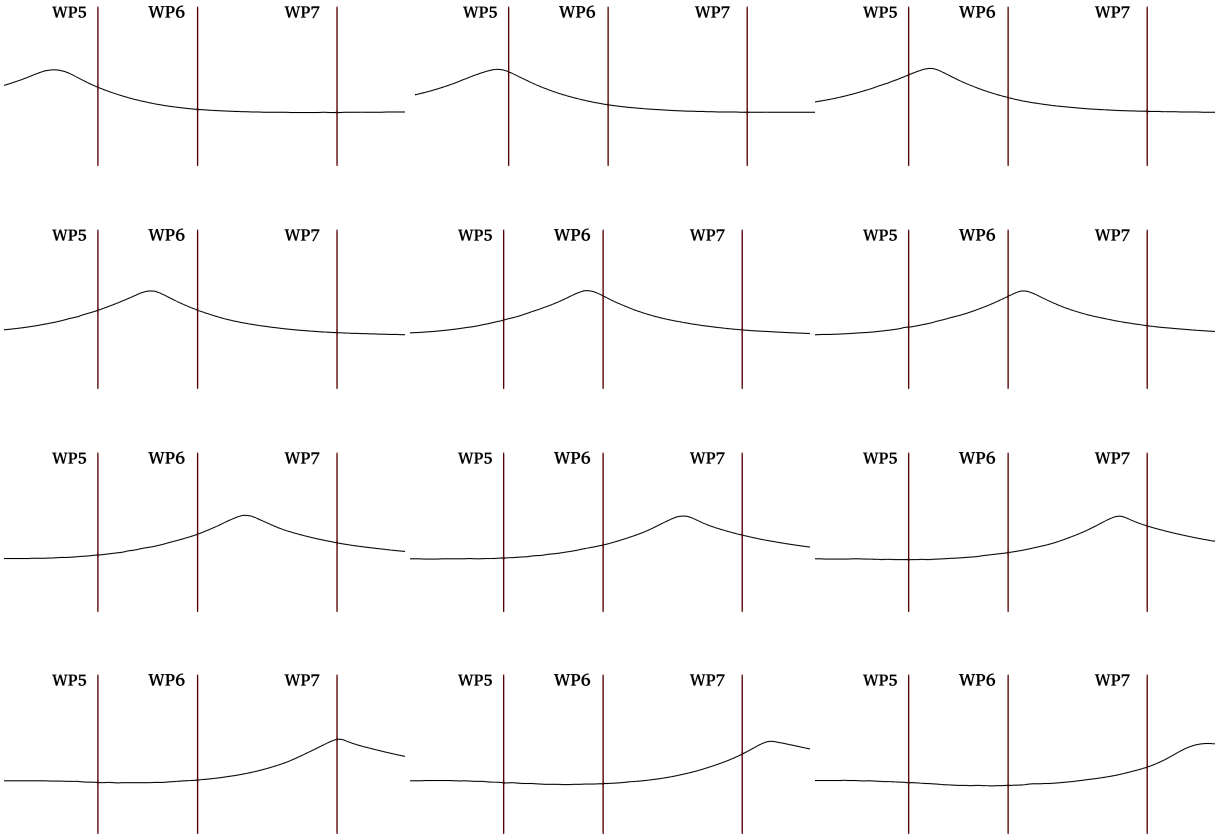


Figure 3.19 – Computed wave profile during the NBR focused wave propagation at different time instants around the focusing point along the wave probe axis line ($R_0$ frame, yy axis)

mesh(M4) is to enable comparison with the performance of the *foamStarSWENSE* solver which will be discussed in later sections.

The ability of the different meshes to reproduce the focused wave pressure on the cylinder is evaluated here by comparing the time variation of the dynamic pressure recorded on the submerged as well as exposed surfaces of the cylinder (Figure 3.21). The time is normalized by the transient wave period (T), and the dynamic pressures are normalized by $\rho c^2$, where $\rho$ is the water density and c is the maximum fluid velocity at the focusing point (i.e. 1.4 m.s$^{-1}$ obtained from HOS). The simulated time histories of the submerged pressure probes (PP2-PP3) in stagnation point are expected to follow the wave elevation. Accordingly, all the test cases exhibit similar trends but with similar discrepancies to those observed in the wave elevation study. A pressure drop is observed for the probes around the cylinder (PP6, PP7 and PP8) due to flow acceleration and wake effects. Although the free surface refinement is poor in some cases (M1 and M4), but with very fine refinement around the cylinder, the majority of the test cases correctly reproduce the pressure loading, as shown in Figure 3.21. There is a small difference in the simulated pressure peaks in PP4 and PP5 (air probes), which depends mainly on the accurate wave run-up over the cylinder during the focusing event. Hence the probe PP5 was chosen to study the cross correlation estimation in comparison with the fsCo0.01M3 for

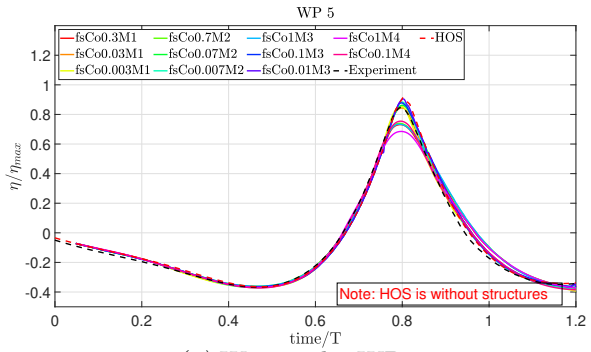


*(a)* Waveprobe WP5

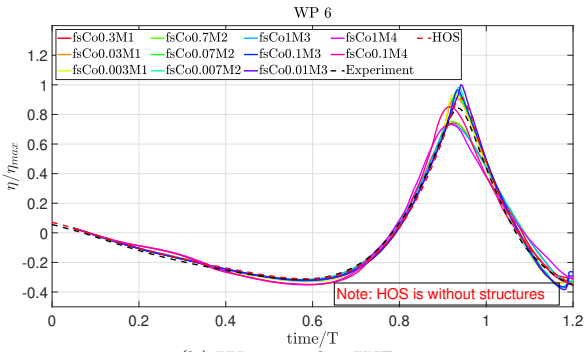


*(b)* Waveprobe WP6

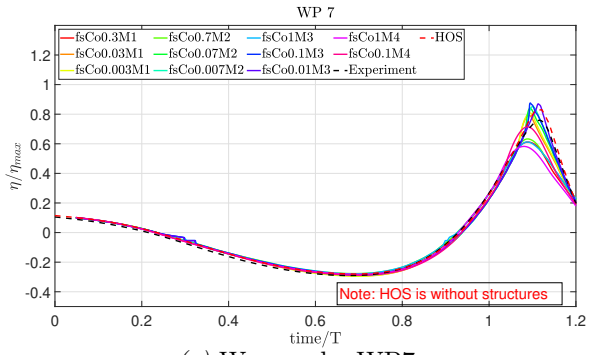


*(c)* Waveprobe WP7

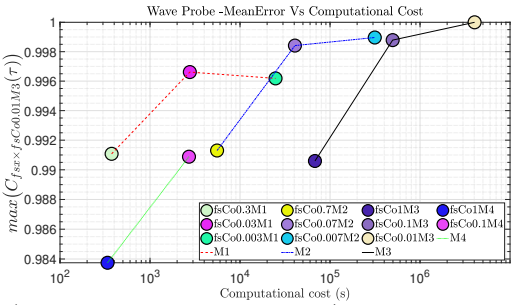


*(d)* Wave Probe mean error (with respect to the wave probes WP5 - WP7) cross correlation in relation with fsCo0.01M3

Figure 3.20 – Wave probe comparison between different Mesh types M1,M2,M3 and M4 with the *foamStar* solver

the convergence behavior. From the figure, it can be observed that decreasing the Co number increases accuracy for all the mesh types. However, refining from a medium to a fine grid has only a negligible impact on the pressure estimation. Overall, the results are more accurate when the mesh is refined from M1 (0.99) to M3 (0.999), and it is abundantly evident that the pressure parameter is approaching towards convergence as the mesh is refined.

The force on the cylinder was also investigated. Figure 3.22 depicts the time history of the force recorded for each mesh type during the focused wave interaction. In the experiment, the cylinder experienced the "ringing" phenomenon after impact, which cannot be simulated numerically as the body is assumed to be rigid. So the time trace is compared only up to impact and the details after the interaction are ignored. The simulated forces are normalized for the convenience of comparison with the factor $\rho g r^3$, where r represents the radius of the cylinder. Similar to the wave and pressure results, the test case with less refinement in the free surface exhibits a discrepancy (the force is over predicted) but further refinement in both space and time results in a convergent behaviour. The numerical convergence is demonstrated in the cross correlation (Figure3.22b) as accuracy is improved for each refinement from 0.997 to 0.999. The mesh type M4 is the least accurate among the mesh types, as shown in the time series. The associated maximum correlation is 0.992. This demonstrates a crucial point: the coarsest mesh with the coarsest time step (with $10^3$ s, computational time) can predict the force acting on the cylinder with a deviation of less than 10%(based on peak magnitude comparison). This

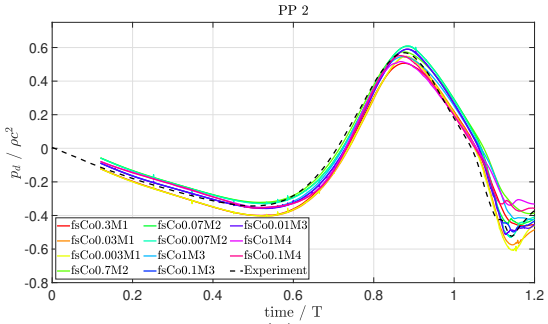


*(a)* PP2

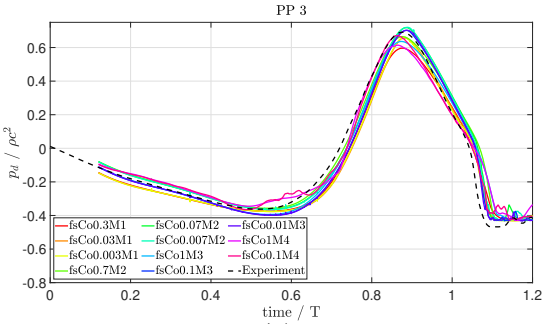


*(b)* PP3

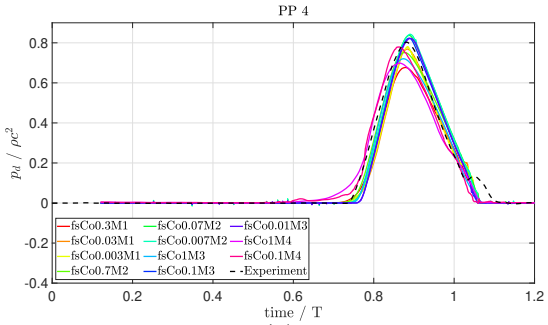


*(c)* PP4

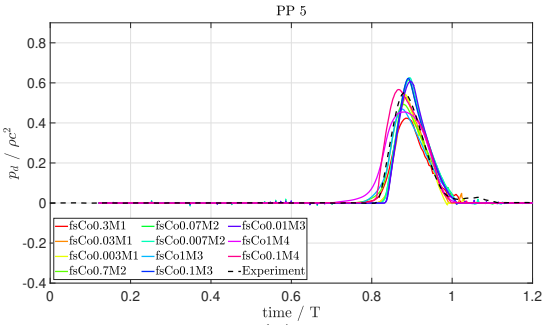


*(d)* PP5

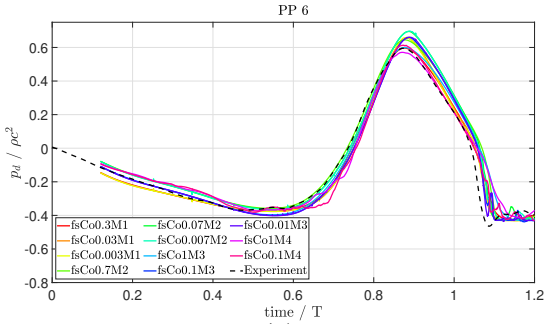


*(e)* PP6

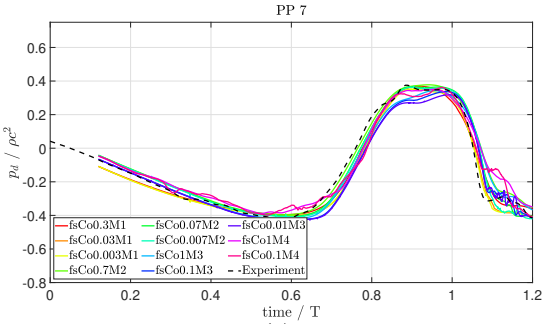


*(f)* PP7

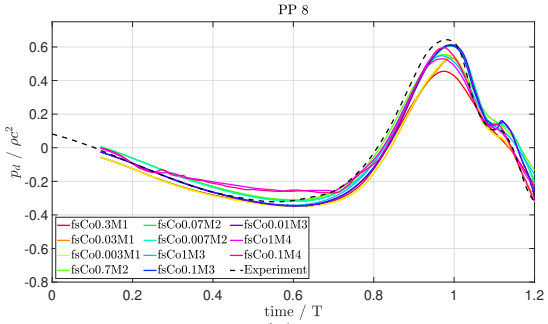


*(g)* PP8

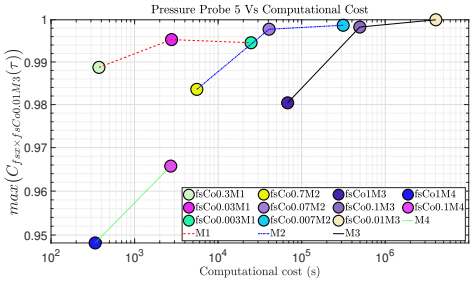


*(h)* Correlation coefficient for pressure probe PP5 with fsCo0.01M3

Figure 3.21 – Pressure time history of the fixed cylinder in NBRfocusing waves for different mesh types simulated by the *foamStar* solver

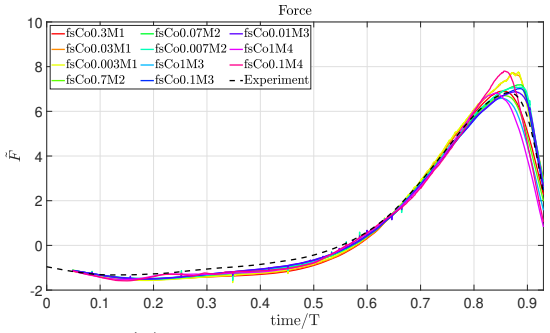


*(a) foamStar* Force comparison

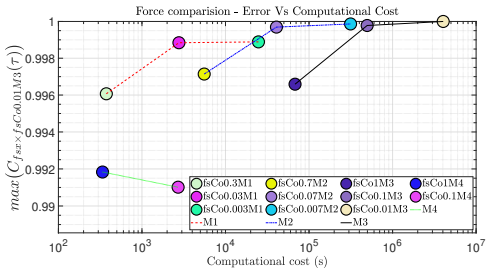


*(b) foamStar*- Force cross correlation

Figure 3.22 – Force recorded for a fixed cylinder in NBR focusing waves by the *foamStar* solver (left) and its correlation coefficient with fsCo0.01M3 (right)

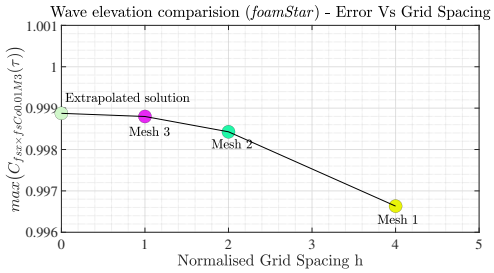


*(a) foamStar*- Wave probe Grid Convergence study

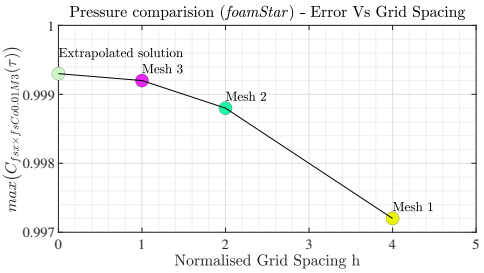


*(b) foamStar*- Pressure Grid Convergence study

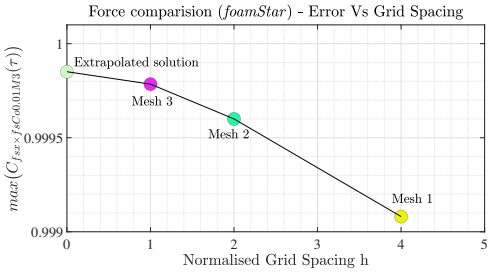


*(c) foamStar*- Force Grid Convergence study

Figure 3.23 – Extrapolation of coefficient with the Richardson method and its corresponding convergence for *foamStar*

highlights the benefit of DD coupling in overcoming the high computational cost required, if the simulation is solely a CFD problem (for other solvers computational cost on the similar problem refer (Sriram et al., 2021c)).

The Richardson extrapolation technique was used to verify the grid convergence and verify that the M3 mesh type as a converged configuration. The convergence was estimated based on the cross correlation coefficient values obtained for each mesh type (Mesh 1 (M1), Mesh 2 (M2) and Mesh 3 (M3)) under the time step of 0.001s (fixing a time step). The convergence study was carried out for all the parameters (surface elevation, pressure and force) and the outcome is presented in Figures 3.23a, 3.23b and 3.23c. The extrapolated coefficient shows that the coefficients values tend to zero $h \to 0$, which would correspond to infinite mesh resolution. The extrapolated coefficient from Mesh 2 and Mesh 3 reaches a value of 0.999 for the wave elevation.The slope between each coefficient is calculated from the cross correlation coefficients

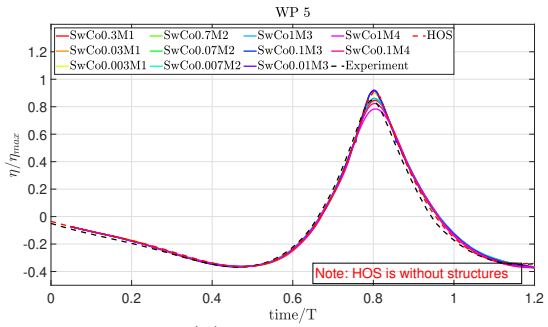


*(a)* Waveprobe WP5

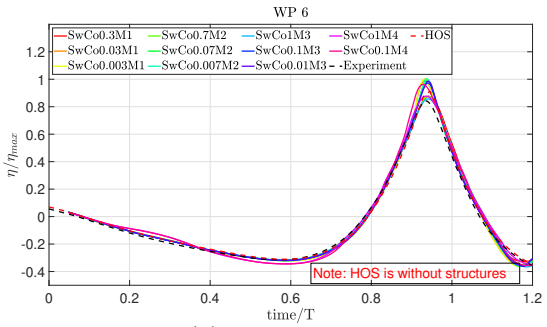


*(b)* Waveprobe WP6

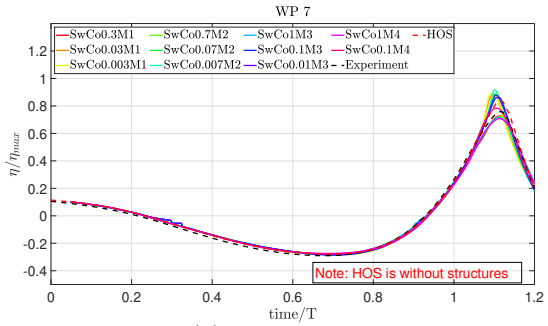


*(c)* Waveprobe WP7

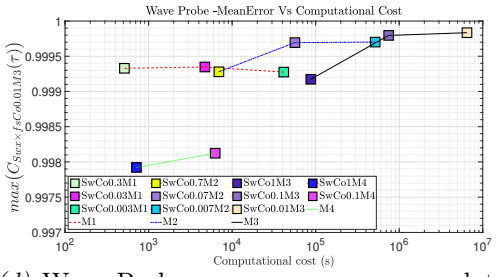


*(d)* Wave Probe mean error cross correlation with respect to fsCo0.01M3

Figure 3.24 – Wave probe comparison between different Mesh types M1,M2,M3 and M4 in the *foamStarSWENSE* solver

and extrapolation coefficient to see if the curves flatten to demonstrate the convergence of the solution while refining. The slope of convergence from Mesh 1 to Mesh 2 looks to be 0.17%, and from Mesh 2 to Mesh 3 it appears to be 0.03% ($L1$ norm). Similarly, between Mesh 3 and the extrapolated coefficient, the slope is 0.01%. This demonstrates that the solution has already reached convergence. A similar trend is observed for the pressure, and the only exception is that accuracy is slightly better.

Lastly, the extrapolated coefficient for force is estimated at 0.9999. The solution for the force appears to have already converged, since the grid convergence from Mesh 1 to 2, Mesh 2 to 3 and Mesh 3 to extrapolated coefficient (Figure 3.23) is found to be 0.04%, 0.02% and 0.01% respectively. This observation highlights two interesting findings. One is that even the coarsest mesh has a decent estimation of force and the second is that all the results have already converged and have a smaller slope than other parameters. The results confirm that an accurate enough solution had been already found with the finest mesh, justifying the decision to keep fsCo0.01M3 as a base result for cross correlation. Overall, the study's observations of wave propagation, pressure, and force in the cylinder performed reasonably well, and this temporal problem also exhibited decent convergence behaviour. The computational effectiveness of this DD coupling is evaluated in Section 3.3.1.3.

**3.3.1.2.1.2 foamStarSWENSE** This section aims to demonstrate the two-phase *foamStarSWENSE* solver's ability for focussing wave interaction with the cylinder. Both the mesh geometry and the wave conditions are analogous to those followed in the *foamStar* simulation.

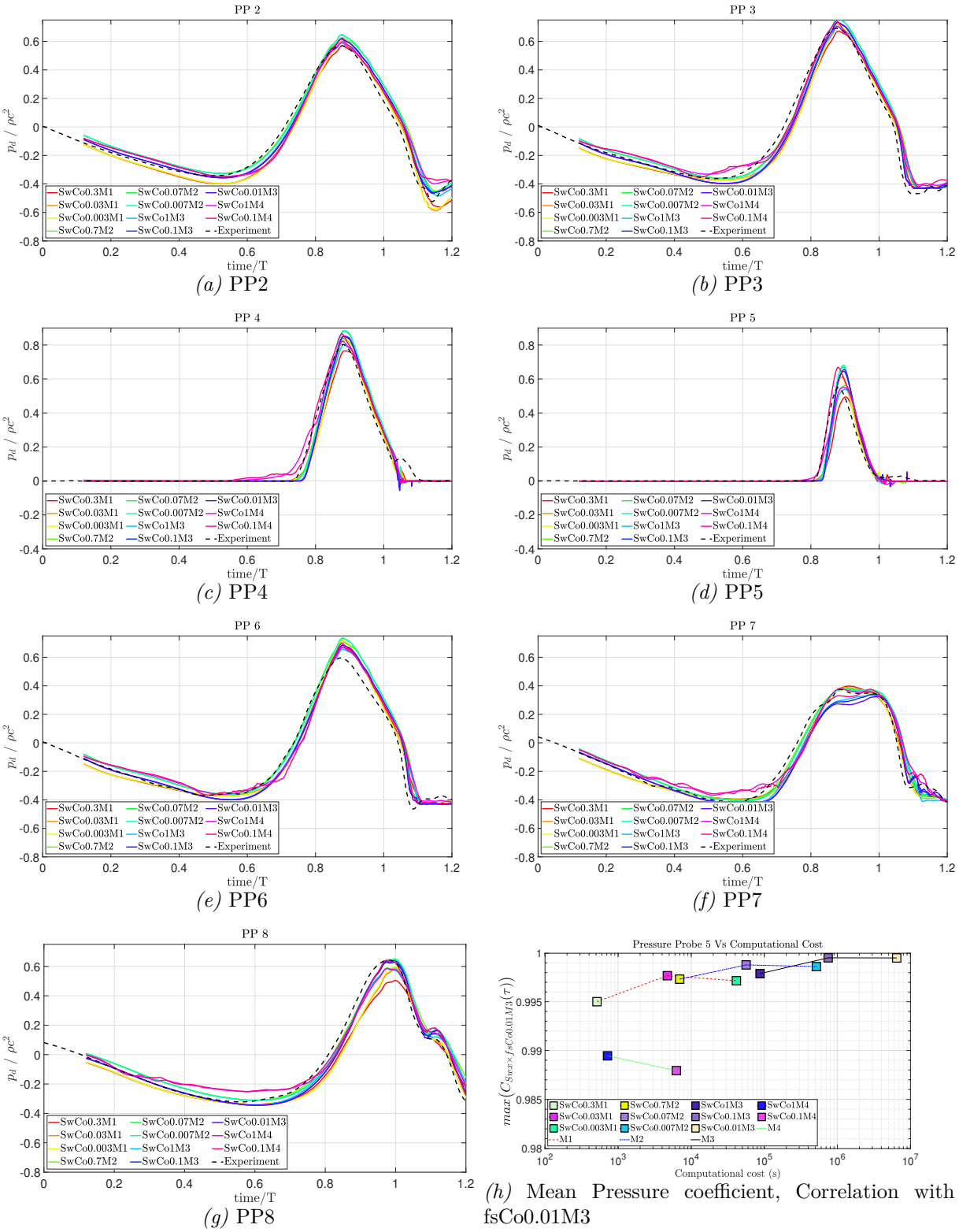


*(a)* PP2 *(b)* PP3 *(c)* PP4 *(d)* PP5 *(e)* PP6 *(f)* PP7 *(g)* PP8 *(h)* Mean Pressure coefficient, Correlation with fsCo0.01M3

Figure 3.25 – Pressure time history of fixed cylinder in NBR focusing waves recorded by *foamStarSWENSE* for different mesh types

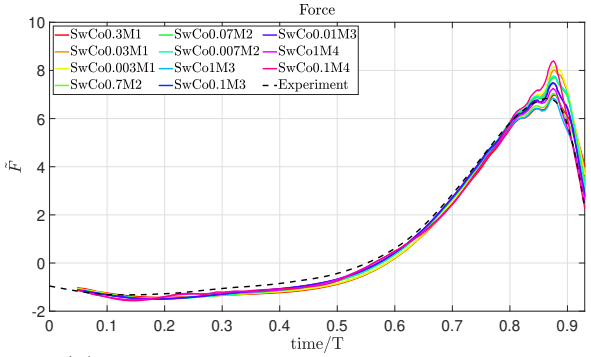


*(a) foamStarSWENSE* Force comparison

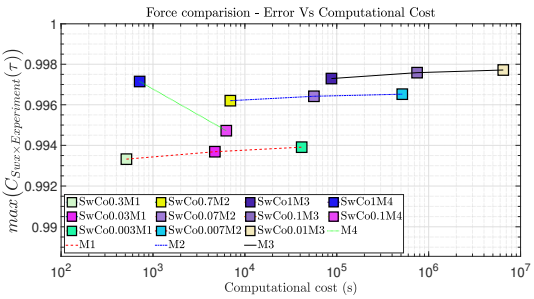


*(b) foamStarSWENSE-* Force cross correlation

Figure 3.26 – Force comparison for fixed cylinder in NBR focusing waves between different mesh types under *foamStarSWENSE*

Similarly, surface elevation, pressure, and force are compared among different mesh types to validate the results. The mesh types' results were cross-correlated with the reference foamstar results obtained with the finest mesh and time step, namely fsCo0.01M3. This guarantees a comprehensive comparison between the two solvers. A grid convergence study was also carried out in *foamStarSWENSE* to confirm the convergence of the mesh types. The non-dimensional surface elevation, pressure and force are also identical to those used with *foamStar* solver.

Figure 3.24a to Figure 3.24c outline the surface elevation for the wave probes WP5 to WP7, respectively. The mesh types M1 and M4 are numerically damped a little even before interacting with the cylinder. This difference is observed everywhere, both during and even after interaction with the cylinder, as shown by WP6 and WP7. To recap, one of the main advantages of *foamStarSWENSE* is the explicit treatment of incident waves; hence, even a coarse mesh in the far-field can produce the incident wave information accurately. This is visible in the cross correlation study since compared with the finest mesh in *foamStar*, even the coarsest mesh types M1 and M4 accuracy range is 0.9995 and 0.9985 respectively. This holds good even with the coarser time step (it was 0.984 in *foamStar*). This confirms that with SWENSE, the size of the computational domain and number of cells can be drastically reduced for such problems, reducing the computational cost. A more in-depth comparison of the solvers will be presented in Section 3.3.1.3, together with some recommendations.

Figure 3.25 represents the dynamic pressure variation on submerged and surface probes for different mesh types in *foamStarSWENSE*. The submerged pressure probes show good agreement among different mesh types other than specific discrepancies coming from waves. Other than PP8, the probes around the cylinder in the wake region show good agreement with each other. The difference arises in PP8, where the formation of water jet occurs as the coarser mesh types under predict the pressure. A similar disagreement arises in the air probes PP4 and PP5, where the coarser mesh analysis of the pressure were also under predicting the pressure slightly near the focusing point in time. The cross correlation coefficient of the pressure probe PP5 is plotted against computational cost as shown in Figure 3.25h. It can be perceived that refining the mesh and time improves accuracy and progress towards convergence. The coarser mesh types have an accuracy range of 0.995. The only exception is mesh M4, which had an accuracy of only 0.985

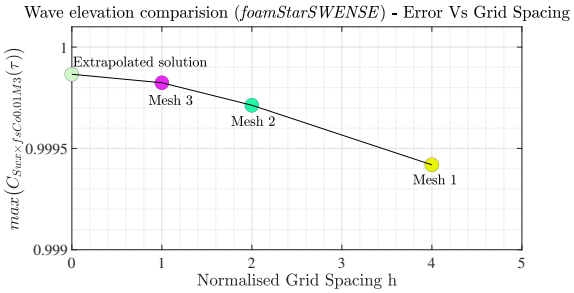


*(a) foamStarSWENSE-* Wave elevation Grid Convergence study

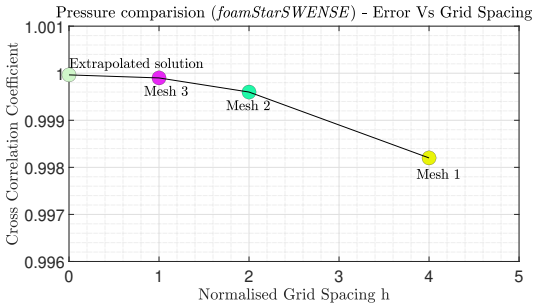


*(b) foamStarSWENSE-* Pressure Grid Convergence study

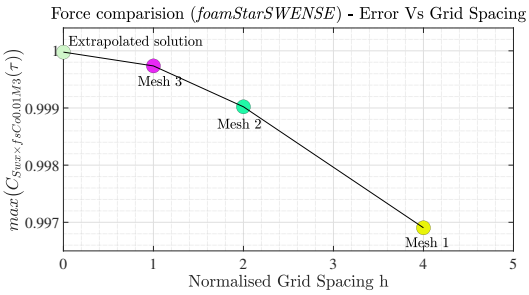


*(c) foamStarSWENSE-* Force Grid Convergence study

Figure 3.27 – Extrapolation of Coefficient with the Richardson method and its corresponding GCI for *foamStarSWENSE*

in *foamStar*, against 0.99 in *foamStarSWENSE*.

Another relation for force measured among all mesh types is given in Figure 3.26a. The simulated results agree well among different test cases, and as mentioned earlier, there are some discrepancies for coarser mesh types. Each time series is compared with the force obtained from fsCo0.01M3, and the resulting correlation coefficient is shown in Figure 3.26b. The *foamStarSWENSE* solver seems to predict the force closely enough even for the coarser mesh types (M1 and M4). The accuracy of the results is in the range of 0.994 -0.998, and the results clearly show that reducing the timestep has very little impact on the accuracy, whereas refining the mesh leads to a good improvement in the results. The Mesh M4 results show a decrease in accuracy when the timestep is refined because of its slight over prediction of force at the focusing event.

Finally, to verify the convergence for this study, the corresponding Richardson extrapolation technique was used. Figure 3.27 illustrates the grid convergence and the extrapolated solution for wave elevation, pressure and force for the *foamStarSWENSE* cases. In all cases, the extrapolated solution derived using Mesh 2 and Mesh 3 parameters is almost 1. Due to the SWENSE method, the slope between the coefficients seems to be converging in the case of wave elevation with Mesh 1-2, Mesh 2-3 looks to have 0.03% and 0.01%, respectively, and it approaches the extrapolated solution with the slope of 0.05% proving the statement. Pressure and force behaviour are shown to have a similar pattern. Mesh 1-2 and Mesh2-3 have slopes of 0.14% and 0.013% for pressure and 0.135% and 0.04% for force, respectively. Despite the fact that the slope

in the force parameter is rather high, it is converged with the slope between Mesh 3 and the extrapolated coefficient of 0.015%. The Mesh M4 results show a decrease in accuracy when the timestep is refined because of its slight over prediction of force at the focusing event.

Mesh 1's refinement around the cylinder is coarser, hence its accuracy coefficient with *foamStarSWENSE* is often much lower than with *foamStar* (in *foamStar* 0.999 and *foamStarSWENSE* 0.9968). However, refining a cylinder for Mesh 2 indicates a significant improvement whereas refinement to Mesh 2 in *foamStar* showed only a minor improvement, indicating that it is already close to the converged solution. With Mesh 3, the convergence of *foamStarSWENSE* has been nearly achieved while *foamStar* has a already achieved convergence. Only with higher refinement near the cylinder can *foamStarSWENSE* make a reliable force prediction. However, even with the coarser refinement near the cylinder, *foamStar*'s force estimation is fairly accurate. This is illustrated in the next section with a comparison based on computational efficiency.

**3.3.1.2.2 Validation with experiments** In this subsection, both the *foamStar* and *foamStarSWENSE* methods are validated by comparing the test cases with the experiment conducted by Sriram et al. (2021a). The cylinder with all the pressure sensors and wave gauges is the same as in Figure 3.1. In the previous results and discussion, the experimental time series for surface elevation, pressure and force obtained on the cylinder were already shown for reference. The numerical simulation results agree favourably with the experiment but with some differences. It should also be remembered that above [Section 3.3.1.2.1], the coefficient for all the mesh types was given in correlation with the finest mesh (fsCo0.01M3) in the *foamStar*. Now all the simulated results are correlated with the experimental time series. Figure 3.28 compares the correlation for wave elevation, pressure and force with *foamStar* and *foamStarSWENSE*. None of the results converge towards one showing the model uncertainty in comparison with the experiment. Wave and pressure converge towards 0.995 and 0.99, respectively and force towards 0.998. The uncertainty between the experiment and numerical simulation can be attributed to factors such as experimental errors (Sriram et al., 2021a), HOS generated focusing wave, CFD assumptions (discretization, time scheme, schemes) and so on. Furthermore, the behaviour of *foamStar* and *foamStarSWENSE* is similar to the observations made earlier. The accuracy of *foamStar* increases on refining the mesh and time, but *foamStarSWENSE* shows no drastic improvement in wave and pressure accuracy when refining the mesh. An improvement is observed in the force due to an increase in refinement around the cylinder. Another advantage of the *foamStarSWENSE* solver is that on the coarsest grid (M4), the solution accuracy in wave and force prediction is significantly better than that of *foamStar* solver on the same mesh. Out of the two solvers, the *foamStarSWENSE* model is better in all mesh configurations for accurate wave propagation inside the computational domain, as it was proven that refining did not improve the results (Figure 3.28b), which were already converged. As a result, any configuration from M1 to M4 can be chosen with the minimal computational cost for the wave propagation problem. However, by refining the free surface region in *foamStar*, the waves improved a lot (Figure 3.28a), eventually reaching the similar accuracy level as that of *foamStarSWENSE*. Hence to achieve a wave profile similar to *foamStarSWENSE*, either M2 or M3 with less Co must be chosen in the

*foamStar* solver. For the pressure observed over the cylinder, the solvers showed only a marginal accuracy improvement, and no drastic difference was observed (Figure 3.28c and 3.28d). Hence both models with a finer refinement near the cylinder are good enough to measure the pressure accurately. Lastly, the appropriate model for force prediction over the cylinder is discussed in the following section along with its computational cost.

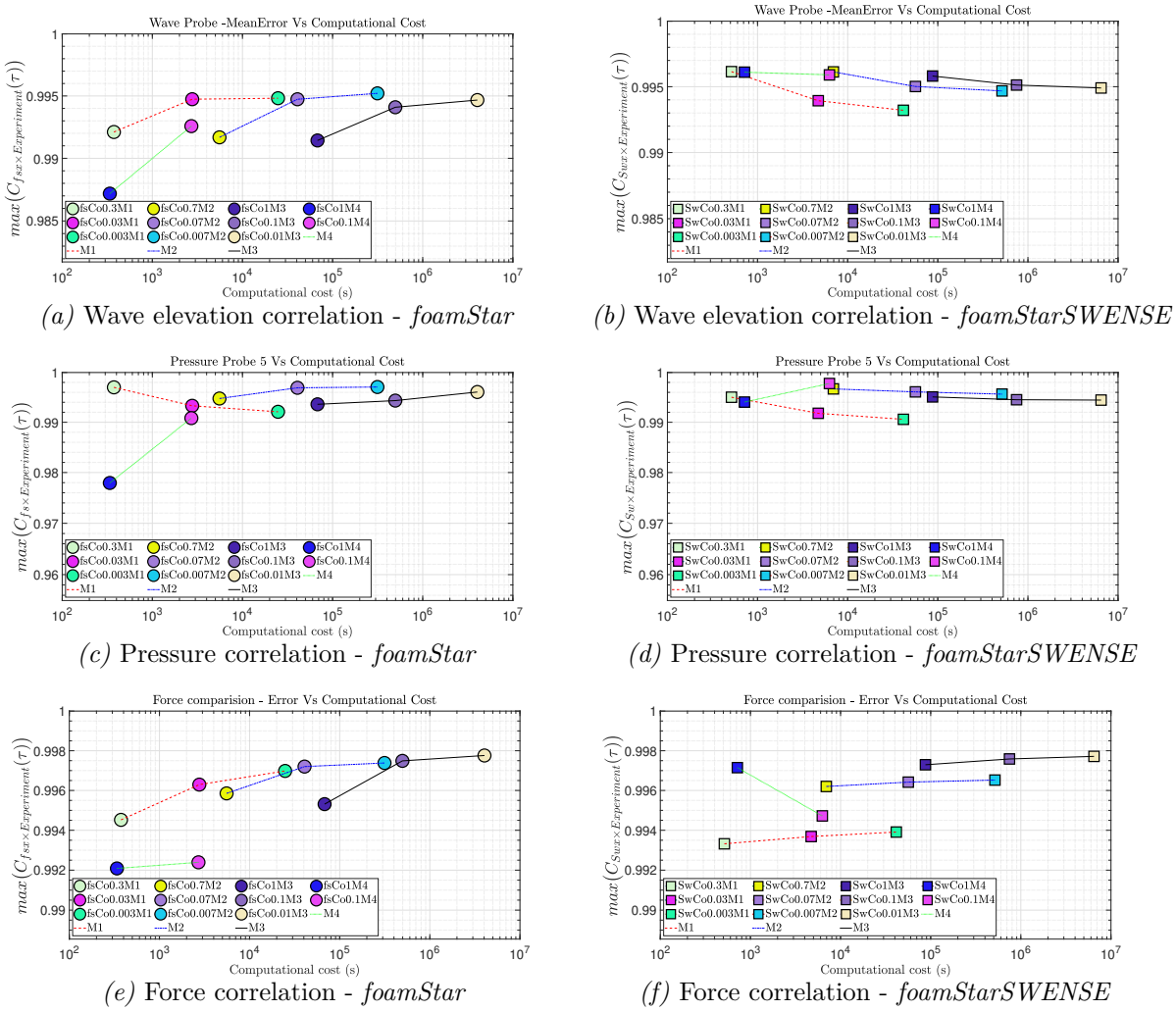


*(a)* Wave elevation correlation - *foamStar*

*(b)* Wave elevation correlation - *foamStarSWENSE*

*(c)* Pressure correlation - *foamStar*

*(d)* Pressure correlation - *foamStarSWENSE*

*(e)* Force correlation - *foamStar*

*(f)* Force correlation - *foamStarSWENSE*

Figure 3.28 – Comparison of correlations between different Mesh types M1, M2, M3 and M4 of *foamStar* (Left) and *foamStarSWENSE*(right) with experimental data. (From top to bottom) Wave elevation, pressure and force

#### 3.3.1.3 Computational efficiency

The primary advantage of this hybrid coupling (DD and FD) is faster simulation than the full/conventional NS solvers while still achieving a comparable level of accuracy. Refer to Section 3.3.1.1 for computational cost estimation procedure and CPU core discretization for all mesh types. Of the factors examined, including wave height, pressure, and force, only force is a global, non local quantity that does not change across the medium. Also, the ultimate goal is to create a numerical model that can precisely predict the forces acting on a monopile or similar structures.

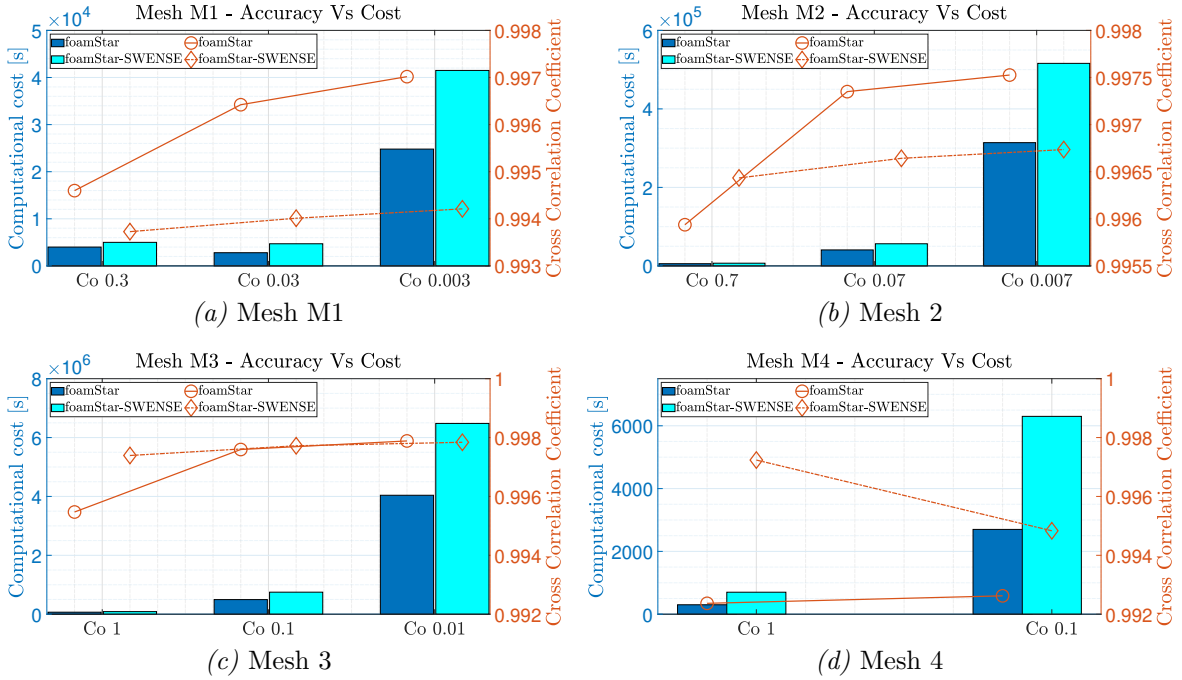


*(a)* Mesh M1 *(b)* Mesh 2

*(c)* Mesh 3 *(d)* Mesh 4

Figure 3.29 – Correlation between different Mesh types M1, M2, M3, and M4 as well as the computational cost by comparing force recorded by the solvers *foamStar* and *foamStarSWENSE* with the experiment

Hence, force applied over the cylinder is used to compare the numerical models foamStar and foamStarSWENSE and the experiment. The comparison for each mesh type is plotted in Figure 3.29 with the computational cost found earlier on one vertical axis and the cross correlation coefficient on the other vertical axis. The plotline indicates the accuracy in terms of coefficient in each case, while the bar chart represents the recorded computational cost. Both solvers yield reasonably accurate answers with minimal errors. The accuracy of *foamStar* is slightly better than that of the *foamStarSWENSE* solver for mesh types M1 and M2 (because of the coarser grid around the cylinder). The computational cost of *foamStarSWENSE* is always 1.1-1.25 times higher that of *foamStar* for a similar setup. The computational cost of the *foamStarSWENSE* solution is slightly higher for the finer mesh M3, but accuracy is comparable to that of the *foamStar* solver thanks to a higher refinement around the cylinder. The coarser time step (Co 0.7 and Co 1) *foamStarSWENSE* prediction outperforms the *foamStar* prediction in both M2 and M3, demonstrating its advantage. Finally, the *foamStarSWENSE* mesh M4 shows that *foamStarSWENSE* is more accurate than the *foamStar* solver for a similar setup. Despite the fact that the computational cost is still larger than that of *foamStar*, it can be clearly seen that *foamStarSWENSE* with this configuration takes 100 times less time to estimate results to obtain the same accuracy (check M3 - all Co). Hence *foamStarSWENSE* can be used to make an initial guess in an industrial estimation of any offshore wave-structure problem at a minimal cost and with high precision. However, *foamStarSWENSE* is more expensive than *foamStar* for similar meshes and timesteps, a drawback that needs to be investigated in the future.

### 3.3.2 Breaking focusing wave interaction with cylinder

The direct modelling of breaking waves is challenging due to the complex nature of the physical processes, including highly non-linear interactions. Researchers carried several experiments (Goda, 1966; Arntsen et al., 2013; Wienke and Oumeraci, 2005; Sruthi and Sriram, 2017) that led to a better understanding of the breaking wave forces. However, the accurate measurement of velocity and acceleration during the impact is still challenging. Also,literature indicated that parameters that influence the breaking forces can be breaker type, the distance of the structure from the breaker location, the shallow water depth that induces breaking etc. In shallow waters, waves deform as they propagate into decreasing water depth. The effects of the sea bottom and shoaling are included as additional terms in defining the breaking criteria. But in deep waters, it is always related to the physical properties of the highest steady wave, which limits the wave growth and causes breaking. Most numerical solvers develop breaking waves using a plane slope inside the domain, resembling the breaking phenomenon in shallow water waves (Kamath et al., 2016; Chella et al., 2015; Aggarwal et al., 2020). But another way of generating breaking waves is using the dispersive focused wave breaking near the structure as adopted in (Sriram et al., 2015). This type of wave-wave interaction allows the control of the breaking events location. Hence, different types of breaking load on the structure can be generated by adjusting the focusing point. In the present research, the BR focusing wave technique is adopted and validated for wave generation and propagation in HOS-NWT and *foamStar* solvers in the Sections 3.2.1.3 and 3.2.4, respectively. This section validates the method to calculate the breaking wave force on a fixed cylinder using parameters from the previous studies. The surface elevation, pressure over the cylinder are also measured and validated with the experimental results.

#### 3.3.2.1 foamStar

The three-dimensional simulation of the BR focused wave-structure interaction is performed with a vertical circular cylinder in a NWT. The interaction modifies the kinematics and the flow field around the cylinder as shown in Figure 3.30. To understand the figure, a new parameter $t_h$ is introduced, where it is the time at which wave impacts over the cylinder. This figure displays the free surface features with velocity magnitude when the focused wave interacts with the cylinder for different time instants. Figure 3.30a represents the wave reaching its maximum height and the wave front is about to start curling. The highly curled wave crest impacts the cylinder much below the top wave crest level in Figure 3.30b. Figure 3.30c shows the separation of the incident wavefront and the formation of a semi-circular wavefront meeting behind the cylinder. The broken wave separated around the cylinder propagates further with a region of low velocity in the shadow region behind the cylinder. A mildly developed chute-like jet is seen in Figure 3.30d which is close to its collapsing stage, and this weakly developed chute wave is seen to rejoin the free surface at some distance behind the broken wave crest in Figure 3.30e. At last, the broken wave appears to spread over the domain and disrupts the incoming waves, as shown in Figure 3.30f.

The numerically captured free surface elevation probe readings are presented in Figure 3.31.

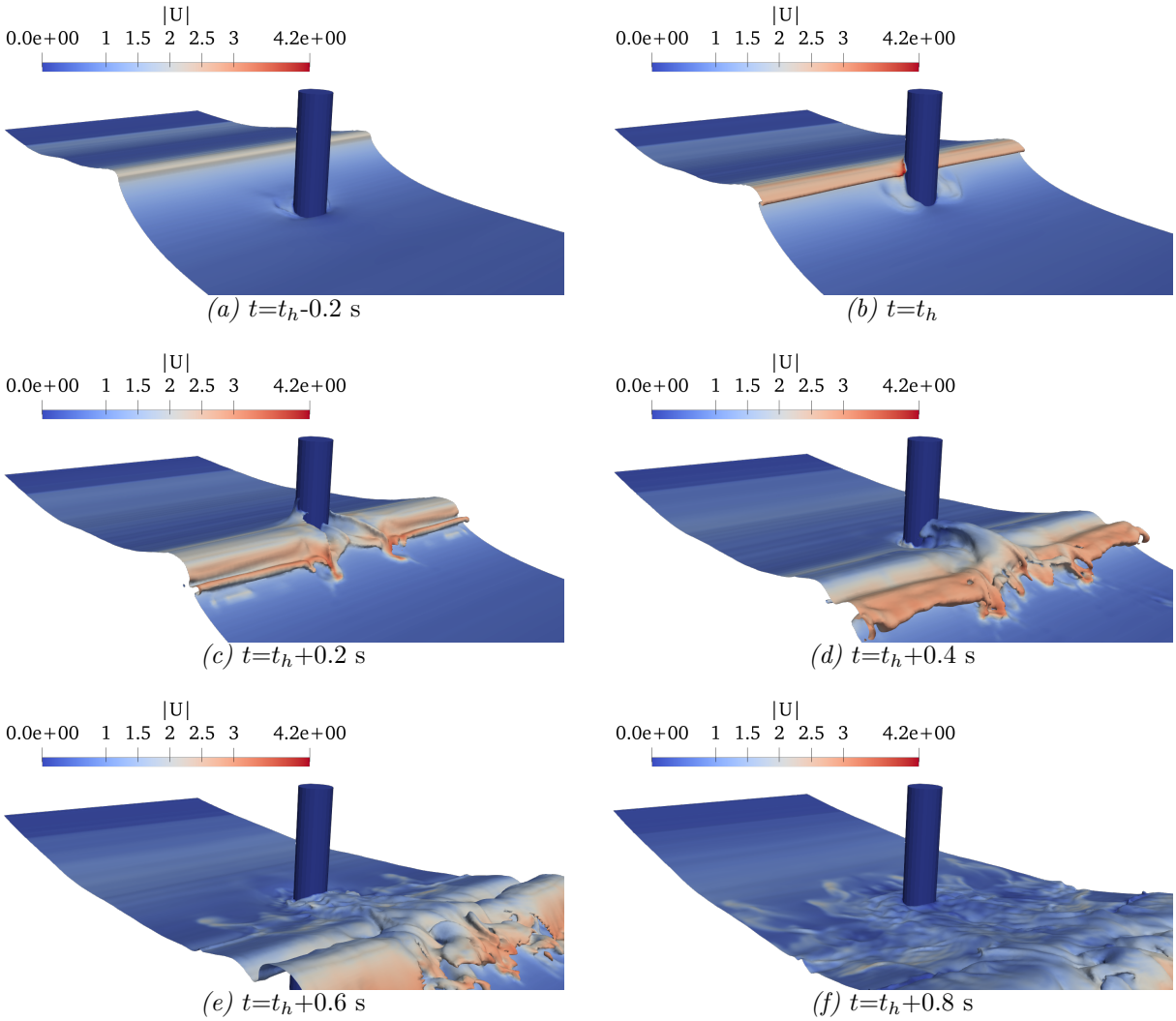


(a) $t$=$t_h$-0.2 s (b) $t$=$t_h$

(c) $t$=$t_h$+0.2 s (d) $t$=$t_h$+0.4 s

(e) $t$=$t_h$+0.6 s (f) $t$=$t_h$+0.8 s

Figure 3.30 – Isometric views of breaking wave interaction towards the cylinder for different time instant with contour representing the velocity profile in the free surface

It allows us to investigate the changes in the free surface elevations during and after the focused wave interaction with the cylinder. The figure illustrates the wave elevation and its comparison with the experimental recordings. It is to be noted that only three wave gauges (WP5, WP6 and WP7) are accessible in the CFD computational domain. To remind the reader, probe WP6 is at the cylinder location, WP5 and WP7 are placed before and after the cylinder location (See Section 3.1). The present investigation aims to determine the accurate breaking force that occurs over the cylinder when interacting with focussed breaking waves. In that instance, the primary necessity for this inquiry is the precise breaking wave generated. Therefore, it follows from the preceding parametric study (Section 3.2.4) that the fsRe3e5 mesh type combined with Co 0.1 is an effective combination for producing the precise breaking wave. As a result, this arrangement is maintained for this 3D WSI, and the results validate our assumption. The numerical results obtained with the Mesh fsRe3e5Co0.1 for WP5 and WP6 replicate the focused wave profile with minor discrepancies. The discrepancies are due to the uncertainty between the HOS and

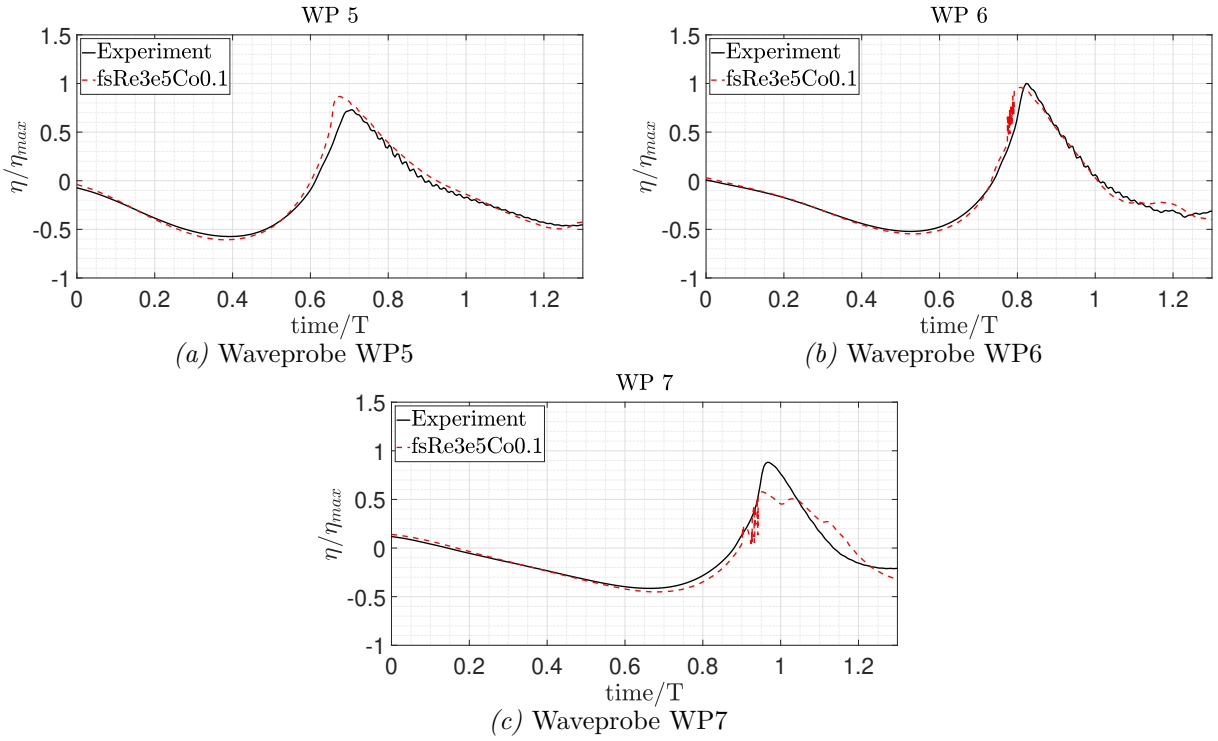


*(a)* Waveprobe WP5 *(b)* Waveprobe WP6 *(c)* Waveprobe WP7

Figure 3.31 – Illustration of Wave probe comparison between Mesh type fsM4Co0.1 of *foamStar* solver and Experiment

experimental results and the missing accuracy from the convergence study reported in the Section 3.2.4. The WP7 displays a considerable difference as the fact that after the cylinder interaction, free surface dynamics are very complex (Figure 3.30e), and the probe is in the middle of the foam. The numerical probe is subjected to two to three levels of the mixed free surface which cannot record the proper surface elevation irrespective of adequate recording in the physical probe in the experiment.

Next, the focused wave pressure onto the cylinder is evaluated here by comparing the time variation of the dynamic pressure recorded on the submerged as well as the exposed surfaces of the cylinder (See Figure 3.32). The simulated time histories of the submerged pressure probes (PP1-PP3) in the stagnation point are expected to follow the wave elevation. Accordingly, the mesh-type fsM4Co0.1 exhibits similar trends, but minor discrepancies are observed. A similar difference exists in simulated peak pressure in PP4 and PP5 (air probes), which depends only on proper wave run-up over the cylinder during the focusing event. Even probes around the cylinder (PP6-8) can capture the trend neatly. The slight deviations in the amplitude of the wave elevation between fsM4Co0.1 and the experiment resulted in the overestimation of pressure amplitudes in almost all the probes.

Figure 3.33 illustrates the time history of the force recorded for fsM4Co0.1 during the focused wave interaction. In the experiment, the cylinder has experienced the "ringing" phenomenon (Saincher et al., 2022) after impact, which cannot be simulated in numerical simulation as the body is assumed to be rigid. So the time trace is compared only up to impact and ignored the details after the interaction. The hybrid model could represent the breaking force trend

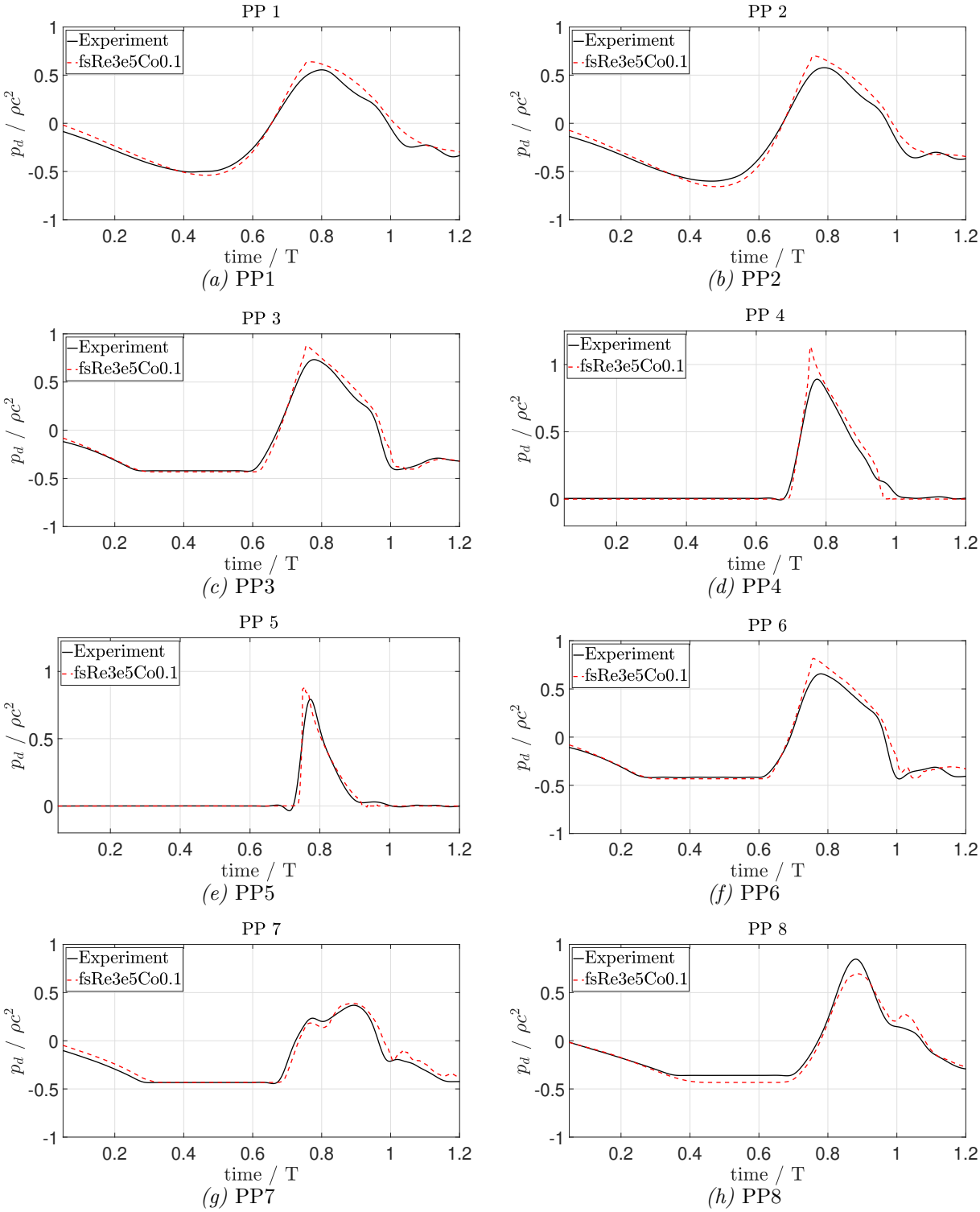


*(a)* PP1 *(b)* PP2 *(c)* PP3 *(d)* PP4 *(e)* PP5 *(f)* PP6 *(g)* PP7 *(h)* PP8

Figure 3.32 – Pressure time history comparison for fixed cylinder in BR focusing waves between *foamStar* and experiment

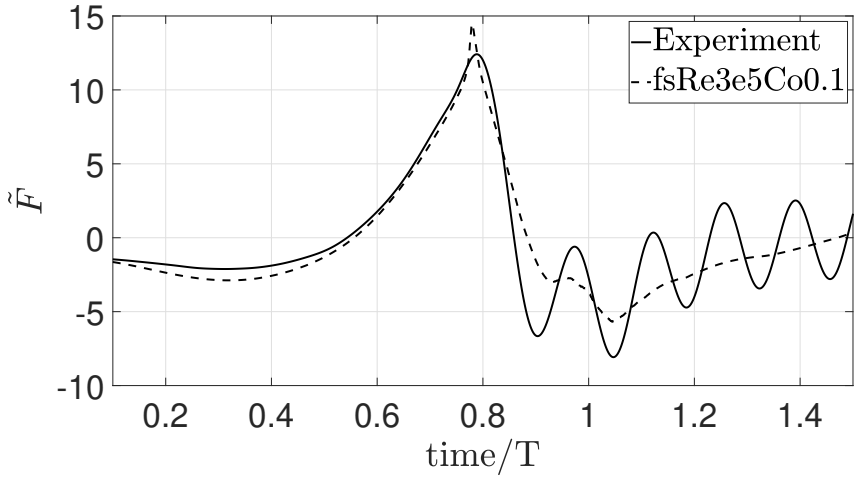


Figure 3.33 – Comparison of the breaking force between Mesh type fsM4Co0.1 of *foamStar* and experiment

accurately but with little overprediction of the force in amplitude. It comes directly from the pressure prediction and the earlier uncertainties mentioned. But assessing the quality of the numerical model shows that it can treat such a complex problem that is of huge importance in ocean engineering at maximum accuracy.

## 3.4 Closure Discussion

**NBR focusing wave interaction with cylinder :** The domain and functional decomposition approach based solvers (*foamStar* and *foamStarSWENSE*) have been validated in the OpenFOAM framework based on the focused wave kinematics generated from the HOS-NWT using the time-reversal technique. Both coupling strategies are currently one-way schemes, implying that information is exchanged from HOS to CFD but not vice versa. Here CFD represents both the NS/SWENSE solvers. The CFD domain is restricted to the zone where vorticity and viscous effects are predominant, and a potential flow solver is considered for input waves only. Initially, both approaches were applied to a 2D NWT to generate a focusing wave from HOS to CFD. The study has addressed HOS initiation time, relaxation zone, spatial and temporal requirements, and different cell ratios. It was found that, due to the coupling, HOS initiation can start immediately before the focusing time and that the simulation does not need to be started from the beginning. This significantly reduces the computational time by a factor of 10. Focusing wave's spatial and temporal requirement in the CFD domain was also explored based on cell-based Reynolds and Courant numbers. In addition, the problem's relaxation zone has been significantly reduced, saving computational cost.

The coupling approach was then applied in a 3D wave-structure interaction study representing a fixed surface-piercing circular cylinder interacting with the focusing wave. Three different mesh types (coarse (M1), medium (M2) and fine (M3)) were developed with a refinement ratio of 2. The cross correlation coefficient was adopted to identify the relative error difference between the time series, thus taking care of the difference in the wave profile, phase shift and peak

magnitude. The parameters compared were the wave elevation, pressure over the cylinder and induced force. The mesh types results were initially compared with the finest mesh combination (fsCo0.01M3), and a numerical uncertainty study was carried out based on the Richardson extrapolation. The simulated results were also validated with experimental data. Compared to addressing a similar subject in the complete CFD problem, both coupling algorithms yield good agreement with experimental results with slight uncertainties and significantly reduced the CPU time. Even the coarsest mesh (M1 and M4) of the *foamStar* and *foamStarSWENSE* solvers can predict the forces over the cylinder with a difference of only 10%. The *foamStarSWENSE* solver estimates the wave and pressure over the cylinder more accurately on multiple occasions (M3 and M4) than *foamStar*, but it takes 1.25-1.5 times longer computational time. But one benefit is that the accuracy of the mesh type without any free surface refinement (M4) in *foamStarSWENSE* achieved accuracy similar to medium mesh refinement in *foamStar*. This is because of the explicit treatment of incident waves in SWENSE, even a coarse mesh in the far-field can accurately produce the incident wave information and also finer refinement near the cylinder. In no instances, however can the performance of *foamStar* claimed to be lower than that of *foamStarSWENSE*. It consistently produced good results in all types of meshes with a modest computational cost, despite the fact that refining increased the accuracy of the results. Overall, the *foamStar* and *foamStarSWENSE* solvers performed well for NBR focused wave generation and interaction with a fixed vertical cylinder.

**Breaking focusing wave interaction with cylinder :** The CFD based solver *foamStar*, in coupling with potential theory-based *HOS-NWT* (Domain decomposition), is used to simulate the focused breaking wave interaction with a vertical cylinder. The interaction study is carried as a two-step procedure. First, the focused breaking wave is validated in both the *HOS-NWT* and the *foamStar*. Also, necessary parametric studies are carried out in two dimensional NWT and reported. Second, the breaking wave interaction with the cylinder is carried out. The numerical results for the wave force, the free surface elevation, pressure over the cylinder are compared to the experiment. The experimental data are from tests carried out at the Ludwig-Franzius-Institute, Germany, and obtained an excellent agreement. The highlighted things in the study are the breaking wave model introduced in the potential solver HOS-NWT is tested and the application of domain decomposition methodology for breaking wave interaction problems. The study concludes that this hybrid coupled model as NWT can be a valuable tool for evaluating breaking wave interaction over any offshore or coastal structures, replacing the physical tank's difficulties at maximum accuracy.

Chapter 4

# FOCUSING WAVE INTERACTION WITH MOVING CYLINDER

Bottom fixed offshore wind turbines are generally built in shallow water or intermediate waters like Walney wind farm (depth ≈ 19 m-23 m), Ormonde wind farm (depth ≈ 17 m-21 m), Alpha Ventus wind farm (depth ≈ 30 m). Although some advantages of deployment and accessibility come with operating wind turbines in shallow water, the foundation structure must be built to withstand hydrodynamic loads imposed by both waves and currents. These currents can alter the wave dispersion, the wave-induced velocities, the shear stress on the seafloor, and other factors, which affect the wave loading on structures and the wave propagation near coasts. Due to the action of vortices, hydrodynamic scouring of the structure's foundation is a significant phenomena in wave-current interaction (Chen et al., 2020; Welzel et al., 2019). It is vital to understand this subject since offshore wind farms are increasingly being launched in shallow water. Also, the dynamic response brought on by a combination of drag, inertia, impact, and aerodynamic loads is another design consideration for structures situated in combined wave-current fields. An improved understanding of this complicated process and its impact on structures would be beneficial for engineering applications such as the design of bottom fixed OWT structures in shallow waters and its protection as well as the evaluation of sediment transport and coastal erosion.

Currents are commonly generated by wind-driven shear at the air-water interface in shallow water regions located in windy areas. As Beyer et al. (2017) demonstrated, these so-called "sheared currents" are not depth-uniform and consequently rotational. It can be difficult to generate sheared currents in a wave-current flume because of the interactions between the current generator and the subsurface wave kinematics that must be kept to a minimum. Due to the difficulty of producing a constant current in the lab, researchers typically rely on the towing of the structure of interest (Sarpkaya and Storm, 1985; Vengatesan et al., 1999; Saincher et al., 2022) to mimick the local current near the structure. It is solely of academic and fundamental interest to comprehend the physics of nonlinear wave-current loading on a structure because a depth-uniform current never occurs in reality (Beyer et al., 2017). The towing approach is conservative because a depth-uniform current would naturally impart higher loads than a depth-varying current (Saincher et al., 2022).

The design challenge is expressed in accounting for the unpredictability of wave climate in model studies, in addition to simulating a realistic sheared current field. The waves may be regular, random, or short extreme waves like focused waves. As covered in the previous

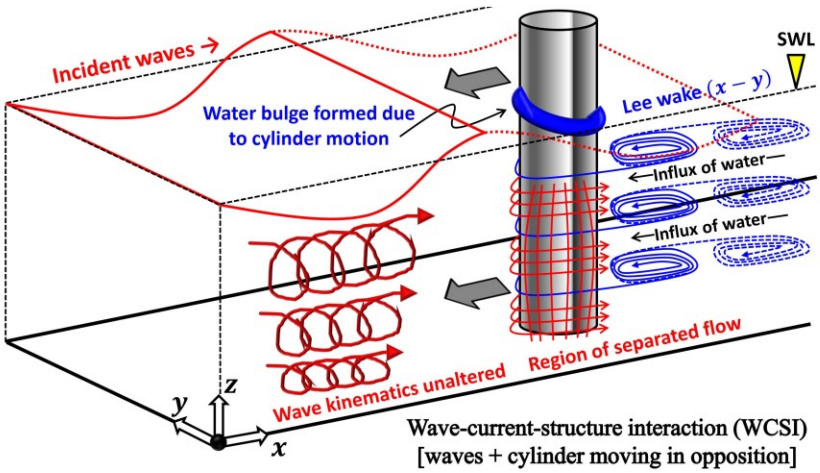


Figure 4.1 – Wave-current-structure interaction for waves + moving cylinder (illustration considers waves and moving cylinder kinematics separately) (Saincher et al., 2022)

chapter, focused waves are an idealistic concept that can result from wave-wave, wave-current, or wave-water depth interaction effects. This means that the interaction of focused wave groups propagating on either following or adverse sheared currents with surface piercing cylinders has direct practical implications. The present study in this chapter aims to numerically analyze the type of hydrodynamic loading imposed on a slender cylinder while it is being towed in a NWT and hit by non breaking focused waves.

Before proceeding with the objectives of this study, it is crucial to understand the physics of a coexisting wave-current field interacting with a cylinder being towed in waves from the perspective of wave-current-structure interaction. As shown in the Figure 4.1, the wave and current fields can be physically separated, and the kinematics for undisturbed waves and a cylinder subjected to uniform flow can each be described separately. When moving forward at a steady speed, the cylinder seems to develop a bulge at the front, creating wake vortices. Next, unaltered wave kinematics impact the cylinder, and these changes in the flow field and impact parameters are explained in more detail in the following sections of this chapter. Overall, this chapter tests two test cases of a cylinder moving forward at a speed of 0.33 m.s$^{-1}$ (Re=57000) and 0.75 m.s$^{-1}$ (Re=126000). As in the previous chapter, the FD and DD solvers *foamStar* and *foamStarSWENSE* are applied to each test cases studied, and the surface elevation, the pressure across the cylinder, and the forces are examined. In other words, this chapter will be a replica of the one before it, but this time the cylinder is moving resembling a uniform current.

This chapter is divided into the following sections. First, the experimental details for the validation study are discussed, followed by NBR focusing wave interaction with the moving cylinder at 0.33 m.s$^{-1}$ is detailed and validated in the first half of the following section, and the interaction of the NBR focusing wave with the moving cylinder at 0.75 m.s$^{-1}$ is presented in the second half of the chapter.

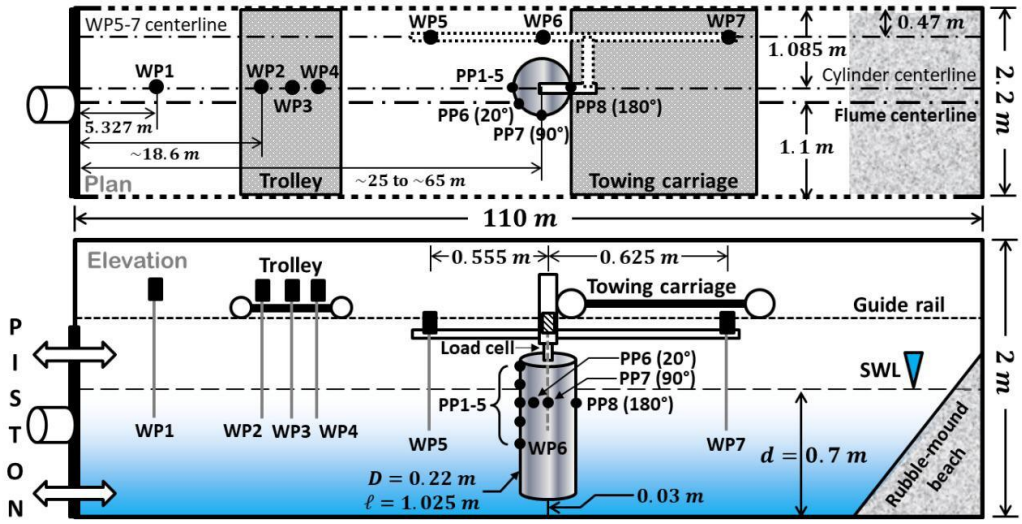


Figure 4.2 – Typical experimental domain used for the application of focusing waves interacting with towing cylinder (Saincher et al., 2022)

## 4.1 Experimental set up and Testing conditions

For the present study, experimental specifications are similar to the one presented in Section 3.1. This is because, under the same experimental campaign, both the fixed and moving cylinder were tested, and hence it will not be repeated here for the sake of brevity. The wave and cylinder characteristics investigated in this chapter are shown in Table 4.1. From the table, $f_c$ and $\Delta f$ represents center frequency and bandwidth ratio, **N** represents the number of components and $G_a$ is the wave steepness. The two different towing speeds ($\boldsymbol{v}_{cyl}$) considered are 0.33 m.s$^{-1}$ and 0.75 m.s$^{-1}$, and the corresponding Reynolds number (Re) is rounded off to nearby whole numbers such as 57000 and 126000, respectively, for easier representation. Typical experiment domain is illustrated in the Figure 4.2. The cylinder is positioned 3 cm above the tank bottom for towing operations, which causes it to oscillate at its natural frequency when a focusing wave hits the cylinder. The dominant force measured in the load cell for Case 2 (Re 126000), demonstrates this phenomenon as shown in Figure A.11, along with the numerical results. For more details related to the experiment on moving cylinder interaction with BR and NBR focusing wave can be read at Saincher et al. (2022).

| **Case** | $f_c$ **(Hz)** | $\Delta f/f_c$ | $f_1$ **(Hz)** | $t_f$ | **N** | $G_a$ | $\boldsymbol{v}_{cyl}$ **(m.s$^{-1}$)** | **Re** |
|---|---|---|---|---|---|---|---|---|
| Case 1 | 0.68 | 1 | 0.33 | 38.0 | 32 | 0.002 | 0.33 | 57000 |
| Case 2 | 0.68 | 1 | 0.33 | 38.0 | 32 | 0.002 | 0.75 | 126000 |

Table 4.1 – Testing wave packet and cylinder characteristics

## 4.2 Numerical setup

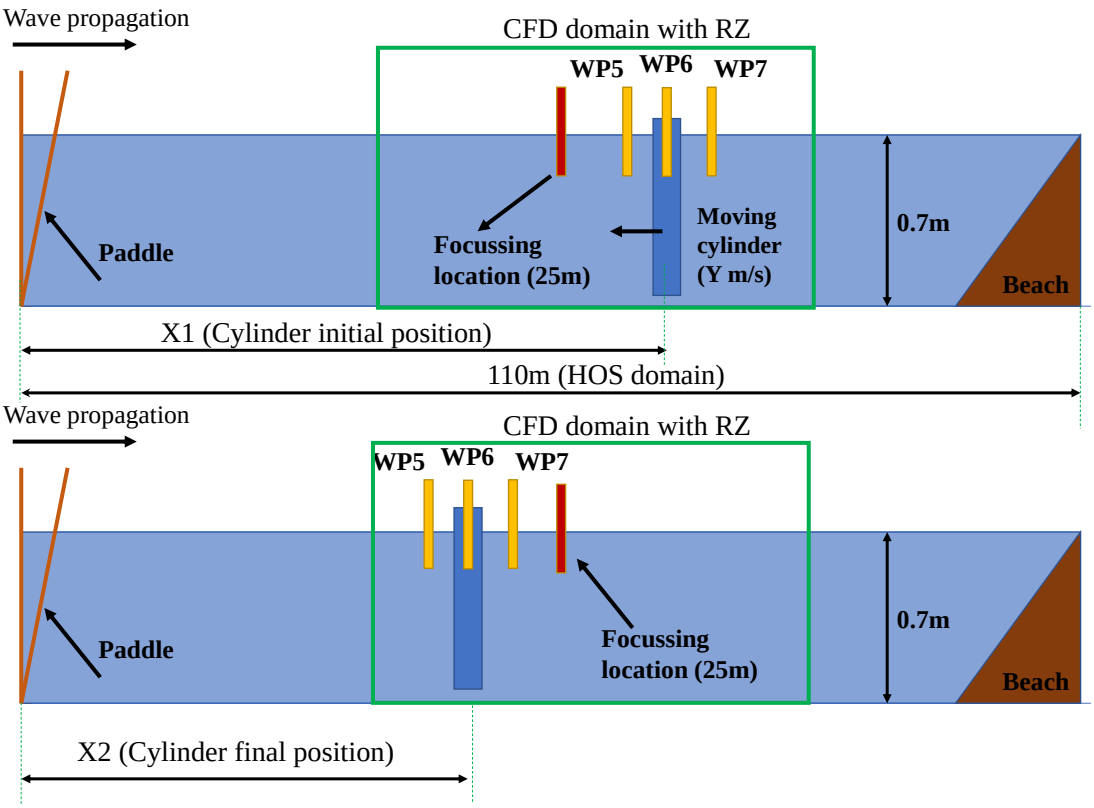


Figure 4.3 – Domain description of moving cylinder along with wave probes WP5, WP6 and WP7 in the CFD domain with upper figure showing the initial position and lower figure showing the final position of the cylinder. RZ represents relaxation zone

For the Case 1 (Re 57000), the cylinder's initial position is 45.56 m in the $R_0$ frame from HOS origin (X1 in Figure 4.3), and it moves towards the wave paddle at the speed of 0.33 m.s$^{-1}$(Y in Figure 4.3). Similarly for the Case 2 (Re 126000), the initial position is 65.87 m in the $R_0$ frame from HOS origin (X1 in Figure 4.3), and it moves towards the wave paddle at the speed of 0.75 m.s$^{-1}$(Y in Figure 4.3). The starting point is chosen so that the cylinder will reach the focusing location (25m from the wave paddle) at the appropriate focusing time of 38 seconds after the paddle started. Since there is no effect on the numerical simulation of the chosen initial time (as explained in Section 3.2.3.2), the total duration of the simulation was set to 5 s. The focusing time happens after around 2s and aftereffects lasting for the remaining duration. The initial position of the cylinder centre is fixed at +0.66m and +1.5m in the CFD domain in $R_0$ frame from CFD origin (25.66 m and 26.5 m in the $R_0$ frame from HOS origin) for the Case 1 and Case 2 respectively, and the cylinder is moving in a negative x direction (with respect to $R_0$) reaching the focusing location ±0 ( 25 m in the $R_0$ frame from HOS origin) at 2 s and final position at −0.99 m and −2.25 m (24 m and 22.75 m in the $R_0$ frame from HOS origin, see X2 in the Figure 4.3) at the end of the simulation.

Similar to the setup presented in Table 3.1, there are seven wave gauges WP1 to WP7, with

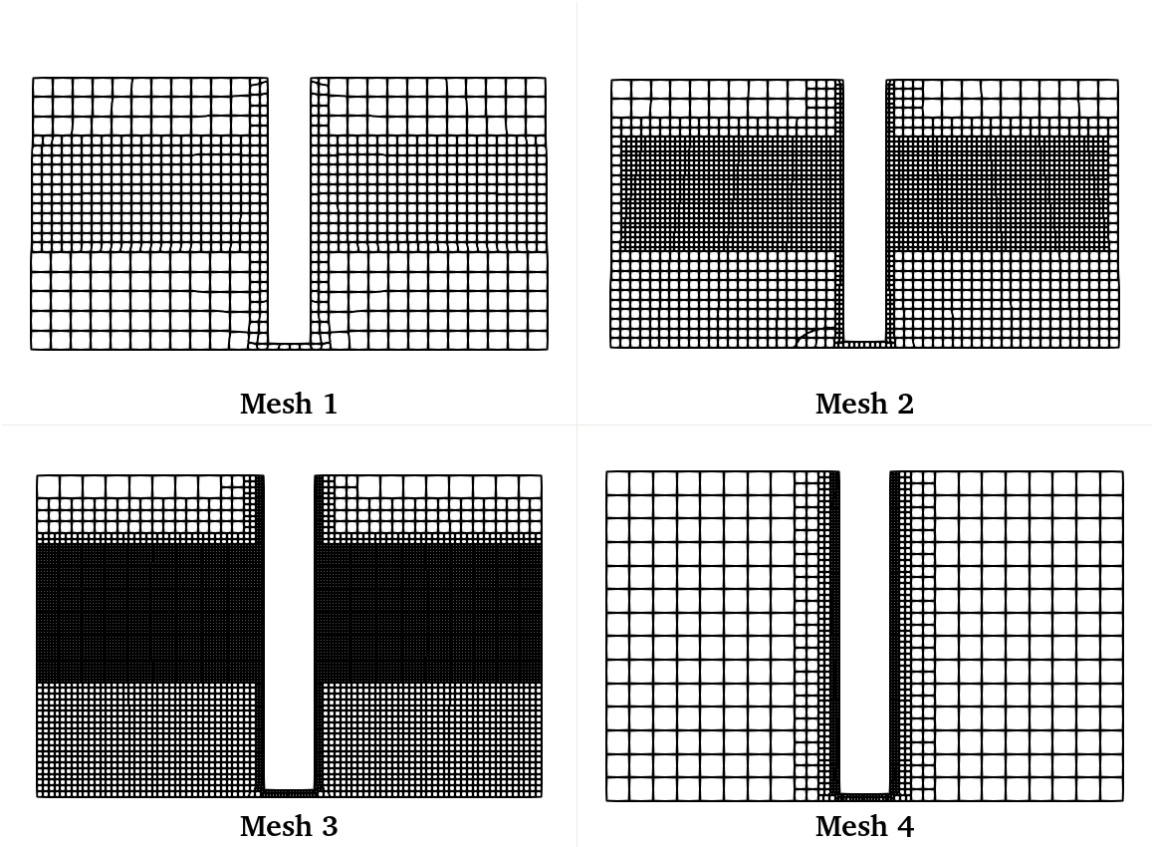


Figure 4.4 – Mesh configuration of three levels Coarse, medium and fine mesh with refinement ratio of 2 for each case and Mesh 4 without free surface refinement to investigate the performance of SWENSE

the first wave gauge placed 4.98m from the wave paddle and the following three wave gauges (WP2-WP4) in the middle from the focusing location. In the moving cylinder experiment, WP5, WP6 and WP7 probes are moving along with the cylinder at the same speed. Hence in the $R_0$ frame from CFD origin, WP5 is located 0.57 m in front of the cylinder centre (focusing point), WP6 is located at a point of the tank cross section in line with the centre of the cylinder and WP7 is located 0.71 m behind the cylinder. Only three-wave gauges WP5 to WP7 fall in the CFD zone. Eight pressure transducers are used, five are located at 0° with equal spacing in the front face, and the remaining three are located at $20°, 90°$ and 180° near the still water level as shown in Figure 3.1 and Figure 4.2.

The numerical convergence study is carried using three different mesh configurations with different discretization levels similar to the fixed cylinder validation study (Section 3.3.1). A refinement ratio of 2 was used to establish control over the mesh growth. Mesh 1 (M1), Mesh 2 (M2), and Mesh 3 (M3) will be used to represent these configurations as illustrated in Figure 4.4. The only difference between the fixed cylinder validation and moving cylinder is the bottom of the cylinder is 3 cm higher than the bottom of the tank. In summary, Mesh 1 (coarse mesh) has 32496 elements, Mesh 2 (medium mesh) has 241476 elements, and Mesh 3 (fine mesh) has 1898760 elements. An additional mesh, Mesh 4, was made similar to Mesh 3 but without any free surface

Table 4.2 – Test Matrix and its nomenclature for moving cylinder interaction with non breaking focusing wave ($\boldsymbol{v}_{cyl} = 0.33$ m.s$^{-1}$ and $\boldsymbol{v}_{cyl} = 0.75$ m.s$^{-1}$)

| **Mesh** | **TimeStep (s)** | **Co** | **TestCase (Nomenclature)** |
|---|---|---|---|
| Mesh 1 (M1) | 0.0001,0.001, 0.01 | 0.003,0.03,0.3 | *foamStar*- fsCo0.3M1.. *foamStarSWENSE* -SwCo0.3M1.. |
| Mesh 2 (M2) | 0.0001,0.001, 0.01 | 0.007, 0.07, 0.7 | *foamStar*- fsCo0.7M2.. *foamStarSWENSE* -SwCo0.7M2.. |
| Mesh 3 (M3) | 0.0001,0.001, 0.01 | 0.01. 0.1, 1 | *foamStar*- fsCo0.1M3.. *foamStarSWENSE* -SwCo0.1M3 |
| Mesh 4 (M4) | 0.0001, 0.001, 0.01 | 0.01, 0.1,1 | *foamStar*- fsCo0.01M4.. *foamStarSWENSE* -SwCo0.01M4 |

refinement to investigate the advantage of the SWENSE methodology. Three constant time steps of 0.01 s, 0.001 s, and 0.0001 s were investigated for each mesh to investigate the influence of temporal variation in each solvers. This constant time steps are based on physical Co, which is directly related to the maximum velocity of the wave and the minimum cell size in the mesh. More details about the test matrix are presented in Table 4.2. The *foamStar* and *foamStarSWENSE* solvers were tested for each combination of mesh type and Co. Similar to the fixed cylinder investigation (Section 3.3.1.3), the discretization for parallel simulations is maintained at 1 CPU for every 30000 cells. The same residual limits and schemes are used for all simulations and simulations were run on the cluster (supercomputer LIGER, at Centrale Nantes, France). For comparing the computational cost between the mesh types, the methodology adopted in Chapter 3, Section 3.3.1.3 is adopted in the present study, which is also based on reference from Agarwal et al. (2021a). The $Np$ for mesh types M1,M2,M3 and M4 are $1, 8, 64, 1$ respectively. The convergence of the results is studied similarly to what is presented in Chapter 3, using Richardson extrapolation and Cross Correlation. Hence it is not repeated in this chapter but presented in the Appendix. From those tests, two numerical setups were identified as a good compromise, fsCo0.01M3 for the *foamStar* solver and SwCo0.01M3 for the *foamStarSWENSE* solver (see Appendices A.1 and A.2 for Cases 1 and 2, respectively). In the next sections they are qualitatively compared with the results of experiments and presented. It is followed by a quantitative comparison of different mesh types with the experiment.

Before proceeding with the analysis, a typical numerical portrayal of the moving cylinder and its interaction is provided for better understanding. In the numerical (*foamStar*) and experimental framework, a moving cylinder at forward speed and its interaction with the wave are depicted at three different time snaps: (Figure 4.5), before, at and after the interaction with the cylinder. Before the wave interaction, a bulge of water is formed in front of the cylinder due to the towing and this bulge would steepen with increasing $\boldsymbol{v}_{cyl}$ to the extent that it acts to "step up" the wave elevation of the signal recorded by WP5. Although it is difficult to visualise in the experiment (faintly visible in Figure 4.5b), this water bulge can be clearly seen with the *foamStar* visualisation at the same time instant (Figure 4.5a). In the next instant, the water bulge is no longer predominantly visible because of the interaction with incident waves. The

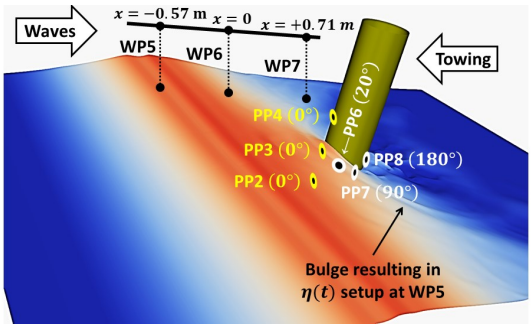


*(a)* Before interaction-(*foamStar*)

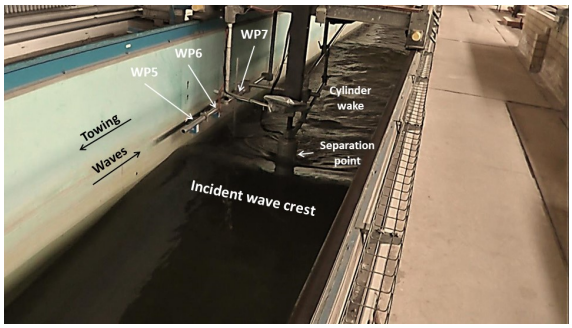


*(b)* Before interaction-(Experiment)

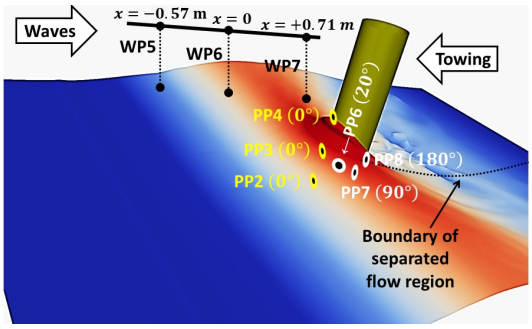


*(c)* During interaction-(*foamStar*)

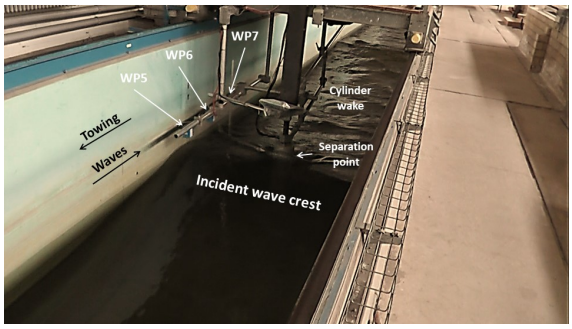


*(d)* During interaction-(Experiment)

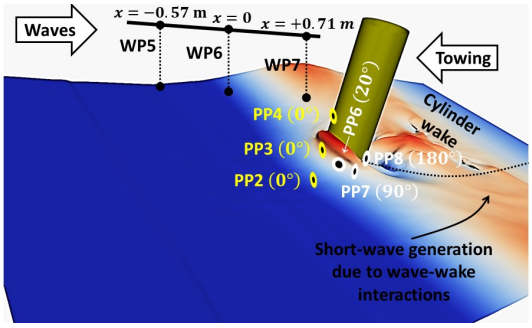


*(e)* After interaction-(*foamStar*)

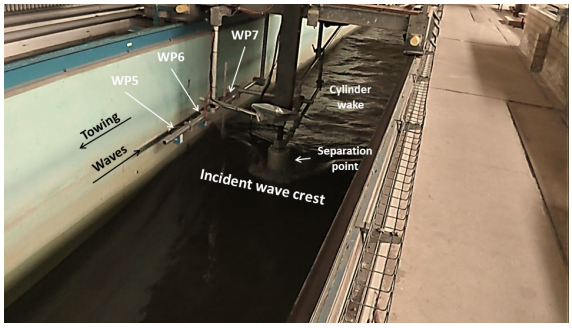


*(f)* After interaction-(Experiment)

Figure 4.5 – Numerical and experimental snapshots of the moving cylinder interacting with the incident wave crest. Positioning of the wave probes (WP) is relative to center of the cylinder.

boundary of the separated flow regions are narrowly modified (Figure 4.5c and Figure 4.5d). After the interaction, pervasive short-wave generation occurs after passing the main crest owing to wave–wake interactions, as shown in Figures 4.5e and 4.5f. At higher towing speed, the wave–wake interactions result in an overall reduction in wave height (due to viscous damping), with the trough elevation becoming more significant than the crest elevation. Thus, the validation at WP7 demands that the solvers correctly capture the wake-induced viscous effects in addition to the short-wave generation following the main trough.

## 4.3 Case 1 : NBR focusing wave interaction with moving cylinder (Re 57000)

This section is split into two parts. The first part compares converged mesh simulations (fsCo0.01M3 and SwCo0.01M3) with the experimental results and its qualitative discussion with both *foamStar* and *foamStarSWENSE* solvers. The second part quantitatively compares different mesh type combinations with the experimental results.

### 4.3.1 Validation with finest mesh simulations

The WP5, WP6, and WP7 probes measure the free surface elevation of the *foamStar* simulations before, at and after the focusing point, and the results are shown in Figure 4.6. Both solver results have peak amplitudes of 4% to 7% higher than the experimental measurement because the HOS-generated focusing wave has a slightly higher peak amplitude than the experiment. Both fsCo0.01M3 and SwCo0.01M3 completely replicate the focusing wave event, except for a few minor changes at the peak crest.The wake generated after the focusing wave event is slightly different in the trough region generated in the numerical simulations for WP6 and WP7. After testing different parameters to improve the numerical results to capture the wake accurately, it is realized that this is the maximum accuracy that can be attained from the numerical simulation. The reason for the difference can only be attributed to experimental uncertainties.

Next, the experimental pressure measurements and dynamic pressure observed by the numerical probes PP2-PP8 with *foamStar* and *foamStarSWENSE* solvers for the finest mesh simulations are presented in Figure 4.7. As in the previous chapter discussion, the time and dynamic pressures are normalized by the transient wave period (T) and $\rho c^2$, (where $\rho$ is the water density and $c$ is the maximum fluid velocity at the focusing point (i.e. 1.4 m.s$^{-1}$ obtained from HOS)) respectively. Looking at the pressure probes PP2-PP8, both the *foamStar* and *foamStarSWENSE* solvers agree well with the experimental results. The pressure time histories at PP2, PP3, and PP6 compare well observing the same dynamic pressure before and after the focusing event. After the focusing impact, a minor pressure decrease and wake effects were visible in PP7 and PP8. Nonphysical oscillations were initially observed at PP7, and Figure 4.7f shows this initial instability for a limited number of timesteps and later got corrected as the simulation progressed. Peak pressure measurements from air probes (PP4, PP5) show a slight variation in peak amplitude, but the overall observation is relatively accurate.

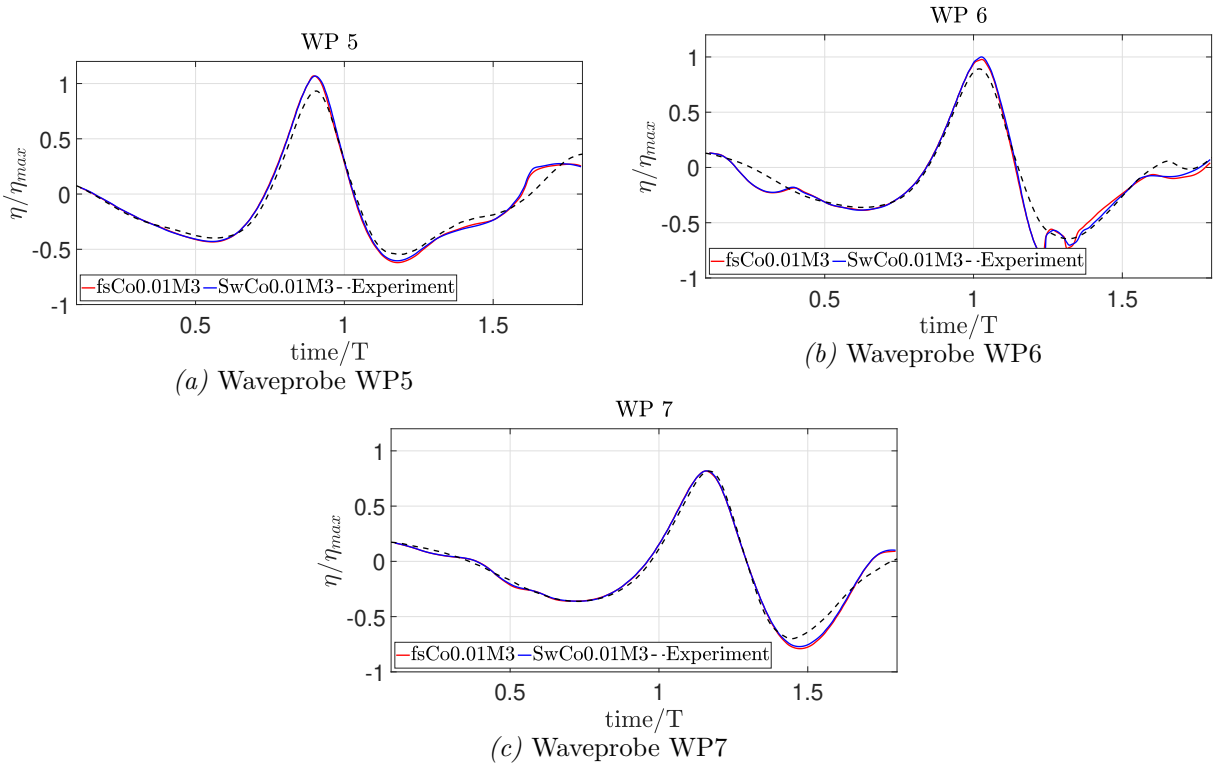


*(a)* Waveprobe WP5

*(b)* Waveprobe WP6

*(c)* Waveprobe WP7

Figure 4.6 – Wave probe comparison of the converged simulations (fsCo0.01M3 and SwCo0.01M3) with the experimental results for Re 57000

Figure 4.8 shows the unidirectional forces observed for a NBR focusing wave plunging a moving cylinder travelling at a speed of 0.33 m.s$^{-1}$. The simulated forces are normalized for the convenience of comparison with the factor $\rho g r^3$, where r represents the radius of the cylinder. Little to no difference was observed between the *foamStar* and *foamStarSWENSE* results here, and the maximum amplitude during the crest is well captured. As noted in WP and PP observations, the trough force observation also failed to capture it adequately, and there is also a slight ringing response, but it is not severe as observed for Case 2 (Section 4.4).

### 4.3.2 Learning's from the convergence study (Section A.1.1 and Section A.1.2)

The convergence study proposed in APPENDIX A.1 is performed on several quantities the wave elevation at three wave probes, the pressure at multiple locations, and the total force on the cylinder. The conclusions from the study are briefly recalled below for both solvers.

- **Surface elevation:** According to the *foamStar* investigation, *foamStar* can still retain decent accuracy for the coarsest mesh and time step, even in the absence of free surface refinement (Mesh M4). Additionally, M1 with medium temporal refinement is the most cost-effective choice if the demand for wave accuracy is not high. M2 with medium temporal refinement is adequate enough to give equivalent results with less computational cost than M3 with medium and fine temporal refinement, which produces similar accuracy. The convergence analysis for *foamStarSWENSE* (Figure A.5) showed that all mesh types

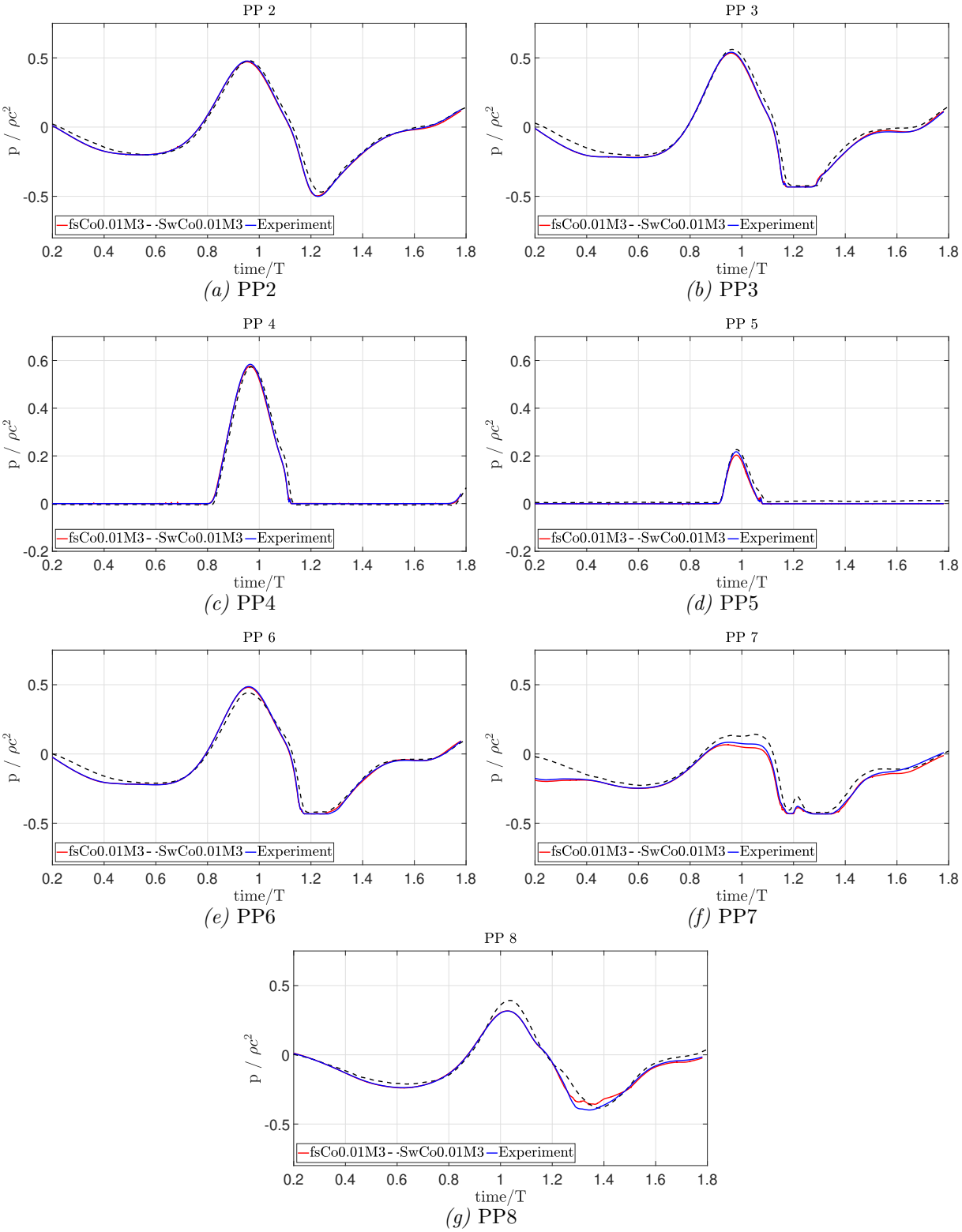


*(a)* PP2 *(b)* PP3 *(c)* PP4 *(d)* PP5 *(e)* PP6 *(f)* PP7 *(g)* PP8

Figure 4.7 – Pressure time history of the moving cylinder (Re = 57000) in NBR focusing waves for converged mesh simulations (fsCo0.01M3 and SwCo0.01M3) with the experimental results

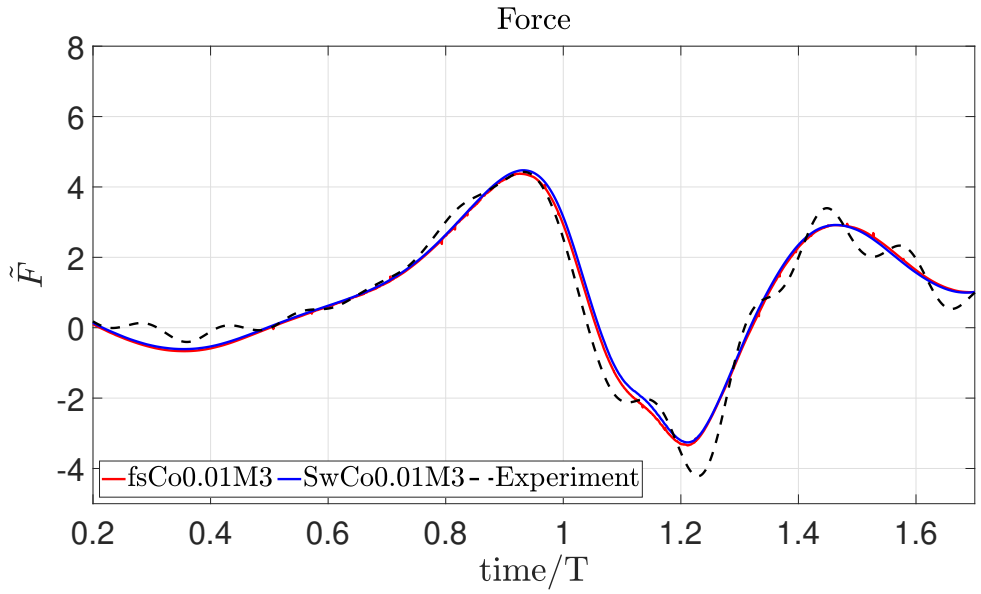


Figure 4.8 – Force recorded for a moving cylinder (Re = 57000) in non breaking focusing waves by the converged mesh simulations (fsCo0.01M3 and SwCo0.01M3) compared with the experimental results

had excellent convergence behaviour and had overall good results. To restate, one of the primary advantages of *foamStarSWENSE* is the explicit treatment of incident waves. As a consequence, even with a coarse mesh in the far-field, accurate incident wave information may be obtained. The correlation amplitudes of M1 clearly show this advantage and are progressing toward an exact solution as they get more refined in timescale. This further supports the claims made in the previous chapter about the SWENSE technique on the benefit of employing coarser cells for wave propagation to lower the computing cost.

- **Pressure:** From the convergence study on the pressure time history computed with the *foamStar* solver (Section A.1.1), M2, M3, and surprisingly even M4 exhibit a proper convergence trend with decreasing Co, and reasonable accuracy. Despite being well-refined in the timestep, M1 has a subpar trend in pressure readings due to the coarser refining near the cylinder. In *foamStarSWENSE* (Section A.1.2), wave run-up observed is not accurate for coarser mesh but improves with spatial and temporal refinement. Temporal refinement does not improve the accuracy in M1, similarly to what was observed with *foamStar*. But unexpectedly, M4 begins with the accuracy of M2 medium temporal refinement but at a low computational cost and then increases to even higher accuracy with temporal refinement. This further demonstrates the advantages of the SWENSE technique, including the need for high refinement around the structure, lower computational costs, and the ability to produce reasonably accurate simulation results.
- **Force:** From the convergence study (Figure A.3 and Figure A.7) for force observation, all the mesh types have good convergence behaviour throughout temporal and spatial refinement in both the *foamStar* and *foamStarSWENSE*. One of the notable accuracy is the force prediction in M4 (no free surface refinement) in *foamStar*, exhibiting an average

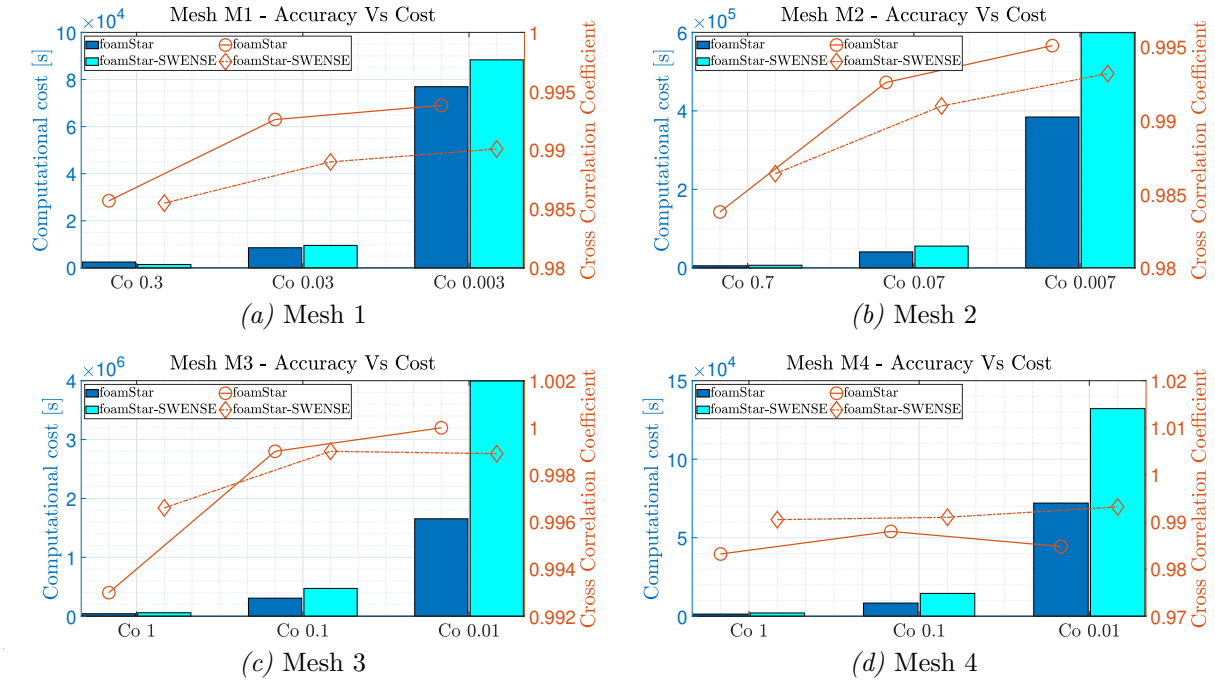


*(a)* Mesh 1 *(b)* Mesh 2

*(c)* Mesh 3 *(d)* Mesh 4

Figure 4.9 – Correlation between different Mesh types M1, M2, M3, and M4 as well as the computational cost by comparing force recorded by the solvers *foamStar* and *foamStarSWENSE* with the experiment

accuracy with very low computational cost, which shows the solver's ability to obtain the rough estimation of force to be expected on the structure in an extreme event as a quick CFD simulation. In the case of *foamStarSWENSE*, mesh M1 accuracy is slightly less accurate than Mesh M2 and M3. The SWENSE advantage mesh M4 predicts the force with accuracy comparable to medium temporal refinement in the M3 type at the lowest cost, and with further refinement, it attains the maximum accuracy at the cost of 100 times less than the finest mesh simulations (M3). Once again, this highlights the value of applying the SWENSE technique to issues of a similar kind to get a reasonable estimate of forces at the minimum cost.

### 4.3.3 Computational efficiency

Figure 4.9 shows the comparison for each mesh type with the cross-correlation coefficient on one vertical axis and the computational cost that was previously determined on the other vertical axis. The bar chart shows the recorded computational cost, and the plotline shows the accuracy in terms of coefficient in each case. The only difference between the fixed cylinder test case and this investigation is that this study's test case was force observations from the numerical model and its comparison among them (Section A.1.1 and Section A.1.2) rather than its comparison with the experiment because the experiment comparison did not have a good trend to investigate the efficiency and cost differences between the solvers. Both the solvers produce results that are largely accurate and error-free. For mesh types M1 and M2, the accuracy of *foamStar* are marginally better than that of the *foamStarSWENSE* solver (because

of the coarser grid around the cylinder). For a similar setup, the computational cost of *foamStarSWENSE* is always 1.1–1.6 times higher than that of *foamStar*. Due to a high refinement around the cylinder, the *foamStarSWENSE* solver's mesh type accuracy is equivalent to that of the *foamStar* solvers, despite having a slightly higher computational cost for the finer mesh M3. The *foamStarSWENSE* prediction performs better than the *foamStar* prediction in M3 at the coarser time step (Co 1). Finally, the *foamStarSWENSE* mesh M4 demonstrates that for a similar setup, *foamStarSWENSE* is more accurate than the *foamStar* solver. It is evident that *foamStarSWENSE* with this configuration requires 100 times less time to estimate results to reach the same accuracy than *foamStar*, despite the computational cost still being higher (check M2 - all Co).

### 4.3.4 Quantitative comparison with experiment

After assessing the convergence properties of the solvers, it is interesting to extend the validation of the *foamStar* and *foamStarSWENSE* by assessing the ratio accuracy/computational cost. This subsection compares all test cases (Table 4.2) with the corresponding experimental results of (Saincher et al., 2022) using cross-correlation analysis. The surface elevation, pressure, and force numerically evaluated with both solvers are cross-correlated with the experimental recordings, and the coefficients are displayed against their computational cost in Figure 4.10. The experiment results are used as the reference results for this comparison, used to validate the numerical results that are shown to converge in previous sections. The experimental time series for surface elevation, pressure, and force measured on the cylinder were already displayed for reference in the prior results and discussion. Figure 4.10 compares the correlation for wave elevation, pressure and force with *foamStar* solver on left side and *foamStarSWENSE* on the right side. None of the results converges towards one showing the uncertainty in comparison with the experiment. Wave and pressure converge towards 0.992 and 0.98, respectively and force towards 0.975.

Cross-correlation for probes WP5-WP7 is conducted with the test case and experiment, and an average of the coefficients are shown as a wave probe mean error in Figures 4.10a and 4.10b. When comparing foamStar and *foamStarSWENSE* with the experiment, there is no significant improvement in wave surface elevation accuracy. The accuracy range is 0.99 to 0.992 and is retained even after refining with spatial and temporal requirements. Even with PP5, accuracy is maintained similarly to surface elevation and ranges from 0.98 to 0.985 for *foamStar* and 0.975 to 0.985 for *foamStarSWENSE*. In contrast, the correlation of the *foamStar* force and the experimental results seems to have a slight convergence behaviour, and the improvement ranges from 0.972 to 0.976. However, the correlation between the *foamStarSWENSE* force and the experimental measurement shows a flattened trend, with similar ranges to those obtained with *foamStar*. The convergence is achieving an asymptotic state with an accuracy range of 0.97-0.98 in all the parameters. The uncertainty between the experiment and the numerical simulation can be attributed to factors such as experimental errors (Sriram et al., 2021a), HOS-generated focusing wave, CFD assumptions (discretization, time scheme, schemes), and the

ability to reproduce the moving cylinder wake, among other factors.

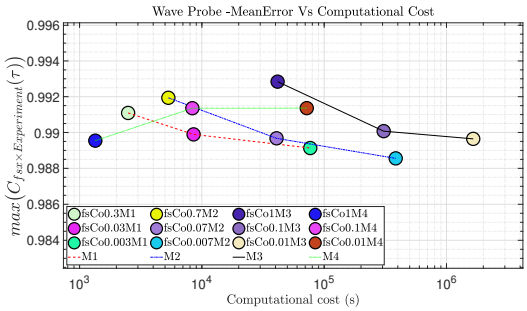


*(a)* Wave elevation correlation - *foamStar*

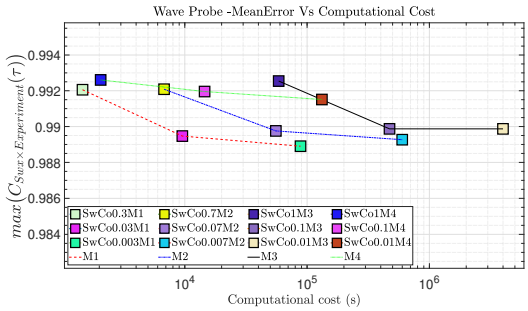


*(b)* Wave elevation correlation - *foamStar-SWENSE*

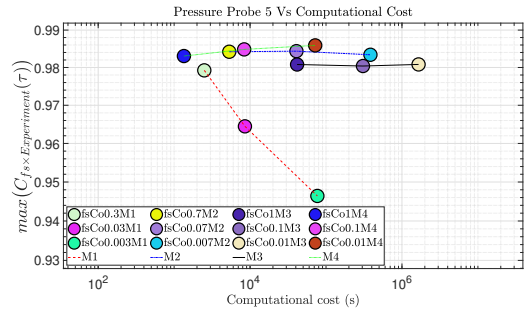


*(c)* Pressure correlation - *foamStar*

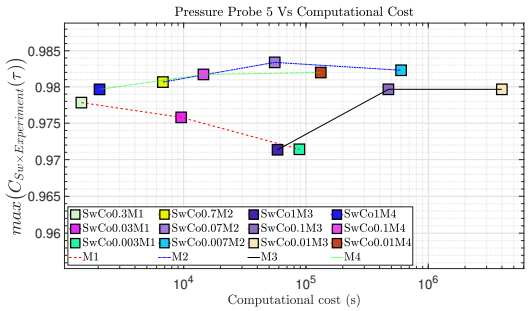


*(d)* Pressure correlation - *foamStar-SWENSE*

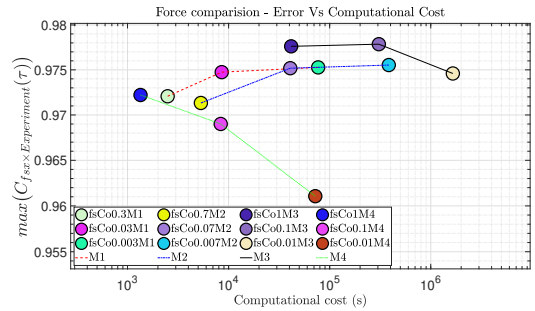


*(e)* Force correlation - *foamStar*

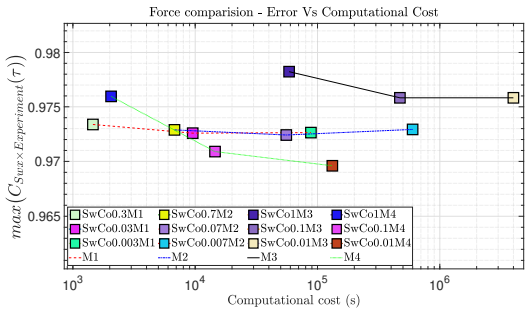


*(f)* Force correlation - *foamStar-SWENSE*

Figure 4.10 – Comparison of correlations between different Mesh types M1, M2, M3 and M4 of *foamStar* (Left) and *foamStarSWENSE*(right) with experimental data. (From top to bottom) Wave elevation, pressure and force

## 4.4 Case 2 : NBR focusing wave interaction with moving cylinder (Re 126000)

With the exception of the cylinder's speed, this section of the chapter deals with a situation that is similar to that of the previous section (Section 4.3). Instead of the 0.33 m.s$^{-1}$ in the preceding section, the cylinder is moving at a speed of 0.75 m.s$^{-1}$ (Re=126000). The convergence study with the Richardson extrapolation technique and its outcome is detailed in Appendix A.2. This section is split into two parts. The first part compares converged mesh simulations (fsCo0.01M3 and SwCo0.01M3) with the experimental results and its qualitative discussion with both *foamStar* and *foamStarSWENSE* solvers. The second part quantitatively compares

different spatial and temporal combinations (Table 4.2) with the experimental results.

### 4.4.1 Validation with finest mesh simulations

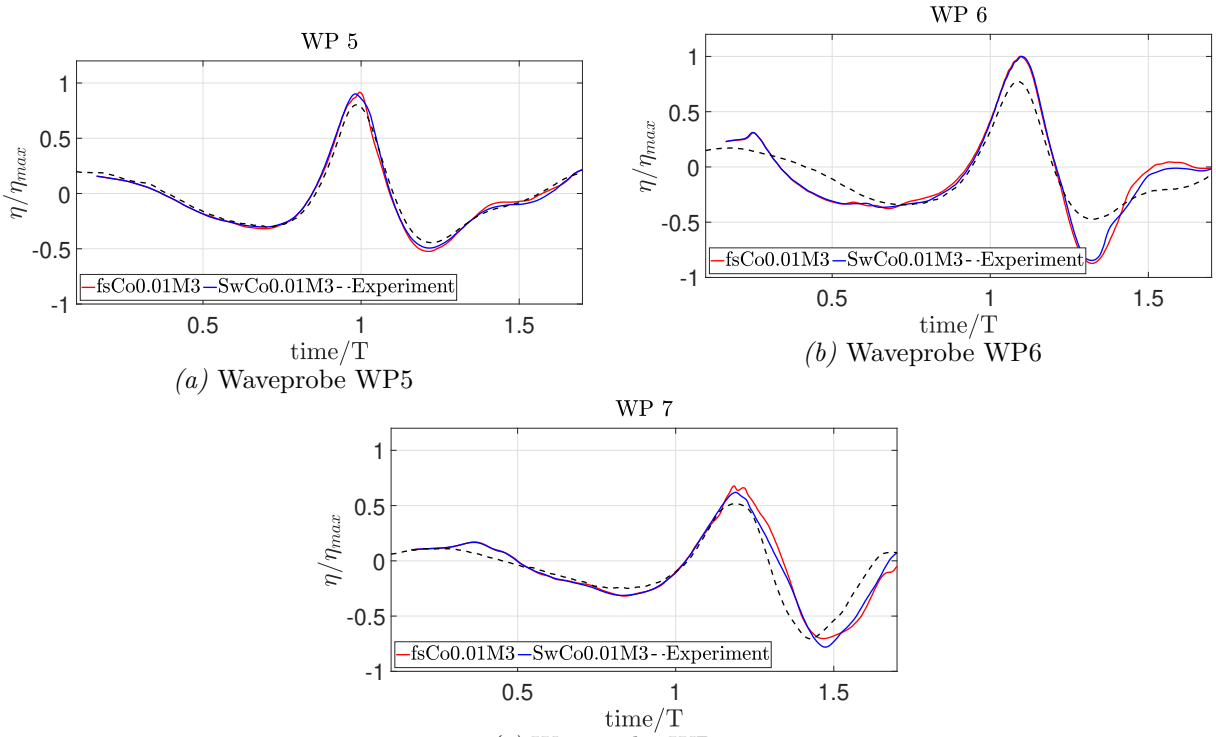


*(a)* Waveprobe WP5

*(b)* Waveprobe WP6

*(c)* Waveprobe WP7

Figure 4.11 – Wave probe comparison of the converged mesh simulations (fsCo0.01M3 and SwCo0.01M3) with the experimental results for both *foamStar* and *foamStarSWENSE* solver for Re 126000

The observations from the numerical probes of the converged mesh simulations (fsCo0.01M3 and SwCo0.01M3) made by the WP5, WP6, and WP7 are shown in Figure 4.11 along with the results of the experiment. The WP5 results, before the focusing wave hitting the cylinder were observed to be similar to each other and to the experiment. The only difference is at the peak amplitudes, numerical results are little higher than the experiment. Probes WP6 and WP7 appear to vary from the experimental observation due to a slight increase in wave amplitude during impact at the crest and trough, as well as a slight change in phase with WP7 in the wake region. This is the maximum accuracy observed for both the solvers since further refining did not improve the results. This is proven in the convergence study for wave probes reported in Appendix A.2.1 and A.2.2.

The next discussion is to compare the numerical dynamic pressure recorded on the cylinder's pressure probes (probe locations: Figure 4.2) for the converged mesh simulations (fsCo0.01M3 and SwCo0.01M3) with the experiment as displayed in Figure 4.12. Nearly all test cases for the pressure probes PP2-PP8 showed satisfactory agreement with the experimental observations. Both before and after the focusing event, the submerged pressure probes PP2 and PP3, air probe PP4, and free surface probe PP6, where the separation begins, displayed a better com-

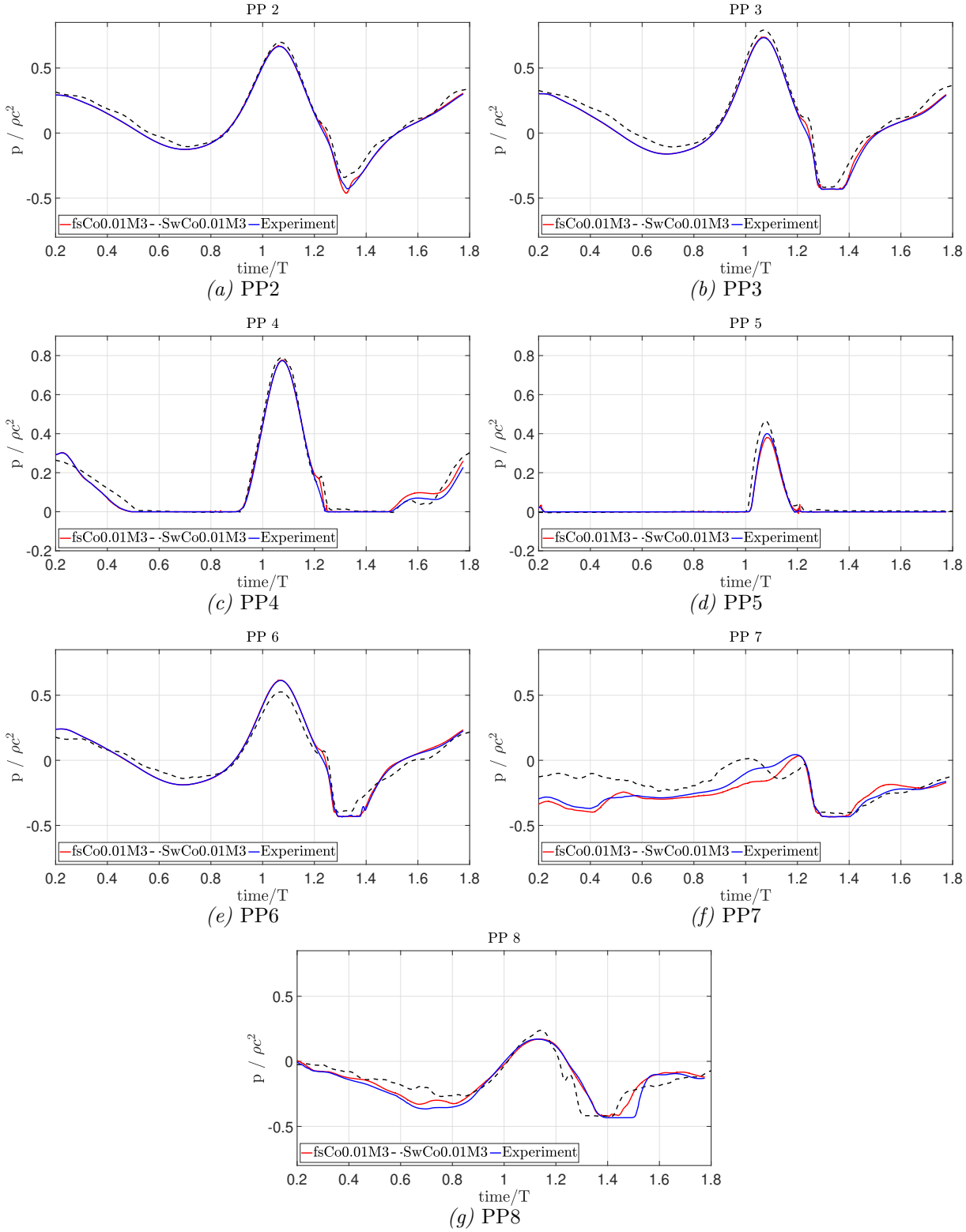


*(a)* PP2 *(b)* PP3 *(c)* PP4 *(d)* PP5 *(e)* PP6 *(f)* PP7 *(g)* PP8

Figure 4.12 – Pressure time history of the moving cylinder (0.75 m.s$^{-1}$) by the converged mesh simulations (fsCo0.01M3 and SwCo0.01M3) with the experimental results for both *foamStar* and *foamStarSWENSE* solver

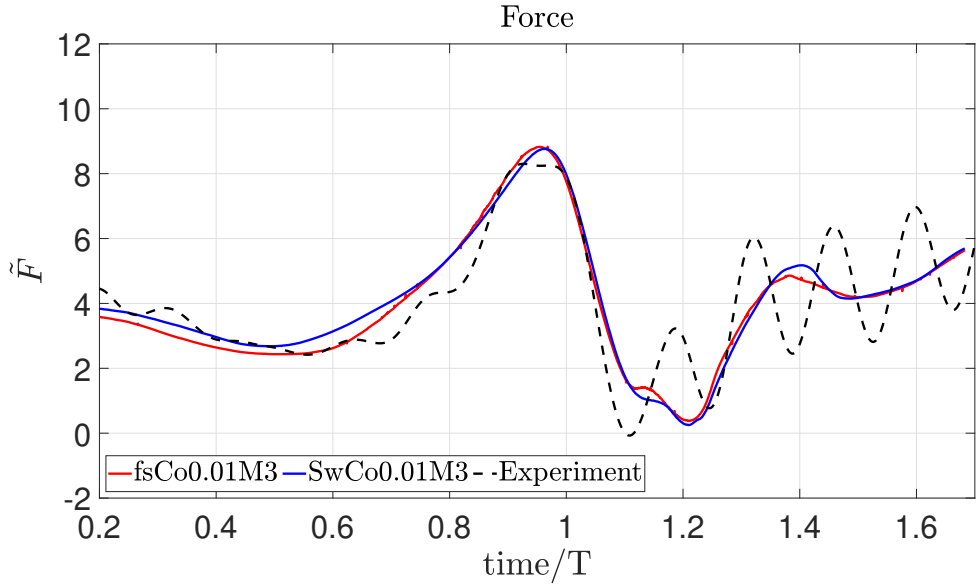


Figure 4.13 – Force recorded for a moving cylinder(0.75 m.s$^{-1}$) by the converged mesh simulations (fsCo0.01M3 and SwCo0.01M3) with the experimental results for both *foamStar* and *foamStarSWENSE* solver

parison with the experiment than other probes. The PP5 pressure probe which is above the free surface requires a good wave runup to have proper pressure observation. This probe demonstrated a similar discrepancy to earlier validation. The new observation in this study is that the pressure measurements made by the probes PP7 and PP8, located in the cylinder's wake, differ between mesh types and from the experimental results, as indicated by the comparison of wave probes WP6 and WP7. However, further refinement on spatial and temporal refinement did not improve the results, as proved in figures, Figure A.10 and Figure A.14. It is concluded that improvement/validation is still needed in this case study to accurately capture the wake region of this complex nature if the interest of observation is in the flow field.

Figure 4.13 shows the unidirectional forces observed when a NBR focusing wave hits a cylinder moving at a speed of 0.75 m.s$^{-1}$(Re=126000) for the converged mesh simulations (fsCo0.01M3 and SwCo0.01M3) with the experimental results. The simulated forces are normalized with the factor $\rho g r^3$, where $r$ represents the radius of the cylinder. Both the mesh types are able to reproduce the force observed by the experiment with only a few minimal differences. After the wave hits the cylinder in the experimental observation, the cylinder encounters a ringing phenomenon that is ignored in the numerical simulations due to the assumption that the solid body is rigid.

### 4.4.2 Learning's from the convergence study (Section A.2.1 and Section A.2.2)

The wave height at three wave probes, the pressure at multiple points, and the total force on the cylinder are all used in the convergence study described in APPENDIX Section A.2.1 and Section A.2.2. The study's findings are briefly recalled here for both the solvers.

■ **Surface elevation:** Compared to the preceding case (Re 55000), when wave probe ac-

curacy (Figure A.1 and Figure A.5) was in the excellent range, discrepancy in accuracy is seen among all mesh types for both the *foamStar* and *foamStarSWENSE* solvers in this case. In *foamStar* test cases (Figure A.9), only for mesh type M3, as opposed to almost flat curves for M1 and M2, appears to have a convergence behaviour with temporal refinement found. Also, because of the DD coupling, mesh type M1 with very coarse free surface refinement and coarser time steps can achieve satisfactory accuracy with minimum computational cost. The accuracy of all mesh types in the *foamStarSWENSE* solver (Figure A.13) has a strong convergence behaviour with good accuracy compared to the *foamStar* solver's finest mesh. Only M4 is less accurate than other mesh types in terms of accuracy, and even then, its accuracy was comparable to M3's medium temporal refinement. After additional refinement, the correlation amplitudes of M1 approached almost one, confirming the SWENSE advantage again.

- **Pressure:** For the *foamStar* evaluation, the Cross-Correlation between the various mesh types and the finest mesh, fsCo0.01M3, demonstrated good convergence behaviour with decent accurate. Except for M1, where a negative convergence is seen, mesh types M2 and M3 displayed a good convergence with temporal refinement. Because of its higher refinement close to the cylinder, the mesh M4 type also gains good accuracy. Even the *foamStarSWENSE* test cases demonstrated good convergence behaviour for all the mesh types. The M4 (no free surface refinement) and M1 have an accuracy range similar to M2 and M3 medium temporal refinement but at a computational cost of 100 to 1000 times less than the finer meshes (M3) requirement.
- **Force:** As shown in Figure A.11 and Figure A.15, this is the most accurate solution that can be obtained by refining the spatial and temporal requirements. One of the primary conclusions of this study is that, in the case of *foamStar*, even the M4 mesh type offers excellent accuracy with a refined time step when the study's target is the force over the moving cylinder. The coarser and medium mesh types (M1 and M2) exhibit a little amplitude fluctuation at the focusing event in the case of *foamStarSWENSE* for different mesh types, whereas M3 and M4 (no free surface refinement) match the experimental force observations exact. The accuracy of mesh type M4, with all coarse mesh and only refinement near the cylinder, was comparable to M3's best refinement (at 100 to 1000 times reduced computational time), complementing prior wave and pressure observations. Overall this again emphasizes the benefit of using the SWENSE approach to solve similar problems to obtain a good estimate of forces at the highest accuracy with the lowest cost.

### 4.4.3 Computational efficiency

Figure 4.14 shows the comparison for each mesh type with the cross-correlation coefficient on one vertical axis and the computational cost on the other vertical axis for the case of Re 126000. The bar chart shows the recorded computational cost, and the plotline shows the accuracy in terms of coefficient in each case. In this investigation, all the test cases force observations from the numerical model cross-correlated with fsCo0.01M3 is presented to investigate the efficiency

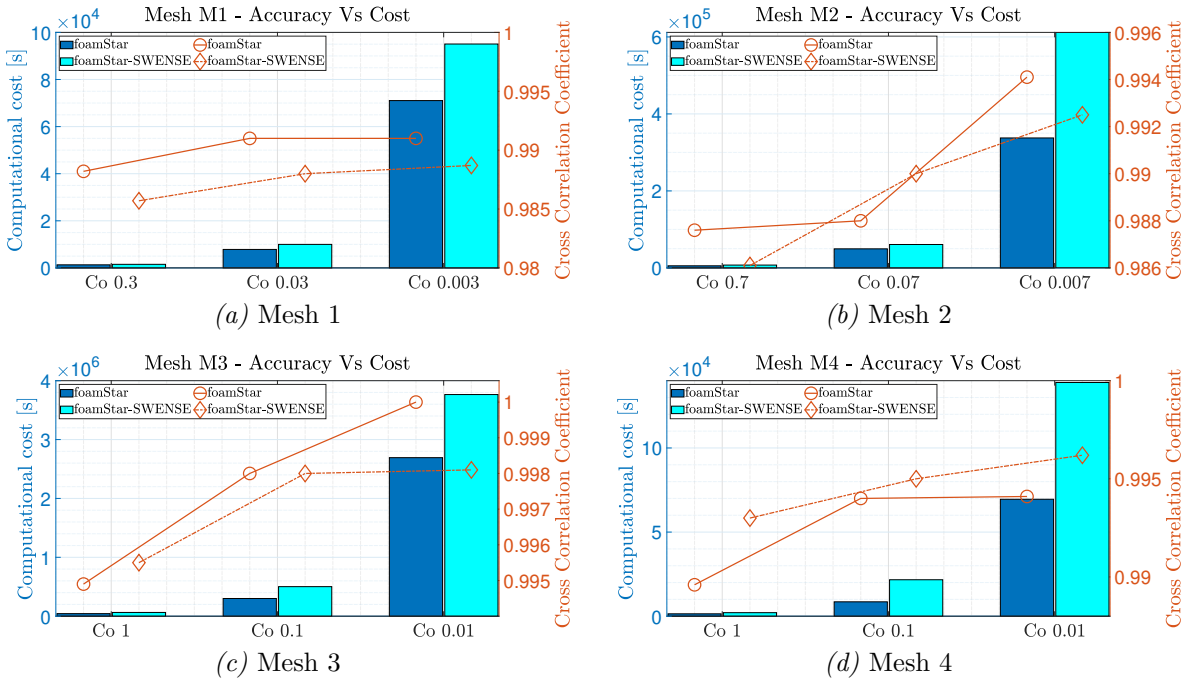


*(a)* Mesh 1 *(b)* Mesh 2

*(c)* Mesh 3 *(d)* Mesh 4

Figure 4.14 – Correlation between different Mesh types M1, M2, M3, and M4 as well as the computational cost by comparing force recorded by the solvers *foamStar* and *foamStarSWENSE* with the experiment

and cost differences between the solvers (Similar to Section 4.3.3). This validation pattern is comparable to the fixed-cylinder and moving-cylinder-first cases (Re 57000). For mesh types M1, M2 and M3, the accuracy of *foamStar* is marginally better than that of the *foamStarSWENSE* solver (because of the coarser grid around the cylinder). For a similar setup, the computational cost of *foamStarSWENSE* is always 1.1–1.6 times higher than that of *foamStar*. Due to a higher level of refinement around the cylinder, the *foamStarSWENSE* solution's accuracy is equivalent to that of the *foamStar* solver despite having a slightly higher computational cost for the finer mesh M3. Finally, the *foamStarSWENSE* mesh M4 demonstrates that for a similar setup, *foamStarSWENSE* is more accurate than the *foamStar* solver. It is evident that *foamStarSWENSE* with this configuration requires ten to hundred times less time to estimate results to reach the same accuracy than *foamStar*, despite the higher computational cost (check M2, M3 - all Co). Only for M4, *foamStarSWENSE* trend is more accurate than *foamStar*; otherwise, *foamStar* solution shows to be accurate and cost-effective.

### 4.4.4 Quantitative comparison with experiment

This subsection uses cross-correlation analysis to compare all numerical test cases with the experiment to validate the *foamStar* and *foamStarSWENSE* solvers. Surface elevation, pressure, and force from all the test cases (of both solvers) are cross-correlated with the experiment, and the coefficients are displayed against their computational cost in Figure 4.15. In this section, the experiment results are used as the reference results for the analysis. In the earlier results and discussion, the experimental time series for surface elevation, pressure, and force measured

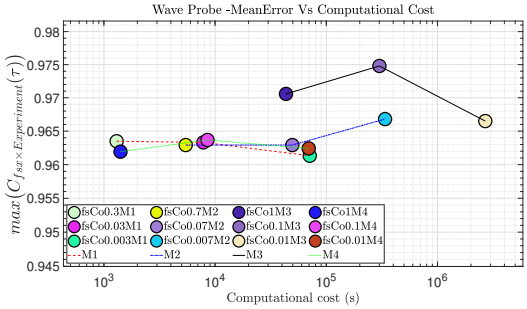


*(a)* Wave elevation correlation - *foamStar*

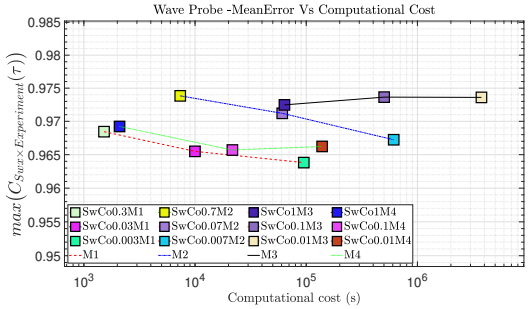


*(b)* Wave elevation correlation - *foamStar-SWENSE*

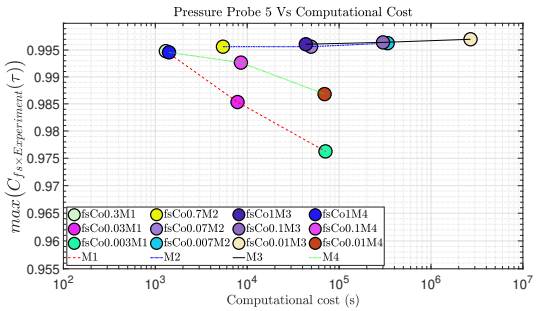


*(c)* Pressure correlation - *foamStar*

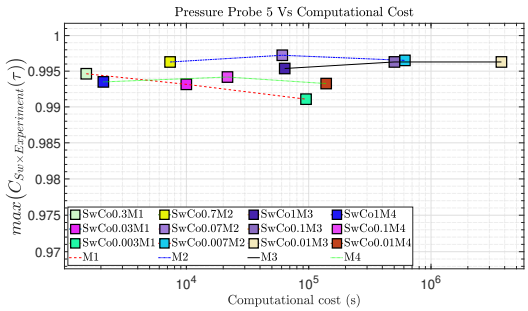


*(d)* Pressure correlation - *foamStar-SWENSE*

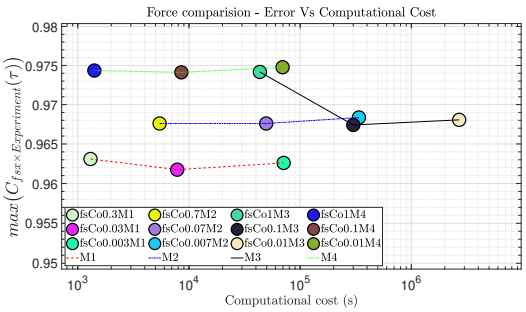


*(e)* Force correlation - *foamStar*

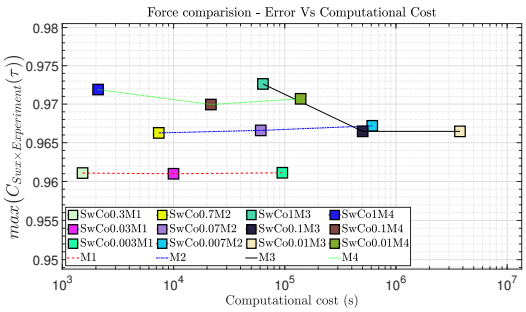


*(f)* Force correlation - *foamStar-SWENSE*

Figure 4.15 – Comparison of correlations between different Mesh types M1, M2, M3 and M4 of *foamStar* (Left) and *foamStarSWENSE*(right) with experimental data. (From top to bottom) Wave elevation, pressure and force

on the moving cylinder were already shown for reference. Figure 4.15 compares the correlation for wave elevation, pressure and force with *foamStar* solver on left side and *foamStarSWENSE* on the right side. None of the test cases where the coefficient was close to one which confirmed uncertainty between the experiment and the numerical results. However, all the coefficient value is still higher than 0.95, demonstrating the numerical results minimum guarantee of the pattern with the experiment. Cross-correlation for probes WP5-WP7 is conducted with the test case and experiment, and an average of the coefficient is shown as a wave probe mean error in Figures 4.15a and 4.15b. Due to the small difference in the peak amplitudes of the crest and trough and the phase shift in the wake region, the wave converges around 0.965 in both solvers (0.992 in the Re=57000 scenario). When comparing *foamStar* and *foamStarSWENSE* with the experiment, there is only marginal improvement in wave surface elevation accuracy (0.965 to 0.97). Surprisingly, PP5 shows a good wave run-up, and the accuracy ranges for M2 and M3 in

the *foamStar* solver are 0.99 to 0.995, but for all mesh types in the *foamStarSWENSE* solver, they are 0.99 to 0.995. *foamStar* solver loses its accuracy with M1 and M2, but the loss is not seen in the *foamStarSWENSE* solver showing its efficiency. In contrast, force seems to have slight convergence behaviour with the experimental results in *foamStar* and *foamStarSWENSE* cases, and the improvement ranges from 0.96 to 0.975. The numerical model is achieving an asymptotic state rather than perfectly matching the experiment with overall accuracy range of 0.96-0.98 in all the parameters. As stated in the previous validation study, the uncertainty between the experiment and numerical simulation can be attributed to factors such as experimental errors (Sriram et al., 2021a), HOS-generated focusing wave, CFD assumptions (discretization, time scheme, schemes), and ability to reproduce moving cylinder wake, among other factors.

## 4.5 Closure discussion

This chapter addresses the use of *foamStar* and *foamStarSWENSE*, a DD-based and a FD-based numerical solver respectively, to the problem of focused waves interacting with a moving cylinder. The two moving speeds (0.33 m.s$^{-1}$and 0.75 m.s$^{-1}$) under investigation have been studied in model test experiments, which are used as validation references. The parametric studies, such as HOS focused wave generation and the need for spatial and temporal resolution in solvers are identical to those in the preceding chapter and are not reported in this chapter. There are two sections to the chapter. The moving cylinder at 0.33 m.s$^{-1}$and its interaction with the focusing wave are described in the first section using the solvers *foamStar* and *foamStarSWENSE*. The second section is identical to the previous section, but the moving cylinder speed is 0.75 m.s$^{-1}$. The following observations are drawn from the investigation:

- The numerical solvers *foamStar* and *foamStarSWENSE* are adequately met for validating the interaction of a moving cylinder with focused waves. Both solvers performed well and efficiently enough to capture the trend with respect to the experimental results, even with the coarsest mesh. However, there are certain discrepancies in the results for coarse discretization, which have been eliminated by refining the mesh.
- For such temporal situations where the solutions do not approach the experimental results, the Richardson extrapolation method is used to measure the extrapolated solution between the mesh types and promptly calculate the asymptotic accuracy.
- In capturing free-surface variations around the moving cylinder, the solvers are observed to achieve good agreement against experiments for low towing speed. At high towing speed, additional complications arise, such as bulging of water in front of the cylinder and strong 3D deformations of the waves in the cylinder wake. These phenomena are proved challenging in both the solvers, as shown in WP6 and WP7 observations.
- The dynamic pressure is measured by seven pressure probes (PPx) for this interaction investigation (Figures 4.7,4.12. Four pressure probes are in the free surface line encircling half the cylinder, two are slightly above the free surface (air probes), and two are submerged. Both solvers fully reflect the submerged pressure observation (PP2, PP3) in both cases.

There are discrepancies in air probes (PP4, PP5) that are notably noticeable in PP5's pressure capture. This is a sensitive probe because a correct wave run-up is required to record the pressure; therefore, a cross-correlation study of this pressure trend is discussed in detail. For a cylinder moving at a slow speed (0.33 $m.s^{-1}$), pressure probes in the wake regions (PP7, PP8) are well captured by solvers. However, an accurate evaluation of the dynamic pressure at the separation (PP7) and rear stagnation points (PP8) at high towing speed is also demonstrated to be highly challenging. Despite, the overall difference is not too high and the trend is well represented.

- Such an experiment or model study's primary goal is to investigate the force acting on the structure precisely. In this case, both solvers for various mesh types are employed to validate the experiment's force measurement at the time of focused wave impact on the cylinder. Surprisingly, it has been verified that all test case results (even those for the coarsest combinations) provide accurate measurements of forces. With coupling, both solvers can be used to get accurate answers at a reasonable computational cost.
- For the similar problem, the *foamStarSWENSE* solver incurs an average of 1.1–1.6 times higher computational costs than the *foamStar* solver. This is similar conclusion observed in the fixed cylinder interaction study. *foamStar* solver is typically more accurate than *foamStarSWESNE* solver for analysis based on mesh types M1 and M2. For M3, both solvers have yielded results that are pretty close. However, due to its coupling, the *foamStarSWESNE* solver performs better with M4. The overall conclusion from this study is to use M4 for a preliminary estimation of any parameters study, such as forces and pressure over the structure in *foamStarSWENSE*, to spend as little time and cost on computation as possible. However, M3 in the *foamStar* solver demonstrated highly accurate results, producing a converged solution in all the parameters studied in both the validation studies.

Chapter 5

# WAVE-STRUCTURE INTERACTION OF MOORED OC3 HYWIND SPAR

## 5.1 Introduction

Floating Offshore Wind Turbine (FOWT) technology is a new trend that allows wind turbines to be installed in larger, deeper offshore locations for increased wind potential. Typical representations of the world's first commercial floating offshore wind farm Hywind and the first French offshore wind turbine, FLOATGEN, are given in Figure 5.1. The accurate prediction of floater behaviour in such a dynamic environment is still challenging (Pinguet, 2021; Huang et al., 2021; Zhang and Kim, 2018). The model testing directly compares to physical reality within the limitations of experimental uncertainty and wave tank constraints. However, it is rarely possible to employ a real-scale test model and accurately calculate critical loads for the complex multi-physics problem. There is a restriction in choosing the scaling factors based on the experimental facilities available in model testing (Aliyar et al., 2021). These scaling effects cannot be ignored in predicting the elemental forces acting over the substructure of wind turbine models (Make, 2014). Also, moored FOWT experimental models add multiple uncertainties like the shifts in the equilibrium position, mooring dynamics, and motion effects which are difficult to control during the experiment for the exact representation of the prototype. On the other hand, numerical techniques without scaling limitations may improve model reliability by lowering uncertainties. Some articles portray the robustness of hybrid coupling numerical solvers (DD and FD) for coastal engineering applications (Lachaume et al., 2003a; Biausser et al., 2004; Sriram et al., 2014a) and bottom-fixed support structures (Hildebrandt et al., 2013a; Paulsen et al., 2014b; Li et al., 2021a; Sriram et al., 2021c; Agarwal et al., 2021a). The extension to the floating structures is the recent research interest inside the offshore wind and ocean engineering communities (Xu et al., 2021; Li and Bachynski, 2021). Several studies have used CFD to model the behaviour of floating structures with a single or multiple degrees of freedom (DoF) (Elhanafi et al., 2017; Simonsen et al., 2013; Dunbar et al., 2015). Assessing moored floating structures necessitates a multidisciplinary approach that includes hydrodynamics, floating body dynamics, mooring, and their interaction. However, there are only a few papers in which CFD-based NWT is used in conjunction with the mooring library to solve mooring line tensions (Nematbakhsh et al., 2015; Benitz et al., 2015; Palm et al., 2016; Jiang et al., 2021; Lee et al., 2021). In addition, most of the research has used a floating box, buoy, or cylinder as a floating structure for validation, and there is a lack of validation for real geometry of floating substructures like SPAR

*(a)* FLOATGEN - Barge Type FOWT

*(b)* Hywind - SPAR Type FOWT

Figure 5.1 – Typical overview of installed FOWT wind farms (Figures taken from official website of each wind turbine)

(Single Point Anchor Reservoir (SPAR)), TLP (Tension Leg Platform) or Semi-submersible for industrial applicability.

This chapter aims to validate a static and dynamic mooring model (MoorDyn (Hall, 2015)) implemented in the *foamStar* and *foamStarSWENSE*, for a fully coupled analysis of moored floating structures replicating the model test in NWT. The static mooring model (Section 2.1.4.3.1) will generate the mooring force based on the displacement in terms of global mooring stiffness coefficients. MoorDyn is a lumped mass based dynamic mooring model (Section 2.1.4.3.3), that has been associated with a potential flow solver and successfully validated against measurements in a wave tank (Hall and Goupee, 2015). The equation governing dynamics of mooring lines is coupled to the six DoF nonlinear rigid body motions equations in *foamStar* and *foamStarSWENSE* (Section 2.2.5). MoorDyn calculates the tensions of the mooring lines, which are added as an external force to compute the resulting response and motion of the moored floating structures. Based on the author's knowledge, there are publications (Lee et al., 2021; Chen and Hall, 2022) about OpenFOAM and MoorDyn coupling that has been published and some publications about coupling CFD with mooring (Huang et al., 2022; Jiang et al., 2020; Palm et al., 2016) available in the literature. Most articles validate simple shape models (box, buoy) and simple mooring setup (catenary) in regular waves. Few articles (Jiang et al., 2020) addressed irregular waves, but the results are not well compared with the experiment. The validation of this coupling (HOS-*foamStar*/*foamStarSWENSE*-MoorDyn) for complex floater shape (SPAR) with a complex mooring system (delta type) in regular and irregular waves with the experimental results, which is rarely addressed in the literature, is the novelty claimed in the present work.

### 5.1.1 Outline and scope of this chapter

The scope of this chapter is to evaluate *foamStar* and *foamStarSWENSE* in conjunction with a mechanical solver developed to simulate the 6 DoF dynamics of rigid floating bodies and

to investigate the floating body's interaction with waves as well as its mooring behaviour. The validation of the two-way coupling between the *foamStar/foamStarSWENSE* and MoorDyn is carried out with the experimental results on a floating SPAR with a delta mooring system. The moored decay tests are examined to ensure the computational model performance compared to the experimental model in terms of its natural period, mooring tension, and damping properties. In the subsequent investigation, the SPAR is subjected to both regular and irregular waves, and simulations and experimental data are compared to confirm that the developed coupled model can accurately estimate body motions and mooring line tensions.

This chapter covers the following topics:

— Experiment model and details from (Arnal, 2020)

— Body mesh generation and its influence over the motion of the floater

— Hydrostatics analysis to verify the draft and stability properties

— Free decay analysis in heave, pitch and surge to evaluate the damping and natural period in different degree of freedom

— SPAR model interaction with regular waves and its validation (in *foamStar*)

— SPAR model interaction with irregular waves and its validation (in *foamStar* and *foamStarSWENSE*)

— Salient conclusions

The first step toward a complete simulation of FOWT has been taken with the development of the hybrid numerical coupled model. We simulate the hydrodynamics of the FOWT substructure in the present research, which is interdisciplinary and demands a thorough understanding of different domains. The present work considerably used many contributions from the scientific community about existing methodology or numerical models. The essential aspects of the associated theories are given in the Chapter 2 and references are provided for more information.

## 5.2 Experimental methodology

Arnal (2020) carried out the design and validation of an experiment to model rotor loads along with FOWT wave tank testing. The main elements extracted from Arnal (2020) and used for setting up the simulations are given in this section. The SOFTWIND SPAR was designed to get the representative behavior of a 10MW floating wind turbine at a scale of 1:40. As indicated in Figures 5.2, 5.3, the main components involved in the model testing were :

- The SPAR floater
- Three chains and a delta connection for the mooring lines
- The tower with its casing for transporting the RNA cables
- Wave probes to measure free surface elevations
- The wave tank itself, dimensions (50 m x 30 m x 5 m) for the length, width, and depth. 48 hinged-flap wavemakers generate the waves.

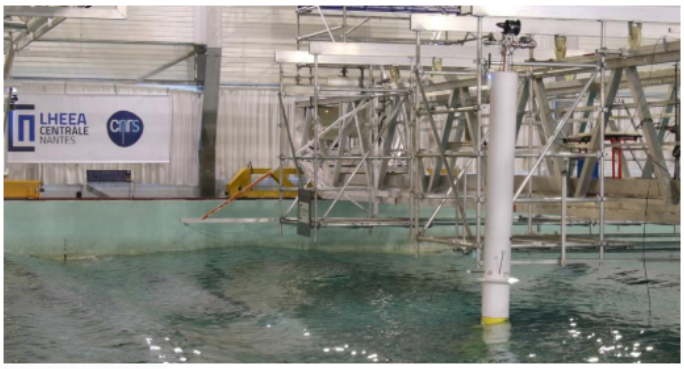


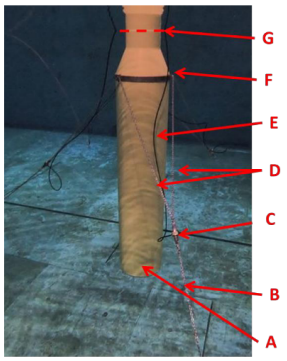


Figure 5.2 – (*Left*) Typical experimental set up in ECN wave basin, (*Right*) Underwater picture of the floater with its mooring system in the wave tank, (Arnal, 2020), A: SPAR, B: Bottom chain, C: Mooring tension sensor, D: Bridles, E: Mooring sensor cable; F: Fairlead, G: Free surface

■ An absorbing beach to limit the reflection

The wavemakers can generate regular waves up to 1 m height and irregular waves up to 0.8 m height. The experiment's goal is to see how the wind turbine controllers affect the global motions of the FOWT. The experimental model tests cover various wave cases in regular and irregular cases. Four wave test cases are investigated for the numerical investigation of SPAR interaction, as indicated in Table 5.2. Regular waves are represented by LC 1, while irregular waves are represented by LC 2 (generated based on the Bretschneider spectrum). The chosen cases in Table 5.2 are based on the number of cases attempted in the experiment, which is likewise investigated with and without wind factors. In the present cases, LC 1.1 represents a severe situation in regular waves, while LC 1.2 represents a normal sea state. For irregular sea states, LC 2.1 and LC 2.2 can be portrayed as normal and severe sea states, respectively. The experiment's general layout is shown in the Figure 5.3. Eight wave probes were used to measure the temporal free surface elevations. Two wave probes, WG1 and WG2, are set 15 m and 17 m from the paddle, respectively, near the sidewall. Wave probes WG3 to WG8 are spaced 15 cm apart at a lateral distance of 7.5 m from the SPAR. The motions were measured using a MOCAP system based on a Qualisys environment that included multiple cameras, reflecting markers, and QTM software for real-time processing. The processing software takes the 3D positions of various markers as input, smooths them out, and then computes the body's 6 DoF positions. The wave elevation data were collected at a sample rate of 100 Hz, and 6-DoF motions are sampled at the rate of 200 Hz.

The SPAR was chosen as a floater with proportions based on the existing OC3 Hywind SPAR platform (Jonkman, 2010) and *Hywind Scotland* as a reference system. The SPAR is made up of two parts: an aluminum shell that gives the floater its outward shape, and a ballast, battery, controller, power units, suspended wires, and other components that make up the floater's core. A vertically truncated cylinder with the taper and transition piece to the tower forms the SPAR floater. The primary dimensions and mass attributes have been summarized in Table 5.1. The three mooring cables were catenary chains positioned symmetrically 120° apart. The main

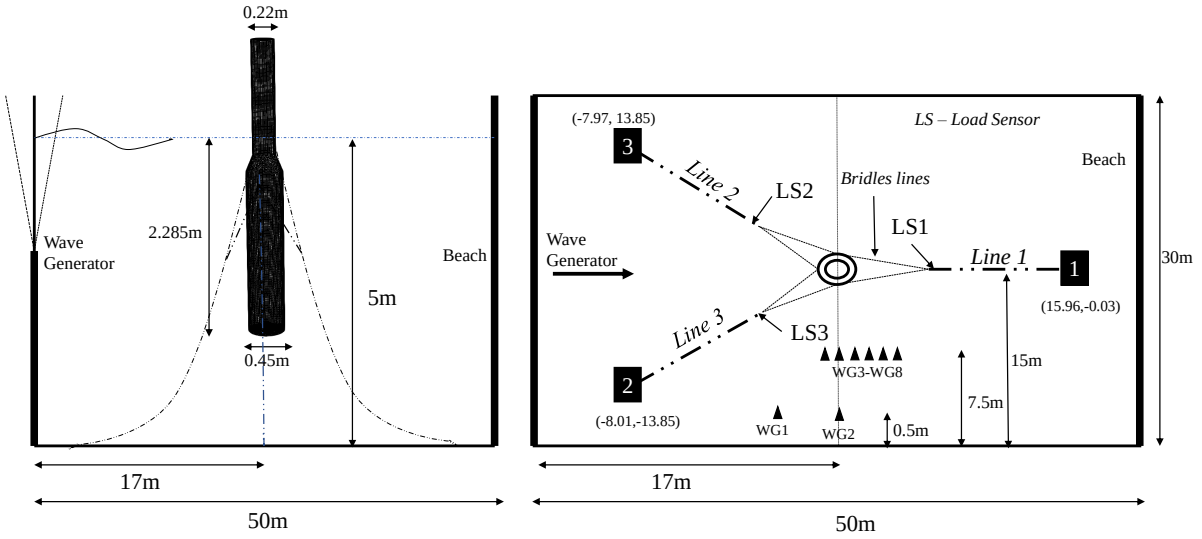


Figure 5.3 – The general layout of the experiment in side and top view with the mooring cable configuration, (Arnal, 2020). Figures are not drawn to scale. WG - Wave

mooring line was fastened to the bottom of the wave tank and connected to two "bridles", which are part of the delta connection on each cable. The attachment points for moorings were 0.335 m below the waterline. Figure 5.3 shows the various pieces that make up the mooring model. The underwater unidirectional load cells (LS1, LS2, and LS3) connect the bottom chains to the bridles and are used to measure the mooring tension. Studless stainless steel chains were chosen in order to preserve the chain's mass properties and geometry. Model scale mooring properties are shown in Table 5.1. The following are the different tests performed during experiment:

- Without waves or wind
  - Decay tests
  - Hammer tests
  - Pull-out tests
- Regular and Irregular waves without wind
- Regular and Irregular waves with wind

The upper part of the model, which includes aerodynamics components (actuator assemblies, nacelles, etc.), is not included in this study (mass properties are considered) because the main focus of this research is on the hydrodynamics of the system. More details about these aspects can be found in Arnal (2020).

| ***Parameter*** | ***Units*** | ***Value*** |
|---|---|---|
| SPAR Mass (including floater, tower and RNA) | kg | 329.4 |
| Centre of Gravity with respect to Inertial Frame | m | $-0.004, 0, -1.535$ |
| Mass Moment of Inertia with respect of CoG FOWT $(I_{xx}, I_{yy}, I_{zz})$ | kg m$^2$ | $490, 490, 10$ |
| Diameter of floater (SPAR) | m | 0.45 |
| Diameter at MSL (after tapering) | m | 0.28 |
| Taper height | m | 0.2 |
| Draft of the SPAR | m | 2.285 |
| Mooring (Delta or Crow foot mooring) | | |
| Anchors depth | m | 5 |
| Chain diameter | mm | 3.7 |
| Mass of chain in air | kg/m | 0.275 |
| Fairlead depth | m | $-0.335$ |
| Bridle chain length | m | 1.2 |
| Bottom chain length (Line 1, Line 2 , Line 3) | m | $15.69, 15.74, 15.72$ |
| Mass of load cell in water (Clumped mass) | kg | 0.43 |

Table 5.1 – Mass and dimensional properties of the SPAR with its mooring parameters

| Parameters | Value | | | |
|---|---|---|---|---|
| | LC 1.1 | LC 1.2 | LC 2.1 | LC 2.2 |
| Wave period ($T$ or $T_p$) [s] | 1.9 | 1.58 | 1.72 | 2.37 |
| Wave height ($H$ or $H_s$) [m] | 0.187 | 0.132 | 0.145 | 0.273 |

Table 5.2 – Progressive wave test case: wave parameters with LC 1 represents regular waves and LC2 represents irregular waves

## 5.3 Numerical setup

In Inertial reference frame $R_0$, HOS-NWT, has its origins in the NWT left corner at the still water level (SWL) and in $R_b$, *foamStar* and *foamStarSWENSE* has its origin at the body's center of gravity. MoorDyn has its origins in an inertial frame of reference ($R_0$) at the SWL in the center of the *foamStar*/*foamStarSWENSE* domain (For more details on reference frames refer Section 2.1.4.1. The generation of the regular waves is achieved by using the stream function wave theory (Section 2.1.3.2) and the computational domain is similar to the *foamStar*/*foamStarSWENSE* domain shown in the Figure 5.4. For irregular waves, a digital twin facility based on HOS-NWT is used. The HOS computational domain reproduces the experimental set-up but without the structure. The wave generated has been transferred into the *foamStar* domain only through the inlet relaxation zone, and in general, all relaxation zones can suppress the waves generated from inside the viscous domain. The *foamStar*/*foamStarSWENSE* domain is solely confined near the SPAR region, which is 6 times the diameter of the SPAR (excluding RZ) and was determined based on the expected motions of the SPAR in 6 DoF from the experiment. The length of the relaxation zones is one wavelength for inlet and outlet and half of the wavelength for side zones decided based on the numerical tests. The numerical domain water depth of 5 m has been maintained in HOS and *foamStar* as similar to that of the experiment. This research aims to

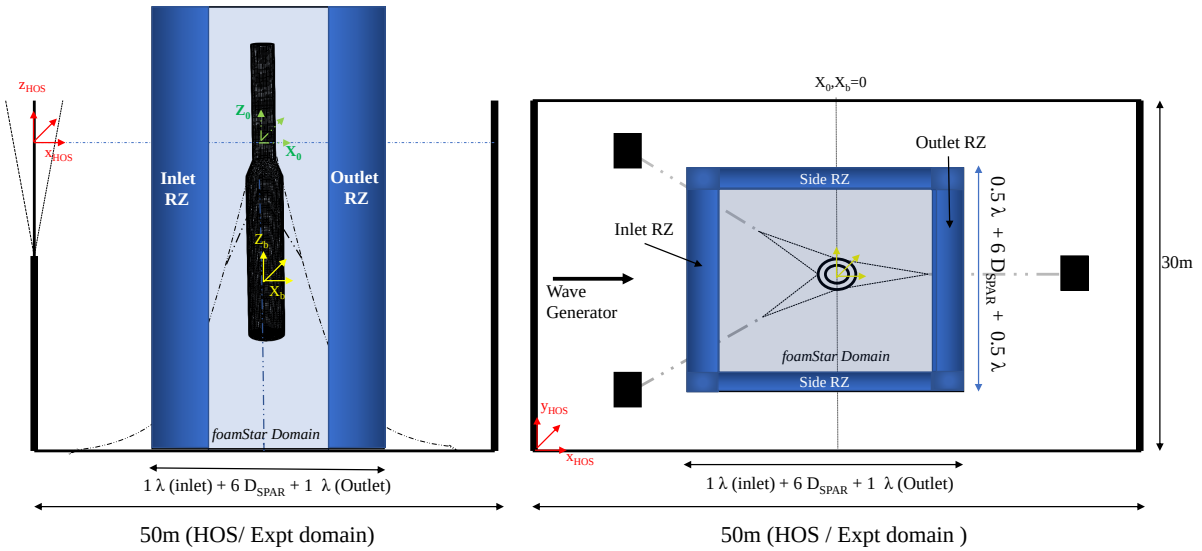


Figure 5.4 – Schematics of the computational domain within the HOS domain with Relaxation zones (RZ) are represented in terms of wavelength ($\lambda$). $R_0$ represents the inertial reference frame, and $R_b$ represents the body reference frame. HOS is based on $R_0$, but its origin is different

evaluate the moored floating SPAR's hydrodynamics. Therefore, rotor-nacelle (RNA) assembly in the upper tower is not considered in modelling or analysis. However, while considering the total mass characteristics of FOWT, the mass, inertia, and COG of the ignored parts are also taken into account. The tower's freeboard has been kept at 1.2 m to appropriately capture the wave run-up during the wave interaction.

### 5.3.1 Solver settings

The Courant-Friedrich-Levy number (Co) is often used in CFD solvers for temporal discretization and it indicates that the how much information (U) travels across a computational grid cell during the unit timestep. If the Courant number is more than one, the information propagates through more than one grid cell at each time step, causing the solution to be inaccurate and potentially resulting in nonphysical results. For adequate resolution and capture of the transient flow field in ocean wave modeling, relatively small Co numbers are necessary. The key advantage of the interFoam solver's PIMPLE algorithm is the possibility to use large Co numbers. When smaller Co numbers are necessary to accurately capture minor variations in the fluid, then the benefit becomes less meaningful. In the present study, the maximum Co number of 0.5 was adopted along with 10 outer (SIMPLE) pressure-momentum corrections, 3 inner (PISO) pressure correction loops have been adopted. The adopted residuals limit in the present study was $10^{-8}$ for all simulations. Table 5.3 summarises the methods of discretization schemes in space and time used in the present study.

| Term | Scheme | Order |
|---|---|---|
| Gradient | Gauss linear | Second |
| Divergence | Gauss vanLeer | Second |
| Laplacian | Gauss linear corrected | Second |
| Time | CrankNicolson | Second |

Table 5.3 – Numerical schemes

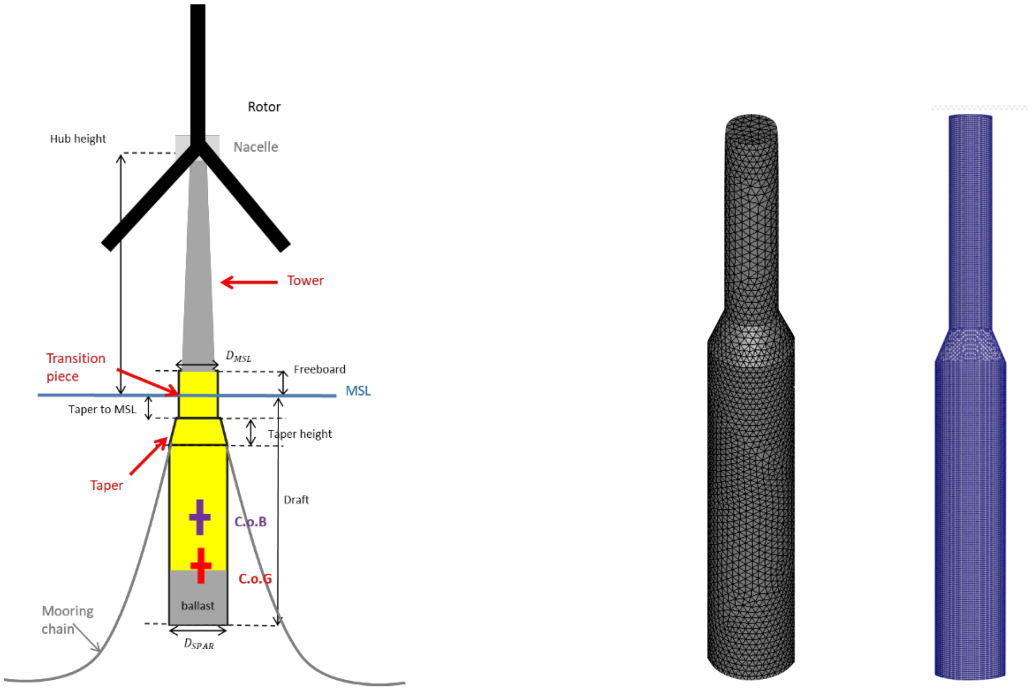


Figure 5.5 – (*Left figure*)Typical experimental SPAR model with its nomenclature, (*Right figure*) SALOME generated SPAR STL model, SnappyHexMesh generated SPAR model(CFD Mesh)

### 5.3.2 SPAR body mesh validation: Hydrostatics

Following a series of trials and errors, it was observed that the STL (stereolithography) geometry file used for meshing influences the submerged volume and consequently the body's draft. SALOME (Ribes and Caremoli, 2007) is a open source software that provides a flexible platform for numerical simulation preprocessing, and it allows the user to manage the triangles formation in the STL file generated. Hence for the current study, an STL file is generated in SALOME and it is used in SnappyHexMesh (meshing tool) for generating the CFD mesh. The spatial domain background hexmesh is discretized by cells with unit aspect ratio, using the blockMesh utility and it is refined based on the solution's convergence. The body is set in the numerical domain using the previously described STL file. The mesh is created by splitting one hexahedral cell into eight split-hexahedra cells and then snapping to the STL geometry using a simple and orthogonal background mesh. It is done with the snappyHexMesh utility, which creates two- and three-dimensional meshes from STL triangulated surface geometries comprising hexahedra and split-hexahedra. It requires an already existing base mesh, where the

body is sculpted, which is repeatedly refined and morphed to the surface geometry. Figure 5.5 depicted the SALOME generated STL file and typical SnappyHexMesh generated SPAR Body mesh.

A perfectly meshed floating body's mass and volume properties must correspond to not create spurious motions. As a result, a hydrostatic investigation is carried out to validate the generated body mesh. With the use of blockMesh and the snappyHexMesh tool, many surface refinements are evaluated, and an accurate mesh is ultimately chosen based on the following methodology.

$$Vol_p = Vol_{floater} + Vol_{cone} + Vol_{submerged\ tower} \tag{5.1}$$

where $Vol_{theoretical}$ represents the theoretical volume of the submerged SPAR. The underwater submerged components of the SPAR are given by $Vol_{floater}, Vol_{cone}, Vol_{submerged\ tower}$.

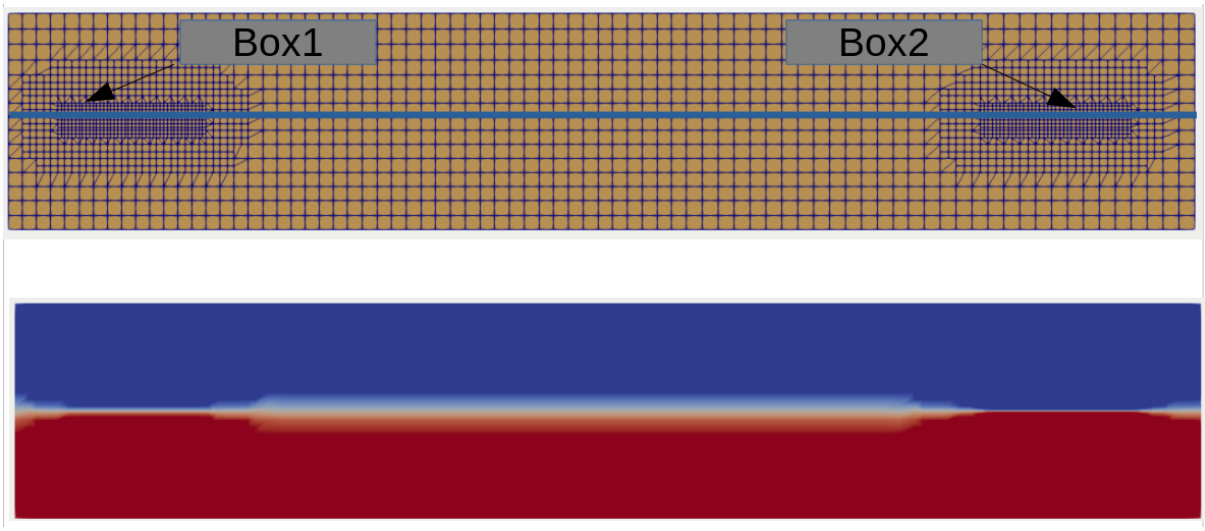


Figure 5.6 – Figures a) Upper figure shows the Free surface with planned box for refinement b) Sample test case : Complex refinement in the free surface with medium in box 1 and fine refinement in box 2

| **Refinement** | **Box1 (Level)** | **Box2 (Level)** | **Th.Volume ($m^3$)** | **foamStar function Volume** |
|---|---|---|---|---|
| No | - | - | 0.539 | 0.539 |
| Medium | 2 | 2 | 0.539 | 0.539 |
| Fine | 4 | 4 | 0.539 | 0.539 |
| Complex | 2 | 4 | 0.539 | 0.539 |

Table 5.4 – Accuracy of the modified *waterVolume* function

The correction/error in the body mesh generated is estimated by

$$Error(\%) = \left(\frac{Vol_p - Vol_{OF}}{Vol_p}\right) \times 100 \tag{5.2}$$

| Parameters | Value | Uncertainty |
|---|---|---|
| Draft [m] | 2.285 | ±0.03 |
| Mass [kg] | 340 | ±1 |
| COG | -1.535 | - |
| Mass Moment of Inertia (Ixx,Iyy,Izz) [kg $m^2$] | 490,490,10 | |

Table 5.5 – Mass properties for analysis of SPAR body mesh

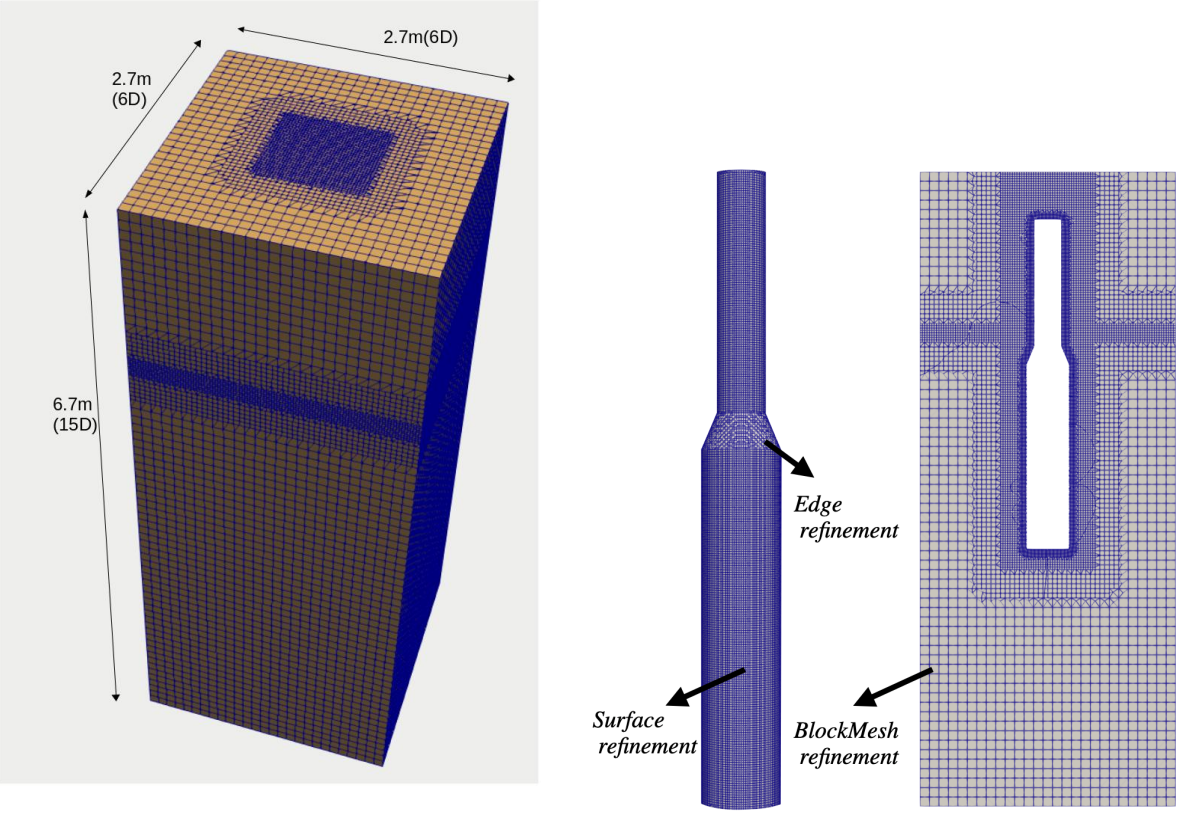


*(a)* Computational domain

*(b)* Cross sectional view of domain

Figure 5.7 – (*Left figure*)Computational Domain 6D X 6D X 15D for body mesh analysis, (*Right figure*) Typical cross sectional view with types of refinement planned in this study

where $Vol$ is read as Volume, and if the meshed submerged volume ($Vol_{OF}$) is known, the accuracy of the body mesh can be obtained. In order to identify the submerged volume of the meshed body, *waterVolume* function from Openfoam is modified and applied. This function object will give water volume ($\alpha = 1$) of the computational domain at every time step and it is modified to get the submerged volume of SPAR such as ,

$$Vol_{OF} = Vol_{domain} - Vol_{water\ volume} \tag{5.3}$$

Before checking the correctness of the results, this modified function is assessed for precision across a selection of free surface refinements. For that, a 2D rectangular domain (see Figure 5.6) with the free surface at the origin plane and a water depth of 0.7 m is considered. Two

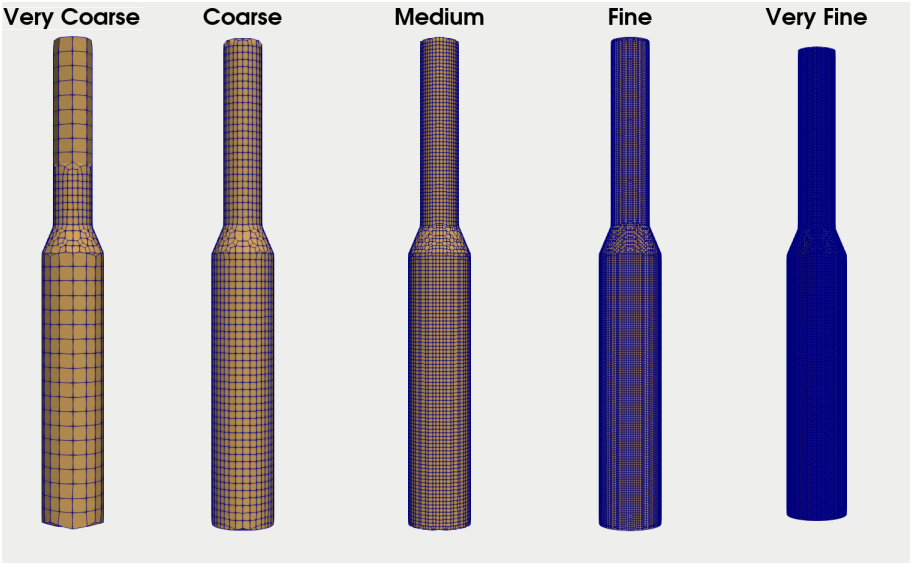


Figure 5.8 – Surface refinement on the SPAR surface (from very coarse to very fine)

refinement boxes are set up at the left and right edges of the free surface. These boxes aim to have unstructured free surface cells that divide the domain, making volume calculation a little more complicated for the *waterVolume* function. As shown in Table 5.4, the function's underwater volume estimated value appears to be accurate, with no dispute. Hence it is applied to estimate the accuracy of the meshed volume of the SPAR.

A numerical study in hydrostatic condition is carried out to evaluate the accuracy of the mesh, with the domain's length and width are six times the SPAR's diameter and the depth set to 5 m water depth along with 2 m freeboard exactly to imitate a physical wave tank (Figure 5.7a). PPSD (Points Per SPAR Diameter), a parameter based on the number of nodes/points in the SPAR bottom face, is introduced here for mesh analysis. Different types of refinement have been carried out for this parametric study, as shown in Figure 5.7. Table 5.5 defines the basic mass properties used in body mesh validation for the hydrostatics study, which were retrieved from the experiment.

PPSD modification includes edge and surface refinement using the SnappyHexMesh utility. The blockMesh utility is responsible for background refinement. Hence blockMesh cell sizes ranging from 0.25 to 1.5 are investigated (non-dimensionalised with SPAR diameter). Surface features ranging from very coarse to very fine (Level 1 to Level 5) are evaluated for surface refinement (Figure 5.8). As a result, an overall combination of 25 setup is performed, such as five surface refinements for each background configuration to achieve acceptable precision while minimising the number of cells. It was also decided to use a mesh combination parameter with an error of less than 0.1% as a suitable numerical body mesh for future research. The results of the study are as shown in the Figure 5.9 and Figure 5.10. The Figure 5.9 depicts a bar chart for each surface refinement with varying background meshes (from coarsest to finest), with the horizontal axis representing the error obtained from the equation (Eqn 5.2) and the vertical axis representing the number of cells created. In all graphs, the results demonstrate a well-known

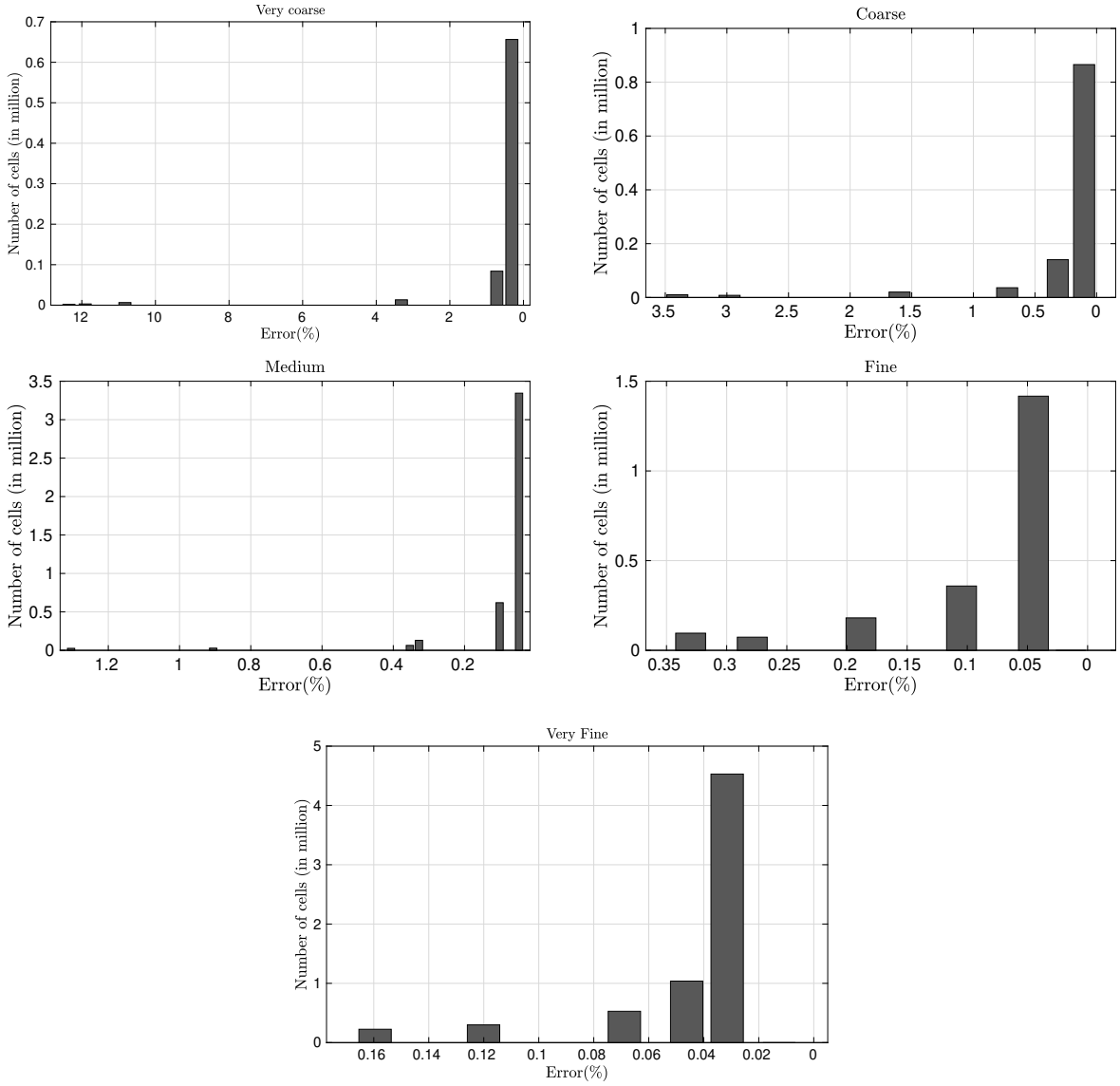


Figure 5.9 – Accuracy of mesh based on submerged volume vs Number of cells for different levels of refinement

trend of maximum error in the coarser case and a minimal error in the finer refinement. Similarly, when refining reaches the finest level, the number of cells increases.

From very coarse surface refinement with very fine background refinement to very fine surface refinement with very fine background refinement, the number of cells increased by a factor of 10, while the error decreased from 1% to 0.1% and further. Figures 5.10a and 5.10b shows other ways of illustrating the above finding. Figure 5.10b is a derived version of Figure 5.10a (zoomed window). In the Figures, $Vol_p$ represents the theoretical volume, and $Vol_{OF}$ represents the actual volume from the OpenFOAM utility. The previously noted pattern can also be seen in this illustration. With a coarser background, medium and all additional finer refinements have an error of less than 1%. The upcoming investigation will use a combination of fine surface refinement and a background mesh size less than 0.6, such that accuracy of more than 99.9%

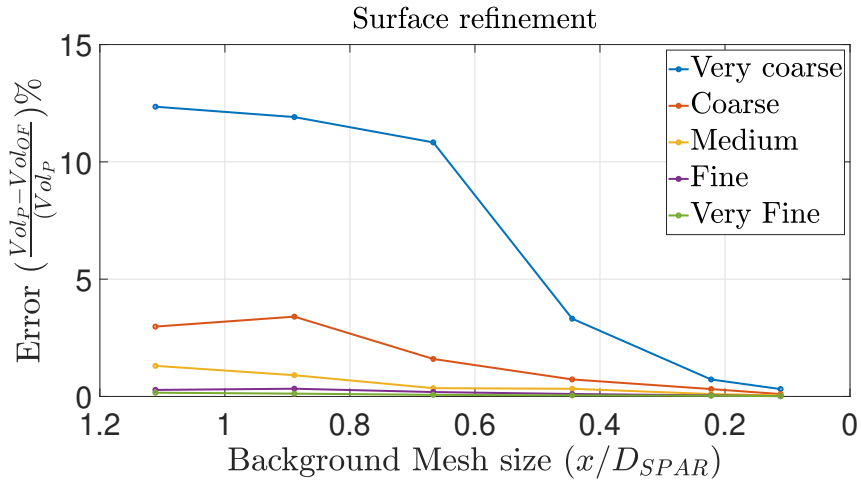


*(a)* Background Mesh Vs surface mesh refinement

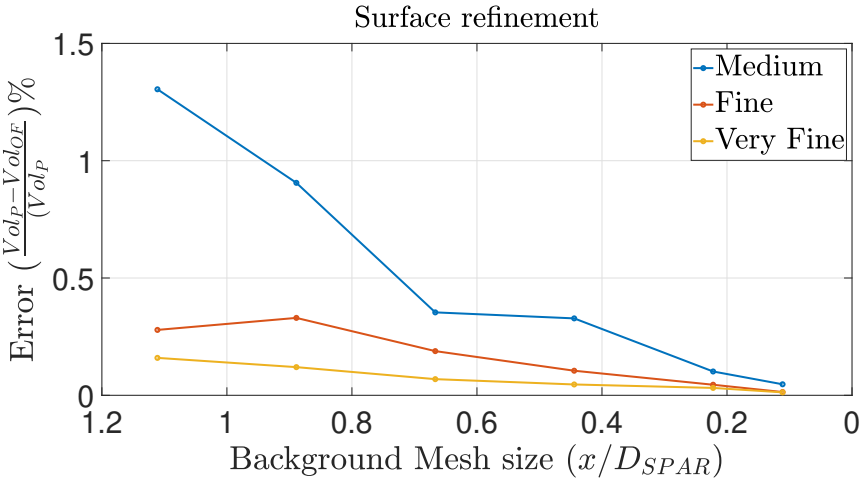


*(b)* Background Mesh Vs surface mesh refinement (zoomed to 3 cases)

Figure 5.10 – Error difference between meshed volume and correct volume for a different level of surface refinement

will be achieved. This combination is also represented in terms of PPSD for a fixed background mesh size and the results are shown in the Table 5.6. With the objective of error less than 0.1%, the value of 35 is chosen for its economical (low cell volume) and minimal loss in accuracy.

### 5.3.3 Spatial and temporal verification: wave propagation

In this section, the validation of the irregular waves generated in the NWT is done in absence of body. First, the results from HOS-NWT are compared with the experimental time trace, and then the validation is done with the CFD model for the regular and irregular waves for various spatial and temporal discretization combinations. Details about the wave cases chosen for the present study can be found at Table 5.2. The *foamStarSWENSE* solver is only validated for the irregular wave condition LC 2.1 and LC 2.2, whereas *foamStar* is validated for all four wave conditions.

| P.P.S.D | No of cells (millions) | Meshed volume | Difference (%) |
|---|---|---|---|
| 5 | 0.01 | 0.328157 | 3.4% |
| 10 | 0.07 | 0.338551 | 0.35% |
| 25 | 0.23 | 0.339112 | 0.18% |
| 35 | 0.5 | 0.339407 | 0.1% |
| 50 | 1.2 | 0.339518 | 0.06% |
| 75 | 3.88 | 0.339599 | 0.04% |

Table 5.6 – Mesh accuracy evaluation using PPSD for different mesh refinement

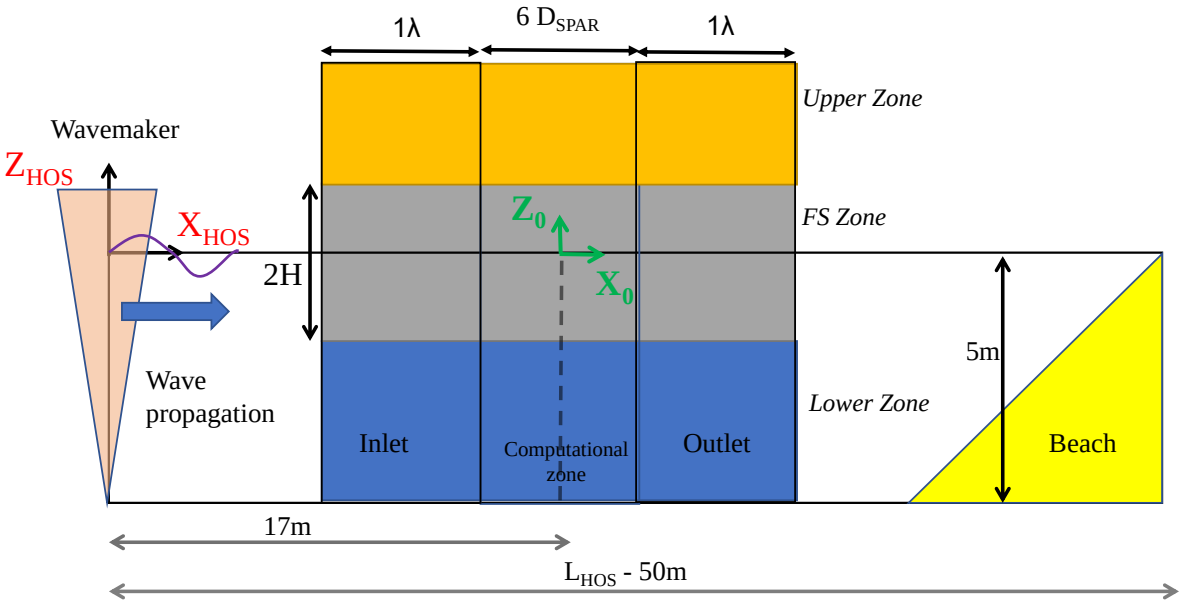


Figure 5.11 – Sketch of the HOS and CFD domains for wave propagation validation in 2D NWT and the position $x_{HOS} = 17$m is identical to $x_0 = 0$

#### 5.3.3.1 Irregular wave validation: HOS wave Vs experiment

It is important to remember that the HOS-NWT formulation was effectively validated with studies on various cases during the last decade(Ducrozet et al., 2012, 2006; Canard et al., 2020; Hasan et al., 2019). LC 2.1 and LC 2.2 cover a wide variety of wavemaker motions with large nonlinearities in order to validate our current concept and implementation. The experimental paddle motion has been used in the HOS-NWT to simulate the wave characteristics and compare the generated waves with the experimental measurements. For this simulation, 325 modes in the flow direction ($N_x$) and 33 modes in the vertical direction ($N_z$) have been used. Throughout the simulation, the HOS order is kept at 3. Figures 5.12a and Figure 5.12b shows the comparison of the HOS-NWT and the experimental wave elevation time traces at the WG2 probe location, for LC 2.1 and LC 2.2 respectively. In both figures, we can see that the agreement between the experiment and numerical models is very good. After 50 s, however, some slight deviations were noted in the peak magnitude of the crest or trough. This error is connected with the wavefront

of reflected waves coming back at the wave probe location after 60 s for LC 2.1 and 45 s for LC 2.2, but the cross-correlation coefficient for these simulations is around 0.994, which makes the discrepancy quite small, hence disregarded. It should also be noted that these deviations in the incident wave will have a minor impact on the motion responses in the wave-floating body simulations.

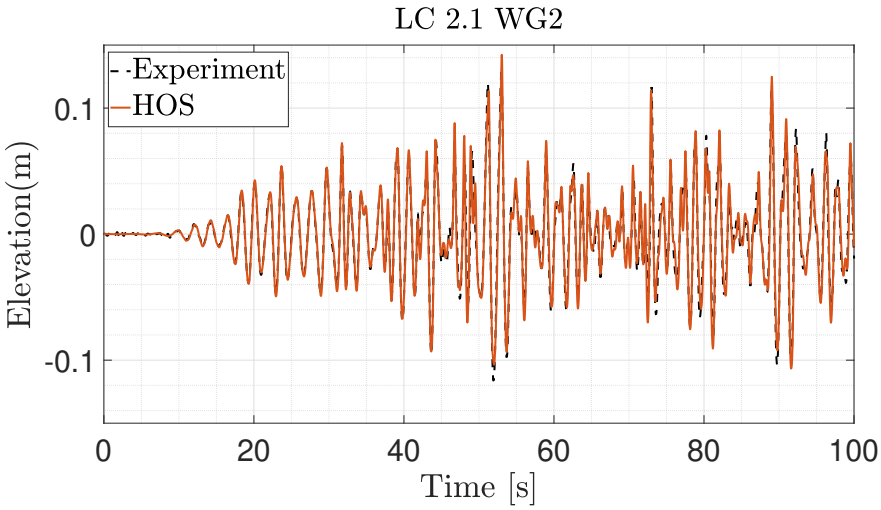


*(a)* LC 2.1 - Irregular wave

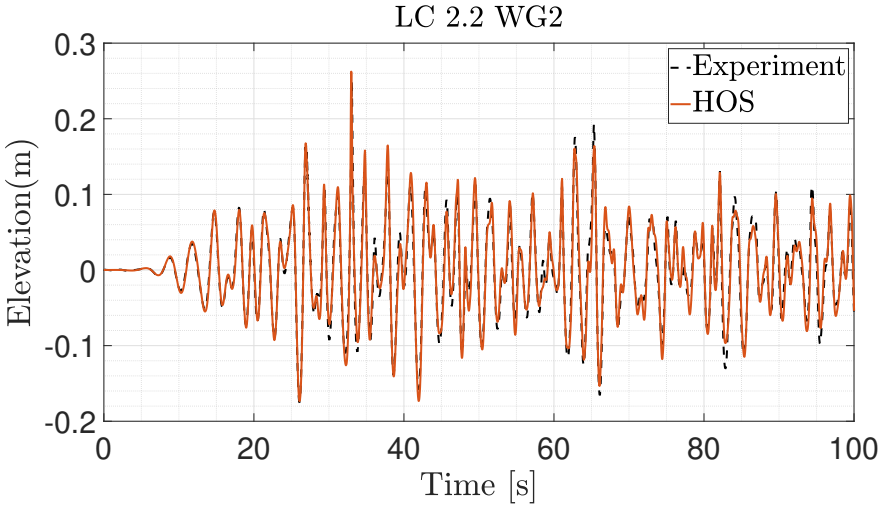


*(b)* LC 2.2 - Irregular wave

Figure 5.12 – Comparison between experimental and HOS-NWT numerical time series of wave elevation for the two Irregular wave test cases - LC2.1 and LC 2.2

#### 5.3.3.2 CFD validation : Regular and irregular waves

The mesh and temporal convergence studies for all four test cases for wave propagation are carried out in a 2D NWT. The sketch of the computational domain is depicted in Figure 5.11. The domain is a two-dimensional plane that is an exact reproduction of the three-dimensional domain illustrated in the Figure 5.4, but without the structure. The regular waves (LC 1.1 and LC 1.2) are generated using the *foamStar*'s built-in stream function wave theory and HOS-

| Mesh level | Mesh size (Δx, Δz) |
|---|---|
| Very Coarse | $\lambda/32$, H/2 |
| Coarse | $\lambda/64$, H/5 |
| Medium | $\lambda/100$, H/8 |
| Fine | $\lambda/150$, H/10 |
| Very Fine | $\lambda/200$, H/15 |

Table 5.7 – Progressive waves test case: Test matrix for convergence study

NWT is used for irregular waves (LC 2.1 and LC 2.2). To be noted, in the $R_0$ reference system, the origin is different for the HOS domain and CFD domain (Figure 5.11). The HOS domain ($L_{HOS}$) has a length of 50 meters and a water depth of 5 m. The length of the CFD domain is $1\lambda + 6D_{SPAR} + 1\lambda$, and its origin is positioned from $x_{HOS} = 17$ m at the inertial frame origin. The relaxation zones length is set to $1\lambda$ for both inlet and outlet, respectively. To be noted, for irregular wave cases, the HOS domain must entirely include the CFD computational domain into it.

Upper zone, free surface zone, and lower zone are the three zones that make up the computational domain in the vertical direction (Figure 5.11). Between $z = -H(or H_s)$ and $z = H(or H_s)$ is the free-surface refinement zone. As per the suggestion of (Kim, 2021c), the cell aspect ratio ($\Delta z/\Delta x$) in the free-surface refinement region is maintained at 0.5, and the outer zones are kept at ratio of four. To understand the solver's convergence, several discretizations are used to investigate the computing grid and time steps. Table 5.7 shows the cell length $\Delta x$ and height $\Delta z$ that were examined. Based on the wave period ($T$ or $T_p$) considered, different temporal resolutions for wave propagation are performed for each cell arrangement (Table 5.7), such as T/100, T/200, T/400, and T/800. Two investigations performed: modify the cell size while keeping the time step constant, and the grid is fixed while the time step is only varied in the second set of investigations. From Mesh32H2T100 to Mesh200H15T400, eighteen combinations of mesh and temporal resolutions were tested. Mesh32H2T100 indicates that there are 32 cells per wavelength in the wave propagation direction, 2 cells per wave height in the vertical direction, and 100 time steps per wave period. With all of the above factors mentioned, the outcomes or validation of the regular wave is described initially followed by the irregular wave.

**Regular wave validation:** For the regular wave validation, *foamStar* computational domain was considered with periodic boundary conditions. In this study, the duration of the simulation is kept at 35 wave periods for investigation. Figures 5.13a, 5.14a and 5.14b presents the wave generated at the location of the probe WG5 in the case of LC1.1. Similar observations are noticed for LC 1.2 and hence results are not reproduced here. Figure 5.13a depicts the observed surface elevation for all cases, demonstrating that all cases are in phase with one another and despite using the coarser condition, the wave barely loses 10% of its amplitude. Figure 5.14b displays the peak wave amplitude ($\eta_{max}$) for each combination of mesh and time step measured at nearly $20T_p$ and Figure 5.14a represents the first harmonic amplitude variation for the whole duration of the wave and its damping behavior. In both the figures, the parameters clearly demonstrates good convergence when refining the mesh and time step. From the results,

a cell size of 150 cells per wavelength, 10 cells per wave height, and 400 time steps per wave period seem to be computationally efficient and used for further analysis.

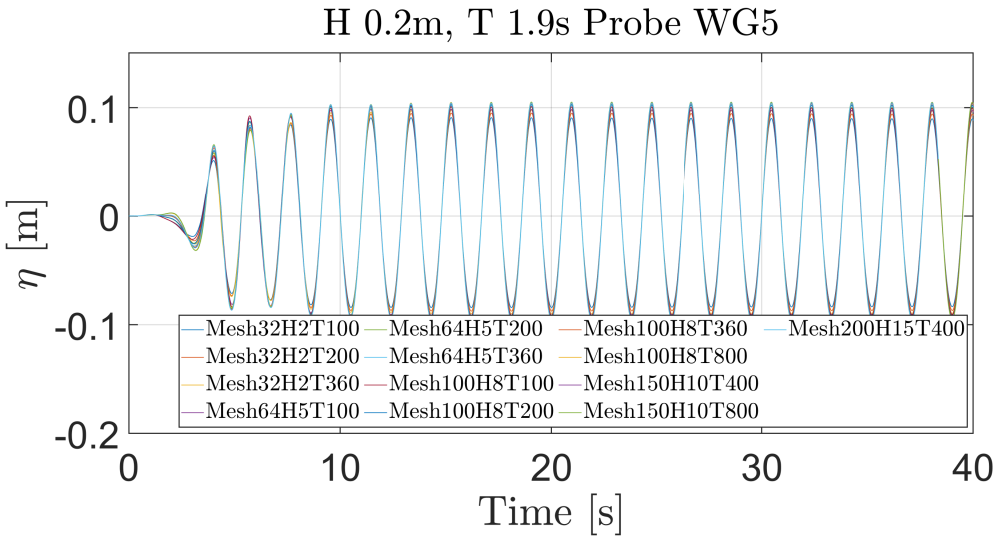


*(a)* Wave elevation measured at WG5

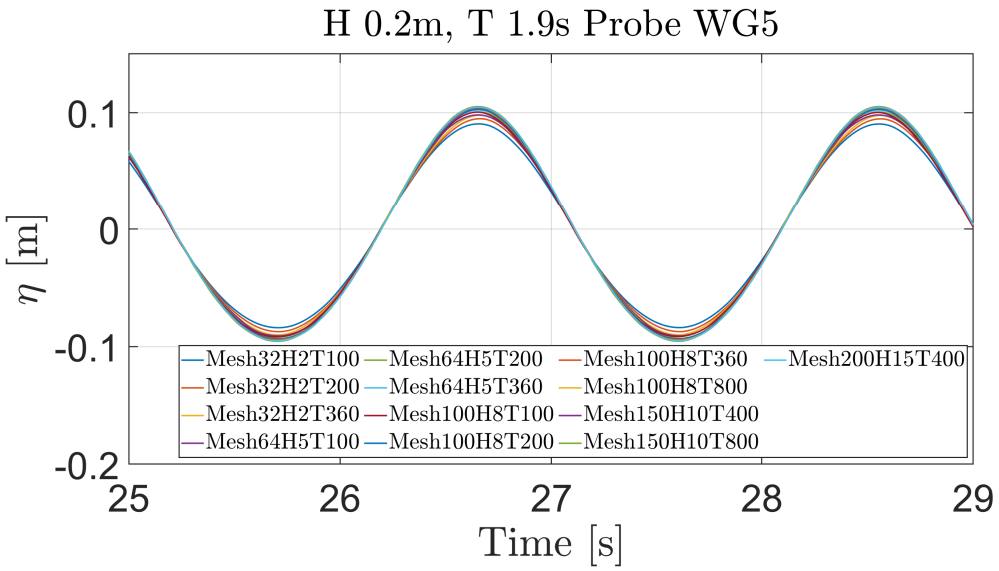


*(b)* Zoomed window of above Figure at 25-29s for clear representation

Figure 5.13 – Progressive waves propagation measured at the WG5 for different mesh and time configurations

**Irregular wave validation:**

The irregular waves for various combinations of spatial and temporal discretization (as in regular waves) measured at WG5 were used in the following analysis. The results from *foamStar* and *foamStarSWENSE* (for LC 2.2) are cross-correlated with the HOS simulations to investigate the spatial and temporal convergence (Table 5.7) . For theory behind the cross correlation, Section 2.1.6.1 can be referred. Free surface elevation recorded in the probe WG2 in the case of LC 2.1 and LC 2.2 are shown in Figure 5.15a and Figure 5.15b respectively. For reference purposes, the experimental recording at the same location as well as the HOS probe recordings are also

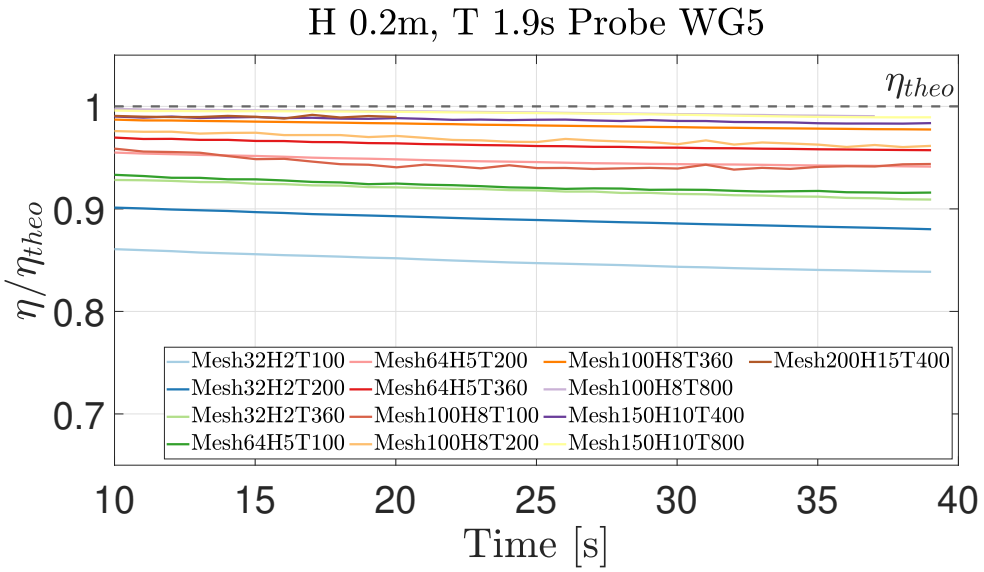


*(a)* Regular waves peak amplitudes measured at the WG5 across the duration

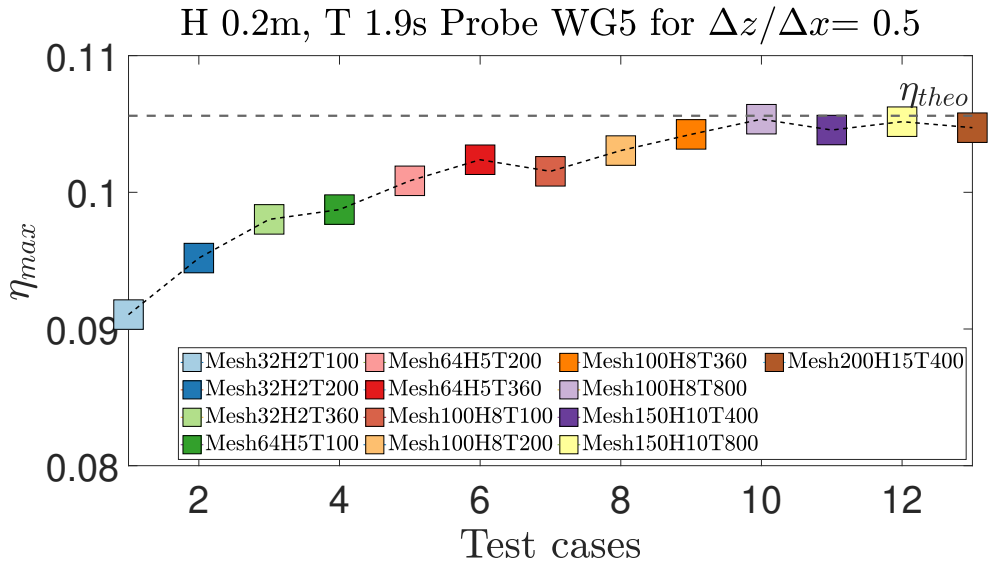


*(b)* Regular waves first harmonic peak amplitudes measured at the WG5 at 10th peak period for different test cases

Figure 5.14 – Progressive waves propagation measured at the WG5 for different mesh and time configurations

shown in the Figures. Typical cross-correlation results between reference signal (HOS) and numerically recorded signals (*foamStar*) for LC 2.1 and LC 2.2 are shown in Figure 5.16. Although the experiment and HOS were conducted for a total of 600 s, to avoid the large computational cost, the comparisons were carried out for 100 s (i.e. around $50T_p$). Eighteen different configurations were carried out for both LC 2.1 and LC 2.2, as indicated by the circles and squares in the Figure 5.16. The lines connect meshes that are of the same type but with varying temporal discretization. The findings demonstrate that even the coarser combinations have an accuracy of approximately 0.97 and that refining the discretizations will bring the accuracy closer to 1. For the wave-structure interaction study, the mesh combination of Mesh150H12T400 which is

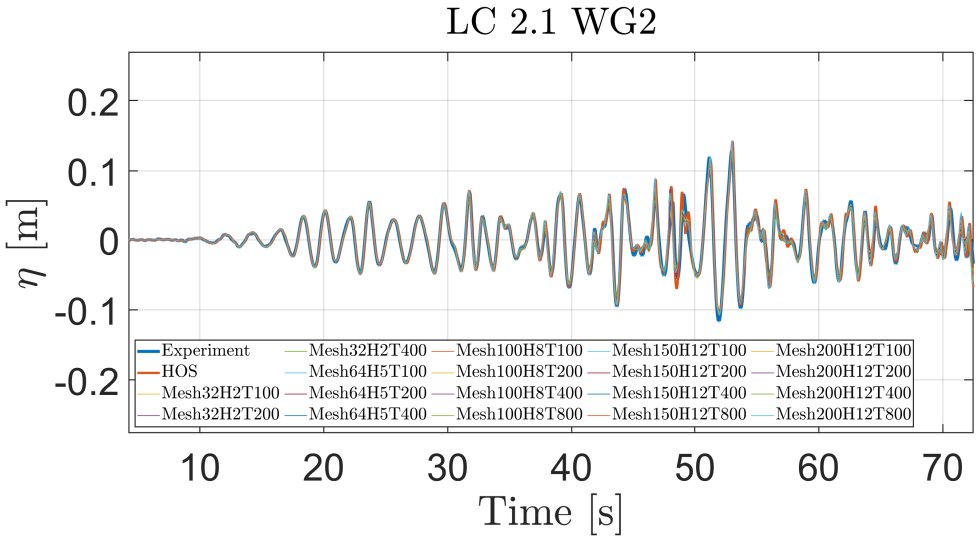


*(a)* LC 2.1 - Irregular wave

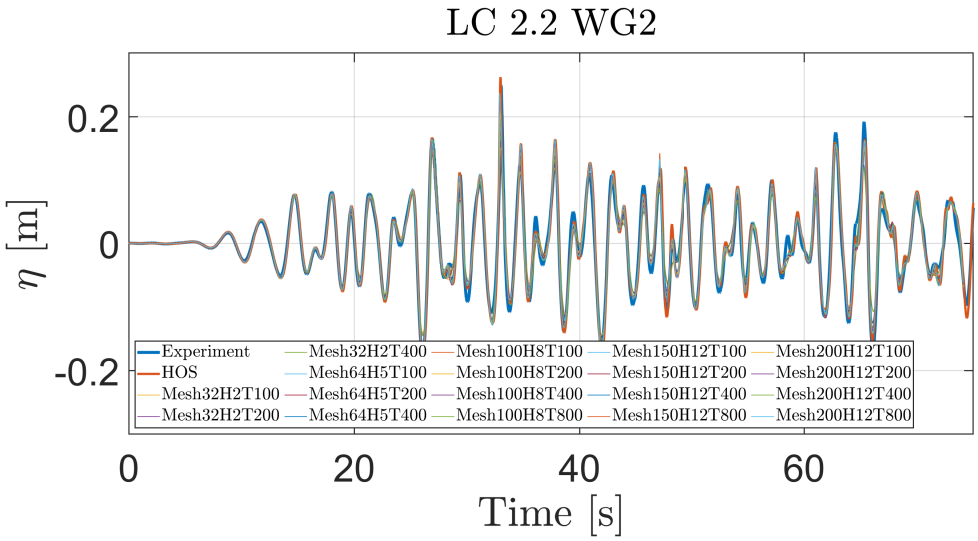


*(b)* LC 2.2 - Irregular wave

Figure 5.15 – Irregular waves test case: Free surface elevation at the WG2 for different mesh and time configurations

nearly on and above 0.99 in both load cases is proven to be an affordable combination and hence this combination is used in the present study.

Only LC 2.2 is validated in a 2D NWT for *foamStarSWENSE*, the probe findings are cross-correlated with HOS, as done with the *foamStar* solver. Figure 5.17 displays the cross-correlation analysis's findings. It can be seen that the accuracy of the *foamStarSWENSE* solver was 0.98–0.99 up to Mesh100T400 and 0.99–0.995 for the other cases. After further analysis, it is observed that the wave produced in the *foamStarSWENSE* can be accurate provided the free surface zone has a constant aspect ratio, as indicated in the left figure of Figure 5.18. In the present case, the free surface zone aspect ratio must be kept at one rather than 0.5 in order to mesh the floating body smoothly (SnappyHexMesh requirement). When interpolating from the HOS grid to the SWENSE grid, it has been realised to add a small amount of extra frequency,

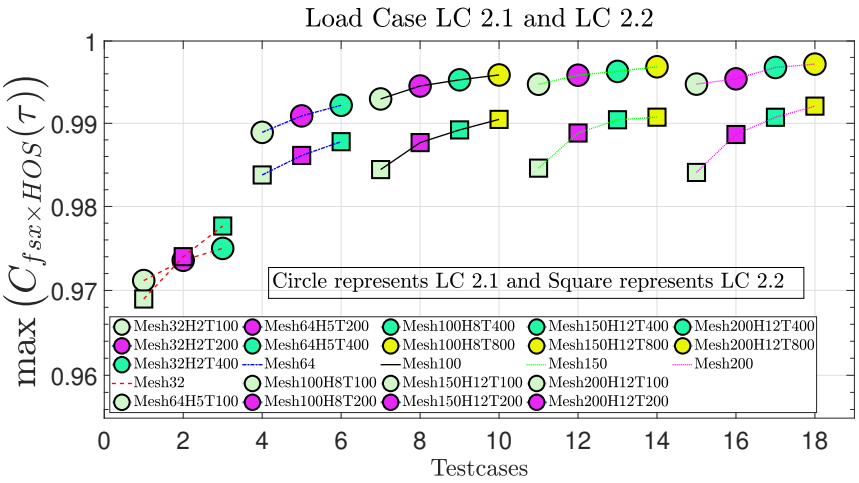


Figure 5.16 – Cross-Correlation Coefficient for LC 2.1 and LC 2.2 between different mesh and time combination in *foamStar* and HOS

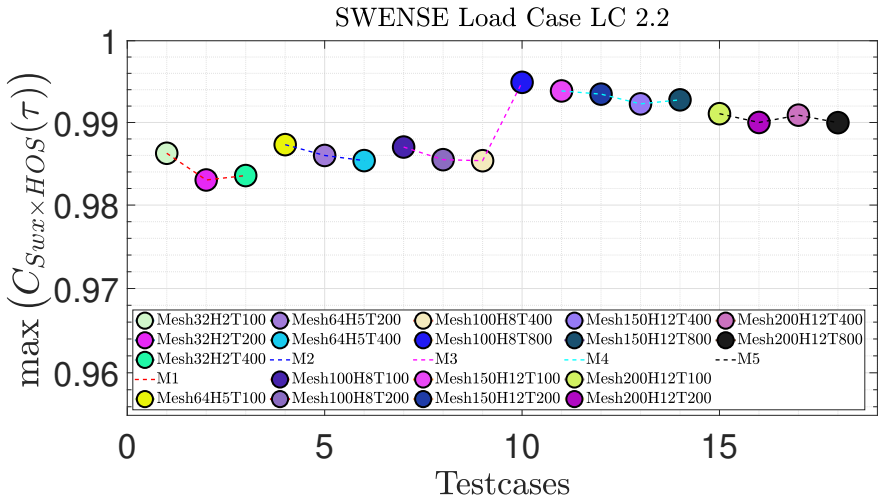


Figure 5.17 – Cross-Correlation Coefficient for LC 2.2 for different *foamStarSWENSE* mesh and time combination with HOS

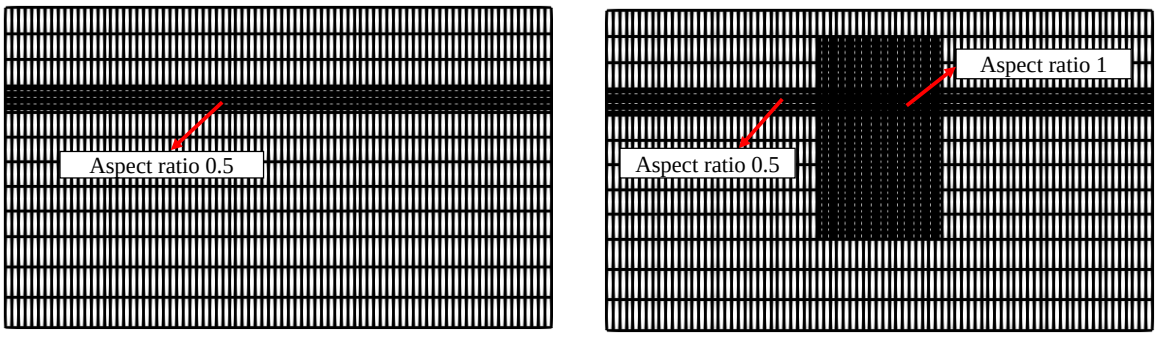


Figure 5.18 – Cross section of 2D NWT domain with different aspect ratio in the free surface zone

however as the data indicate, it is a minor inaccuracy to be concerned about. To improve the *foamStarSWENSE* solver, it will be one of the future changes required.

### 5.3.4 Mooring validation : MoorDyn

The MoorDyn standalone solver is validated for delta type mooring in this subsection with different mooring models (MoorPy (Hall et al., 2021), MAP (Masciola, 2018), and AQWA) as similar to the Section 2.1.4.4. Also the input conditions for the actual SPAR problem are validated in the standalone solver for identifying their accurate input characteristics.

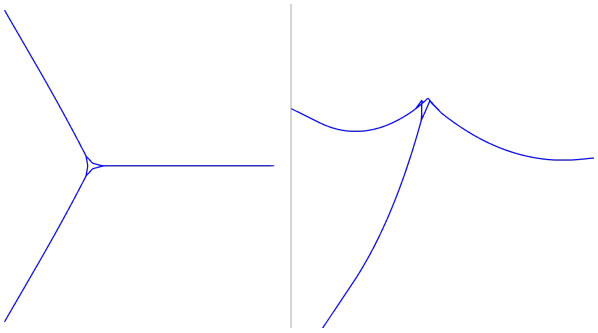

Figure 5.19 – Typical delta mooring model adopted in the present study with its top view(left) and isometric view (right)

For the validation, the mooring setup used in the present study, the crowfoot model having 3 main lines connecting 6 bridle lines with the load sensor (LS1 to LS3) as shown in the Figure 5.3 are tested. This configuration is validated in a standalone MoorDyn model for a total of 9 mooring lines and 9 nodal locations, and the typical setup is as illustrated in Figure 5.19. It is important to validate input characteristics such as connecting nodes, unstretched length, mass, and stiffness properties from the experiment. The primary mooring properties from the experiment are listed in the Table 5.1. In order to obtain proper tension, in the numerical model symmetry adjustment of the anchor and fairlead positions ($120^o$ to each main line) are considered, because of the fact that achieving symmetry while doing physical tests was difficult. The axial stiffness (AE) and equivalent diameter are obtained from ORCINA recommendations (ORCINA). In the transverse direction (Eqn. (2.53)), quadratic damping coefficients are set to 1.8, and in the axial direction (Eqn. (2.54)), they are set to 0.25 based on the numerical analysis. The added mass coefficient in the transverse direction are set to the value of 1.0. The convergence with respect to the number of segments in the mooring line was studied, and it was determined that from the 75 segments in the main line and 6 segments in the bridle were the most efficient and converged solution.

As stated in MoorDyn validation section (Section 2.1.4.4), the mooring properties used in the experiment are modified to prototype values (1:40 scaled model of FOWT) using Froude and Cauchy scaling, and the updated mooring properties are shown in Table 5.8. Similar setups were also built in various mooring models, and the pretension at the static conditions for major lines Line 1 to 3 (Figure 5.3) are compared as shown in Figure 5.20. The pretension aligns well with MAP, and only minor variations were noticed compared to MoorPy and AQWA proving

| **Parameters** (Froude Scale 40) | **Units** | **Prototype Values** |
|---|---|---|
| Diameter of chain | [m] | 0.266 |
| Mass density | [kg/m] | 440 |
| EA | [N] | 6E9 |
| Added mass coefficient | | 1.0,0.0 |
| Drag coefficient | | 1.8, 0.25 |
| Clumped mass (sensor) | [kg] | 2.75e4 |
| UnstrLen (Major and Bridle) | [m] | 638.2, 48 |

Table 5.8 – Parameters of the mooring lines in prototype scale

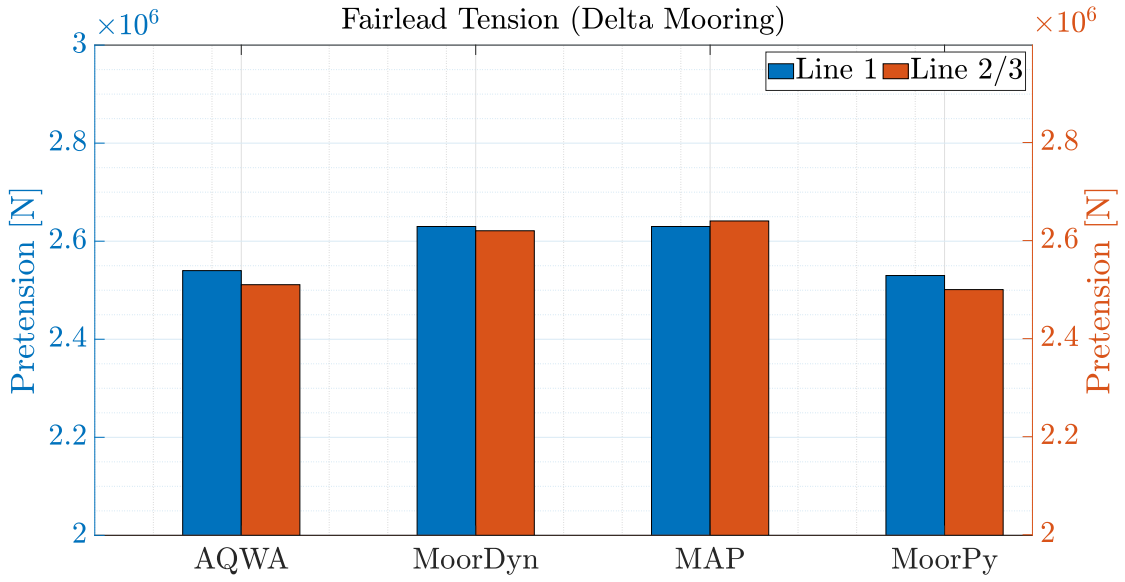


Figure 5.20 – Comparison of line tensions along delta type mooring lines for different mooring models

the efficiency of the MoorDyn and input conditions considered. The final system of coupling considered is as shown in Figure 2.15, wherein the mooring analysis will be carried out in prototype scale for motions and velocities and the computed forces are then scaled-down and coupled with the *foamStar*/*foamStarSWENSE*.

Also, the MoorDyn results are validated from the experimental pull-out tests for the estimation of stiffness. To characterize the horizontal mooring stiffness for the platform surge DoF, various pull-out tests were done during the experiments. One such test comparison with experiments is shown in Figure 5.21, wherein the mooring stiffness is nearly 75 N . $m^{-1}$ based on the slope of the force/surge relationship. The mooring restoring force can be quite similar to a linear force, which is interesting for a catenary system since the total restoring force in DeepCWind campaigns and the related OC4 numerical model (Robertson et al., 2014) tends to be nonlinear at larger offset values.The average surge response in the experiment rarely exceeds 10 cm in amplitude, thus over the range of 10cm to 20cm, the restoring coefficients' linear trend agrees well with the experiment, and the slope difference beyond 25 cm displacement (Figure 5.21) will

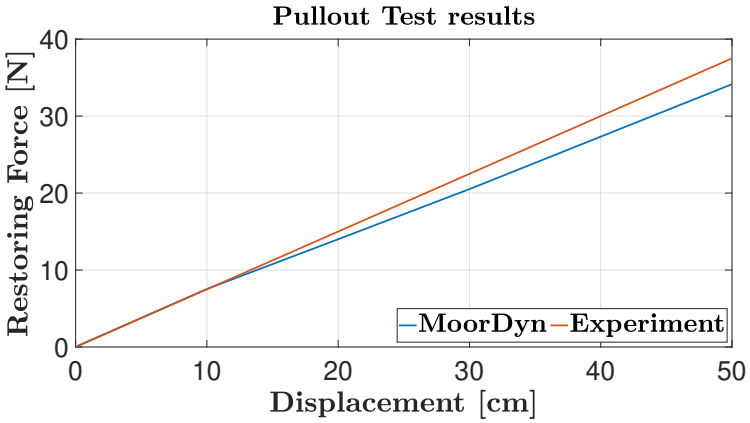


Figure 5.21 – Comparison of the results of the Pullout test in the MoorDyn solver with the findings of the experiment

not impact the results. It is important to note that the restoring force stated here refers to the overall restoring of all 9 lines, not just the catenary line.

### 5.3.5 Stiffness matrix coefficients

The stiffness coefficient as determined by the pull-out test for surge ($K_{11}$) mooring lines is 75 N.m$^{-1}$. Similarly, the sway ($K_{22}$) and yaw coefficients ($K_{66}$) were calculated using similar conditions and also modeling the mooring lines in ORCAFLEX (ORCINA) for validation. The values are 80 N.m$^{-1}$ and 127 N.m rad$^{-1}$, respectively for sway and yaw. Non-diagonal stiffness in terms of restoring stiffness in heave, roll, or pitch from the mooring appeared to be extremely minimal in this investigation. In the case of solving wave-structure interaction with stiffness matrix, the mooring line mass of 11.4 kg (±1 kg) is added to the SPAR's total mass. Based on the hydrostatics and the objective to maintain the same draft for to experiment, the total mass is adjusted as discussed in Section 5.3.2.

## 5.4 Results and Discussion

The validation of the developed numerical approach with the experimental measurements is discussed in the following manner in this section : (1) Moored decay test (natural period estimation, and damping for surge and heave along with their mooring tension) (2) *foamStar* - regular and irregular waves interaction with SPAR (3) *foamStarSWENSE* - Irregular waves interaction with SPAR

### 5.4.1 Moored Decay

In the coupled *foamStar*-MoorDyn solver, two independent DoF decay tests are carried out with delta mooring lines. The SPAR is perturbed along the DoF of interest, then released to move freely from that point. Surge, heave and pitch are the decay tests performed. The mooring tensions and their accompanying modeling results are discussed. The moored decay

test performed by the *foamStarSWENSE* solver will be comparable to the *foamStar* solver since the *foamStarSWENSE* solver will only be solving the NS equation if there is no incident wave field ($\chi = \chi_I + \chi_C \rightarrow \chi = \chi_C$). As this will duplicate the *foamStar* results, it will be ignored in this investigation.

#### 5.4.1.1 Surge decay

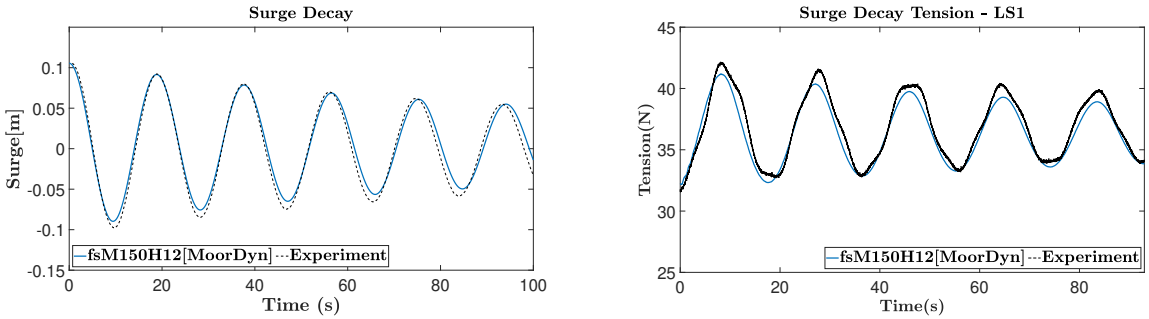


*(a)* Surge motion

*(b)* Surge mooring tension

Figure 5.22 – Comparison between experimental and numerical time series of surge decay test with its corresponding DoF and mooring tension

The initial displacement for the Surge in *foamStar* is accomplished using the moveDynamicMesh utility, which only conducts the dynamic mesh motion without solving the flow field while monitoring the mesh quality aspects. The SPAR floater with delta mooring lines is moved 0.11m and then released to move freely from its initial position. The COG is set to a displaced position, and the mooring lines are given initial displacement and zero initial velocity and are free to move with the body motions. The surge had a strong influence on the pitch and a weak influence on the heave, making it difficult to estimate the proper surge natural period. Hence only for this specific test case, the sole surge DoF is taken into account. The findings of the motion shown in comparison to the experiment (Figure 5.22a and Figure 5.22b), as well as the mooring tension in Line 1(ref Figure 5.3 for Line nomenclature), appear to be quite accurate. All of the line tensions were in good agreement, but $Line1$ was the most critical (as it is in every test scenario), therefore it is the only one shown. When the SPAR is shifted towards $Line1$ for initial displacement, there is a loss of up to $8N$ in pretension at first, and the variation approaches $\pm 10N$. Surge's natural period is found to be 18.82 s, while the experiment's natural period is $18.6 - 18.7$ s. The overall damping ratio is calculated using the logarithmic decrement method, and it is found that the percentage changes between 2.2% to 2.3% for the experiment, but from the numerical simulation it is between 2.35% to 2.45%. In the instance of the surge decay test, the overall difference is found to be less than 1%, indicating that the coupling model performs well for both motion and tension estimation in the surge decay problems.

#### 5.4.1.2 Heave decay

The heave decay follows a similar procedure as that of the surge simulation, with the SPAR being moved in the heave direction for an initial displacement (in this case 0.045m) and then

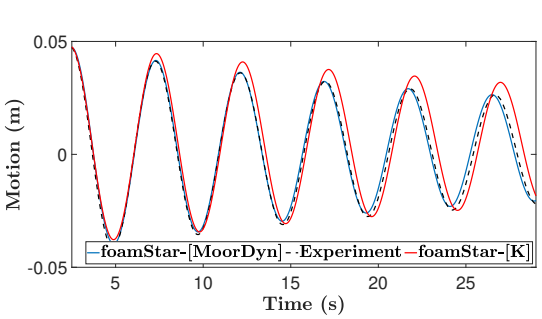


*(a)* Heave motion

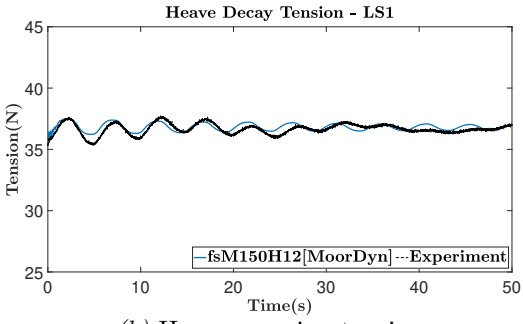


*(b)* Heave mooring tension

Figure 5.23 – Comparison between experimental and numerical time series of heave decay test with its corresponding DoF and mooring tension

released in calm water. The decay simulation in heave is carried out with all 6 DoF motions active since the heave motion has only slight influences from all other motions. Also note that the mooring in the form of stiffness matrix was examined as well (although it did not have any stiffness in the heave direction) for the present heave decay. The motion recorded in both mooring scenarios is shown in the Figure 5.23a. The figure has a few noteworthy observations as follows. The mooring in the form of a stiffness matrix component can be thought of as having no resistance in the heave direction ($K_{33}$). As a result, the motion characteristics only depict the body motions for a given mass and displacement. In this situation, the natural period appears to be $4.91s$, and the damping ratio appears to be 1.5%. Incorporating the mooring into the problem changes the damping of the problem by adding $0.5-0.6\%$ to total damping, resulting in a natural period of $4.8s$. The natural period in the experiments was determined to be $4.8-4.9s$, and the damping was found to be similar to that of the moored simulation. Figure 5.23b compares the numerical tension of Line 1 (at LS1) with the experiment, to illustrate the effect of mooring tension variation. The vertical axis is kept the same as in the surge free decay tension figure to show the reader that the influence in the heave is too small when compared to the surge but cannot be ignored.

#### 5.4.1.3 Pitch decay

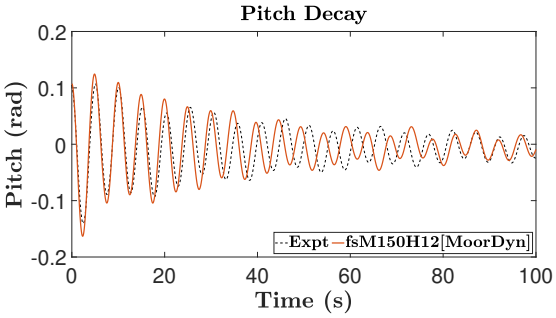


*(a)* Pitch motion

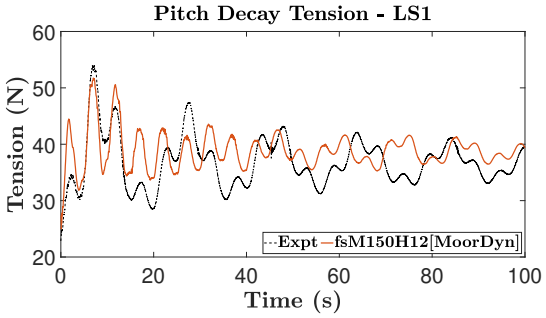


*(b)* Pitch mooring tension

Figure 5.24 – Comparison between experimental and numerical time series of pitch decay test with its corresponding DoF and mooring tension

Similar to the surge and heave simulation, the pitch decay involves moving the SPAR in all six directions for an initial displacement and rotation (in this case, Pitch 0.11 radians) before releasing it in calm water. Since the pitch motion has significant influences from the surge and heave motions, the decay simulation in pitch is performed with all 6 DoF motions active. Also, note that the stiffness matrix in the form of mooring is not considered for the present pitch decay investigation because the motion is coupled strongly and involves restoring from surge motion. The numerically predicted pitch response has a lower pseudo-period and more damped than the corresponding experimental results, as shown in the Figure 5.24a. Also a different pattern of mooring tension in mooring lines was observed (Figure 5.24b) in pitch-free decay, due to coupled response of surge motion. The initial six degrees of freedom positions, the moment of inertia and pretension (initial mooring position), etc., are all closely related to the pitch response. The results will be different even if there is a little adjustments to the moment of inertia and COG location (Palm et al., 2016). For this study, the number of test cases has been evaluated, although obtaining an accurate depiction of the natural period and mooring tension was more challenging. Some possible explanations for this other than mass properties are mostly related to the exact initial 6 DoF positions of the SPAR in experiment and the initial position of mooring lines. Also, reason for the slight difference in the damping (Figure 5.24a) can be attributed to the sharp corners of the numerical SPAR which is expected to yield higher drag forces than the smoother physical model.

### 5.4.2 Wave interaction with SPAR

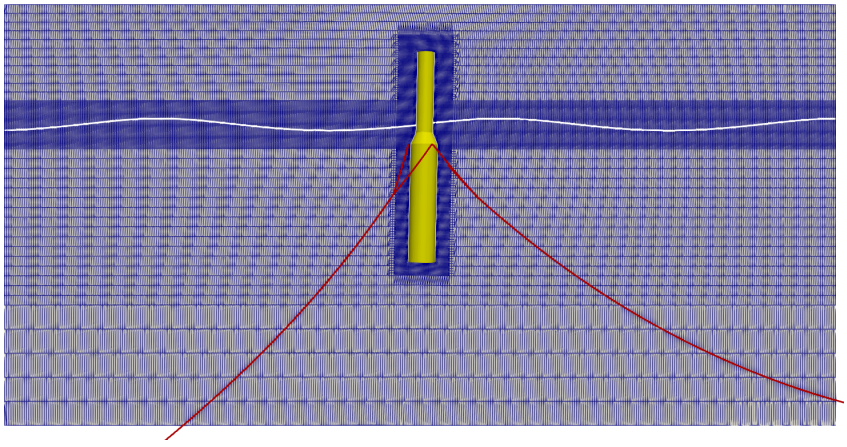

Figure 5.25 – Typical representation of computational domain in the wave-structure interaction study with mooring

In this section, the performance of the *foamStar* and MoorDyn coupling in reproducing the experiments on wave interactions with SPAR is reported. The wave interaction's computational domain and relaxation zones are the same as those described in Section 3. A common Mesh150H12T400 is chosen in order to make a similar discretization for regular (Mesh150H10T400) and irregular waves studies (Mesh150H12T400), and it will be represented in the results with the prefix 'fs' denoting *foamStar* and 'Sw' represents *foamStarSWENSE*. The Figure 5.25 depicts a

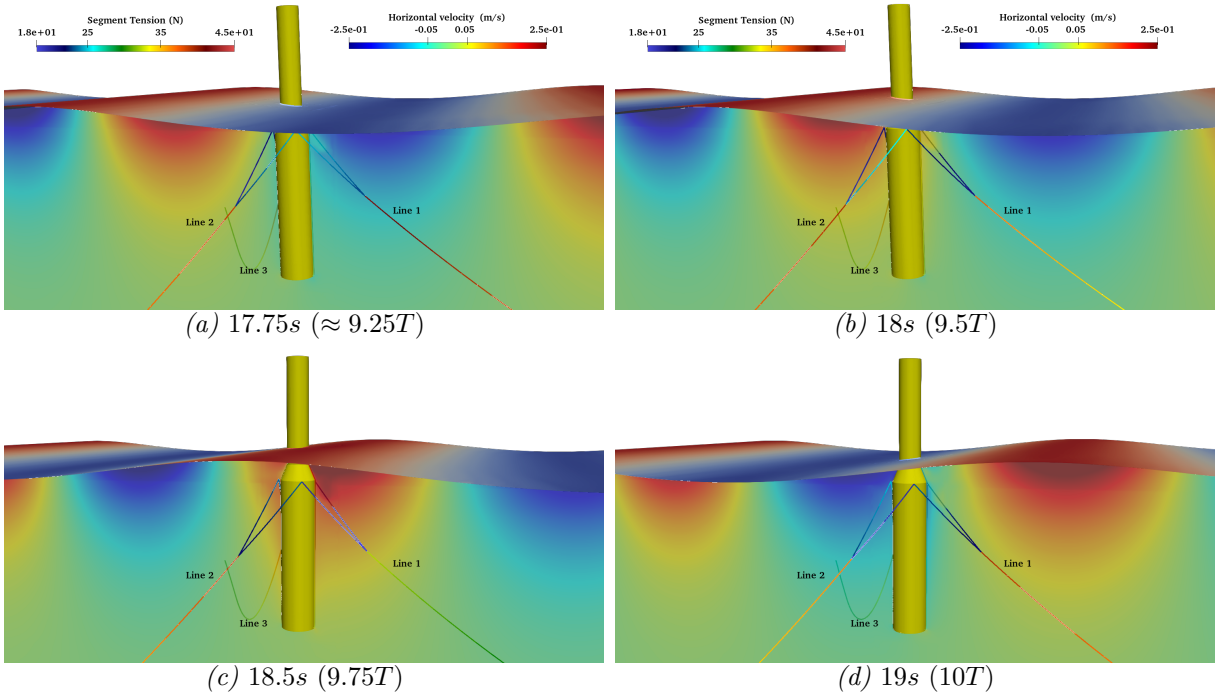


*(a)* 17.75$s$ ($\approx 9.25T$) *(b)* 18$s$ (9.5$T$)

*(c)* 18.5$s$ (9.75$T$) *(d)* 19$s$ (10$T$)

Figure 5.26 – Typical representation of different time instants of the interaction of regular waves with the moored floating SPAR using *foamStar*-MoorDyn coupling for case LC 1.1

typical computational domain with mooring lines. The fine refinement in the free surface and near the SPAR can be seen in this figure, along with the typical contour of the free surface. The SPAR body is fine-tuned based on the previous estimates in order to maintain PPSD 35 and a little mass modification to ensure the same drafts. Based on the wave being considered, the wavelength will vary for each load case, influencing the number of cells. In the present study of LC 1.1 to LC 2.2, it varies from 1 to 2.5 million cells, and the code was executed concurrently using MPI on the LIGER supercomputer at Ecole Centrale Nantes. The duration of the simulation as a whole varies from case to case. Only 25$T$ is kept as the simulation duration for regular wave cases (LC 1) because the steady state is reached within 4 to 5 peaks of the simulation, but 50$T_p$ has been kept as the simulation duration for irregular wave cases (LC 2). One CPU per 30000 cells is chosen for parallel processing and computational time varies from 10 hours in LC 1 to 36 hours in LC 2. Each LC involves two methods of coupling to handle the mooring line, one in the form of a stiffness matrix and the other with dynamic mooring (MoorDyn). As previously indicated, two regular wave test cases (LC 1.1 and LC 1.2) and two irregular wave test cases (LC 2.1 and LC 2.2) are being carried out and discussed in the following sections.

#### 5.4.2.1 *foamStar* - Regular wave interaction

The hydrodynamic responses of the SPAR under regular waves are investigated in this section. All the waves propagate in the positive surge direction. The waves characteristics are as listed in Table 5.2. At various time instants, a typical interaction between the wave, structure, and mooring is demonstrated in the Figure 5.26. The wave LC 1.1 (T= 1.9 s) has an initial ramp

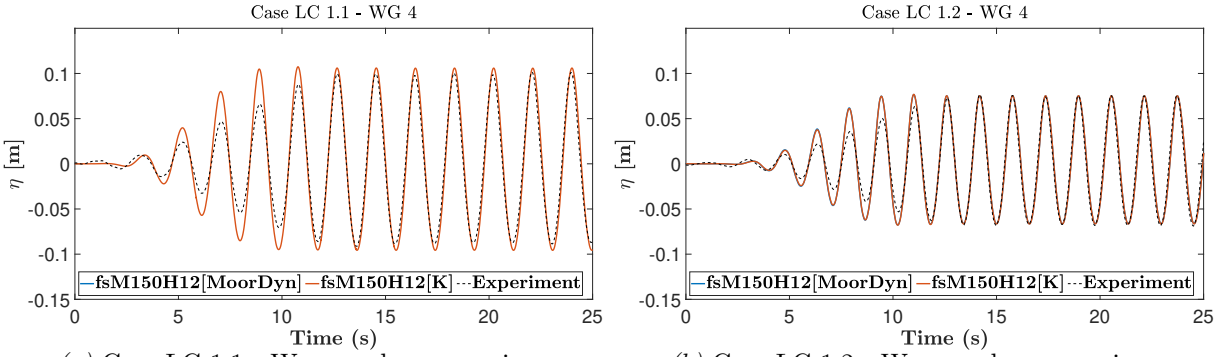


*(a)* Case LC 1.1 - Wave probe comparison

*(b)* Case LC 1.2 - Wave probe comparison

Figure 5.27 – Comparison between experimental and numerical time series of wave elevation at WG4 of the Floating SPAR for the two regular wave test cases - LC1.1 and LC 1.2

of 10 s, hence the steady-state time instant of 17.5 s to 19 s was chosen for the presentation of figure. The magnitude of velocity in the x-direction as the wave progresses is shown in red and blue on the graph. For clarification, the free surface contour is also displayed ($\alpha = 0.5$). The mooring is represented by segment tension, which varies from 18 N to 45 N and is colored blue to red. The crest of the wave approaches before SPAR (already has its own motion during transient and few wave periods before) at 9.25 T. Line 1 has the highest mooring tension and Lines 2 and 3 have slightly lower tension. As the wave progresses, the crest reaches the SPAR (9.5 T) and impacts (9.75 T), then SPAR travels in lockstep with the wave orbital, reducing the tension in Line 1 to 30-35 N and causing significant tension in Line 2 and Line 3. Line 3 is on the opposite side of the figure, making it difficult to visualize in colour. Because Line 3 is symmetric, it can be said that the behaviour will be similar to Line 2. When the trough reaches the SPAR at the final instant ($10T$), it gently returns to its previous motion, which is similar to 9.25 T, lessening the tension in Lines 2 and 3 and achieving equilibrium before the next cycle begins.

The comparison between experiments and numerical simulation for wave probe WG4 is shown in Figure 5.27. Out of all the probes, the probe WG,4 which is aligned with the initial center of the SPAR, is shown for the comparison. The initial ramping in the experiment is different from the numerical ramping leading to a small difference up to 10 s. After achieving a steady-state, the wave appears to achieve suitable amplitudes and is in phase with the experiment. For both the LC, the total duration of simulation recorded in the experiment is 30 s. Both the LC 1.1 and 1.2 were initially evaluated for 30 s, however, to quantify the surge effects (Surge natural period roughly 19 s) the LC 1.1 simulations were extended for a few additional seconds. The numerical and experimental time series for surge, heave, and pitch angles (LC 1.1 and LC 1.2) are shown in the Figure 5.28. To demonstrate the influence of LC 1.1 over LC 1.2, the vertical axis limit is kept constant, indicating that LC 1.1 has larger amplitudes than LC 1.2. Sway, roll, and yaw motions were not shown since they were negligible, both in the numerical simulations as well as in the experiments. The surge motions shown in Figures 5.28a and 5.28b, appears to oscillate with increased amplitudes at the ramping time itself before the steady-state due to the difference in the ramping. The rate of change of oscillation amplitude compares well to the

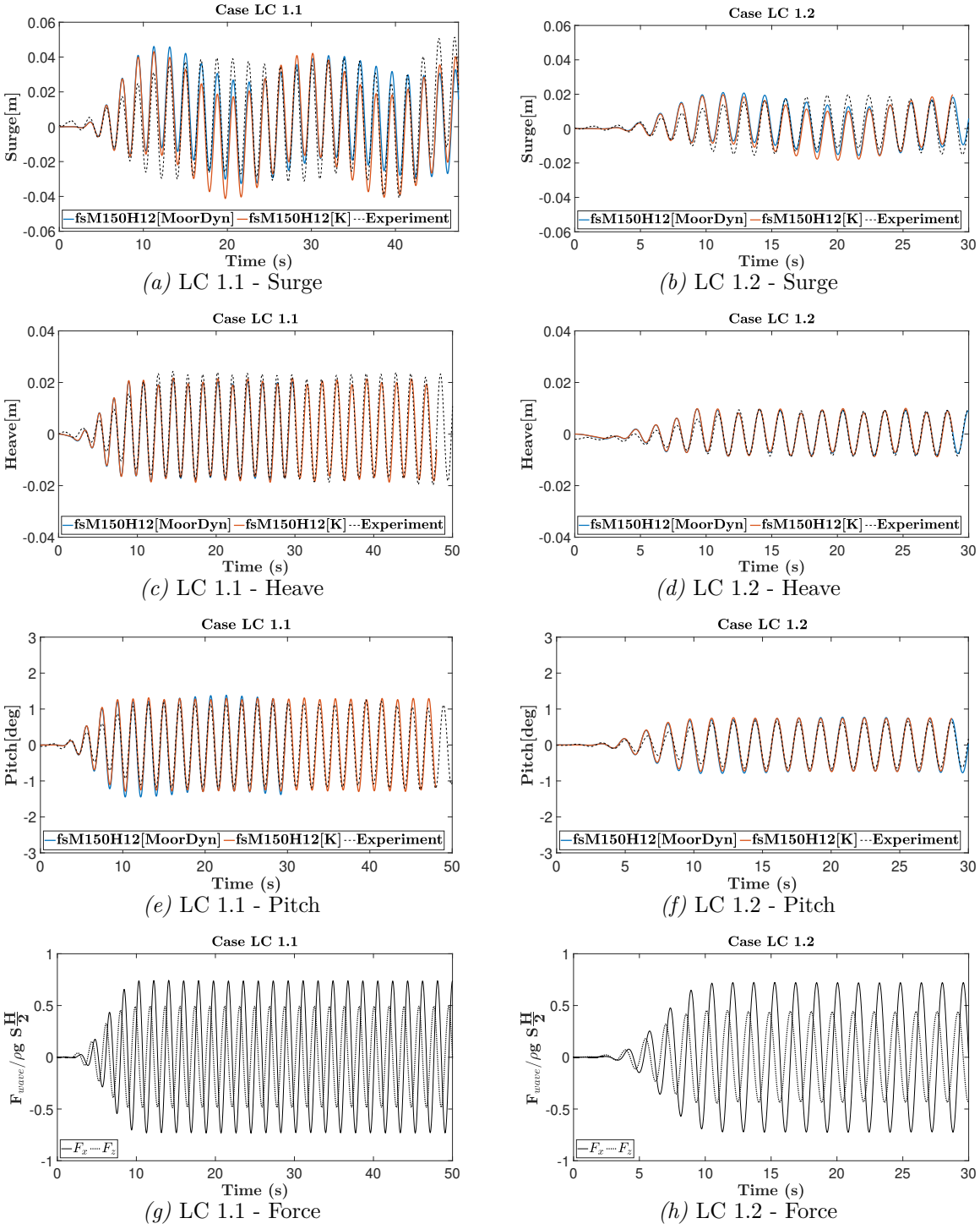


*(a)* LC 1.1 - Surge *(b)* LC 1.2 - Surge

*(c)* LC 1.1 - Heave *(d)* LC 1.2 - Heave

*(e)* LC 1.1 - Pitch *(f)* LC 1.2 - Pitch

*(g)* LC 1.1 - Force *(h)* LC 1.2 - Force

Figure 5.28 – Comparison between experimental and numerical time series of the surge, heave, and pitch of the floating SPAR and wave excitation forces for the two regular wave test cases - LC1.1 and LC 1.2

surge experimental period. In the case of LC 1.2, the surge motion follows a similar trend as LC 1.1, albeit with a much smaller amplitude. The behavior of the stiffness matrix component and MoorDyn is virtually identical, although MoorDyn has a very slightly higher amplitude. This

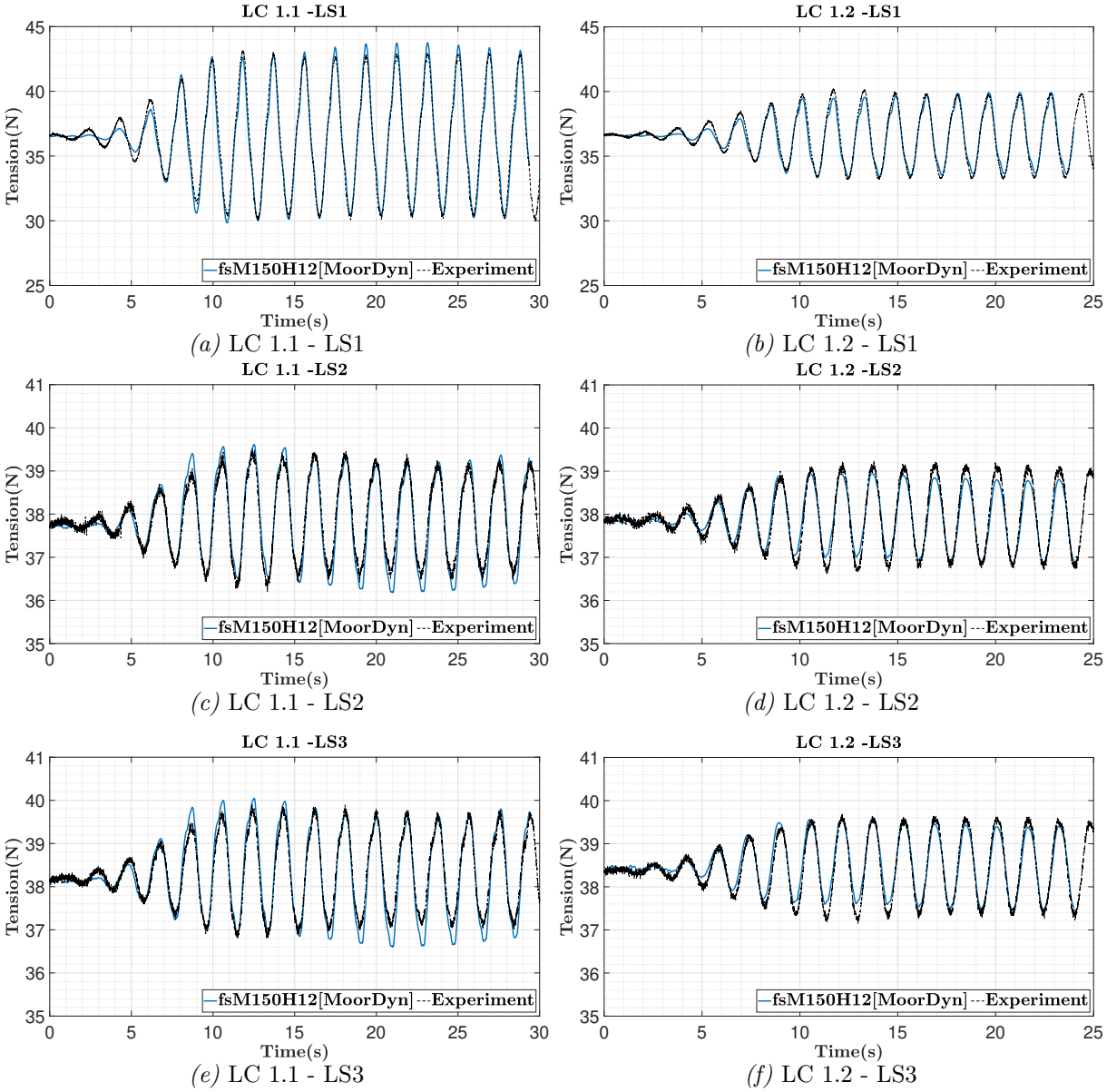


*(a)* LC 1.1 - LS1 *(b)* LC 1.2 - LS1

*(c)* LC 1.1 - LS2 *(d)* LC 1.2 - LS2

*(e)* LC 1.1 - LS3 *(f)* LC 1.2 - LS3

Figure 5.29 – Comparison between experimental and numerical time series of tensions of the front, line 1(LS1), and rear mooring lines, line 2 and line 3 (LS2 and LS3), for the two regular wave test cases - LC1.1 and LC 1.2

is due to the fact that MoorDyn includes coupling of all DoF, whereas, in the stiffness matrix approach, we have considered only three DoFs. The heave and pitch motions of the LCs are depicted in the Figures 5.28c and 5.28d, and Figures 5.28e and 5.28f. The motions were well simulated by both the stiffness matrix approach and MoorDyn and both the motion amplitudes are quite small, with heave amplitudes of nearly 2 cm and 1 cm and pitch amplitudes of $1.25^o$ and $0.8^o$. From the results. it proves that the accurate stiffness matrix components are sufficient to handle the problem for this small amplitude of motions (even if LC 1.1 have larger amplitude). Thus, dynamic mooring analysis may not be required in such cases. However, MoorDyn has an advantage if the requirement is for the estimation of restoring force or the mooring tension

assessment. Figure 5.28g and Figure 5.28h represent the wave excitation forces over the floating SPAR for the load cases LC 1.1 and LC 1.2 respectively. As stated in section (2.1.4.1), the total force acting on the SPAR is influenced by a number of factors like mass, buoyancy, gravity, mooring, fluids (including pressure and viscosity), and so on. Using fluid forces, we can derive solely the wave excitation forces operating over the SPAR by taking into account the normal pressure acting over the SPAR and its tangential viscous component.

Following Huseby and Grue (2000), the wave excitation forces (removing the hydrostatic forces), are normalized by $\rho g S \frac{H}{2}$, where $S$ represents the cross-sectional area of the SPAR. Because the motions closely match the experiment, the forces calculated by the solver should be fairly accurate, and also the numerical cases (stiffness matrix form and MoorDyn form) have similar motions, only results from one form (MoorDyn) is presented. The obtained force trend is proportional to each case's wave elevation, and the x component of the force ($F_x$) amplitude appears to dominate the vertical force ($F_z$) by closely 1.5 times. Otherwise, the normalized amplitude has only a $5\% - 7\%$ difference between LC 1.1 and LC 1.2.

Figure 5.29 shows the line tensions from both LC. It should be noted that the experiment uses three load sensors at the LS position, therefore only Lines 1, 2, and 3 are considered, and since the bridle lines had no tension measurements, they were ignored. In the MoorDyn, the top most segment tensions in the major lines were used for comparison, which was near to LS in the experiment. The experimental data (sampled at 200 Hz) was subjected to an average filter, whereas numerical results are saved at a sampling rate (as determined by the CFD solver) with no filter. The figure shows good comparisons and it's worth noting that Line 1 is at the receiving end of the wave, at the back of the SPAR. As a result, the tension oscillations are up to four times larger than the oscillations of Lines 2 and 3 at the SPAR's front junction. Another point to note is that LS2 and LS3 are symmetric, therefore the tension and variation are identical in both the lines. Despite the input conditions, LC 1.2 tension amplitudes are small when compared to LC 1.1, it demonstrates that *foamStar*-MoorDyn coupling could solve for both the smaller and higher amplitude regular wave interactions with the floating body. Similar observations for motions and tensions were also seen with the quantitative analysis as presented in Section 5.4.2.3. Hence concluding that the regular wave generated inside the *foamStar* by the CN-Stream function wave model has been evaluated for floating SPAR interaction with mooring models, and it appears that the coupling is effective in accurately predicting the motions and forces. The next step is the validation of wave-structure mooring in irregular conditions.

**5.4.2.1.1 Run up on upstream tower** Figure 5.30 shows the run-ups on the upstream SPAR tower from a port side view during one wave period (8.42 T - 9.34 T) for the regular wave case LC 1.1. As the wave amplitude increases, the runup on the tower increases when the crest passes the tower, the maximum runup is 1.26 times the amplitude of the wave, and the maximum run down is identical to the amplitude of the trough passing. It should be emphasized that SPAR is also moving under the influence of the wave, therefore the wave runup recorded is the relative motion between the SPAR motion and the wave.

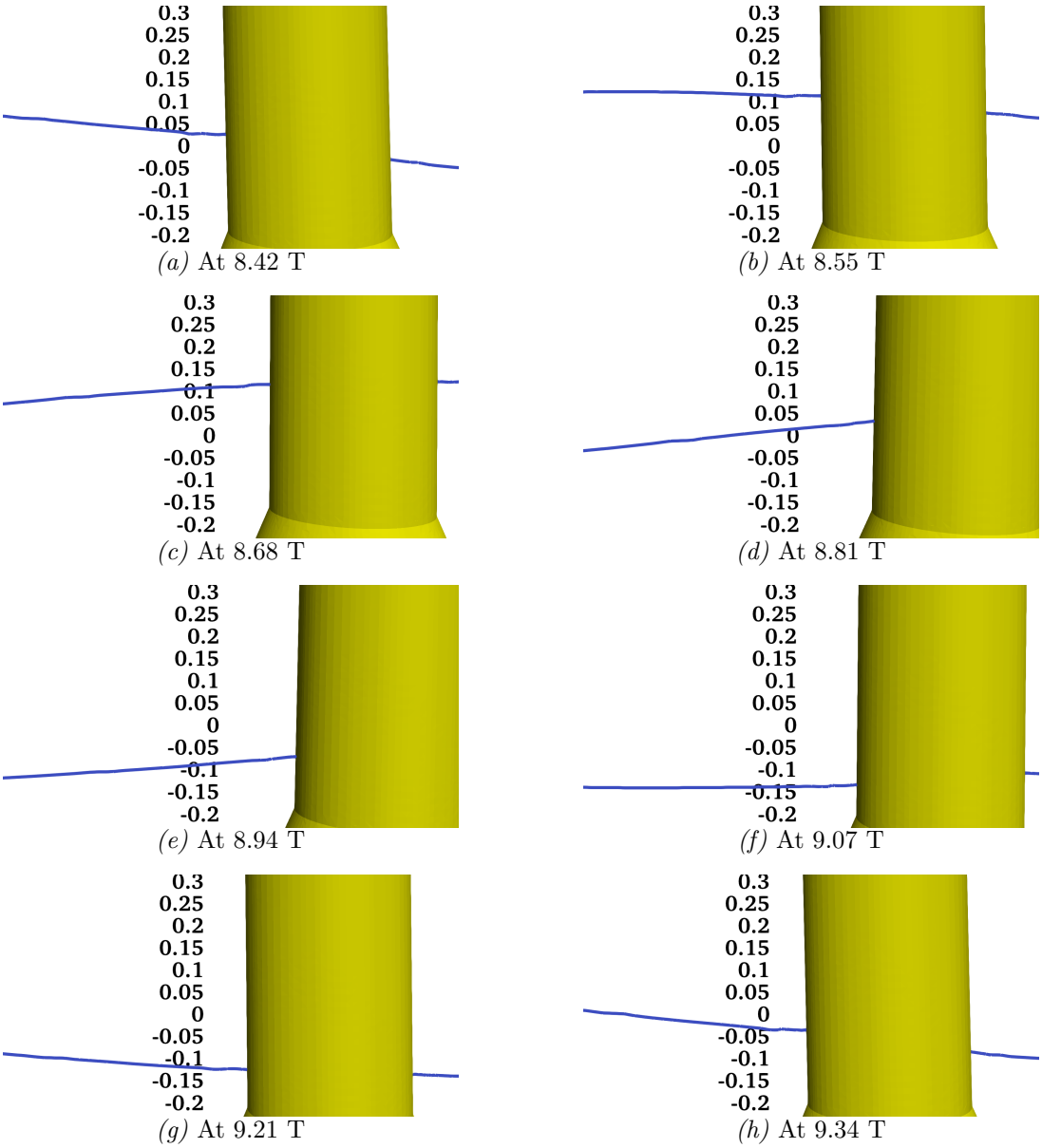


*(a)* At 8.42 T *(b)* At 8.55 T

*(c)* At 8.68 T *(d)* At 8.81 T

*(e)* At 8.94 T *(f)* At 9.07 T

*(g)* At 9.21 T *(h)* At 9.34 T

Figure 5.30 – Run up around the upstream SPAR tower during one wave period for the case LC 1.1

**5.4.2.1.2 Influence of turbulence model** The majority of natural flows are turbulent. Each of the relevant parameters in a turbulent flow can be divided into a "mean" component and a "fluctuating" part, which both change over time and space in an unstable computation. There are different methods to solve the turbulence in the flow. With Direct Numerical Simulation (DNS) solvers, the flow is not decomposed and the governing equations cover the whole range of turbulence scales, which requires very high mesh resolution and temporal resolution for solving the computation. The Large Eddy Simulation (LES) is a numerical model that controls the smallest turbulence length scale via low-pass filtering of the Navier-Stokes equation, reducing the computational cost with respect to DNS. The computationally cheapest technique is using Reynolds-Averaged Navier-Stokes Equations (RANSE). $\kappa-\omega$ *SST* is the widely used turbulence

model in hydrodynamics. The in-house developed turbulence model ' free-surface $\kappa - \omega$ $SST$ (*fskOmega*)' which applies the idea of buoyancy production to the OpenFOAM $\kappa-\omega$ $SST$ model to consider the variation of density of the two-phase flow in the vicinity of the free-surface (Kim, 2021b). This turbulence model is tested for the SPAR for the case of LC 1.1 and the results obtained are as shown in the Figure 5.31. The wave observed between the models (with and without turbulence model *fsKOmega*) is found to be almost identical, with a variation of less than 0.1% in the peak amplitude of crest and trough. The wave comparison between the models is not provided for a concise representation. The addition of the turbulent model is seen to cause a slight variation in amplitude, but overall, the model without turbulence is seen to have captured the motions well in relation to experiment. It holds true for each of the three motions depicted in the figure. The computational cost is further increased by the inclusion of the turbulence model due to the increased number of variables that must be solved. Therefore, for all further upcoming cases, just the model without turbulence is being used.

#### 5.4.2.2 *foamStar* - Irregular wave-structure interaction

Next the SPAR response was investigated for the uni-directional irregular sea state generated based on the Bretschneider spectrum (Table 5.2) in HOS-NWT. Two different irregular sea states were analyzed, Case LC 2.1 is a relatively mild sea state, and Case LC 2.2 corresponds to severe sea state conditions. HOS-NWT is used to simulate the incidence wave field in the whole wave tank based on the motion of the wavemaker from the experiment. The simulation has been carried out for 500-600 s in the experiment and HOS, however in the CFD, it is arranged to keep 50 $T_p$ to restrict the computational cost. The computational domain is comparable to that of the domain used in regular wave interaction study, with the exception that $\lambda_p$ is used instead of $\lambda$. Based on the peak wavelength and the significant wave height ($H_s$), the domain zones were updated to maintain 150 cells per peak wavelength and 12 cells per significant wave height. Time integration is achieved with 400 timesteps per peak wave period (fsM150H12T400). The time history comparison between the *foamStar* and the experimental measurements for WG4 is shown in Figure 5.32. Unlike regular waves, here the experimental wave paddle motion has been used, so there is no ramping issue in both the test cases. However, it should be noted that the HOS has few discrepancies in comparison with the experimentally measured wave for some amplitudes and that these discrepancies (Section 5.3.3.1) are also seen in the *foamStar* produced waves. Also, as noted in the parametric study, discrepancies created owing to mesh and time discretization in *foamStar* could also be added to the total discrepancy. However, the difference is very small in the case of a small amplitude case (LC 2.1) and a little higher for a higher amplitude case (LC 2.2). It should also be emphasized that the waves recorded are with the SPAR in place in experiment and hence the influence of scattered waves from the SPAR will also contribute to the wave elevation recorded.

The SPAR response in surge, heave, and pitch for the cases of LC 2.1 and LC 2.2 are shown in the in Figure 5.33 and mooring tensions from the corresponding cases are shown in Figure 5.34. The influence of the two mooring approaches is discussed similar to regular wave

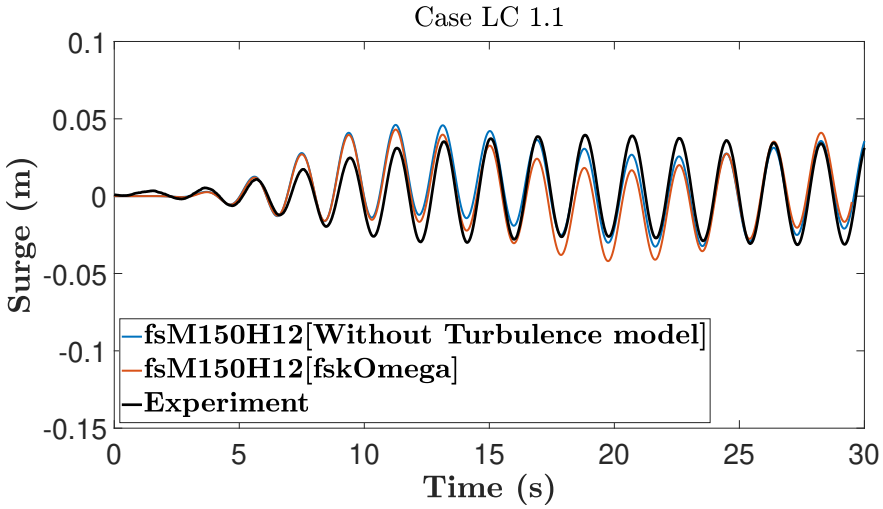


*(a)* LC 1.1 - Surge

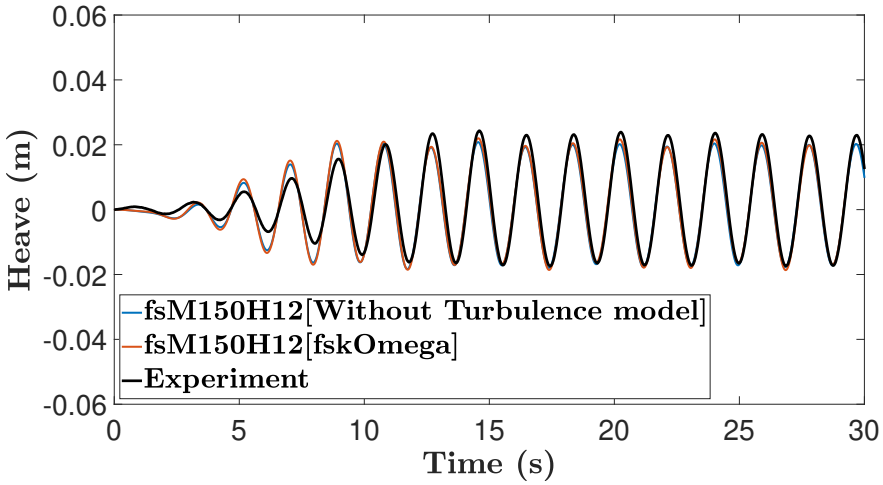


*(b)* LC 1.1 - Heave

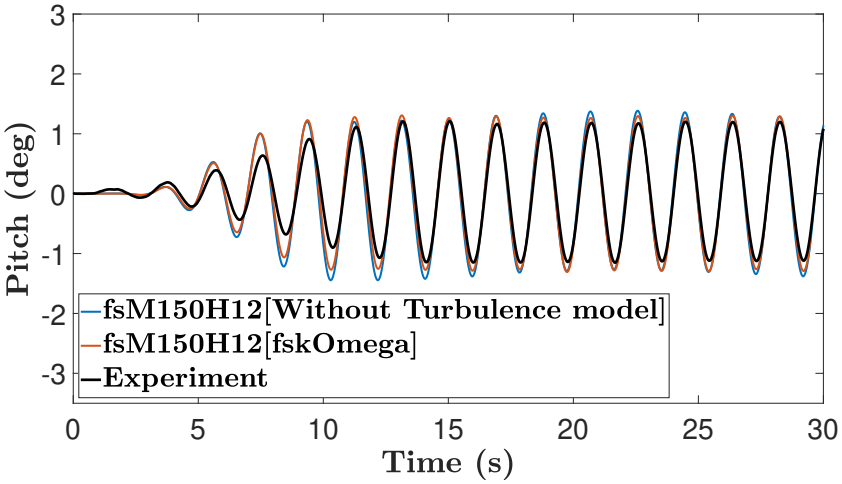


*(c)* LC 1.1 - Pitch

Figure 5.31 – Comparison between laminar and turbulent time series of the surge, heave and pitch of the floating SPAR and wave excitation forces for the LC1.1

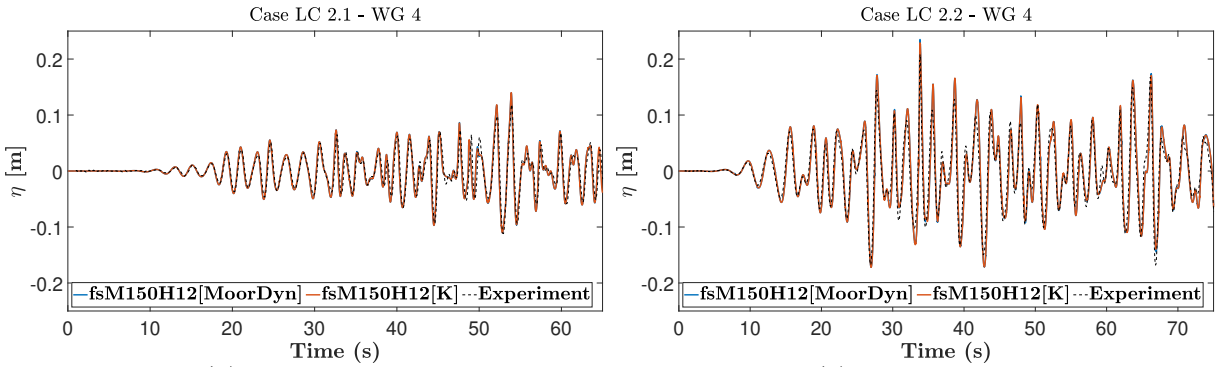


*(a)* LC 2.1 - WG4 *(b)* LC 2.2 - WG4

Figure 5.32 – Comparison between experimental and numerical time series of Wave elevation WG4 of the Floating SPAR for the two irregular wave test cases - LC 2.1 and LC 2.2

interaction with SPAR. In the case of LC 2.1, there were very few to no discrepancies between the motions predicted in surge, heave, and pitch with the experiment. Figure 5.33a and Figure 5.33b depict the surge motions recorded for LC 2.1 and LC 2.2. For LC 2.1, fsM150H12[MoorDyn] predicted comparable motions than when using stiffness matrix for mooring modelling. However, for the case of LC 2.2., the comparisons were accurate at the beginning, but when the wave amplitudes increased, the stiffness matrix approach leads to more deviation modifying the SPAR response. However, the fsM150H12[MoorDyn] prediction compared well with the experimental surge motion. For the heave (Figure 5.33c, Figure 5.33d) and pitch (Figure 5.33e, Figure 5.33f) motions also, mild case (LC 2.1) compared well with the experiment but for the severe case (LC 2.2) stiffness matrix approach has certain discrepancies. The differences in the pitch cases are also identical to the wave amplitude variations reported. The MoorDyn simulations overpredict the pitch by a few decimals in the amplitudes and this little over prediction may be seen throughout the LC, although it is of modest size. The cause for this might be that the mooring configuration in the experiment is not perfectly symmetric, resulting in small unsettled moments in the pitch direction. Also, with all of the nacelle RNA supports, it is possible that the $I_{yy}$ provided by the experiment is not highly accurate. Overall, the findings showed that the coupled model's motion prediction is precise for both the sea state conditions. The stiffness matrix approach prediction is very good for mild sea states, but for severe sea states, a dynamic mooring model is required for accurate motion prediction similar to that of the experiment. A similar conclusion is quantitatively obtained in the Section 5.4.2.3. The Figure 5.33g and Figure 5.33h represents the normalized hydrodynamic force components obtained over the SPAR for the cases of LC 2.1 and LC 2.2, respectively. As noted in the regular wave cases, the force trend corresponds very well to the wave elevation, and the amplitude ranges are confined between ±0.5 for both the load cases. Overall, the range of forces with respect to wave height demonstrates that regular waves develop nearly 1.5 times higher force range than the irregular waves, whereas irregular waves display peak amplitudes at certain locations exceeding 0.9-1, indicating the strength of its impact.

The abrupt change of tension (Figure 5.34b to Figure 5.34f) happening in very short interval

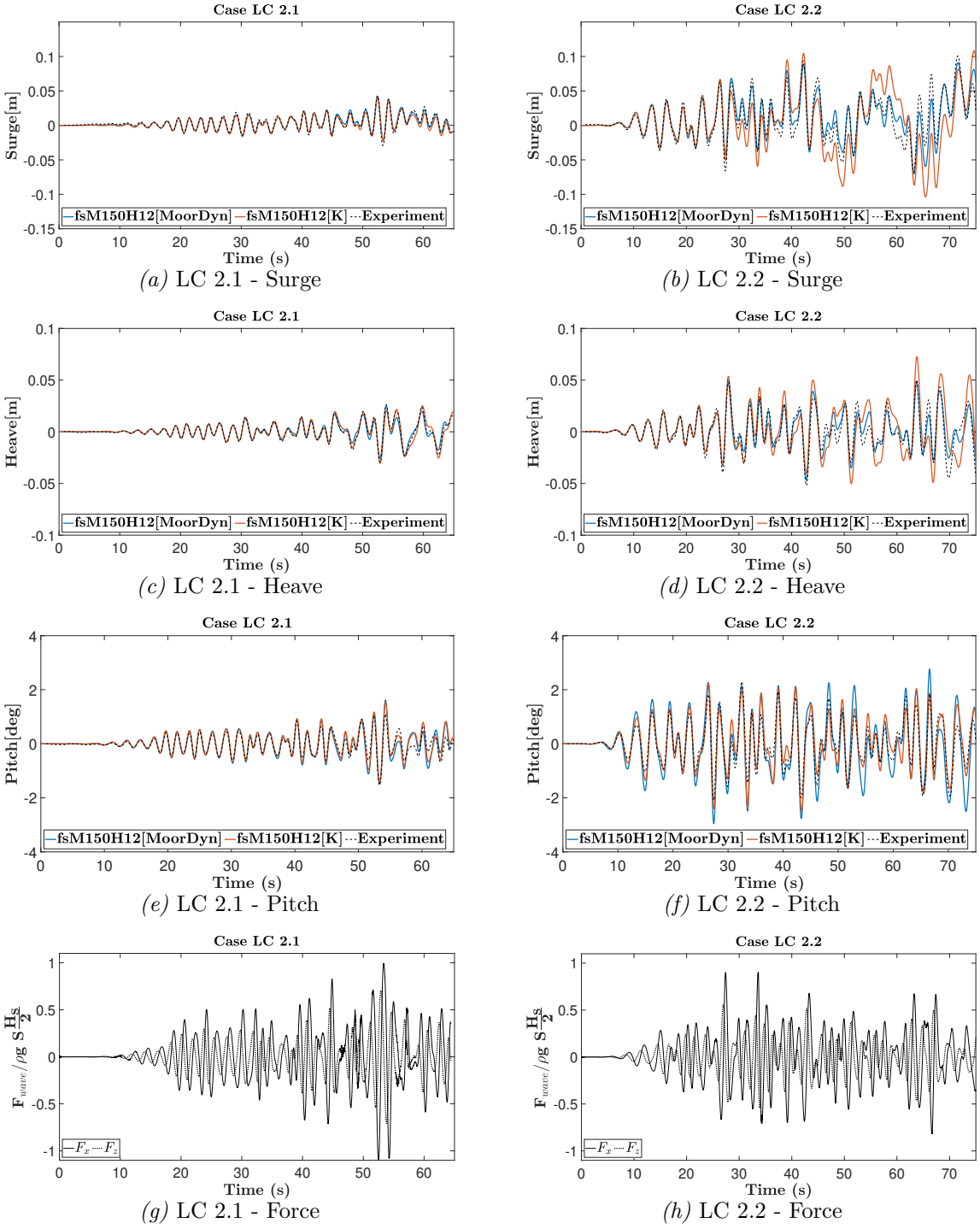


*(a)* LC 2.1 - Surge *(b)* LC 2.2 - Surge

*(c)* LC 2.1 - Heave *(d)* LC 2.2 - Heave

*(e)* LC 2.1 - Pitch *(f)* LC 2.2 - Pitch

*(g)* LC 2.1 - Force *(h)* LC 2.2 - Force

Figure 5.33 – Comparison between experimental and numerical time series of the surge, heave and pitch of the floating SPAR and wave excitation forces for the two Irregular wave test cases - LC2.1 and LC 2.2

of time for the LC 2.2 required robust mooring model to capture tensions accurately. In the case of LC 2.1, the tension forces match quite well in all three lines. In large surge drift offset circumstances, the most substantial tension is evident in the seaward cable. The force amplitudes of the leeward and seaward mooring lines are identical in amplitude when there is little or no

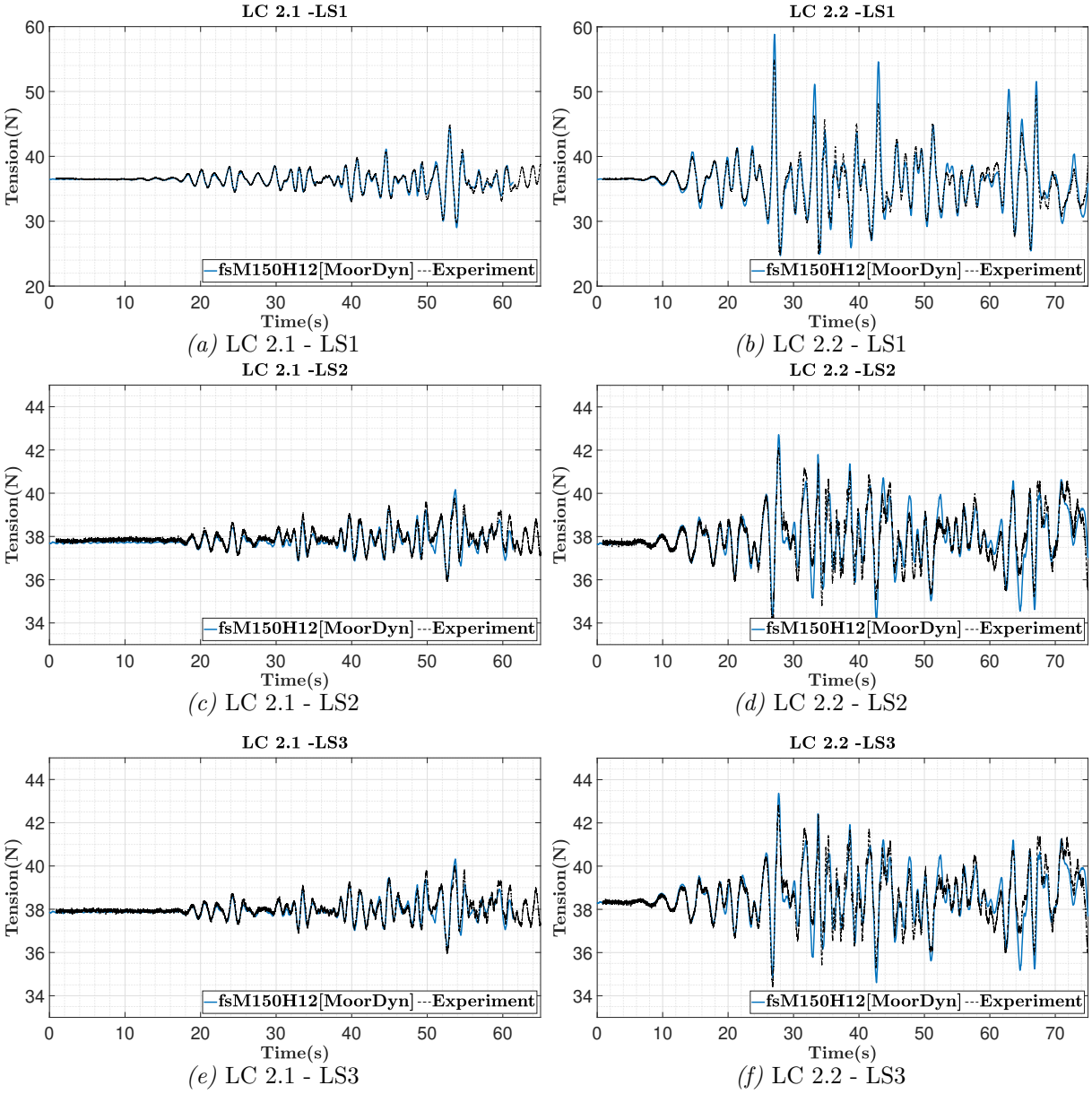


*(a)* LC 2.1 - LS1 *(b)* LC 2.2 - LS1

*(c)* LC 2.1 - LS2 *(d)* LC 2.2 - LS2

*(e)* LC 2.1 - LS3 *(f)* LC 2.2 - LS3

Figure 5.34 – Comparison between experimental and numerical time series of tensions of the front, line 1 (LS1), and rear mooring lines, line 2 and line 3 (LS2 and LS3), for the two irregular wave test cases - LC2.1 and LC 2.2

drift. For LC 2.2, the predicted mooring tension appears to be in phase with the experiment, however, the amplitudes are slightly larger than expected, the reason has been addressed earlier in wave comparison part. The amplitude variation of tension between 15 to 25$N$ in a short time frame of less than a second (LC 2.2) is 3 to 4 times larger than any variations reported earlier (particularly LC 2.1). The coupled solver captures all of these tension variations with little to no inconsistencies, showing the efficiency of the coupling. In comparison to all the cases reported, the LS2 and LS3 lines experience more impact tension variations only in LC 2.2 which is also accurately captured by the *foamStar*-MoorDyn coupled solver.

#### 5.4.2.3 *foamStar* - Quantitative analysis

The qualitative comparison presented in the previous sections is quantitatively compared in this section using a cross-correlation analysis. The coefficient is computed with Eqn. 2.1.6.1, but the motions and the mooring tensions of the numerical model are compared with the experiment instead of the surface elevation. Recalling from Section 5.3.3, the maximum cross-correlation coefficient of +1 indicates a perfect match between the *foamStar* and the experimental results, and the distance to 1 quantifies the difference between the signals. The surge motions in the regular wave were sensitive to the ramp in the wave generation, and the Figures 5.35a and 5.35b illustrate this discrepancy between the signals and the experiment for both the stiffness matrix and dynamic mooring cases. In the stiffness matrix cases, the coefficient are 0.89 and 0.93 for LC 1.1 and 1.2, respectively. However, a minor improvement is seen with MoorDyn (coefficient of 0.94 in both cases), even though the ramp effect is still present. The stiffness matrix approach achieved a good comparison of 0.98 for the mild sea condition LC 2.1 (Figure 5.35c) but lost accuracy to 0.86 for LC 2.2 (Figure 5.35d). With values higher than 0.96 in both LC 2.1 and LC 2.2, MoorDyn appears to perform well, supporting the validity of the discussions from earlier sections. In LC 1.1, LC 1.2, and LC 2.1, heave and pitch motions are well reproduced by the numerical model, with coefficient ranges of 0.99 and higher by both the approaches. While MoorDyn appears to perform well in LC 2.2, reaching a coefficient up to 0.96 and above, the stiffness matrix cases are less accurate, and the coefficient stays at 0.9 to 0.94 (Figure 5.35d). The mooring tensions appear to match well in all the cases with the coefficients in the range of 0.99 to 0.999 (Figure 5.35), proving the efficiency of the mooring model and its coupling.

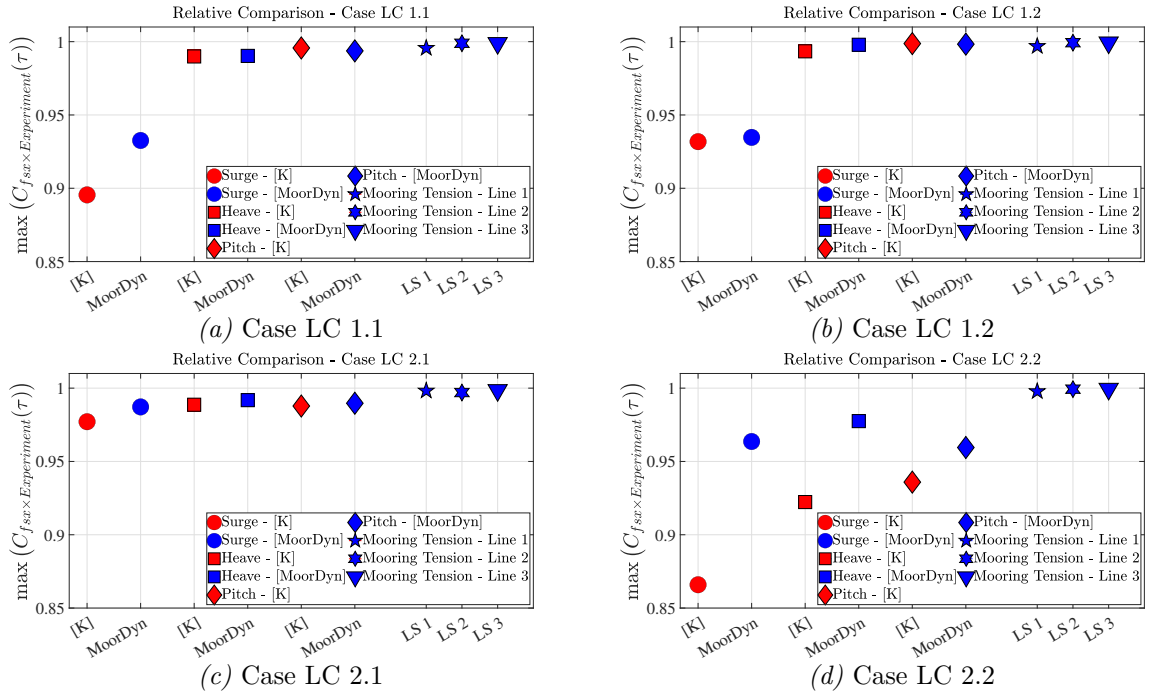


*(a)* Case LC 1.1 *(b)* Case LC 1.2

*(c)* Case LC 2.1 *(d)* Case LC 2.2

Figure 5.35 – Relative analysis using Cross Correlation between foamStar cases and Experiment where [K] represents stiffness matrix approach, MoorDyn represents dynamic mooring coupled approach

#### 5.4.2.4 *foamStarSWENSE* - Irregular wave-structure interaction

Only irregular wave interaction with SPAR is examined in the SWENSE approach to validate the model's efficiency in estimating floating body interaction with mooring. Also, only the mooring analysis with MoorDyn is investigated because of its robustness, and the mooring in the form of a stiffness matrix is ignored. The coupling technique is identical to that of the *foamStar* since the ODE solver and its force calling remains unchanged. Two cases of LC 2.1 and LC 2.2 irregular waves are examined using the same computational domain used with *foamStar*. All other parameters are the same, and the motions recorded for the SPAR are shown in the Figure 5.37 alongside the *foamStar* data taken as a reference. Figure 5.36 shows a typical representation of the complementary velocity field $\boldsymbol{u}_c$ for LC 2.2 snapped at 25 s. The complementary velocity field is shown over the free surface in the computational zone, with a white line denoting the border between the relaxation zones and the full-CFD computational zone. The complementary field distribution over a cross section is shown on the right side of the figure. The legend has been adjusted to reflect even tiny $\boldsymbol{u}_c$ replicas. This complementary field across the free surface represents the scattered wave from the SPAR, together with the modification done by the model to the incoming wave.

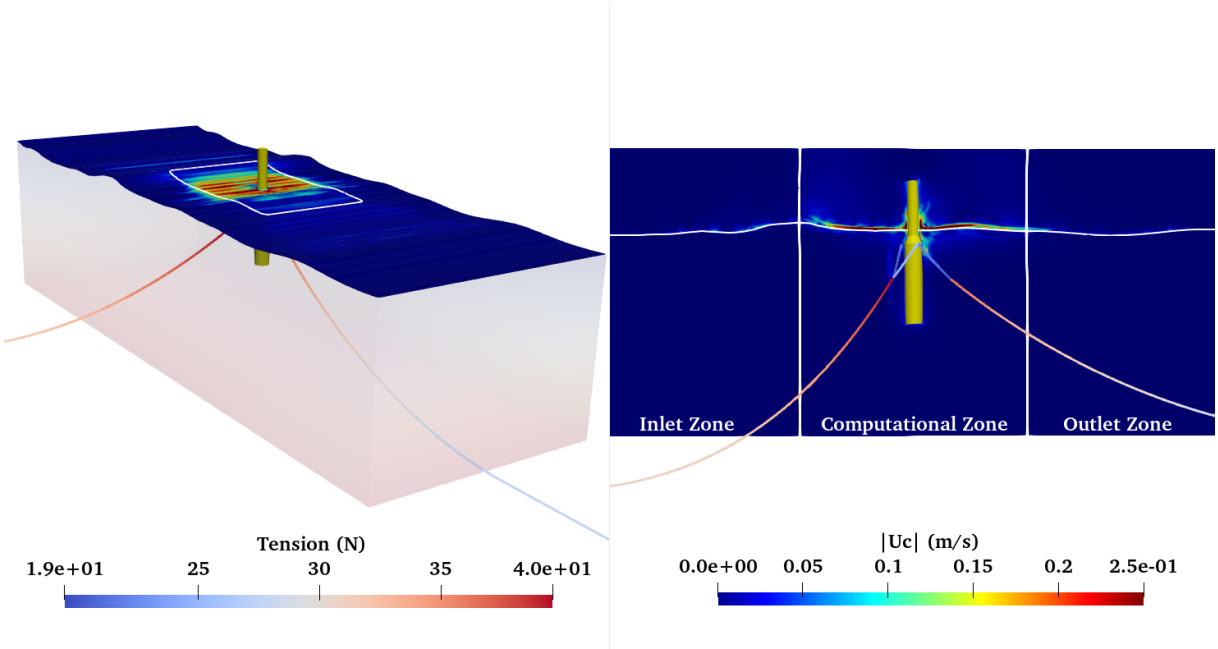


Figure 5.36 – Typical complementary velocity field generated at $T_p = 25s$ for the case of LC 2.2 in both the free surface and vertical plane using *foamStarSWENSE*

On the left and right sides of Figure 5.37, the surge, heave, and pitch motions recorded for LC 2.1 and LC 2.2 are shown. The *foamStarSWENSE* results are strikingly comparable to those of *foamStar*, with the difference in the order only $10^{-4}$ in the case of LC 2.1. With minor differences, the motions measured for a severe sea state of LC 2.2 were nearly identical to either *foamStar* or the experiment. This is demonstrated using a cross-correlation study that quantitatively compares the solutions with the experiment. The results are presented in Figure 5.39. In

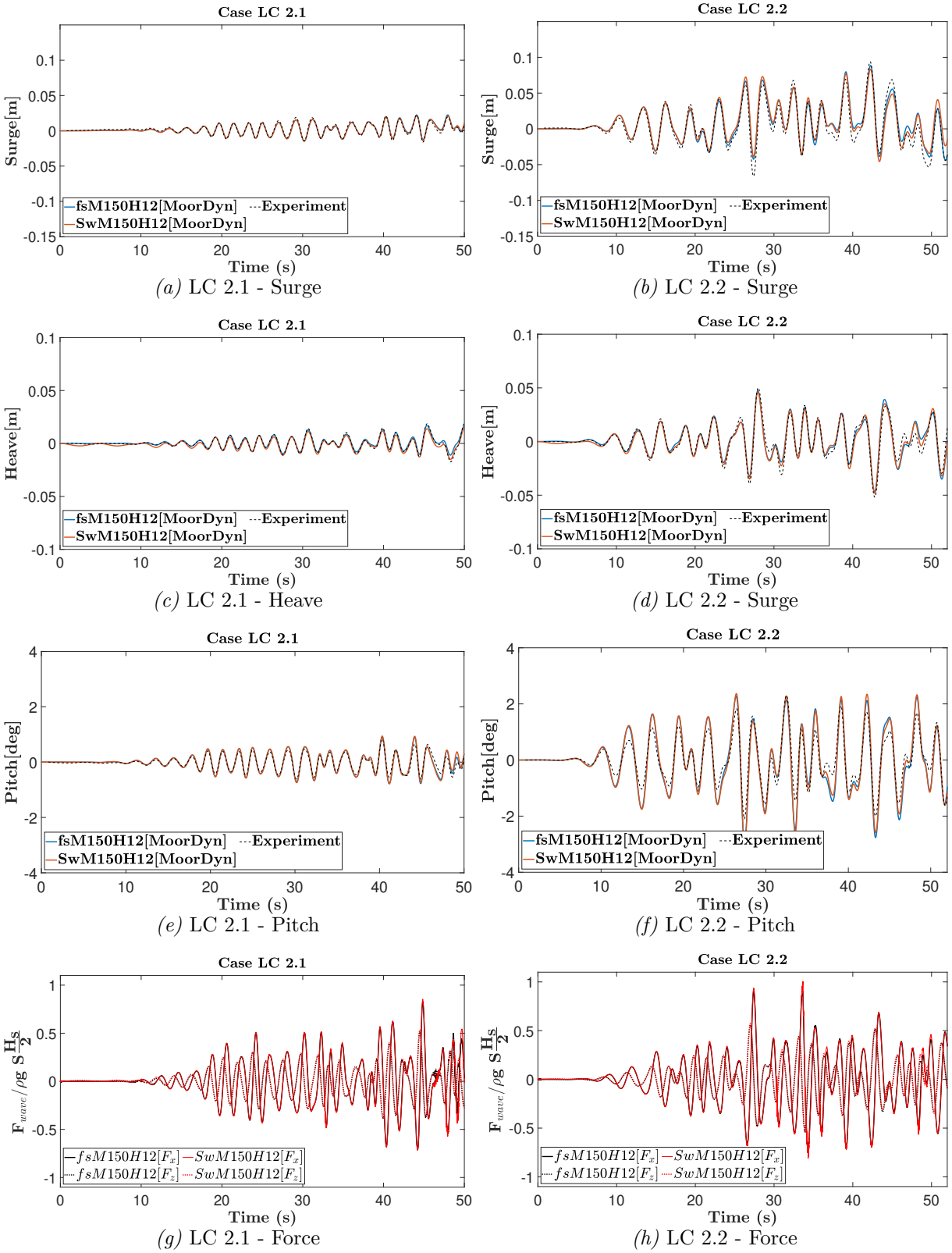


*(a)* LC 2.1 - Surge *(b)* LC 2.2 - Surge

*(c)* LC 2.1 - Heave *(d)* LC 2.2 - Surge

*(e)* LC 2.1 - Pitch *(f)* LC 2.2 - Pitch

*(g)* LC 2.1 - Force *(h)* LC 2.2 - Force

Figure 5.37 – Comparison between experimental and *foamStarSWENSE* time series of the surge, heave and pitch of the floating SPAR and wave excitation forces for the two Irregular wave test cases - LC2.1 and LC 2.2

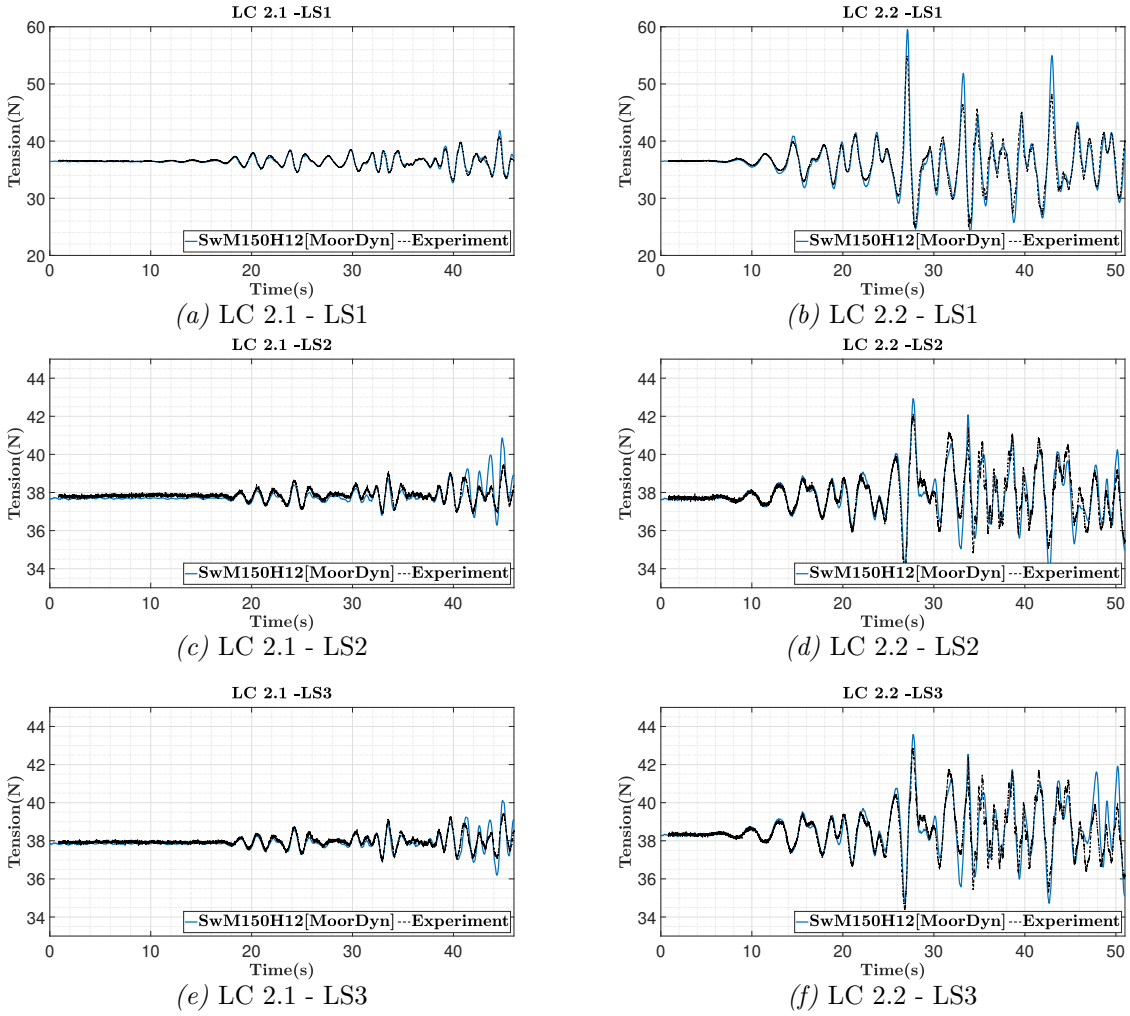


*(a)* LC 2.1 - LS1 *(b)* LC 2.2 - LS1

*(c)* LC 2.1 - LS2 *(d)* LC 2.2 - LS2

*(e)* LC 2.1 - LS3 *(f)* LC 2.2 - LS3

Figure 5.38 – Comparison between experimental and numerical time series of tensions of the front, line 1 (LS1), and rear mooring lines, line 2 and line 3 (LS2 and LS3), for the two irregular wave test cases - LC2.1 and LC 2.2

both irregular wave conditions, the surge and heave motion predicted by the *foamStarSWENSE* solver is marginally more accurate than the one predicted with the *foamStar* solver. However, when comparing the results for pitch motion, *foamStar* solver is somewhat more accurate than *foamStarSWENSE* for LC 2.1. However, in the event of LC 2.2, *foamStarSWENSE* outcomes are marginally superior. Overall, despite the cross-correlation showing that *foamStarSWENSE*'s accuracy is somewhat superior to *foamStar*'s for the analytical time window considered, the differences are minimal. The force comparison at the bottom of the figure verifies the preceding statements by demonstrating a good match in terms of phase and amplitude. This demonstrated that the SWENSE model, like the NS solver, can accurately predict motions and forces over a floating body. Like the motions comparison study, the mooring tension measured in the solver proved to be accurate, as shown in Figure 5.38. A quantitative comparison of mooring tensions between the experiment and *foamStarSWENSE* further confirms this statement. As shown in Figure 5.39, the *foamStarSWENSE* observation of mooring tension exhibits similar

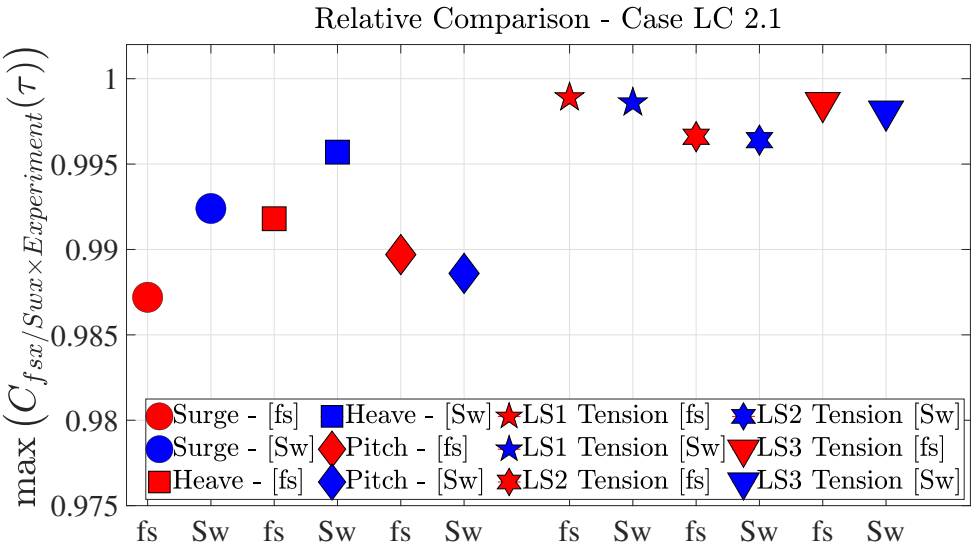


*(a)* Case LC 2.1

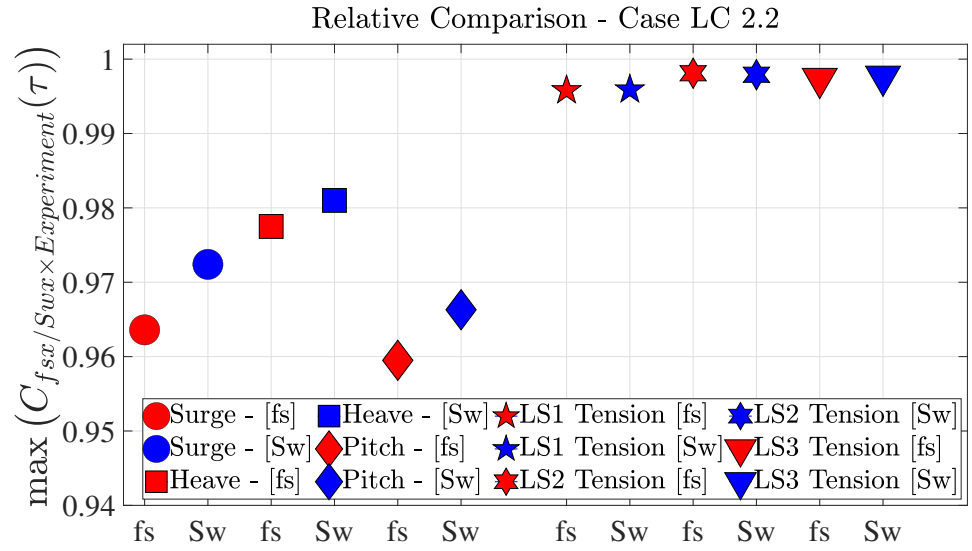


*(b)* Case LC 2.2

Figure 5.39 – Relative analysis using Cross Correlation between *foamStar* and *foamStarSWENSE* cases and experiment where 'fs' represents *foamStar* solver matrix approach, 'Sw' represents *foamStarSWENSE* solver

accuracy to the *foamStar* with only negligible deviations for the analysis window considered. As aforementioned, under large surge drift offset situations, the most significant tension is seen in the seaward line rather than the leeward lines. In LC 2.1, the force amplitudes of the leeward and seaward mooring lines are consistent in amplitude and phase with the experiment. The estimated mooring tension for LC 2.2 also looks to be in phase with the experiment, but the amplitudes are slightly higher, similar to the *foamStar* observation. As a result, the solution produced these tension changes with little to no variance, proving the efficiency of coupling in SWENSE. The computational cost of the *foamStarSWENSE* compared to *foamStar* is similar to the findings of the focusing wave interaction investigation. *foamStarSWENSE* has 1.3 times

higher computational cost than *foamStar* for the same mesh arrangement (Mesh150H12). The objective provided is that both solvers were able to recreate the experiment with a moored floating body. As a result, one of another future study is to determine why the same mesh configuration in *foamStarSWENSE* takes more computational time and how to improve the computational efficiency.

#### 5.4.2.5 *foamStarSWENSE* - Coarsest mesh vs finest mesh

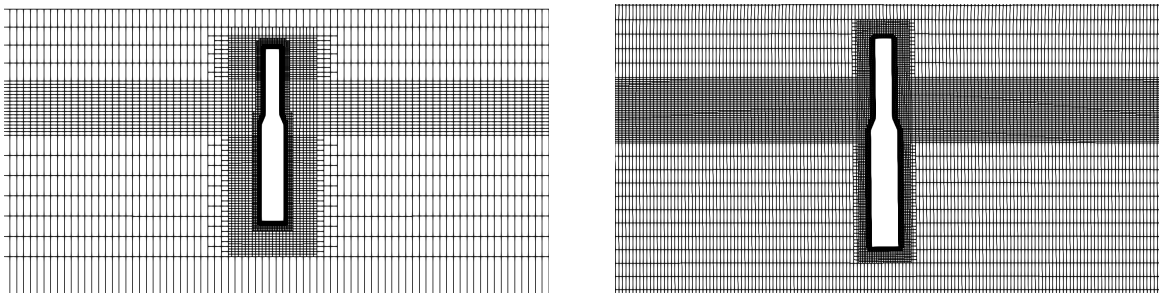

Figure 5.40 – Typical computational domain for investigating the advantage of using *foamStar-SWENSE* solver with mesh type Mesh64H5 on left side and Mesh150H12 on the right side

Next, to evaluate the accuracy of the SWENSE methodology in the moored floating body simulation, a coarse mesh type combination is chosen as similar to the study carried out in earlier chapters (ref Section 3.3.1.1). Mesh types from Figure 5.17 are chosen for the cases, and already, Mesh150H12 has demonstrated a good comparison. This case will be compared with Mesh64H5, which is regarded as a coarser mesh type for this study. Figure 5.40 provides an understanding of the two mesh types that will be examined. Based on the lessons learned from the focusing wave cases, it was decided to maintain the same refinement around the SPAR body. This is because *foamStarSWENSE* requires the same mesh resolution as the one needed with *foamStar*. Hence, In order to study this SWENSE benefit, the refining close to the floating body is kept relatively similar to Mesh150H12, and just the outer domain is made coarser. The number of cells has lowered from 1.8 million cells in the case of Mesh150H12 to 0.6 million cells in the case of Mesh64H5. Since LC 2.2 is a very irregular and extreme wave state, it has been chosen as the wave condition for this investigation. Along with that, the motions observed for LC 2.2 are difficult to simulate as similar to the experimental results as seen in previous *foamStar* sections, this extreme case (LC 2.2) is chosen to study the coarser mesh evaluation for SWENSE advantage. It should be noticed that compared to Mesh150H12, the Mesh64H5 wave accuracy in incident wave generation has little variance. This mismatch is typically seen when predicting waves with shorter or longer amplitudes. It may also show as missing some higher frequencies. Refer to Figure 5.17 for an evaluation of wave elevation for various mesh types to confirm its accuracy. This is to remind the reader that, with this mesh type, the motions and mooring tension measured during the wave interaction with the SPAR will show a minor reduction in accuracy.

Figure 5.41 depicts the motion and force that were seen during this interaction. For reference,

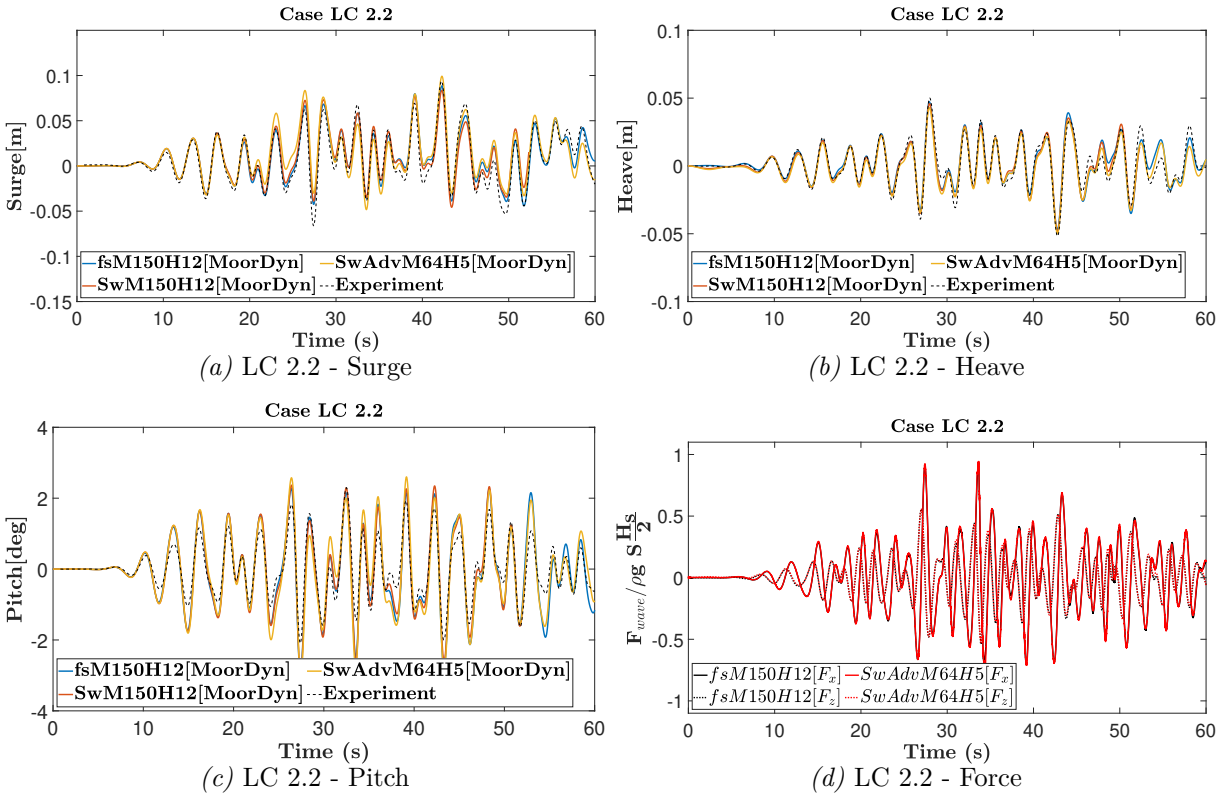


*(a)* LC 2.2 - Surge *(b)* LC 2.2 - Heave

*(c)* LC 2.2 - Pitch *(d)* LC 2.2 - Force

Figure 5.41 – Comparison between experimental and SWENSE advantage mesh type Mesh64H5 of the surge, heave and pitch of the floating SPAR and wave excitation forces for the LC 2.2

the mesh findings from *foamStar* (fsM150H12) and *foamStarSWENSE* (SwM150H12) are also provided with the experiment. It is also included for the reason that a comparison of these types will be discussed at the end of this section. For a qualitative discussion, SwAdvM64H5 (SWENSE Advantage Mesh M64H5) seems to be in good phase with the motions observed in all three motions (Surge, Heave and pitch) recorded. The peak amplitudes of the surge and pitch motions differ slightly about $10-12\%$. Surprisingly, the heave motion seems to be in good phase and amplitude agreement with the experiment and fs/SW M150H12 mesh types. The cross-correlation between the signals in Figure 5.43a is used to analyse and support these statements quantitatively. From the figure, fs stands for *foamStar* mesh results, Sw for *foamStarSWENSE* mesh results (same mesh like *foamStar*- Section 5.4.2.4), and SwAdv for *foamStarSWENSE* advantage mesh. For the heave motions, the results are identical to both the solver's solution, and the surge and pitch results are relatively different from the *foamStar* and *foamStarSWENSE* solutions. Also, based on these findings, a similar trend is observed in the force measured over the SPAR, with some localised areas where there is a small peak amplitude fluctuation of variation around 15%. The overall observation appears to suggest that even the coarsest mesh types on outer regions and finer refinement near the floating body in *foamStarSWENSE* solver, can predict motions and force over the body reasonably well with minor variations.

A few things are to be recalled for the comparative discussion over the mooring tensions. LS represents the load sensor between the mooring lines and bridles, with LS1 representing the line

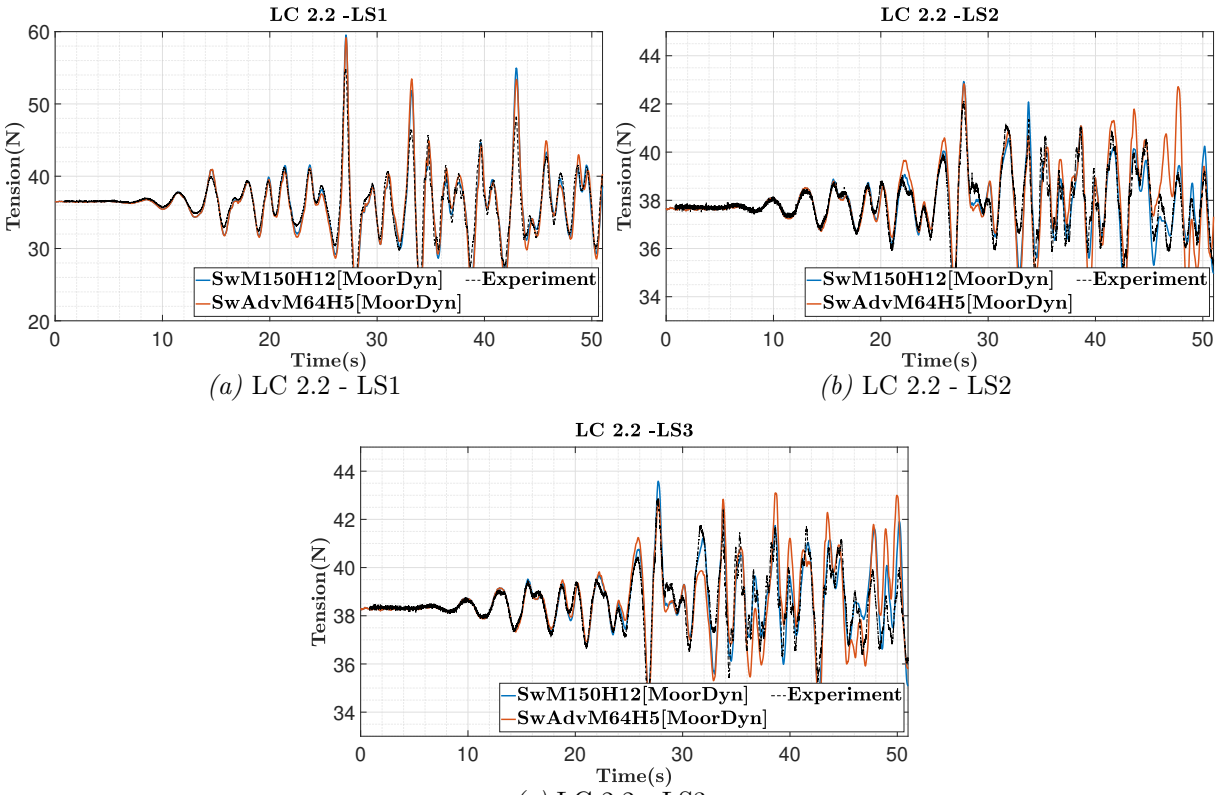


*(a)* LC 2.2 - LS1

*(b)* LC 2.2 - LS2

*(c)* LC 2.2 - LS3

Figure 5.42 – Comparison between experimental and SWENSE advantage mesh type Mesh64H5 of the mooring tensions of the floating SPAR for the LC 2.2

on the leeward side of the SPAR and LS2 representing the lines in front of the SPAR. The mooring tensions encountered during the wave interaction with SPAR for mesh-type SwAdvMesh64H12 are shown in Figure 5.42 . Again, for reference purposes, experimental and SwM150H12 mesh types results are also shown. It could be observed that LS1 mooring tension observed, appears to have minimum variation between the experiment and this coarser mesh. But the LS2 and LS3, although the tension force is in phase with experiment, show variations of order 2%-5% in specific locations in the deterministic comparison. This is also proved with the cross correlation analysis between the simulated mooring tensions with the experimental observations (Figure 5.43b). Although LS1 divergence appears to be very minimal, LS2 and LS3 SwAdvMesh64H12 coefficients indicate wider deviation from the foamStar and foamStarSWENSE finer mesh results. The variations discussed in surge and pitch motions is the main reason for this discrepancy. Overall, using this coarser mesh evaluation (SwAdvM64H5), even though the findings are not extremely accurate with the experiment, we can obtain reasonable values of forces and mooring tensions in a very brief run (Computational cost discussion in following subsection) rather than running the finer cases for a long period of time.

**5.4.2.5.1 Computational efficiency** Recalling the computational efficiency procedure followed from the Section 3.3.1.3, discretization for parallel simulations is maintained at 1 CPU for every 30000 cells. All the simulations are run with the same residual tolerances and schemes.

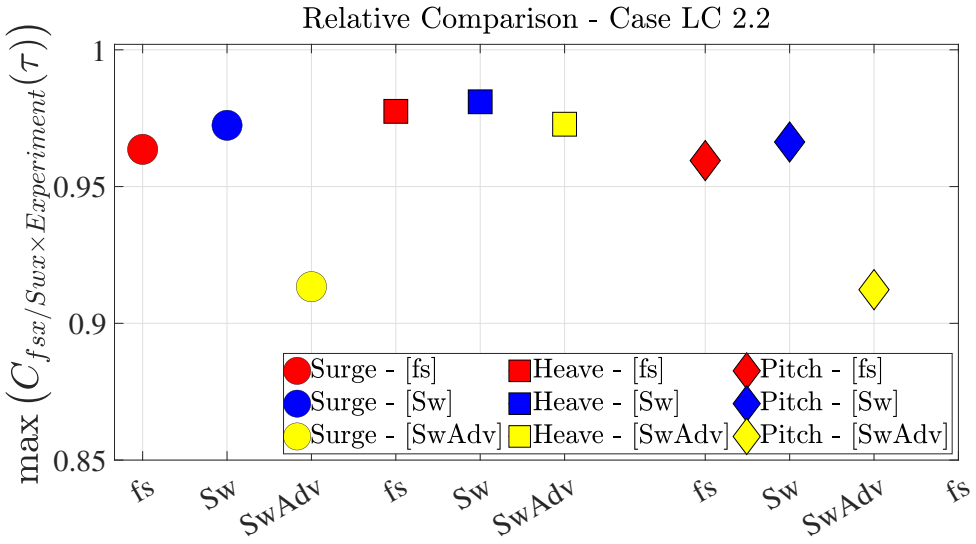


*(a)* Case LC 2.1

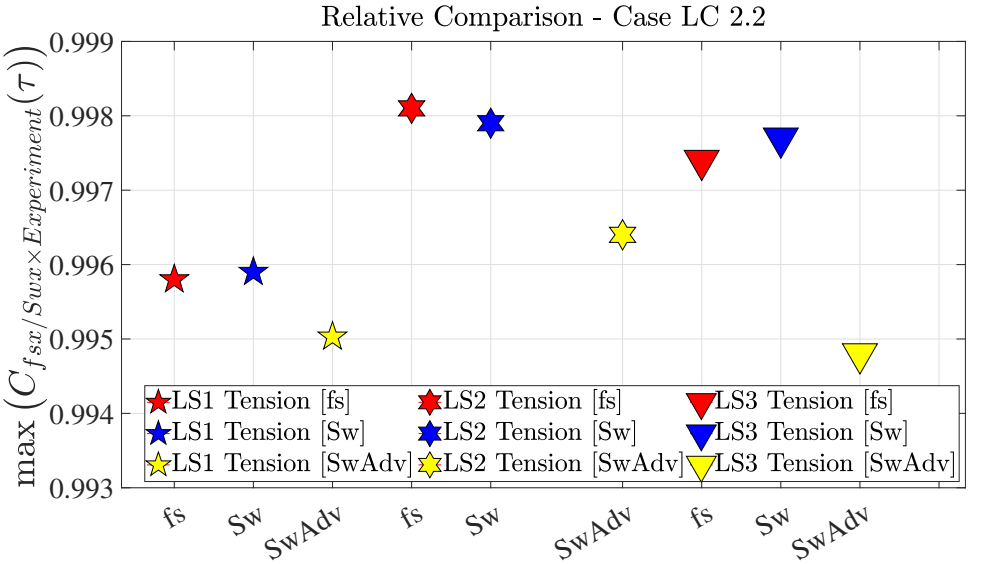


*(b)* Case LC 2.2

Figure 5.43 – Relative analysis using Cross Correlation between *foamStar* and *foamStarSWENSE* solvers and experiment where 'fs' represents *foamStar* solver matrix approach, 'Sw' represents *foamStarSWENSE* solver, 'SwAdv' represents *foamStarSWENSE* advantage mesh types

Considering the variation in the number of CPUs (Np) for different test cases, in an attempt to compare the solvers and mesh types, a CPU effort defined as (Agarwal et al., 2021a) $\frac{T_{CPU}\dot{N}p}{T_{SIM}}$ is is used . $T_{CPU}$ is the overall execution time for the simulation, $T_{SIM}$ represents the duration of the simulation. The comparison for each mesh type is plotted in Figure 5.44 with the computational cost on one vertical axis and cross correlation coefficient on the right axis. For the coefficient, surge motion accuracy from Figure 5.43a is chosen for the accuracy wise comparison for the computational cost.

For the same timestep, SPAR simulations in the *foamStarSWENSE* solver were nearing instability (sudden spike in Co). This was based on the change in aspect ratio in the free surface zone and snappy cut cells close to the SPAR. In order to complete the simulation without any

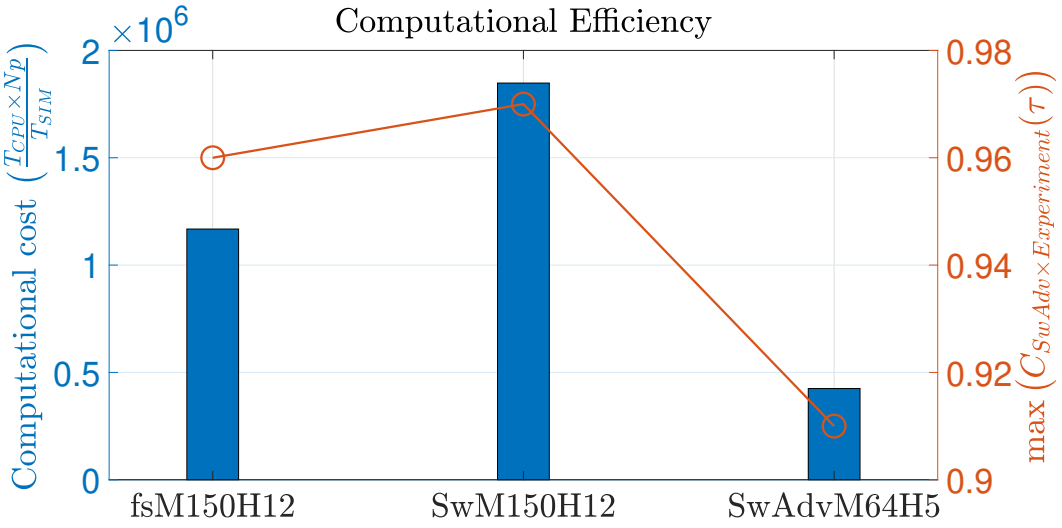


Figure 5.44 – Comparison between different Mesh types for the computational cost in solving LC 2.2 floating body interaction problem by solvers *foamStar* and *foamStarSWENSE*

instability or collapse, the solver took a quarter to half the time step used in the *foamStar* solver. As a result, the simulation time for SwM150H12 takes 1.5 times as long as it would using the *foamStar* solver and even with a coarser mesh formulation (SwAdvM64H5), this problem was still present, necessitating a reduced timestep to prevent the simulation's Co from rising. Although the SwAdvM64H5 simulation is faster and solved 0.35 times earlier than the *foamStar* simulation due to the simulation having three times less computational cells the loss in certain accuracy is unavoidable. There are certain improvements that need to be made to the *foamStarSWENSE* solver such that it can be used to make a initial guess in an industrial estimation of any offshore wave-structure problem with high precision and at a very low cost.

## 5.5 Closure discussion

This chapter presents the development of a coupled numerical model that can simulate the station keeping of real-time floating offshore structures in both normal and severe sea state conditions. In the present study, the interaction of fully nonlinear regular and irregular waves over a floating moored SPAR was simulated using *foamStar/foamStarSWENSE* solver with the floating structure's station keeping was characterized by a static (as a stiffness matrix) and dynamic mooring model (two-way coupling with MoorDyn). The numerical model results were compared with the experiment carried by (Arnal, 2020) in the ECN wave basin. The physical model consists of the SPAR structure moored to the tank bottom using delta type mooring with nine mooring lines. A good agreement between the numerical and experimental motions (surge, pitch, and heave) was observed for the regular and irregular wave interaction over the SPAR. The tensions in the mooring lines also compared well with the measurements. Mooring in the form of a stiffness matrix provides an accurate comparison for wave cases with mild and moderate amplitudes. However, to address mild, moderate, and even severe sea state

conditions with both regular and irregular waves, dynamic mooring simulation (MoorDyn) is proven to be vital. Additionally, the effectiveness of the *foamstar* and *foamstarSWENSE* solvers was compared for different mesh types, and *foamStar* is more mature and efficient for now than *foamStarSWENSE* on the application tested. A quick simulation using *foamStarSWENSE* can be used to estimate rough forces and mooring tensions across the floating body, and *foamStar* is faster than *foamStarSWENSE* for extensive and accurate analysis.

Chapter 6

# CONCLUSION AND PERSPECTIVES

The objective of the thesis is to evaluate and improve the numerical models which are based on the domain decomposition (DD) and functional decomposition (FD) approach to simulate complex interactions between fixed, moving and floating bodies in extreme waves. The thesis briefly reviews existing literature on both the coupling techniques and their numerical formulations. The thesis also studies the contemporary methods for coupling mooring models into fluid and rigid body models and subsequent development of the coupling algorithm.

The potential flow region is modelled by solving the Laplacian equation using Higher Order Spectral (HOS-NWT) method. The viscous flow region is modelled by the Eulerian form of Navier-Stokes equations in the case of DD and by Spectral Wave Explicit Navier Stokes Equations (SWENSE) for the FD coupling approach, respectively. The thesis adopts two solvers *foamStar* and *foamStarSWENSE* for the evaluation of DD and FD coupling strategy. The *foamStar* (Choi et al., 2018a), which is based on the one-way DD approach, is a two-phase viscous CFD solver built with the open-source CFD package OpenFOAM. The two-phase SWENSE method (Li et al., 2021b), which is based on FD approach, is implemented on top of *foamStar* and is called *foamStarSWENSE*. The only difference in the later code is that, the NS equations solved in *foamStar* are replaced by the SWENSE.

With this background, the current work aims to assess and enhance the numerical models for wave structure interaction in fixed and floating wind turbine substructures using both the *foamStar* and *foamStarSWENSE* solver. An extensive validation study has been reported for the interaction of breaking and non-breaking waves with fixed and moving cylinders using both the NS and SWENSE solvers. This investigation reports the influence of coupling over the relaxation zone, initiation time, spatial and temporal requirement, and convergence evaluation procedure and also validates both the DD and FD models against experimental results. A numerical coupling strategy is devised for including additional physics due to mooring lines in the form of static (Stiffness matrix-based) and dynamic mooring models (coupling with MoorDyn), which are developed as part of this study. Both the mooring models are included in the solvers and are validated with the experimental results.

## 6.1 Summary and conclusions

This section provides the summary and conclusion of each validation documented in the thesis. The first and second part of this section discusses the validation of the interaction of the focusing waves with the fixed and moving cylinder, and the third part addresses the interaction of moored spar type FOWT with regular and irregular waves.

### 6.1.1 Application of focusing waves interaction with cylinder

The validation study of the focusing wave interaction with a cylinder is discussed in Chapter 3 and Chapter 4. In Chapter 3, non-breaking and breaking focused wave interaction with a bottom-fixed cylinder is addressed, and in Chapter 4, non-breaking focused wave interaction with the moving cylinder at two different speeds (0.33 $m.s^{-1}$ and 0.75 $m.s^{-1}$) are discussed in detail. The summary and conclusion of each validation study is briefed in this subsection as follows.

#### 6.1.1.1 Non breaking focusing wave on fixed cylinder

The solvers based on domain and functional decomposition approaches (*foamStar* and conservative form of *foamStarSWENSE*) have been validated in the OpenFOAM framework. At first, wave-only simulations using the focused wave kinematics generated from the HOS-NWT using the time-reversal technique are studied. Although the wave is well represented by HOS, it has been found that there is a small discrepancy between the HOS and experimental results, and the average observed cross correlation coefficient value is 0.99 for both focused NBR and BR wave generated.This distinction will also be apparent in the waves generated inside the CFD because the HOS input is the feeder to the DD and FD-based solvers. Both coupling strategies are currently one-way schemes, implying that information is exchanged from HOS to CFD but not vice versa. Here CFD represents both the NS/SWENSE solvers. The CFD domain is restricted to the zone where vorticity and viscous effects are predominant, and a potential flow solver is considered for input waves only.

**Focusing wave validation:** Initially, both approaches were applied to a 2D NWT to generate a focusing wave from HOS to CFD for wave-only validation. The study has addressed the effects of the HOS initiation time, the size of the relaxation zones, the spatial and temporal discretization requirements, and different cell ratios. Following are salient conclusions obtained:

— Due to the coupling, it was found that the CFD initial conditions can be set immediately before the focusing time (only during the focusing event) and that the simulation does not need to start from the beginning of the HOS simulation. This results in ten times the computational time reduction in the present application.

— Focusing wave spatial and temporal requirements in the CFD domain were also explored based on the cell-based Reynolds and Courant numbers. The mesh Re5e4(64 cells per $\lambda$) to Re1e4(300 cells per $\lambda$) for cell-based Co less than 0.25 achieves an accuracy better than 0.99 in both solvers. Also, the SWENSE-based solver can use a grid 2-4 times coarser than

that of NS based solver(in each direction) to achieve identical accuracy for the application of NBR focusing waves.

— In general, the length of the relaxation zones should be 1-1.5 times the wavelength (30-40% of the cells) in the case of regular/irregular waves. The present study used the transient wavelength, which was found using the dispersion relation. As the focusing event being investigated is of short duration, the requirement of 0.04 $\lambda$ shows to be sufficient enough to generate and absorb the focusing wave. This saves a significant amount of computational time further.

— By altering the cell size at outer zones distant from the free surface zone using Cell Ratio (CR), it is found that it has the least influence on wave generation and propagation.

The coupling approach was then applied for a 3D wave structure interaction study representing a fixed surface-piercing circular cylinder interacting with a NBR focusing wave. Three different mesh types (coarse (M1), medium (M2) and fine (M3)) were investigated with a refinement ratio of 2. Another mesh type (M4) of similar to the fine mesh type but has no free surface refinement, and only refinement near the cylinder is also generated. The cross-correlation coefficient was adopted to identify the relative error difference between the time series, thus taking care of the difference in the wave profile, phase shift and peak magnitude. The physical quantities compared were the wave elevation, pressure over the cylinder and force. The mesh types results were initially compared with the finest mesh combination (fsCo0.01M3), and a grid convergence study was carried out based on the Richardson extrapolation. The simulated results were also validated with experimental data. It is realized that the numerical results with both the solvers on further refining reach an asymptotic state and are not converging to experimental results. This uncertainty estimation procedure is detailed in the chapter. The uncertainty between the experiment and the numerical simulation can be attributed to factors such as experimental errors (Sriram et al., 2021b), HOS-generated focusing waves, and CFD assumptions (discretization, time scheme, schemes), among other factors.

Compared to addressing a similar issue in the complete CFD problem (Sriram et al., 2021b), both coupling algorithms yield good agreement with experimental results and significantly reduce CPU time. Even the coarsest mesh (M1 and M4) of the *foamStar* and *foamStarSWENSE* solvers can predict the forces over the cylinder with a difference of less than 10%. The *foamStarSWENSE* solver estimates the wave and pressure over the cylinder more accurately on multiple occasions (M3 and M4) than *foamStar*, but it takes 1.25-1.5 times longer computational time. Also in the *foamStarSWENSE* mesh type without any free surface refinement (M4) showed accuracy similar to medium mesh refinement in *foamStar*. Thanks to an explicit treatment of the incident waves in SWENSE, even a coarse mesh in the far-field can accurately produce the incident wave information. However, the performance of *foamStar* cannot possibly be said to be lower than that of *foamStarSWENSE*. It consistently produced good results in all types of meshes with a modest computational cost, despite the accuracy of the results. Overall, the *foamStar* and *foamStarSWENSE* solvers performed well for NBR focused wave generation and interaction with a fixed cylinder.

#### 6.1.1.2 Breaking focusing wave on fixed cylinder

The focused breaking wave interaction with a vertical cylinder is simulated using the CFD-based solver *foamStar* in combination with the potential theory-based HOS-NWT (One way DD coupling technique). The SWENSE approach's investigation of the breaking wave model necessitates a full reevaluation of its formulation. Therefore, only the *foamStar* model is used to analyse the breaking wave interaction. There is a two steps procedure followed to complete this interaction study. First, both the HOS-NWT and the *foamStar* validate the focused breaking wave. A two-dimensional NWT is used for the appropriate parametric analyses for relaxation zone length, spatial and temporal resolution, and other variables similar to previous validation. HOS initiation time and cells outside the FS zone produce results similar to those of the NBR-focused wave case in regard to all previous parametric analyses. Among the parameters tested (32 cells per $\lambda$ to 1350 cells per $\lambda$) for spatial and temporal refinements based on cell-based Re and Co, fsRe3e5 (256 cells per $\lambda$) at Co 0.1 proven to be reliably accurate and economical enough to reproduce the breaking wave scenario in the numerical domain. Although there is a negligible effect on the wave when varying the zonal length, it is decided to maintain 0.1 $\lambda$ as a zonal length for the breaking wave propagation case based on the relaxation zone study.

Second, the interaction of the breaking wave with the cylinder is performed. Comparisons are made between the numerical and experimental data for the wave force, free surface elevation, and pressure over the cylinder and the results showed good agreement, but still, minor discrepancies are observed. The wave probes behind the cylinder display a considerable difference because, after the cylinder interaction, free surface dynamics are very complex, and the probe is in the middle of the broken wave. Wave probes (in front and at the focusing point) and the pressure probe's numerical results compared well with the experimental results. The numerical force overestimates the force by 1.2 times compared to the experiment. This is because the slightly higher wave amplitude seen in HOS is also generated in the case of CFD, which seems to increase the force. The study's notable aspects are validating the breaking wave model introduced in the potential solver HOS-NWT and applying domain decomposition methodology for breaking wave interaction problems. According to the study's findings, the problems of using a physical tank can be replaced by this hybrid coupled model as NWT, which can be a valuable tool for assessing breaking wave forces over any offshore or coastal structures.

#### 6.1.1.3 Non breaking focusing wave on moving cylinder

The next validation is to use *foamStar* and *foamStarSWENSE* solvers for the problem of focused waves interacting with a moving cylinder. The two different moving speeds (0.33 $\text{m.s}^{-1}$ and 0.75 $\text{m.s}^{-1}$) are investigated. The parametric studies, such as HOS focused wave generation and the spatial and temporal resolution in solvers are identical to those in the previous validations. Both solvers performed well and efficiently enough to capture the trend with respect to the experiment, even with the coarsest mesh, although there are slight discrepancies in the results that cannot be ignored. In capturing free-surface variations around the moving cylinder, the solvers are observed to achieve good agreement against experiments for low towing speed.

At high towing speed, additional complications arise, such as bulging of water in front of the cylinder and strong 3D deformations of the waves in the cylinder wake. These phenomena proved challenging in both the solvers, to accurately capture the wake field similar to the experiment.

For the pressure over the cylinder, both solvers fully reflect exact under water pressure observation in both cases compared to the experimental data. The probes above the SWL have inconsistencies, which are apparent in the results of their pressure measurements. This is a sensitive probe because a correct wave run-up is required to validate the pressure; therefore, a cross-correlation study of this pressure trend is discussed in detail in the Appendix A. For a cylinder moving at a slow speed (0.33 $m.s^{-1}$), pressure in the wake regions are well captured by solvers, but confirming the dynamic pressure at the separation and rear stagnation points at high towing speed proved to be highly challenging. Despite the deviations, the overall error is not too high to be concerned about, and the trend is also well represented. Next, any experiment or model study's primary goal is to investigate the force acting on the structure precisely. In this case, both solvers for various mesh types are employed to validate the experimental force measurement at the time of focused wave impact on the cylinder. Surprisingly, it has been verified that all test case results (even those for the coarsest combinations) provide accurate evaluation of the forces. With the advantage of coupling, both the solvers can be used to get nearly accurate answers (if sufficient precision can be less than 100% ) at a reasonable computational cost.

For the similar problem, the *foamStarSWENSE* solver incurs an average of 1.1–1.4 times higher computational costs than the *foamStar* solver. This is similar conclusion observed in the fixed cylinder interaction study. The *foamStar* solver is typically more accurate than *foamStarSWESNE* solver for analysis based on coarser and medium mesh types. For finer mesh types, both solvers have yielded results that are pretty close. However, due to its coupling, the *foamStarSWESNE* solver performs better with mesh types with only refinement near the structure but no free surface refinement. The overall conclusion from this study is to use later said mesh type for a preliminary estimation of any parameters study, such as forces and pressure over the structure in *foamStarSWENSE*, to spend as little time and cost on computation as possible. However, finer mesh types in the *foamStar* solver demonstrated highly accurate results, producing a converged solution in all the parameters studied in both the validation studies.

### 6.1.2 Application of moored floating body interaction with waves

One of the primary objective of this thesis is to develop a numerical tool that allows the study of the survivability of floating structures in extreme sea states. For evaluation of the floating structures, besides the 6 DoF rigid body model, mooring plays a vital role in the body's station keeping and stability. In this study, the moorings are modelled in two ways. One is by considering the mooring lines as a linear spring with defined spring stiffness, and another is by coupling the solvers (*foamStar*/*foamStarSWENSE*) with a lumped-mass mooring dynamics model (MoorDyn). MoorDyn represents the mooring line behaviour with axial elasticity, hydrodynamic forces, and vertical contact forces with the seabed. The coupling procedure follows three phases: initialization of mooring lines, information sharing between the rigid body solver

and mooring solver, and closing of the mooring solver. To summarize the coupling, *foamStar/-foamStarSWENSE* uses a body reference system ($R_b$) for its governing equation, and MoorDyn uses an inertial frame of reference ($R_0$) for its governing equation. Hence, body displacements and velocities are transferred from *foamStar/foamStarSWENSE* to MoorDyn at the inertial reference frame at each timestep, and mooring tension from MoorDyn will be transferred to *foamStar/foamStarSWENSE* in the body reference frame.

In the present study, the interaction of fully nonlinear regular and irregular waves over a moored SPAR was simulated to validate the developed model. The CN-Stream wave model was used for regular wave generation, while for irregular wave generation, the HOS-NWT was used. The floating structure's station keeping was characterized by a static (as a stiffness matrix) and dynamic mooring model (two-way coupling with MoorDyn). The numerical model results were compared with the experiments carried out in the ECN wave basin, see Arnal (2020) . The physical model consists of a SPAR structure moored to the tank bottom using delta-type mooring with nine mooring lines.

It was critical to mesh a floating body accurately since improper meshing would change the body's volume, change the draft, and make the motions observed irrelevant for validation purposes. Hence, a new parameter, PPSD (points per SPAR diameter), is introduced, and a value of 35 is recommended to accurately mesh the floating structure and avoid significant volume loss. Different types of mooring setups were investigated to see the efficiency of the dynamic mooring model MoorDyn, and the results were compared with other mooring models (MAP, MoorPy, AQWA) for the validation of model. For the present investigation, mooring data was obtained from the experimental data. Since working in the model scale in the MoorDyn caused numerical instability in the delta-type mooring case, the MoorDyn solver was made to operate in the prototype values.

Surge, heave and pitch decay tests were numerically simulated in foamStar, and it is interesting that in the heave-moored decay, mooring-driven damping accounts for nearly 25% of overall damping. In the case of surge decay, the natural period, damping, and mooring tension from the coupled model provided acceptable results compared to the experiments. The pitch decay test was put to the test, and some important conclusions were drawn. Surge and Pitch motion are strongly coupled, while other motions are only weakly coupled. Because pitch is equally sensitive to all six degrees of freedom (DoF) of motion and mooring and experimentally determined COG and mass moment of inertia, the initial setup for pitch decay must be sufficiently accurate in all of these categories. The moored decay test performed by the *foamStar* solver will be similar to the *foamStarSWENSE* solver.

The wave structure interaction is examined under four load cases (LC 1.1, LC 1.2, LC 2.1 and LC 2.2), with LC 1 representing regular waves and LC 2 representing irregular sea states. All four cases are investigated in the *foamStar* solver, and two different types of investigations were done in the *foamStarSWENSE* solver. First, the same mesh setup and other configurations are kept for comparison with the *foamStar* cases, with two cases of LC 2 are investigated. Second, a new mesh arrangement is developed with coarser refinement outside and only higher refinement near the SPAR (similar to SWENSE advantage mesh in the focused wave study). This new mesh

arrangement has been verified solely for the most severe case, LC 2.2.

In the *foamStar* solver, good agreement between the numerical and experimental motions (surge, pitch, and heave) was observed for all the cases. The tensions in the mooring lines also compared accurately with the experimental measurements. Mooring in the form of a stiffness matrix provides an accurate comparison for wave cases with mild and moderate amplitudes. However, to address mild, moderate, and even severe sea state conditions with both regular and irregular waves, dynamic mooring simulation (MoorDyn) is proven to be vital. Using the same mesh configuration with the *foamStarSWENSE* solver, identical behaviour was seen in both LC 2.1 and LC 2.2. Motions and mooring tensions were seen to be accurately represented, but at a cost that was 1.4 times greater than that of the *foamStar* simulation as in the focused wave situations. With the second configuration, SwAdvM64H5, the solver behaved surprisingly in a manner almost identical to that of a highly refined mesh configuration, with only minor variations in the motion and mooring tension. Also, the simulation cost is only 0.6 times that of the original *foamStar* simulation. This conclusion again validated the efficiency of the *foamStarSWENSE* solver in solving the simulation for reasonable accuracy at a low computational cost. Hence, it is proven that the DD and FD coupled solvers can be used to simulate the more complex wave-floating structure interactions at reasonable computational cost. These capabilities will aid in designing and analysing the floating structures and mooring to survive in extreme wave conditions efficiently.

## 6.2 Key contributions from the thesis

The outcomes of the thesis are listed below.

- Development of static (Stiffness matrix) and dynamic mooring (coupling with MoorDyn) models coupling with full NS (DD) and SWENSE (FD) based fluid solvers.
- Performance of the NS and SWENSE solvers for complex floater shape (SPAR) with a complex mooring system (Delta type) in regular and irregular waves.
- Static mooring models are sufficient for mild wave conditions (small displacements), and dynamic mooring models are required for mild and severe wave conditions.
- Detailed procedure for focusing wave generation in the coupled solver's are reported and recommendation of various parameters (initiation time, spatial and temporal requirements, relaxation zone) to significantly reduce computational costs without compromising accuracy.
- Assessment of moving body with constant forward speed methodology for the application of cylinder interacting with waves inside the coupled solvers
- A convergence assessment procedure is formulated to evaluate asymptotic accuracy in temporal problems using Richardson extrapolation and the cross-correlation coefficients.
- The study concludes that the SWENSE solver can deliver solutions with acceptable accuracy at a substantially lower computational cost for a preliminary evaluation of motion, mooring tensions and forces over the fixed and floating structures.

## 6.3 Proposals for future work

The present work provides a proper validation of the NS and SWENSE approach (*foamStar* and *foamStarSWENSE*) for extreme wave structure interaction like focusing wave interaction with fixed and moving cylinders and regular and irregular wave interaction with the moored floating body. Following the implementation instructions provided in this thesis, the reader is encouraged to reproduce this work. The proposals for future works are given as follows.

- **Improvements in *foamStarSWENSE***: Overall, all validation investigations demonstrated that the *foamStarSWENSE* solver has a computational cost of 1.2–1.6 times greater than that of the *foamStar* solver for a given problem setup. Compared to other NS-based CFD solvers, most marine and offshore applications would benefit significantly from the higher precision at much less computational time if the simulation duration per time step could be reduced in the *foamStarSWENSE* solver.
- **Coupling with OpenFAST**: The present study is restricted to calculating the motions and mooring tensions of the floating body under the effect of waves. However, to fully address the FOWT problem, aerodynamics must also be included in the solver. The successful validation of the OpenFOAM-MoorDyn coupling in the present work sets the path for the future coupling of the OpenFAST solvers with the *foamStar* and *foamStarSWENSE* solvers, enabling the complete analysis of any FOWT problem. This tool should allow users to investigate wind turbine and wind plant performance and loading under the full range of atmospheric conditions, different wave types and in different terrain.
- **Hydroelasticity**: Hydroelectricity is a crucial factor when analyzing the behaviour of very large floating structures (VLFS). Due to their geometrical and unusual length scales compared to the wavelength and the characteristic length, VLFS are characterized by their elastic behaviour. Also considering the hydroelastic reactions when wave frequencies are close to the structure's eigenfrequencies, and structural deformations are comparable to rigid body responses is crucial. For FOWTs, structural deformation may also be caused by the transferred aerodynamic loads that pass through the tower and onto the platform. In certain situations, structural deformation might alter the wave–structure interaction responses itself. Several approaches are already developed for hydroelastic analysis of floating structures (**?**) and it can be included in the future for enhancing robustness of the solvers.
- **Overset/ Sliding Mesh motion**: The present study adopts the mesh morphing technique for floating body motion inside the NWT. The deforming mesh has a defined number of cells, and the number of cells remains unchanged during the entire simulation. Compared to the overset and sliding mesh techniques, the deforming mesh technique is superior regarding computational time. However, the deforming mesh has some clear application limitations, the motion of the body has to be limited. A too large body motion creates too much distortion of the cells in the mesh, and the simulation becomes unstable and produces inaccurate results or does not converge (Jasak, 2009). The deforming mesh technique also has limitations when the body is rotating. When the body rotates, the mesh follows the

rotating object. This can also produce instabilities in the simulation. Hence to improve the robustness and efficiency of the solver, overset/sliding mesh motion technique should be tested and implemented for the *foamStar* and *foamStarSWENSE* solvers. As a point of reference for the implementation inside the openfoam solver, the work of Pinguet (2021) applying overset mesh to a semi-submersible platform in the OpenFOAM framework may be taken into consideration.

Appendix A

# Convergence study for NBR focusing wave interaction with moving cylinder

This appendix chapter details the convergence study based on different spatial and temporal refinements for 3D focusing wave interaction with the moving cylinder, which follows similar procedure adopted in Chapter 3. The study based on moving cylinder at Re 57000 is discussed in the first section of the chapter, and the study based on moving cylinder at Re 126000 is discussed in the second section.

## A.1 Case 1 : Re 57000

There are two subsections to this section. Different mesh and temporal combinations are validated with the finest mesh configuration in *foamStar* solver in the first subsection and *foamStarSWENSE* solver in the second subsection.

### A.1.1 Validation with finest mesh combination - *foamStar*

The WP5, WP6, and WP7 probes measured the free surface elevation of the *foamStar* cases before, at and after the focusing point, and the results are as shown in Figure A.1. With only minor variations at the peak crest, all mesh types accurately replicate the whole focused wave. Due to their coarse mesh for wave propagation, M1 and M4 display the major share of these minor variations. All the mesh types are cross-correlated with the fsCo0.01M3 test case results under the assumption that the finer mesh with the finer time step is accurate enough to capture the total flow fields. This assumption will be validated at end of the section. The mean of the coefficients for the wave probes WP5–WP7 is chosen for discussion because each wave probe's numerical wave in each test case is virtually identical. The mean error measured in cross-correlation is plotted against the computational cost as shown in Figure A.1d.

A similar accuracy of about 0.995 is shared by the meshes M1, M2, and M3, but the accuracy of each mesh is improved by lowering the Co. For mesh type M1, accuracy is 0.998, but for mesh types M2 and M3, accuracy has increased to 0.999 and is approaching one. The M1 shows no improvement after the third Co refinement, but the M2 and M3 show a slight increase in accuracy. Even without free surface refinement for Mesh M4, *foamStar* can still maintain accuracy of 0.989

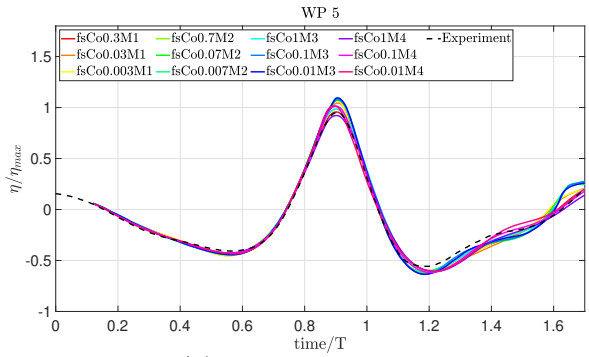


*(a)* Waveprobe WP5

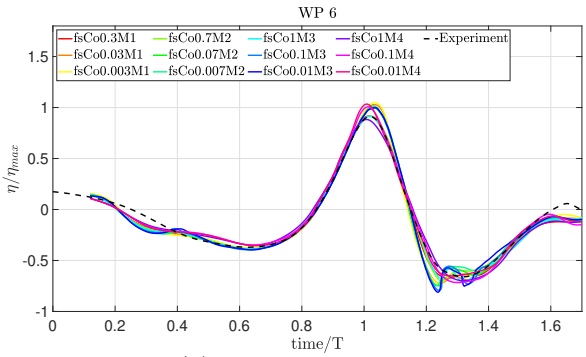


*(b)* Waveprobe WP6

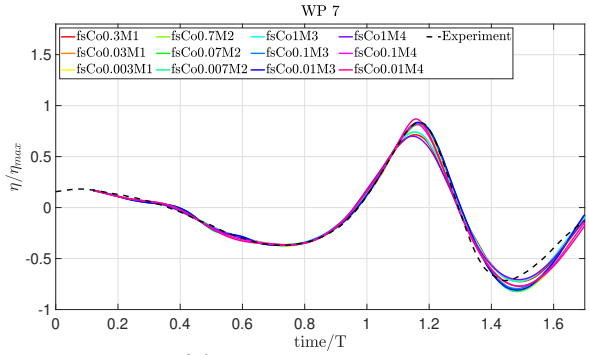


*(c)* Waveprobe WP7

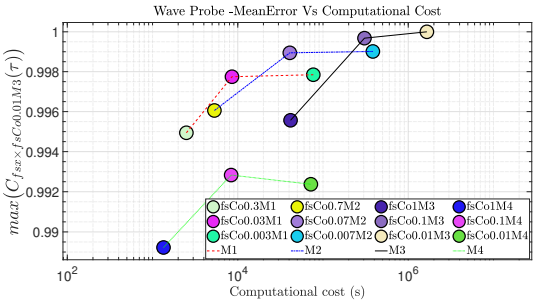


*(d)* Wave Probe mean error (with respect to the wave probes WP5 - WP7) cross correlation in relation with fsCo0.01M3

Figure A.1 – Wave probe comparison between different Mesh types M1,M2,M3 and M4 with the *foamStar* solver

and above for the coarsest mesh and coarsest time step. This is one of the coupling's key benefits. Further refinement of the Co increased accuracy to 0.993, but subsequent refinement shows little to no improvement compared to other mesh types. In terms of computational cost, the study follows a standard trend that an improved accuracy will be associated to an increase of the computational effort. M4 with coarser refinement provides good accuracy at a very low cost if the required accuracy on the free surface description is 0.99. However, if 0.998 or higher is needed, M1 with medium refinement is the most affordable option. Compared to M3 with medium and fine temporal refinement, which yields similar accuracy, M2 with medium temporal refinement is sufficient to produce similar results with lower computational costs.

Next, the various mesh type's ability to replicate the focused wave pressure on the cylinder is evaluated by comparing the numerical dynamic pressure recorded on the cylinder's pressure probes (probe locations: Figure 4.2) between different mesh types and the experiment as shown in Figure A.2. A good agreement with the experimental observations could be seen in almost all test cases in the pressure probes PP2-PP8. In terms of observing the similar dynamic pressure in both, before and after the focusing event, PP2, PP3, and PP6 results are well compared to other cases. After the focusing impact, a slight pressure drop and wake effects could be seen in PP7 and PP8 for coarser mesh types. However, finer refinements accurately capture the pressure variations, even behind the cylinder. Even though some test cases (M1 and M4) have poor free surface refinement, these test cases decently reproduce the pressure over the cylinder.

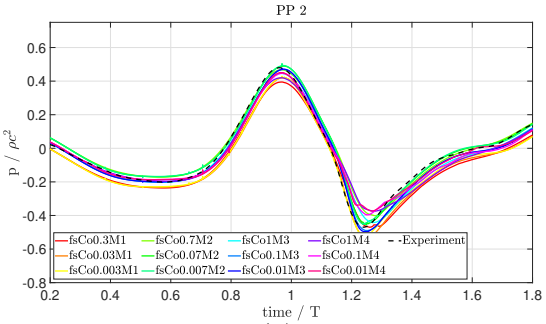


*(a)* PP2

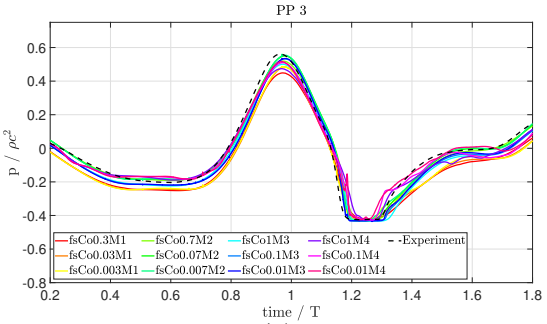


*(b)* PP3

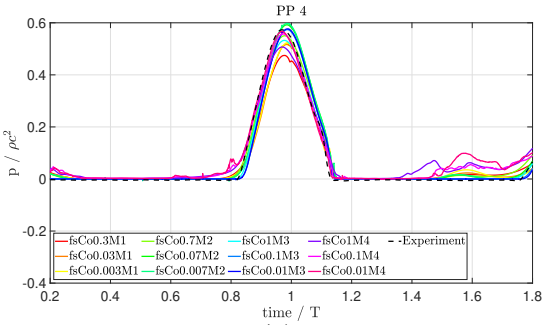


*(c)* PP4

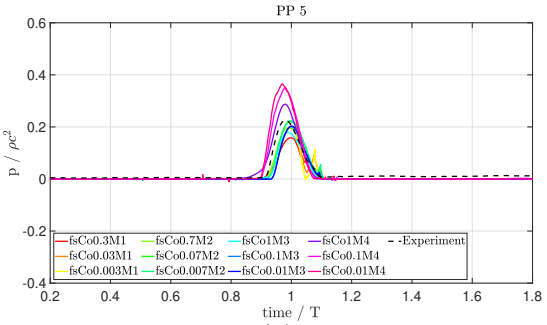


*(d)* PP5

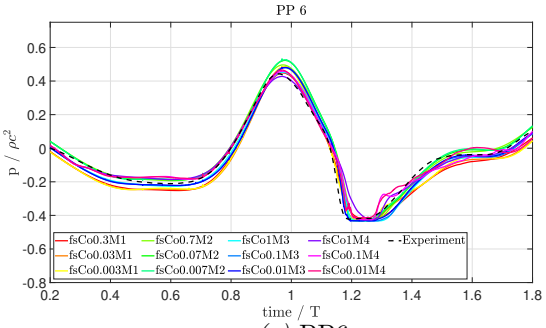


*(e)* PP6

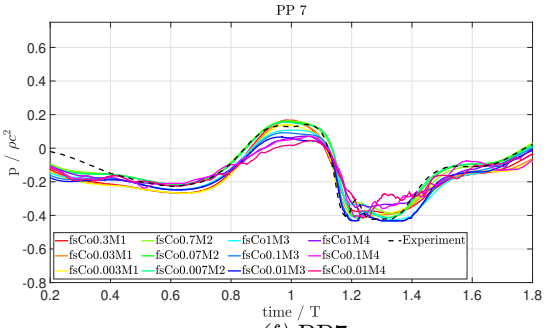


*(f)* PP7

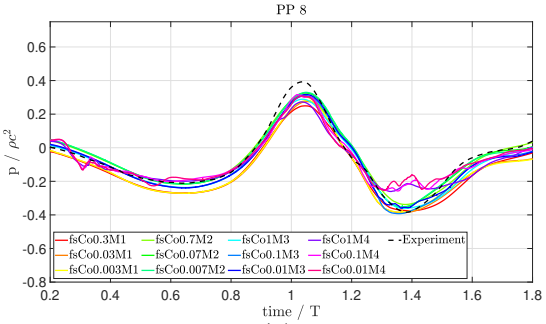


*(g)* PP8

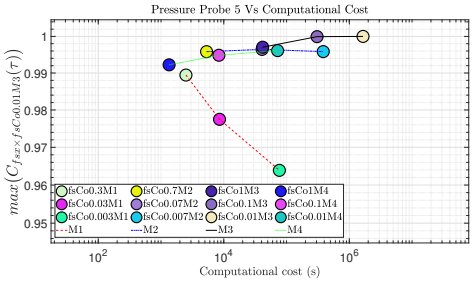


*(h)* Correlation coefficient for pressure probe PP5 with fsCo0.01M3

Figure A.2 – Pressure time history of the moving cylinder (Re 57000) in NBR focusing waves for different mesh types simulated by the *foamStar* solver

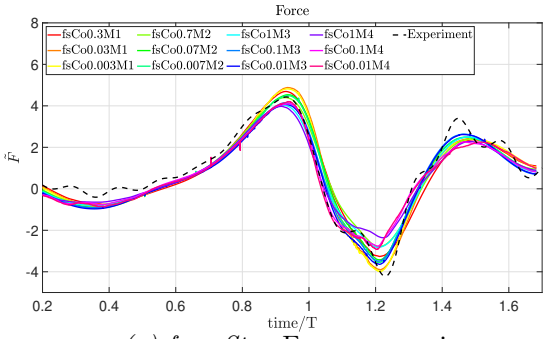


*(a) foamStar* Force comparison

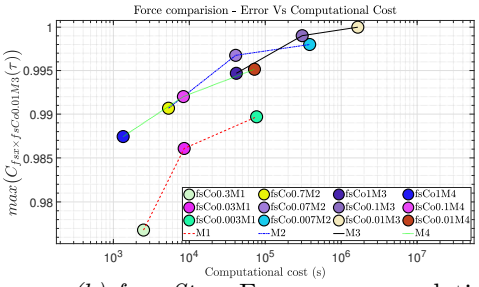


*(b) foamStar*- Force cross correlation

Figure A.3 – Force recorded for a moving cylinder (Re 57000) in NBR focusing waves by the *foamStar* solver (left) and its correlation coefficient with fsCo0.01M3 (right)

Peak pressures in air probes (PP4, PP5) reveal a difference in the peak amplitude and even though the difference is minimal in PP4, it is slightly higher in PP5 to be ignored. Hence, to study the convergence behaviour, cross-correlation estimation for the probe PP5 correlated with the fsCo0.01M3 was chosen. In comparison to fsCo0.01M3, the accuracy is lowered when M1 is refined with respect to Co. This decrease in accuracy is brought on by distortion in the wake that Mesh M1 recorded after the focusing wave hit the cylinder (Figure A.2d). Other mesh types M2, M3, and surprisingly even M4, exhibit a decent convergence trend when refined with Co, and their accuracy is nearly 0.995 and steadily increases in the direction of convergence.

Figure A.3b shows the unidirectional forces exerted by a NBR focusing wave hitting a moving cylinder travelling at a speed of 0.33 m.s$^{-1}$ . The simulated forces are normalized for the convenience of comparison with the factor $\rho g r^3$, where r represents the radius of the cylinder. The total force predicted by all the mesh types is quite similar to each other, with minor differences. The correlation study for forces for each mesh type with the finest combination fsCo0.01M3 is shown in Figure A.3b. All the mesh types exhibit well-defined convergence when refining the mesh and time step. The accuracy of mesh M1 with the coarsest timestep is 0.975 but spatial refinement improved accuracy to 0.99 and further to 0.995. Similarly, temporal refinement improved accuracy from 0.975 to 0.99. This is similar to other mesh types, but the curve was nearly flattened after medium refinement in M2 and M3. One of the notable accuracy is the force prediction in M4 (no free surface refinement), exhibiting an accuracy of 0.987 with low computational cost, which shows the solver's ability to quickly obtain the rough estimation of force to be expected on the structure in extreme events.

In order to confirm that the fsCo0.01M3 mesh type is a converged configuration, the Richardson extrapolation method was applied. Based on the cross-correlation coefficient values obtained for each mesh type (Mesh 1 (M1), Mesh 2 (M2), and Mesh 3 (M3)) by fixing the time step of 0.001s, the convergence was determined. The surface elevation, pressure, and force were all included in the convergence investigation, and the results are shown in Figures A.4a, A.4b, and A.4c. The convergence slope from Mesh 1 to Mesh 2 appears to be 0.07%, and from Mesh 2 to Mesh 3, it appears to be 0.03% ($L1$ norm). The extrapolated coefficient between Mesh 2 and Mesh 3 reaches a value of 0.9999 for wave elevation, and its slope from Mesh 3 is 0.01%. This

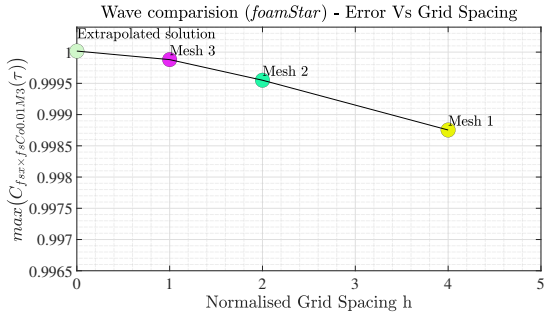


*(a) foamStar*- Wave probe Grid Convergence study

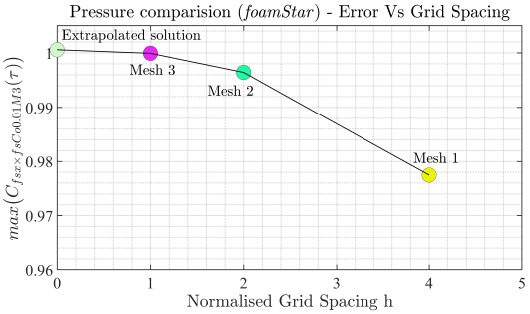


*(b) foamStar*- Pressure Grid Convergence study

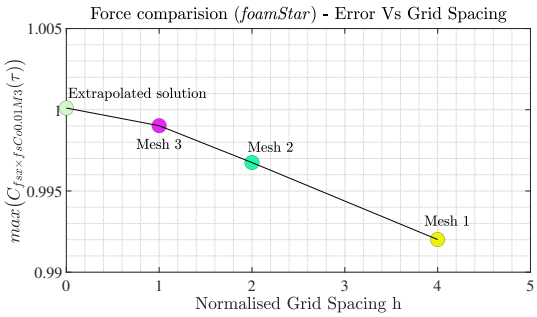


*(c) foamStar*- Force Grid Convergence study

Figure A.4 – Extrapolation of coefficients with the Richardson method and its corresponding convergence for *foamStar*

proves that convergence of the solution has already been achieved. The pressure PP5 shows a similar pattern, except that accuracy is marginally lower, and the reasons have already been discussed. The extrapolated coefficient for force is estimated to be 0.9999. Since the grid convergence from Mesh 1-2, Mesh 2-3, and Mesh 3-extrapolated coefficient is 0.5%, 0.2%, and 0.09%, respectively, the solution for the force also appears to have already converged. This study shows that even the coarsest mesh has a good estimate of force, and all the results had already converged, indicating that the finest mesh (fsCo0.01M3) had already produced a solution that was accurate enough to be kept as the base result for cross-correlation.

### A.1.2 Validation with finest mesh combination - *foamStarSWENSE*

This section investigates focused wave interaction with the moving cylinder at a constant speed of 0.33 m.s$^{-1}$ using *foamStarSWENSE* solver. Wave parameters and mesh types in this case are identical to those used in the previous *foamStar* section. The surface elevation, pressure and force are cross-correlated with fsCo0.01M3 to have a comparable conclusion between the solvers. Additionally, because each non-dimensional parameters are similar to the previous section, they are not repeated in this section.

Figure A.5 compares the time series of numerical wave probe recording with experiment for probes WP5, WP6 and WP7. Because the peak amplitude of the HOS-generated focusing wave is a bit higher than the experiment, the *foamStarSWENSE* solver also has a peak amplitude for all mesh types 4 to 7% higher. Interestingly, the solver can capture the focusing event (WP6) and the wake effects very well, despite having minimal differences with the experiment (WP7). This

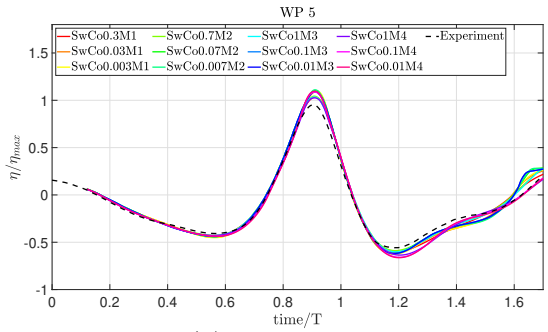


*(a)* Waveprobe WP5

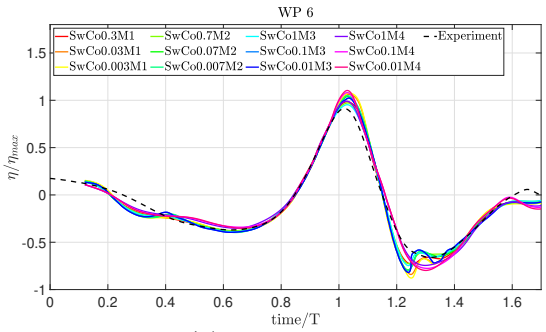


*(b)* Waveprobe WP6

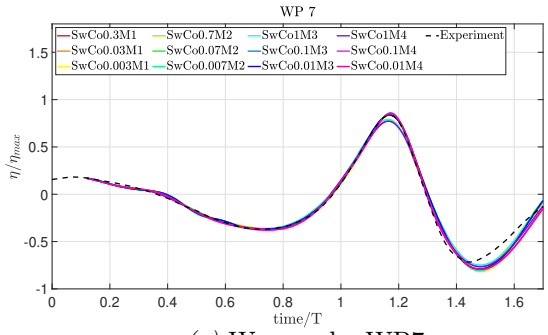


*(c)* Waveprobe WP7

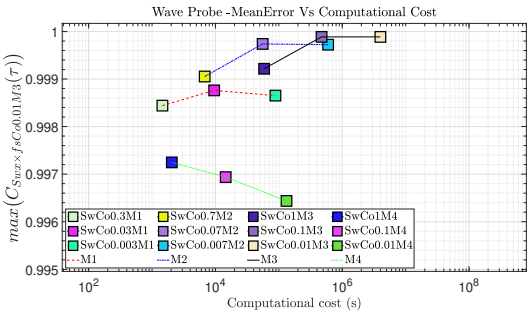


*(d)* Wave Probe mean error cross correlation with respect to fsCo0.01M3

Figure A.5 – Wave probe comparison between different Mesh types M1,M2,M3 and M4 in the *foamStarSWENSE* solver

is reflected in the wave probe mean error (Figure A.5d), which was calculated using the same method as in the previous section by averaging the cross-correlation between all the mesh types in each probe. All mesh types indicated good convergence behaviour with fsCo0.01M3, and the overall accuracy is more than 0.994. To reiterate, one of the key benefits of *foamStarSWENSE* is the explicit treatment of incident waves; as a result, reliable incident wave information may be produced even with a coarse mesh in the far-field. This is evidently demonstrated by the correlation amplitudes of M1, which have magnitudes of 0.998 and are further heading towards 0.999 as they refine. This further proves the comments about the SWENSE approach from the Chapter 3 regarding the advantage of using coarser cells for wave propagation in reducing the computational cost.

Next, the experimental pressure measurements and dynamic pressure observed by the numerical probes PP2-PP8 with *foamStarSWENSE* solver are presented in Figure A.6. Every mesh type's pressure is accurately captured and virtually equivalent to the experimental pressure, similar to the pressure observations made by the *foamStar* solver. The PP5 probe exhibits a noticeable difference, where the wave run-up is poor for coarser mesh and improves with spatial and temporal resolution. This probe is cross-correlated with fsCo0.01M3 for a comparable discussion between the solvers. The accuracy of the mesh M1 is 0.987, and temporal refinement does not significantly improve this. M2 and M3 have a similar pattern. However, M3 is seen to attain 0.999, demonstrating the similarity between the solvers. The unexpected outcome again is that M4 starts at 0.992 with minimal computational cost and improves to 0.995 on temporal

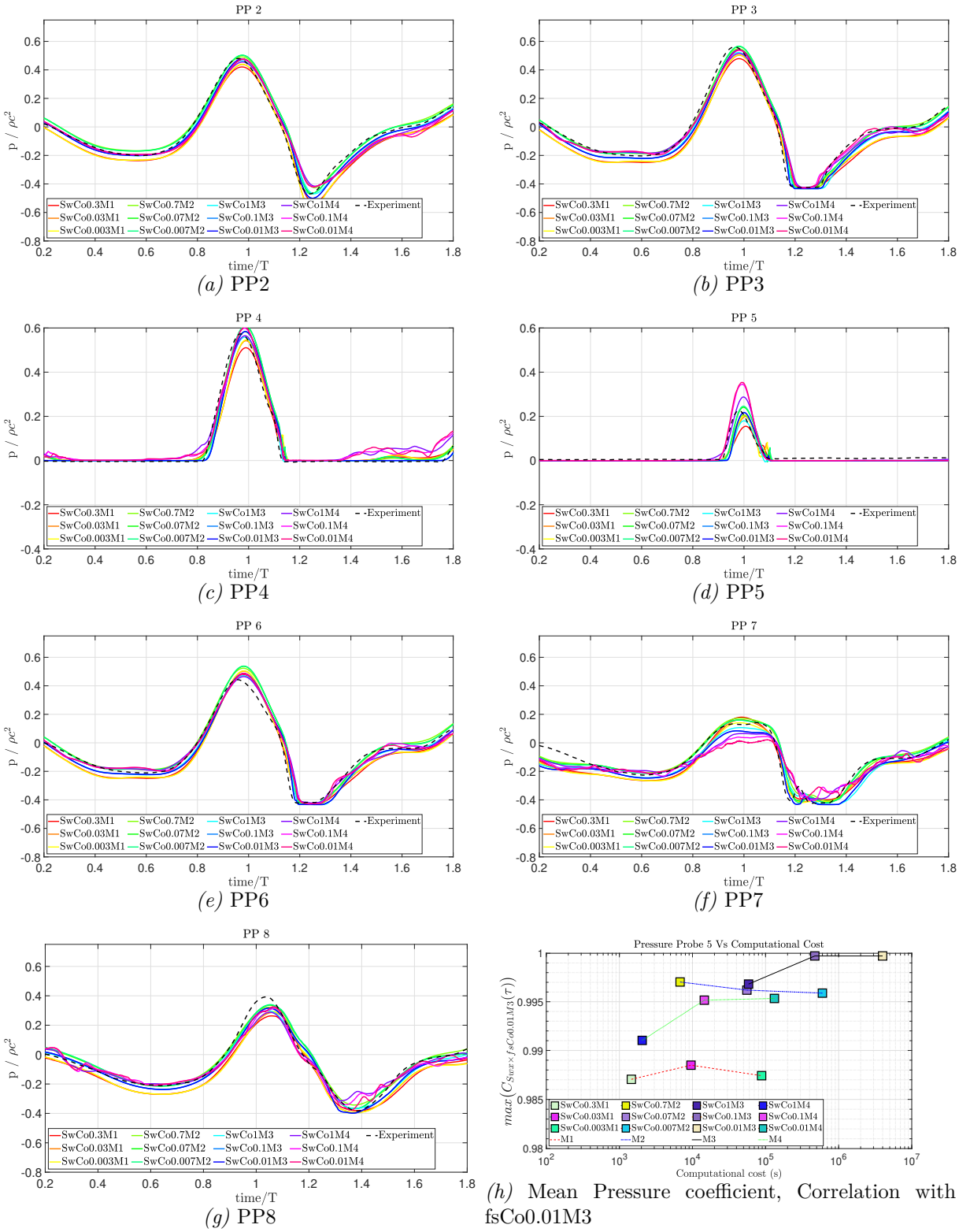


*(a)* PP2 *(b)* PP3 *(c)* PP4 *(d)* PP5 *(e)* PP6 *(f)* PP7 *(g)* PP8 *(h)* Mean Pressure coefficient, Correlation with fsCo0.01M3

Figure A.6 – Pressure time history of moving cylinder (Re 57000) in NBR focusing waves recorded by *foamStarSWENSE* for different mesh types

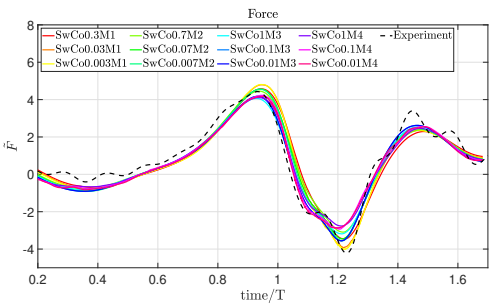


*(a) foamStar-SWENSE* Force comparison

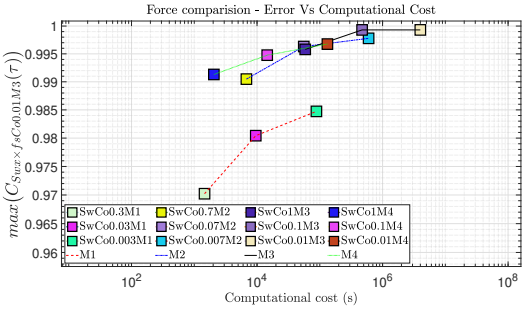


*(b) foamStar-SWENSE-* Force cross correlation

Figure A.7 – Force comparison for moving cylinder (0.33 m.s$^{-1}$) in NBR focusing waves between different mesh types under *foamStarSWENSE*

refinement. This again supports the SWENSE approach's benefit of only requiring refinement close to the structure, with lower computational costs and the ability to produce acceptable accurate simulation results.

Finally, for forces, the *foamStarSWENSE* mesh types demonstrate that, it can accurately replicate the force observed across the moving cylinder during the impact with focused waves, as shown in Figure A.7. Minimal differences between solvers are seen for combinations of mesh types. Cross-correlation analysis with fsCo0.01M3 (Figure A.7b) reveals, however, that all mesh types exhibit convergence behaviour during temporal and spatial refinement. The accuracy of Mesh M1 is observed to be 0.97 and increases to 0.985. However, for M2 and M3, the accuracy starts at 0.99 and converges to 0.998. The SWENSE advantage mesh M4 predicts the force with a precision of 0.991 at the lowest possible cost, and with further refinement, it achieves 0.995 at a cost 100 times lower than the finest mesh combinations (M3). This again demonstrates the benefit of using the SWENSE approach for problems of a similar nature in order to obtain a reasonable estimate of forces at the lowest possible cost.

The Richardson extrapolation method was used based on the cross-correlation coefficient values obtained for each mesh type (Mesh 1 (M1), Mesh 2 (M2), and Mesh 3 (M3)) at the time step of 0.001s to demonstrate that the surface elevation, pressure, and force results showed are a converged configuration. Figures A.8a, A.8b, and A.8c shows the extrapolation convergence plot for all the three parameters. The extrapolated coefficient is almost one in each of the three parameters, and Mesh 3 is consistently close to the convergence point. In each plot, the slopes from Mesh1 to Mesh2 are 0.08%, 1.7%, and 0.45%, and from Mesh2 to Mesh3, they are 0.03%, 0.04%, and 0.2%, respectively. The extrapolated coefficient's final slope is 0.01%, 0.02%, and 0.1%, demonstrating that the curve is flattening and that further improving outcomes would mostly affect computational cost rather than accuracy.

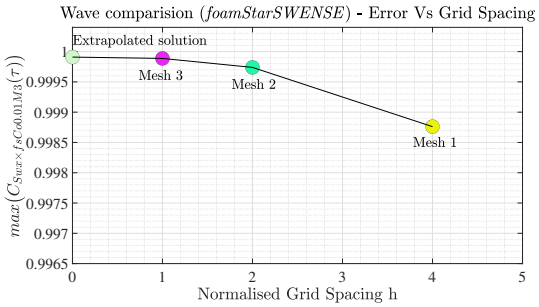


*(a) foamStar-SWENSE-* Wave elevation Grid Convergence study

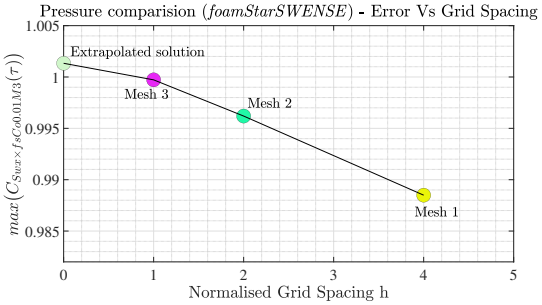


*(b) foamStar-SWENSE-* Pressure Grid Convergence study

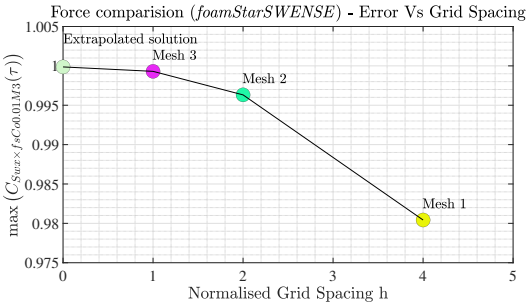


*(c) foamStar-SWENSE-* Force Grid Convergence study

Figure A.8 – Extrapolation of Coefficient with the Richardson method and its corresponding GCI for *foamStar-SWENSE*

## A.2 Case 2 : Re 126000

There are two subsections to this section. Different mesh and temporal combinations are validated with the finest mesh configuration in *foamStar* solver in the first subsection and *foamStarSWENSE* solver in the second subsection.

### A.2.1 Validation with finest mesh combination - *foamStar*

Figure A.9 displays the results from the observations made by the WP5, WP6, and WP7 numerical probes of the *foamStar* case's free surface elevation. The WP5 probe results, before the focusing wave hitting the cylinder were similar to each other and also to the experiment. The only difference is at peak amplitudes between the coarser and finer mesh types. However, virtually no mesh types precisely match the experimental results with the probe at the focusing point and probe in the wake (WP6 and WP7), yet the deviations are not that large. This can be proved by observing the mean error of the cross correlation coefficient shown in Figure A.9d. Compared to the earlier case (Re 55000), where wave probe accuracy (Figure A.1d) was in the range of 0.996 to 0.999, here more loss in accuracy amongst the mesh types is observed. The accuracy of all mesh types relative to the finest one falls in the range of 0.99 to 0.995, and for the mesh type M4 (no free surface refinement) accuracy range is between 0.975 to 0.98. Only with mesh type M3 is convergence with temporal refinement observed as opposed to almost flat curves with M1 and M2. The advantage of DD coupling is proven here as that the Mesh type

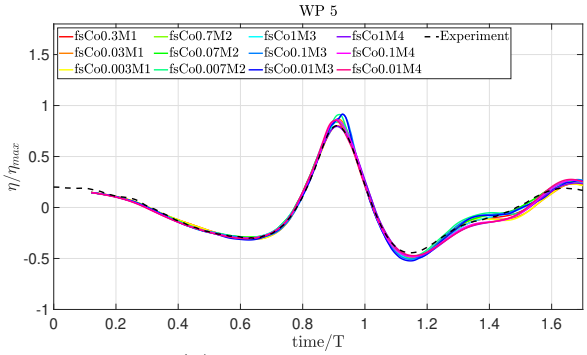


*(a)* Waveprobe WP5

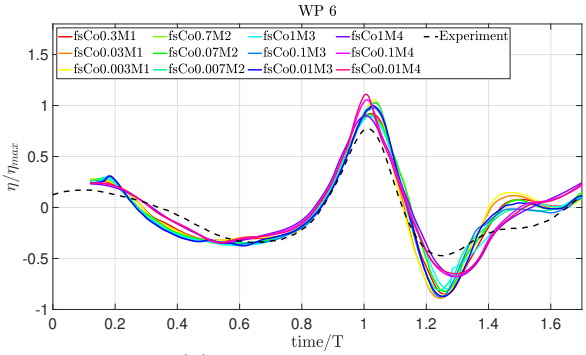


*(b)* Waveprobe WP6

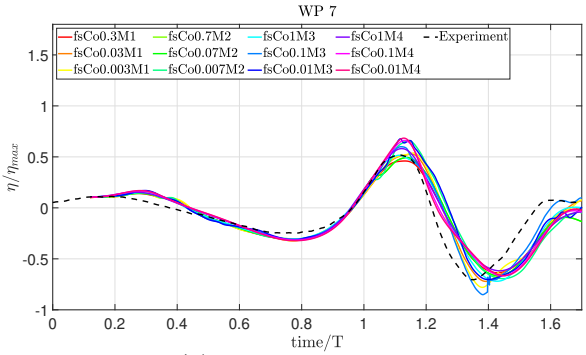


*(c)* Waveprobe WP7

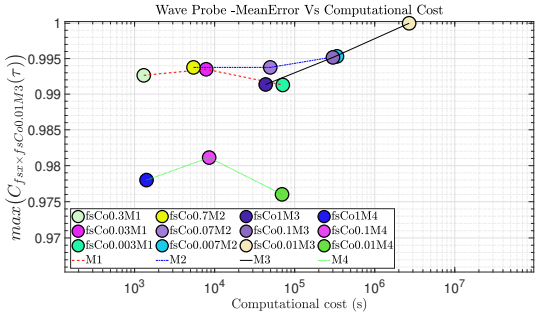


*(d)* Wave Probe mean error (with respect to the wave probes WP5 - WP7) cross correlation in relation with fsCo0.01M3

Figure A.9 – Wave probe comparison between different Mesh types M1,M2,M3 and M4 with the *foamStar* solver for moving cylinder (0.75 m.s$^{-1}$ )

M1 with very coarse free surface refinement and coarser time step can achieve accuracy of 0.992 and beyond with little computational cost. After discussing pressure and force over the cylinder in the following subsections, the solver's loss in accuracy and efficiency for this kind of problem will be compared.

The next discussion is to compare the numerical dynamic pressure recorded on the cylinder's pressure probes (probe locations: Figure 4.2) with the experiment as displayed in Figure A.10. Almost all test cases for the pressure probes PP2-PP8 showed a satisfactory agreement with the experimental observations. Both before and after the focusing event, the submerged pressure probes PP2 and PP3, air probe PP4, and free surface probe PP6, where the separation begins, displayed a better comparison with the experiment than other probes. The PP5 pressure probe in air, which requires a good wave runup to have proper pressure observation, demonstrated a similar discrepancy like earlier validation. The Cross-Correlation (PP5) between the various mesh types and the finest mesh, fsCo0.01M3, demonstrated good convergence behaviour and an accuracy range of greater than 0.99 is observed. Except for M1, where a negative convergence is seen, mesh types M2, M3, and others displayed good convergence with refinement accuracy exceeding 0.995 and approaching one. Because of its higher refinement close to the cylinder, mesh M4 type also surprisingly gains an accuracy of 0.998 and above, similar to results near the finest mesh. The new observation in this study is that the pressure measurements made by the probes PP7 and PP8, which are located in the cylinder's wake, differ between mesh types and

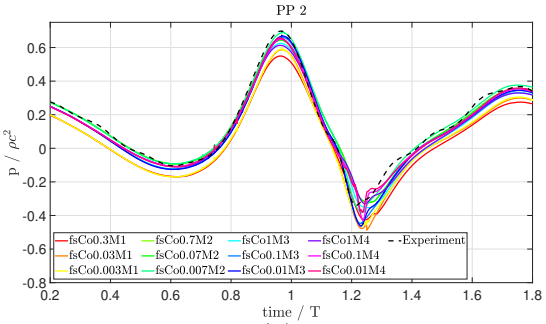


*(a)* PP2

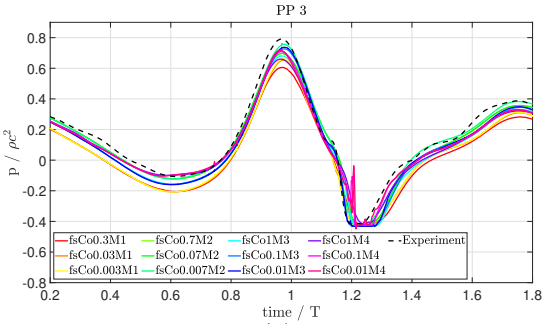


*(b)* PP3

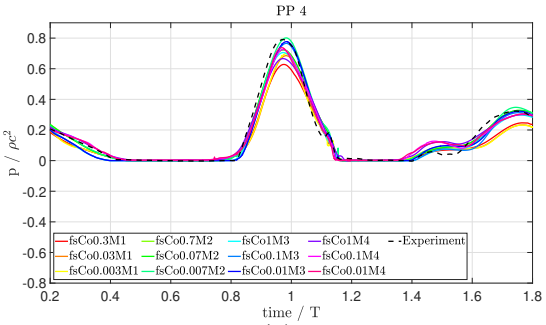


*(c)* PP4

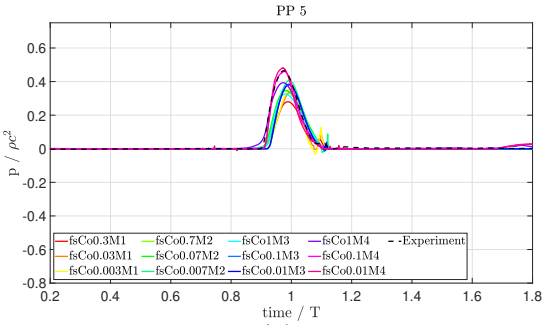


*(d)* PP5

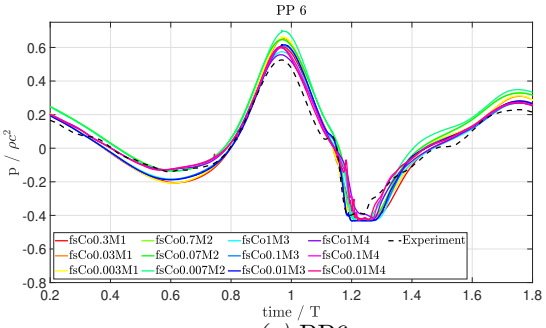


*(e)* PP6

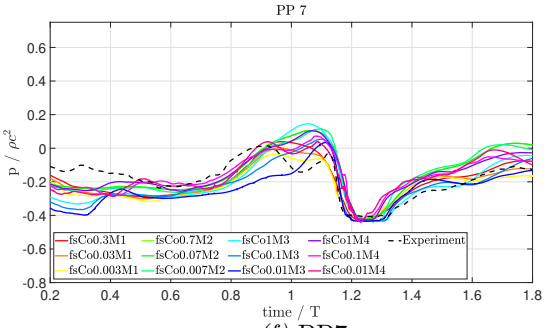


*(f)* PP7

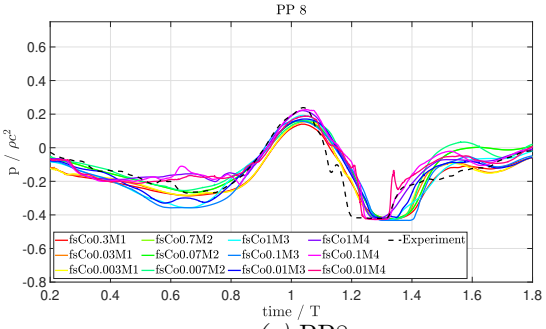


*(g)* PP8

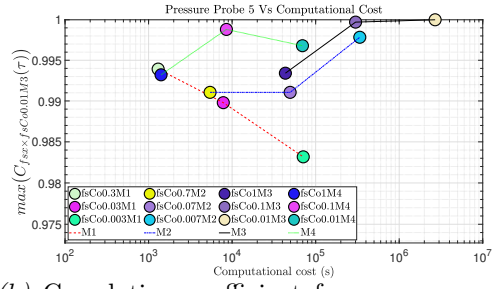


*(h)* Correlation coefficient for pressure probe PP5 with fsCo0.01M3

Figure A.10 – Pressure time history of the moving cylinder (0.75 m.s$^{-1}$) in NBR focusing waves for different mesh types simulated by the *foamStar* solver

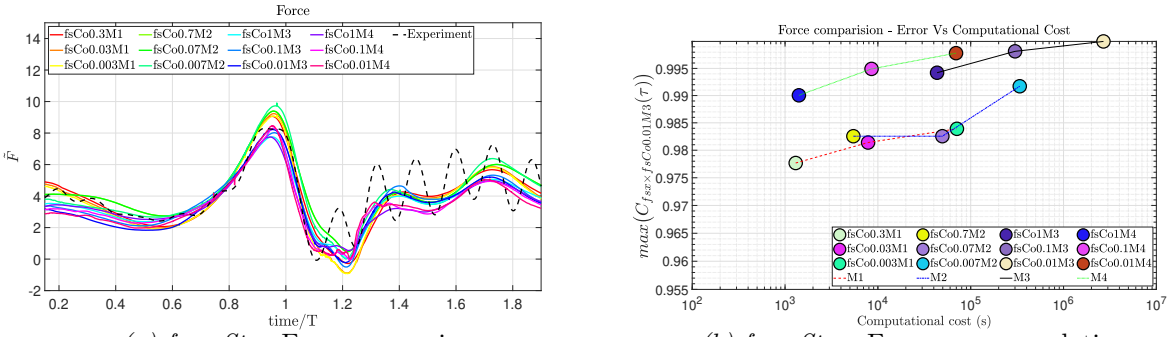


*(a) foamStar* Force comparison

*(b) foamStar*- Force cross correlation

Figure A.11 – Force recorded for a moving cylinder(0.75 m.s$^{-1}$ ) in NBR focusing waves by the *foamStar* solver (left) and its correlation coefficient with fsCo0.01M3 (right)

also from the experimental results, as also indicated by the comparison of the wave probes WP6 and WP7. It is concluded from the present study that improvement/validation are still needed in this case study to accurately capture the wake region of this complex nature.

Figure A.11 shows the unidirectional forces observed when a NBR focusing wave hits a cylinder moving at a speed of 0.75 m.s$^{-1}$ (Re= 165000). All the mesh types estimated a similar trend of total force with only a few minimal differences. After the wave hits the cylinder in the experimental observation, the cylinder encounters a ringing phenomenon that is ignored in the numerical simulations due to the rigid body assumption. Figure A.11b displays the correlation analysis of each mesh type force with the finest combination, fsCo0.01M3. Proper convergence trend is observed for all the mesh types by refining the mesh and time step. With the largest timestep, mesh M1's accuracy is 0.978 and with temporal refinement accuracy increased to 0.98 and further to 0.984. The accuracy improvement for M2 is from 0.982 to 0.992 and M3 is 0.994 to 1. For M4 (no free surface refinement), accuracy of 0.99 improved to 0.997 on refining the timestep. One of the main findings of this study is that if the study's objective is force over the cylinder, even M4 provides excellent accuracy with at very small computational cost.

To verify the convergence between the mesh types and demonstrate that the finest mesh selected for cross-correlation is a converged solution, the Richardson extrapolation technique is applied. The plots for the analysis for surface elevation, pressure and force are shown in Figures A.12a, A.12b, and A.12c respectively. The convergence slope from Mesh 1 to Mesh 2 appears to be 0.09%, and from Mesh 2 to Mesh 3, 0.04%. The extrapolated coefficient between Mesh 2 and Mesh 3 reaches a value of 0.9952 for wave elevation, and its slope from Mesh 3 is 0.025%. This reveals that the solution's convergence has been approached with Mesh 3 is close to the converged solution. The pressure PP5 shows a similar pattern, except that accuracy is marginally lower, and the reasons have already been discussed. The extrapolated coefficient for force is found to be 0.9999 and the grid convergence slope from Mesh 1-2, Mesh 2-3, and Mesh 3-extrapolated coefficient is found to be 0.8%, 0.6%, and 0.4%, respectively. The solution for the force appears to approaching the convergence with grid refinement and Mesh 3 is closely near to the converged solution. The results of this study reveal that even the coarsest mesh has a good estimate of force, and the results are nearly convergent, showing that the finest mesh

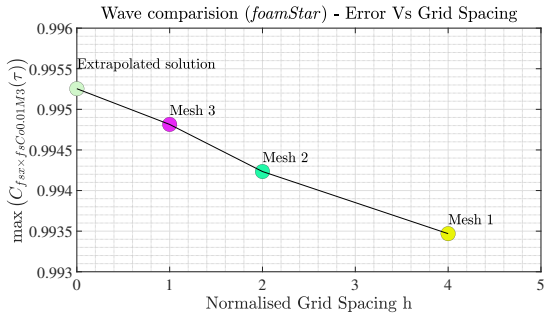


*(a) foamStar*- Wave probe Grid Convergence study

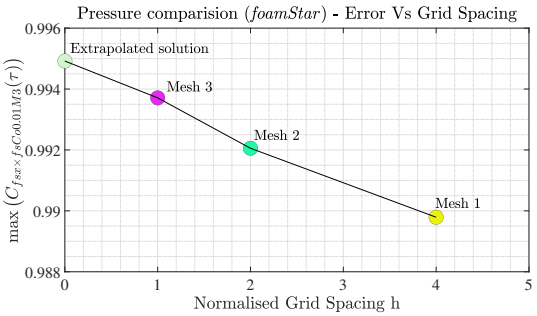


*(b) foamStar*- Pressure Grid Convergence study

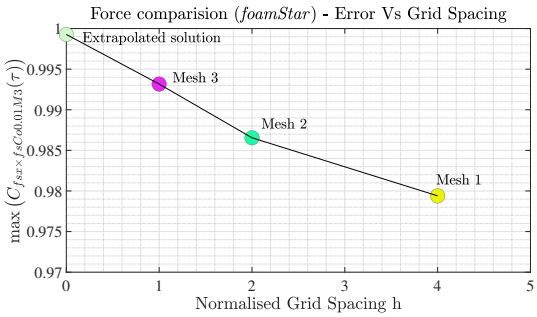


*(c) foamStar*- Force Grid Convergence study

Figure A.12 – Extrapolation of coefficient with the Richardson method and its corresponding convergence for *foamStar*

(fsCo0.01M3) had already provided a solution that was accurate enough to be preserved as the base result for cross-correlation.

### A.2.2 Validation with finest mesh combination - *foamStarSWENSE*

Using the *foamStarSWENSE* solver, this subsection examines focused wave interactions with a moving cylinder moving at a constant speed of 0.75 m.s$^{-1}$ . The mesh types and wave parameters used here are the same as those in the *foamStar* section before. To ensure that the results from the solvers are comparable, the surface elevation, pressure, and force are cross-correlated with fsCo0.01M3. Additionally, none of the non-dimensional parameters is repeated in this section because they were covered in the section before.

Figure A.13 compares the time series of numerical wave probe recording with experiment for probes WP5, WP6 and WP7. Probe WP5 observations are comparable to those of *foamStar* in that they show a similar profile for all mesh types and the experiment as well, with only a slight variation in the peak amplitude of nearly 5%. Once again, WP6 and WP7 appear to vary from the experimental observation due to a slight increase in wave amplitude during impact at the crest and trough, as well as a slight change in phase with WP7 in the wake region. However, compared with the finest mesh in the *foamStar* solver, the accuracy of all the mesh types falls with an accuracy range of 0.994 and has an assertive convergence behaviour. The only mesh type that performed less accurate in contrast to other mesh types was M4, but even it was nearly 0.984. The correlation amplitudes of M1, which have magnitudes of 0.998 and are further approaching 0.999 as they refine, once again confirming the SWENSE advantage.

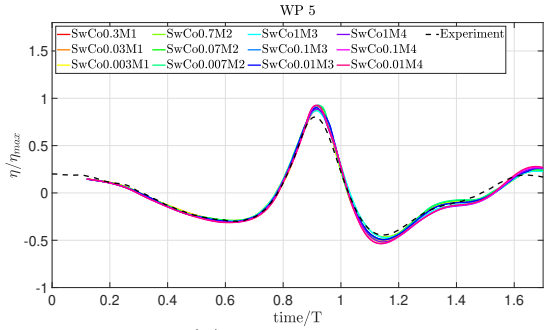


*(a)* Waveprobe WP5

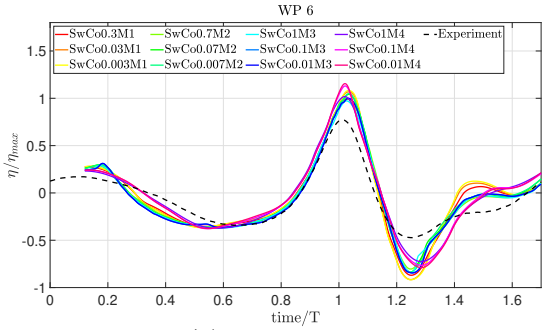


*(b)* Waveprobe WP6

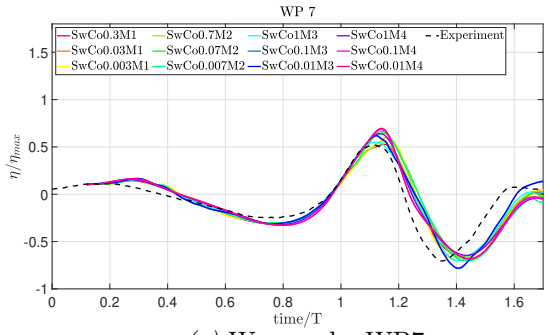


*(c)* Waveprobe WP7

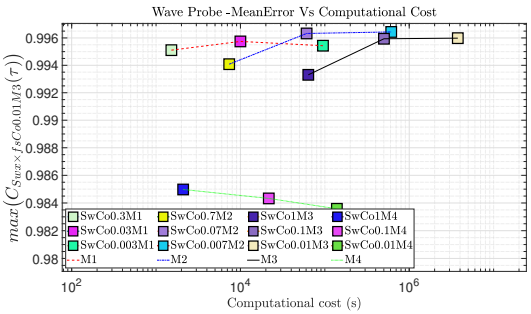


*(d)* Wave Probe mean error cross correlation with respect to fsCo0.01M3

Figure A.13 – Wave probe comparison between different Mesh types M1,M2,M3 and M4 in the *foamStarSWENSE* solver

Figure A.14 displays the dynamic pressures recorded at probes PP2-PP8 for different mesh types compared to the experiment. With a slight discrepancy in amplitudes at the peak crest, pressure readings from PP2, PP3, and PP4 are similar to those from the *foamStar* solver. Also, PP5 observe very slight differences in amplitudes in adequately capturing the wave run-up among different mesh types. This is proven with a cross-correlation plot (Figure A.14h), where the coefficients range from 0.996 to 0.998. Even the M4 (no free surface refinement) and M1 monitor to have an accuracy of 0.996 and above with a computational cost of 100 to 1000 times less than finer meshes(M3). This results also proved the SWENSE efficiency in obtaining highly accurate results in similar to coarsest mesh combinations with *foamStar* (Figure A.10h). However, the pressure sensors in the wake regions (PP7 and PP8) have a similar disparity to the *foamStar* solver but are robust enough to catch the trend with minor changes in amplitude for all the mesh types.

Like the *foamStar* solver solutions for different mesh types, *foamStarSWENSE* is also able to reproduce the force observed by the experiment during focusing wave interaction , as shown in Figure A.15a. The coarser and medium mesh types (M1 and M2) shows slight amplitude variation at the focusing event, but M3 and M4 (no free surface refinement) match almost perfectly with the experimental force observations. This is demonstrated by the cross-correlation of all the mesh types with regard to fine mesh fsCo0.01M3 (Figure A.15b). All mesh types were found to have a convergence trend, with M1 and M2 falling within ranges of 0.986 to 0.99 and 0.987 to 0.994, respectively. Even the most refined mesh M3 begins its accuracy with 0.995 for the coarsest

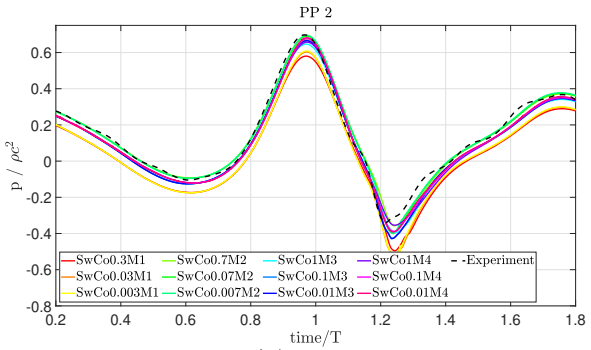


*(a)* PP2

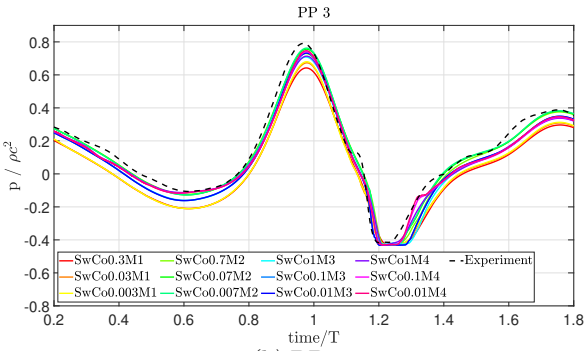


*(b)* PP3

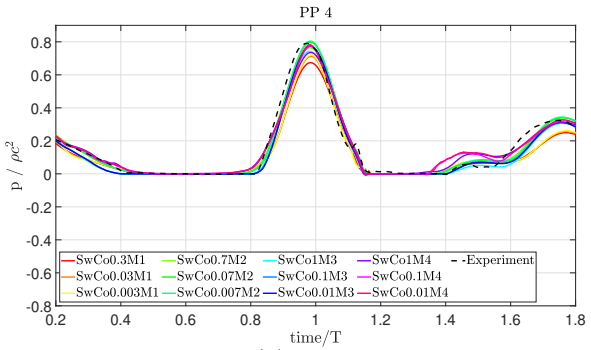


*(c)* PP4

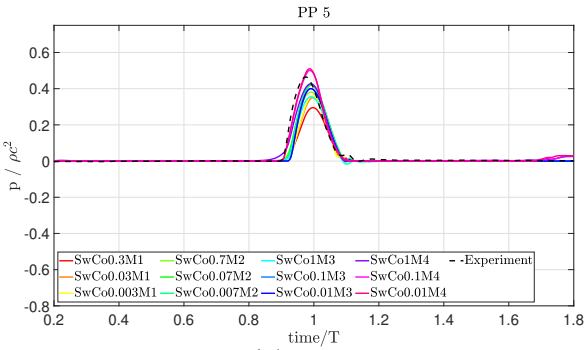


*(d)* PP5

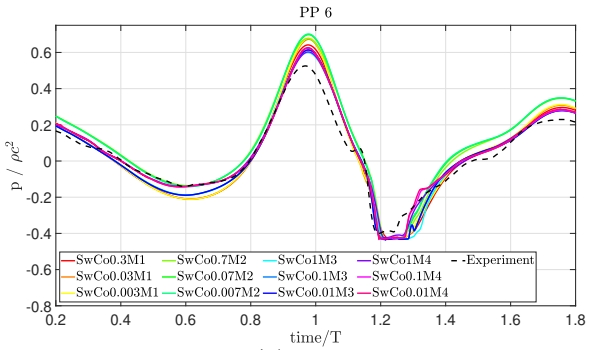


*(e)* PP6

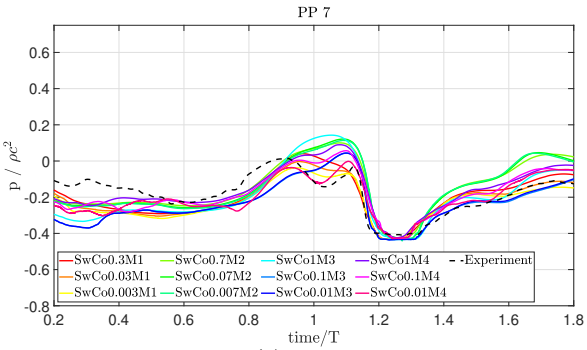


*(f)* PP7

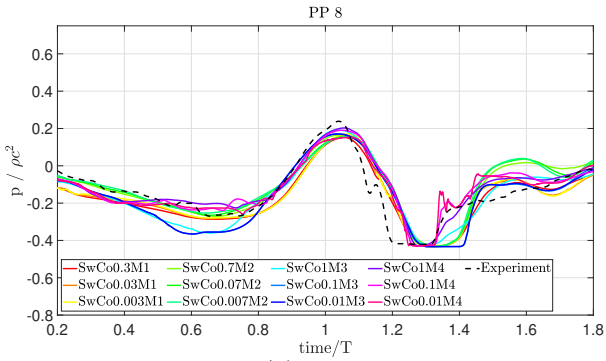


*(g)* PP8

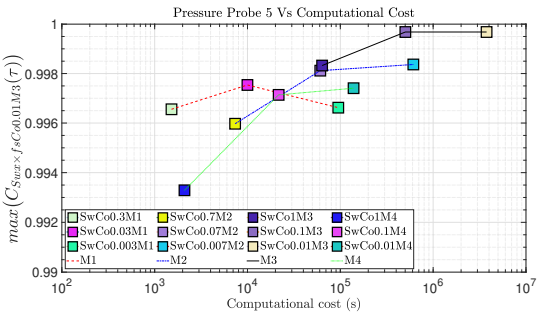


*(h)* Mean Pressure coefficient, Correlation with fsCo0.01M3

Figure A.14 – Pressure time history of the moving cylinder (0.75 m.s$^{-1}$) in NBR focusing waves for different mesh types simulated by the *foamStarSWENSE* solver

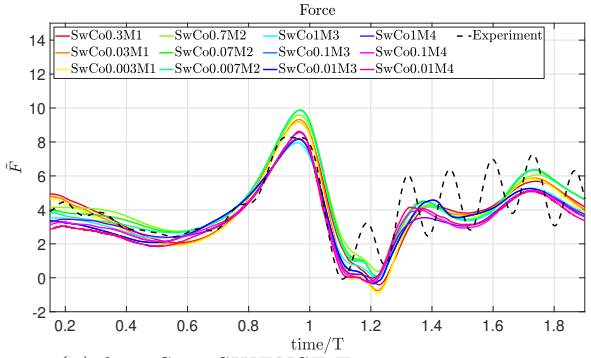


*(a) foamStar-SWENSE* Force comparison

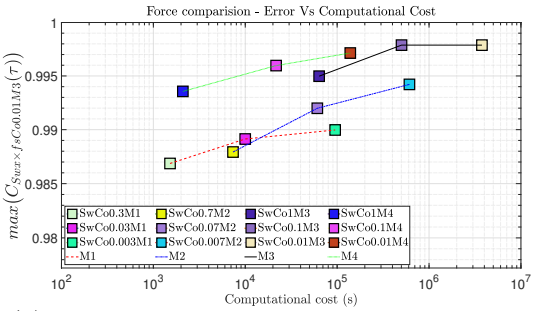


*(b) foamStar-SWENSE-* Force cross correlation

Figure A.15 – Force recorded for a moving cylinder(0.75 m.s$^{-1}$ ) in NBR focusing waves by the *foamStarSWENSE* solver (left) and its correlation coefficient with fsCo0.01M3 (right)

time step and converges to 0.998. Similar to previous wave and pressure results, mesh type M4, with all coarsest mesh outside and only refinement near the cylinder achieved an accuracy of 0.994 and converged to 0.998 (at 100 to 1000 times reduced computational time) . This again highlights the advantage of applying the SWENSE technique to similar issues to get a good estimate of forces at the lowest cost with high accuracy.

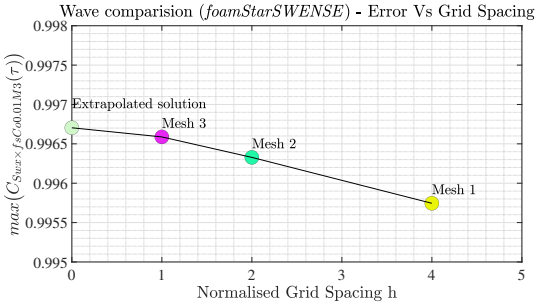


*(a) foamStar-SWENSE-* Wave elevation Grid Convergence study

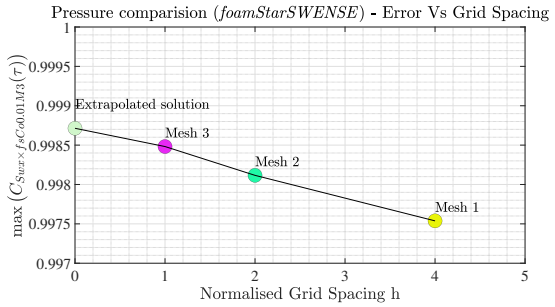


*(b) foamStar-SWENSE-* Pressure Grid Convergence study

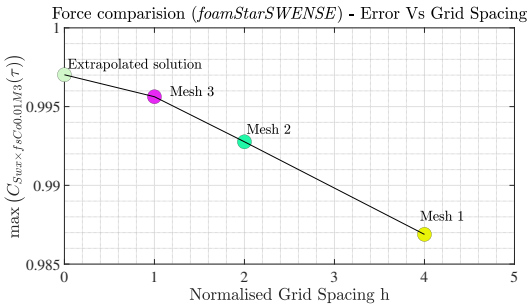


*(c) foamStar-SWENSE-* Force Grid Convergence study

Figure A.16 – Extrapolation of Coefficient with the Richardson method and its corresponding GCI for *foamStar-SWENSE* moving cylinder case (0.75 m.s$^{-1}$ )

In order to demonstrate, the converged solution was obtained using mesh type M3, and further no refinement was required, Richardson extrapolation was carried out as earlier, for each mesh type (Mesh 1 (M1), Mesh 2 (M2), and Mesh 3 (M3)) at the time step of 0.001s. Figures

A.16a, A.16b, and A.16c shows the extrapolation convergence plot for surface elevation, pressure and force respectively. In each of the three cases, the extrapolated coefficient is not close to one, and Mesh 3 is consistently close to the convergence point. This demonstrates that the results of the *foamStarSWENSE* solvers are not approaching the exact results of fsCo0.01M3 and instead reach an asymptotic that is somewhat off the result. M3 from *foamStarSWENSE* is close to the extrapolated value, which shows that convergence is nearly attained; further refining will raise the computing cost rather than accuracy. This convergence is also proved by comparing the slope between the solutions. The convergence slope from Mesh 1 to Mesh 2 in each case is 0.07%, 0.05%, 0.06% and it reduces for Mesh 2 to Mesh 3 like 0.03%, 0.03% and 0.3% respectively. Finally, towards the extrapolated coefficient, the slope is further reduced to 0.01%, 0.02%, and 0.1%, demonstrating that the curve is flattening and that further refining would mostly affect computational cost rather than accuracy.

# BIBLIOGRAPHY


Agarwal, S., Saincher, S., Sriram, V., Yan, S., Xie, Z., Schlurmann, T., Ma, Q., Yang, X., Wan, D., Gong, J., et al., 2021a. A comparative study on the nonlinear interaction between a focusing wave and cylinder using state-of-the-art solvers: part b. International Journal of Offshore and Polar Engineering 31, 11–18.

Agarwal, S., Sriram, V., Yan, S., Murali, K., 2021b. Improvements in MLPG formulation for 3D wave interaction with fixed structures. Computers & Fluids 218, 104826. doi:10.1016/j.compfluid.2020.104826.

Aggarwal, A., Chella, M.A., Bihs, H., Myrhaug, D., 2020. Properties of breaking irregular waves over slopes. Ocean Engineering 216, 108098.

Alexandre, A., Percher, Y., Choisnet, T., Buils Urbano, R., Harries, R., 2018. Coupled analysis and numerical model verification for the 2MW Floatgen demonstrator project with IDEOL platform, in: International Conference on Offshore Mechanics and Arctic Engineering, American Society of Mechanical Engineers. p. V001T01A032. doi:10.1115/IOWTC2018-1071.

Aliyar, S., Meyer, J., Sriram, V., Hildebrandt, A., 2021. Experimental investigation of offshore crane load during installation of a wind turbine jacket substructure in regular waves. Ocean Engineering 241, 109979.

Ansys, A., 2013. Aqwa theory manual. ed. Canonsburg, PA 15317, USA .

ANSYS, U., 2009. Ansys fluent 12.0. Theory Guide manual .

Arnal, V., 2020. Experimental modelling of a floating wind turbine using a «software-in-the-loop» approach. Ph.D. thesis. École Centrale de Nantes.

Arnal, V., Bonnefoy, F., Gilloteaux, J.C., Aubrun, S., 2019. Hybrid model testing of floating wind turbines: test bench for system identification and performance assessment, in: International Conference on Offshore Mechanics and Arctic Engineering, American Society of Mechanical Engineers. p. V010T09A078.

Arntsen, Ø., Ros Collados, X., Tørum, A., 2013. Impact forces on a vertical pile from plunging breaking waves, in: Coastal Structures 2011: (In 2 Volumes). World Scientific, pp. 533–544.

Babarit, A., Delhommeau, G., 2015. Theoretical and numerical aspects of the open source bem solver nemoh, in: 11th European wave and tidal energy conference (EWTEC2015).

Barthelemy, X., Banner, M., Peirson, W., Fedele, F., Allis, M., Dias, F., 2018. On a unified breaking onset threshold for gravity waves in deep and intermediate depth water. Journal of Fluid Mechanics 841, 463–488. doi:10.1017/jfm.2018.93.

Beazley, D.M., Ward, B.D., Cooke, I.R., 2001. The inside story on shared libraries and dynamic loading. Computing in Science & Engineering 3, 90–97.

Benitz, M.A., Schmidt, D., Lackner, M., Stewart, G., Jonkman, J., Robertson, A., 2014. Comparison of hydrodynamic load predictions between engineering models and computational fluid dynamics for the OC4-DeepCwind semi-submersible. Technical Report. National Renewable Energy Lab.(NREL), Golden, CO (United States).

Benitz, M.A., Schmidt, D.P., Lackner, M.A., Stewart, G.M., Jonkman, J., Robertson, A., 2015. Validation of hydrodynamic load models using cfd for the oc4-deepcwind semisubmersible, in: International Conference on Offshore Mechanics and Arctic Engineering, American Society of Mechanical Engineers. p. V009T09A037.

Berberović, E., Van Hinsberg, N., Jakirlić, S., Roisman, I., Tropea, C., 2009. Drop impact onto a liquid layer of finite thickness: Dynamics of the cavity evolution. Physical review. E, Statistical, nonlinear, and soft matter physics 79, 036306. doi:10.1103/PhysRevE.79.036306.

Beyer, F., Choisnet, T., Kretschmer, M., Cheng, P.W., 2015. Coupled mbs-cfd simulation of the ideol floating offshore wind turbine foundation compared to wave tank model test data, in: The Twenty-fifth International Ocean and Polar Engineering Conference, OnePetro.

Beyer, M., Swan, C., Christou, M., 2017. Focused waves on depth-varying currents: the role of vorticity, in: The 27th International Ocean and Polar Engineering Conference, OnePetro.

Biausser, B., Fraunié, P., Grilli, S.T., Marcer, R., 2004. Numerical analysis of the internal kinematics and dynamics of 3-d breaking waves on slopes. International Journal of Offshore and Polar Engineering 14.

Bihs, H., Wang, W., Pakozdi, C., Kamath, A., 2020. Reef3d:: Fnpf—a flexible fully nonlinear potential flow solver. Journal of Offshore Mechanics and Arctic Engineering 142.

Bruinsma, N., Paulsen, B., Jacobsen, N., 2018. Validation and application of a fully nonlinear numerical wave tank for simulating floating offshore wind turbines. Ocean Engineering 147, 647–658.

Burmester, S., Vaz, G., Gueydon, S., el Moctar, O., 2020. Investigation of a semi-submersible floating wind turbine in surge decay using cfd. Ship Technology Research 67, 2–14.

Büttner, T., Pérez-Collazo, C., Abanades, J., Hann, M., Harper, P., Greaves, D., Stiesdal, H., 2022. OrthoSpar, a novel substructure concept for floating offshore wind turbines: Physical model tests under towing conditions. Ocean Engineering 245, 110508. doi:10.1016/j.oceaneng.2021.110508.

Campana, E., Di Mascio, A., Esposito, P.G., Lalli, F., 1995. Viscous-inviscid coupling in free surface ship flows. International Journal for Numerical Methods in Fluids 21, 699–722. doi:10.1002/fld.1650210902.

Campana, E., Lalli, F., 1992. Viscous-inviscid coupling in ship hydrodynamics.

Canard, M., Ducrozet, G., Bouscasse, B., 2020. Generation of 3-hr Long-Crested Waves of Extreme Sea States With HOS-NWT Solver, in: International Conference on Offshore Mechanics and Arctic Engineering, American Society of Mechanical Engineers. p. V06BT06A064. doi:doi.org/10.1115/OMAE2020-18930.

Castro-Santos, L., Diaz-Casas, V., 2016. Floating offshore wind farms. Springer International Publishing. doi:doi:10.1007/978-3-319-27972-5.

Chabchoub, A., Fink, M., 2014. Time-reversal generation of rogue waves. Physical review letters 112, 124101.

Chella, M.A., Bihs, H., Myrhaug, D., Muskulus, M., 2015. Breaking characteristics and geometric properties of spilling breakers over slopes. Coastal Engineering 95, 4–19.

Chen, H., Hall, M., 2022. Cfd simulation of floating body motion with mooring dynamics: Coupling moordyn with openfoam. Applied Ocean Research 124, 103210.

Chen, H.C., Lee, S.K., 1999. Rans/laplace calculations of nonlinear waves induced by surface-piercing bodies. Journal of Engineering Mechanics 125, 1231–1242. doi:10.1061/(ASCE)0733-9399(1999)125:11(1231).

Chen, L., Zhai, H., Wang, P., Jeng, D.S., Zhang, Q., Wang, S., Duan, L., Liu, Y., 2020. Physical modeling of combined waves and current propagating around a partially embedded monopile in a porous seabed. Ocean Engineering 205, 107307.

Chen, X., 2011. Offshore hydrodynamics and applications. The IES Journal Part A: Civil & Structural Engineering 4, 124–142. doi:10.1080/19373260.2011.595903.

Cheng, P., Huang, Y., Wan, D., 2019. A numerical model for fully coupled aero-hydrodynamic analysis of floating offshore wind turbine. Ocean Engineering 173, 183–196.

Choi, Y., 2019. Two-way coupling between potential and viscous flows for a marine application. Ph.D. thesis. École centrale de Nantes.

Choi, Y., Bouscasse, B., Seng, S., Ducrozet, G., Gentaz, L., Ferrant, P., 2018a. Generation of regular and irregular waves in navier-stokes cfd solvers by matching with the nonlinear potential wave solution at the boundaries, in: International Conference on Offshore Mechanics and Arctic Engineering, American Society of Mechanical Engineers. p. V002T08A020.

Choi, Y., Bouscasse, B., Seng, S., Ducrozet, G., Gentaz, L., Ferrant, P., 2018b. Generation of Regular and Irregular Waves in Navier-Stokes CFD Solvers by Matching With the Nonlinear Potential Wave Solution at the Boundaries. doi:10.1115/OMAE2018-78077.

Choi, Y., Gouin, M., Ducrozet, G., Bouscasse, B., Ferrant, P., 2017a. Grid2Grid : HOS Wrapper Program for CFD solvers. arXiv preprint arXiv:1801.00026 , 0–45URL: http://arxiv.org/abs/1801.00026, arXiv:1801.00026.

Choi, Y., Gouin, M., Ducrozet, G., Bouscasse, B., Ferrant, P., 2017b. Grid2grid: Hos wrapper program for cfd solvers. arXiv preprint arXiv:1801.00026 .

Choi, Y., Malenica, Š., Bouscasse, B., Seng, S., Monroy, C., Gentaz, L., Ferrant, P., 2018c. Preliminary study on coupling of viscous and potential flow using domain decomposition and relaxation zones, in: Proceedings of the 33rd International Workshop on Water Waves and Floating Bodies (IWWWFB), Guidel-Plages, France, pp. 4–7.

Choi, Y.M., Kim, Y.J., Bouscasse, B., Seng, S., Gentaz, L., Ferrant, P., 2020. Performance of different techniques of generation and absorption of free-surface waves in computational fluid dynamics. Ocean Engineering 214, 107575.

Chorin, A.J., 1968. Numerical solution of the navier-stokes equations. Mathematics of computation 22, 745–762.

Christensen, E., Bredmose, H., Hansen, E., 2009. Transfer of boussinesq waves to a navier-stokes solver: Application to wave loads on a offshore wind turbine foundation, in: Proceedings of the ASME 28th International Conference on Offshore Mechanics and Arctic Engineering, American Society of Mechanical Engineers, United States. pp. 917–926. URL: http://www.seatoskymeetings.com/omae2009/, doi:10.1115/OMAE2009-79629. 28th International Conference on Ocean, Offshore and Arctic Engineering, OMAE 2009 ; Conference date: 31-05-2009 Through 05-06-2009.

Colicchio, G., Greco, M., Faltinsen, O.M., 2006. A BEM-level set domain-decomposition strategy for non-linear and fragmented interfacial flows. International Journal for Numerical Methods in Engineering 67, 1385–1419. doi:10.1002/nme.1680.

Davidson, J., Ringwood, J.V., 2017. Mathematical modelling of mooring systems for wave energy converters—a review. Energies 10, 666.

Delahaye, T., Franc, P., Colmard, C., Gentil, F., 2019. New pendular floater for offshore wind commercial farms, in: Offshore Mediterranean Conference and Exhibition, OnePetro.

Devolder, B., Rauwoens, P., Troch, P., 2017. Application of a buoyancy-modified k-$\omega$ sst turbulence model to simulate wave run-up around a monopile subjected to regular waves using openfoam®. Coastal Engineering 125, 81–94.

Dewey, R.K., 1999. Mooring design & dynamics, a matlab® package for designing and analyzing oceanographic moorings. Marine Models 1, 103–157.

Di Paolo, B., Lara, J.L., Barajas, G., Losada, Í.J., 2020. Wave and structure interaction using multi-domain couplings for Navier-Stokes solvers in OpenFOAM®. Part I: Implementation and validation. Coastal Engineering , 103799doi:10.1016/j.coastaleng.2020.103799.

Dinius, J.D., Damiani, R., Johnson, K., Grant, E., Pao, L.Y., Phadnis, M., 2022. Control actuation options for the spiderfloat floating offshore wind substructure, in: AIAA SCITECH 2022 Forum, p. 2295.

Dommermuth, D.G., 1993. The laminar interactions of a pair of vortex tubes with a free surface. Journal of Fluid Mechanics 246, 91–115. doi:10.1017/S0022112093000059.

Dommermuth, D.G., Yue, D.K., Lin, W., Rapp, R., Chan, E., Melville, W., 1988. Deep-water plunging breakers: a comparison between potential theory and experiments. Journal of Fluid Mechanics 189, 423–442.

Ducrozet, G., Bonnefoy, F., Le Touzé, D., Ferrant, P., 2006. Implementation and validation of nonlinear wavemaker models in a hos numerical wave tank. International Journal of Offshore and Polar Engineering 16.

Ducrozet, G., Bonnefoy, F., Le Touzé, D., Ferrant, P., 2012. A modified high-order spectral method for wavemaker modeling in a numerical wave tank. European Journal of Mechanics-B/Fluids 34, 19–34.

Ducrozet, G., Bonnefoy, F., Le Touzé, D., Ferrant, P., 2016a. Hos-ocean: Open-source solver for nonlinear waves in open ocean based on high-order spectral method. Computer Physics Communications 203, 245–254.

Ducrozet, G., Bonnefoy, F., Mori, N., Fink, M., Chabchoub, A., 2020. Experimental reconstruction of extreme sea waves by time reversal principle. Journal of Fluid Mechanics 884.

Ducrozet, G., Bouscasse, B., Gouin, M., Ferrant, P., Bonnefoy, F., 2019. Cn-stream: Open-source library for nonlinear regular waves using stream function theory .

Ducrozet, G., Fink, M., Chabchoub, A., 2016b. Time-reversal of nonlinear waves: Applicability and limitations. Physical Review Fluids 1, 054302.

Dunbar, A.J., Craven, B.A., Paterson, E.G., 2015. Development and validation of a tightly coupled cfd/6-dof solver for simulating floating offshore wind turbine platforms. Ocean Engineering 110, 98–105.

Düz, B., Bunnik, T., Kapsenberg, G., 2016. Numerical simulation of nonlinear free surface water waves using a coupled potential FLOW-URANS/VOF approach. ECCOMAS Congress 2016 - Proceedings of the 7th European Congress on Computational Methods in Applied Sciences and Engineering 4, 7095–7120. doi:10.7712/100016.2321.10351.

Edmund, D.O., Maki, K.J., Beck, R.F., 2013. A velocity-decomposition formulation for the incompressible Navier-Stokes equations. Computational Mechanics 52, 669–680. doi:10.1007/s00466-013-0839-6.

Elhanafi, A., Macfarlane, G., Fleming, A., Leong, Z., 2017. Experimental and numerical investigations on the hydrodynamic performance of a floating–moored oscillating water column wave energy converter. Applied energy 205, 369–390.

Engsig-Karup, A., 2006. Unstructured Nodal DG-FEM solution of high-order Boussinesq-type equations. Ph.D. thesis.

Engsig-Karup, A.P., Bingham, H.B., Lindberg, O., 2009. An efficient flexible-order model for 3d nonlinear water waves. Journal of computational physics 228, 2100–2118.

Engsig-Karup, A.P., Eskilsson, C., Bigoni, D., 2016. A stabilised nodal spectral element method for fully nonlinear water waves. Journal of Computational Physics 318, 1–21.

Engsig-Karup, A.P., Madsen, M.G., Glimberg, S.L., 2012. A massively parallel gpu-accelerated model for analysis of fully nonlinear free surface waves. International Journal for Numerical Methods in Fluids 70, 20–36.

Engsig-Karup, A.P., Madsen, P.A., Bingham, H.B., Thomsen, P.G., 2007. Unstructured nodal DG-FEM solution of high-order Boussinesq-type equations.

Europe, W., 2018. Offshore wind in Europe offshore wind in Europe. Technical Report. Technical Report, wind Europe. Accessed Mar.

Faltinsen, O., 1993. Sea loads on ships and offshore structures. volume 1. Cambridge university press.

Fenton, R., 2014. On the Fourier approximation method for steady water waves. Acta Oceanologica Sinica 33, 37–47. doi:10.1007/s13131-014-0470-1.

Ferrant, P., Gentaz, L., Le Touzé, D., 2002. A new RANSE/Potential Approach for Water Wave Diffraction. Proc. Numerical Towing Tank Symposium, NuTTS .

Ferri, F., Palm, J., 2015. Implementation of a dynamic mooring solver (moody) into a wave to wire model of a simple wec. Department of Civil Engineering, Aalbor g University .

Ferziger, J.H., Perić, M., 1999. Computational Methods for Fluid Dynamics. 2nd ed., Springer, Berlin.

Finance, B.N.E., 2019. New energy outlook 2019. Executive Summary .

Focus, O., 2020. Blueprint for offshore wind to green ireland's energy supply. URL: https://oceanfocus.ie/offshore-wind/.

Fossen, T.I., 1999. Guidance and control of ocean vehicles. University of Trondheim, Norway, Printed by John Wiley & Sons, Chichester, England, ISBN: 0 471 94113 1, Doctors Thesis .

Fossen, T.I., 2011. Handbook of marine craft hydrodynamics and motion control. John Wiley & Sons.

Fourtakas, G., Stansby, P.K., Rogers, B.D., Lind, S.J., Yan, S., Ma, Q., 2018. On the coupling of incompressible sph with a finite element potential flow solver for nonlinear free-surface flows. International Journal of Offshore and Polar Engineering 28, 248–254.

Fredriksen, A.G., 2015. A numerical and experimental study of a two-dimensional body with moonpool in waves and current.

Gentaz, L., 2004. a Vertical Cylinder in Non-Linear Waves Using an Explicit Incident Wave Model. Simulation , 1–7.

Goda, Y., 1966. A study on impulsive breaking wave force upon a vertical pile. Rept. Port and Harbour Res. Inst. 5, 1–30.

Grilli, S.T., Gilbert, R.W., Lubin, P., Vincent, S., Astruc, D., Legendre, D., Duval, M., Kimmoun, O., Branger, H., Devrard, D., Fraunié, P., Abadie, S., 2004. Numerical modeling and experiments for solitary wave shoaling and breaking over a sloping beach. Proceedings of the International Offshore and Polar Engineering Conference , 306–312.

Grilli, S.T., Skourup, J., Svendsen, I., 1989. An efficient boundary element method for nonlinear water waves. Engineering Analysis with Boundary Elements 6, 97–107.

Guignard, S., Grilli, S., Marcer, R., 1999. Computation of shoaling and breaking waves in nearshore areas by the coupling of bem and vof methods. Proceedings of the International Offshore and Polar Engineering Conference III.

Guillerm, P., 2001. Application de la methode de fourier-kochin au probleme du couplage fluide visqueux-fluide parfait.

GWEC, V.W.P., 2021. Global wind energy council,(2021) .

Hall, M., 2015. Moordyn user's guide. Orono, ME: Department of Mechanical Engineering, University of Maine .

Hall, M., Goupee, A., 2015. Validation of a lumped-mass mooring line model with deepcwind semisubmersible model test data. Ocean Engineering 104, 590–603.

Hall, M., Housner, S., Sirnivas, S., Wilson, S., et al., 2021. MoorPy (Quasi-Static Mooring Analysis in Python). Technical Report. National Renewable Energy Lab.(NREL), Golden, CO (United States).

Hamilton, A., Yeung, R.W., 2011. Viscous and inviscid matching of three-dimensional free-surface flows utilizing shell functions. Journal of Engineering Mathematics 70, 43–66. doi:10.1007/s10665-010-9438-0.

Harlow, F.H., Welch, J.E., 1965. Numerical calculation of time-dependent viscous incompressible flow of fluid with free surface. The physics of fluids 8, 2182–2189.

Hasan, S., Sriram, V., Selvam, R.P., 2019. Evaluation of an eddy viscosity type wave breaking model for intermediate water depths. European Journal of Mechanics-B/Fluids 78, 115–138.

Hestenes, M.R., Stiefel, E., 1952. Methods of conjugate gradients for solving. Journal of research of the National Bureau of Standards 49, 409.

Higuera, P., Lara, J.L., Losada, I.J., 2013. Realistic wave generation and active wave absorption for Navier-Stokes models. Application to OpenFOAM®. Coastal Engineering 71, 102–118. URL: http://dx.doi.org/10.1016/j.coastaleng.2012.07.002, doi:10.1016/j.coastaleng.2012.07.002.

Hildebrandt, A., Sriram, V., 2014. Pressure distribution and vortex shedding around a cylinder due to a steep wave at the onset of breaking from physical and numerical modeling.

Hildebrandt, A., Sriram, V., Schlurmann, T., 2013a. Simulation of focusing waves and local line forces due to wave impacts on a tripod structure, in: The Twenty-third International Offshore and Polar Engineering Conference, OnePetro.

Hildebrandt, A., Sriram, V., Schlurmann, T., 2013b. Simulation of focusing waves and local line forces due to wave impacts on a tripod structure. Proceedings of the International Offshore and Polar Engineering Conference , 575–581.

Hirt, C., Nichols, B., 1981. Volume of fluid (vof) method for the dynamics of free boundaries. Journal of Computational Physics 39, 201 – 225. URL: http://www.sciencedirect.com/science/article/pii/0021999181901455, doi:https://doi.org/10.1016/0021-9991(81)90145-5.

Huang, H., Gu, H., Chen, H.C., 2022. A new method to couple fem mooring program with cfd to simulate six-dof responses of a moored body. Ocean Engineering 250, 110944.

Huang, Y., Zhuang, Y., Wan, D., 2021. Hydrodynamic study and performance analysis of the oc4-deepcwind platform by cfd method. International Journal of Computational Methods 18, 2050020.

Huseby, M., Grue, J., 2000. An experimental investigation of higher-harmonic wave forces on a vertical cylinder. Journal of fluid Mechanics 414, 75–103.

Iafrati, A., Campana, E.F., 2003. A domain decomposition approach to compute wave breaking (wave-breaking flows). International Journal for Numerical Methods in Fluids 41, 419–445. doi:10.1002/fld.448.

IEA, 2019. International energy agency, offshore wind outlook 2019: World energy outlook special report. URL: https://iea.blob.core.windows.net/assets/495ab264-4ddf-4b68-b9c0-514295ff40a7/Offshore_Wind_Outlook_2019.pdf.

India Energy Outlook, 2021. World Energy Outlook, Special Report, INTERNATIONAL ENERGY AGENCY. URL: https://iea.blob.core.windows.net/assets/1de6d91e-e23f-4e02-b1fb-51fdd6283b22/India_Energy_Outlook_2021.pdf.

IPCC, . Global energy transformation report, roadmap to 2050. URL: https://www.irena.org/digitalarticles/2019/apr/-/media.

Issa, R.I., 1986. Solution of the implicitly discretised fluid flow equations by operator-splitting. Journal of computational physics 62, 40–65.

Jacobs, D.A., 1986. A generalization of the conjugate-gradient method to solve complex systems. IMA journal of numerical analysis 6, 447–452.

Jacobsen, N.G., 2017. waves2foam manual. Deltares, The Netherlands 570.

Jacobsen, N.G., Fuhrman, D.R., Fredsøe, J., 2012. A wave generation toolbox for the open-source CFD library: OpenFoam®. International Journal for Numerical Methods in Fluids 70, 1073–1088. doi:10.1002/fld.2726.

Jasak, H., 1996. Error analysis and estimation for the finite volume method with applications to fluid flows. Direct M.

Jasak, H., 2009. Dynamic mesh handling in openfoam, in: 47th AIAA aerospace sciences meeting including the new horizons forum and aerospace exposition, p. 341.

Jasak, H., Tukovic, Z., 2006. Automatic mesh motion for the unstructured finite volume method. Transactions of FAMENA 30, 1–20.

Jasak, H., Tuković, Ž., 2010. Dynamic mesh handling in openfoam applied to fluid-structure interaction simulations, in: Proceedings of the V European Conference on Computational Fluid Dynamics ECCOMAS CFD 2010.

Jensen, J.J., 2001. Load and global response of ships. Elsevier.

Jiang, C., el Moctar, O., Paredes, G.M., Schellin, T.E., 2020. Validation of a dynamic mooring model coupled with a rans solver. Marine Structures 72, 102783.

Jiang, C., el Moctar, O., Schellin, T.E., Paredes, G.M., 2021. Comparative study of mathematical models for mooring systems coupled with cfd. Ships and Offshore Structures 16, 942–954.

Jonkman, J., 2010. Definition of the Floating System for Phase IV of OC3. Technical Report. National Renewable Energy Lab.(NREL), Golden, CO (United States).

Jonkman, J., 2013. The new modularization framework for the fast wind turbine cae tool, in: 51st AIAA aerospace sciences meeting including the new horizons forum and aerospace exposition, p. 202.

Journee, J.M., Adegeest, L.J., 2003. Theoretical manual of strip theory program" seaway for windows". TU Delft, Report 1370 .

Kamath, A., Chella, M.A., Bihs, H., Arntsen, Ø.A., 2016. Breaking wave interaction with a vertical cylinder and the effect of breaker location. Ocean Engineering 128, 105–115.

Karnoski, S., Palo, P., 1988. Validation of a static mooring analysis model with full-scale data, in: Offshore Technology Conference, OnePetro.

Kenny, M., 2016. Flexcom—program documentation .

Keulegan, G.H., Carpenter, L.H., et al., 1958. Forces on cylinders and plates in an oscillating fluid. Journal of research of the National Bureau of Standards 60, 423–440.

Kim, J., O'Sullivan, J., Read, A., 2012. Ringing analysis of a vertical cylinder by euler overlay method, in: International Conference on Offshore Mechanics and Arctic Engineering, American Society of Mechanical Engineers. pp. 855–866.

Kim, K., Sirviente, A.I., Beck, R.F., 2005a. The complementary RANS equations for the simulation of viscous flows. International Journal for Numerical Methods in Fluids 48, 199–229. doi:10.1002/fld.892.

Kim, K., Sirviente, A.I., Beck, R.F., 2005b. The complementary RANS equations for the simulation of viscous flows. International Journal for Numerical Methods in Fluids 48, 199–229. doi:10.1002/fld.892.

Kim, Y.J., 2021a. Numerical improvement and validation of a naval hydrodynamics CFD solver in view of performing fast and accurate simulation of complex ship-wave interaction. Ph.D. thesis. École centrale de Nantes.

Kim, Y.J., 2021b. Numerical improvement and validation of a naval hydrodynamics CFD solver in view of performing fast and accurate simulation of complex ship-wave interaction. Ph.D. thesis. École centrale de Nantes.

Kim, Y.J., 2021c. Numerical improvement and validation of a naval hydrodynamics CFD solver in view of performing fast and accurate simulation of complex ship-wave interaction. Ph.D. thesis.

Krey, V., Clarke, L., 2011. Role of renewable energy in climate mitigation: a synthesis of recent scenarios. Climate Policy 11, 1131–1158.

Kvittem, M.I., Bachynski, E.E., Moan, T., 2012. Effects of hydrodynamic modelling in fully coupled simulations of a semi-submersible wind turbine. Energy Procedia 24, 351–362.

Lachaume, C., Biausser, B., Fraunié, P., Grilli, S.T., Guignard, S., 2003a. Modeling of breaking and post-breakingwaves on slopes by coupling of bem and vof methods, in: The Thirteenth International Offshore and Polar Engineering Conference, OnePetro.

Lachaume, C., Biausser, B., Grilli, S.T., Fraunié, P., Guignard, S., 2003b. Modeling of Breaking and Post-breaking Waves on Slopes by Coupling of BEM and VOF Methods. Proceedings of the International Offshore and Polar Engineering Conference , 1698–1704.

Lamb, W.F., Wiedmann, T., Pongratz, J., Andrew, R., Crippa, M., Olivier, J.G., Wiedenhofer, D., Mattioli, G., Al Khourdajie, A., House, J., et al., 2021. A review of trends and drivers of greenhouse gas emissions by sector from 1990 to 2018. Environmental research letters doi:https://doi.org/10.1088/1748-9326/abee4e.

Landesman, P., 2022. Simulation of wave-structure interaction by a two-way coupling between a fully nonlinear potential flow model and a Navier Stokes solver. Ph.D. thesis. Marne-la-vallée, ENPC.

Larsen, T.J., Hansen, A.M., 2007. How 2 hawc2, the user's manual tech. rep. Risø National Laboratory .

Le Cunff, C., Heurtier, J.M., Piriou, L., Berhault, C., Perdrizet, T., Teixeira, D., Ferrer, G., Gilloteaux, J.C., 2013. Fully coupled floating wind turbine simulator based on nonlinear finite element method: Part i—methodology, in: International Conference on Offshore Mechanics and Arctic Engineering, American Society of Mechanical Engineers. p. V008T09A050.

Lee, C.H., Newman, J.N., 2006. Wamit user manual. WAMIT, Inc , 42.

Lee, S.C., Song, S., Park, S., 2021. Platform motions and mooring system coupled solver for a moored floating platform in a wave. Processes 9, 1393.

Li, H., Bachynski, E.E., 2021. Experimental and numerical investigation of nonlinear diffraction wave loads on a semi-submersible wind turbine. Renewable Energy 171, 709–727.

Li, Z., 2018. Two-phase spectral wave explicit Navier-Stokes equations method for wave-structure interactions. Ph.D. thesis. Ecole centrale de Nantes.

Li, Z., Bouscasse, B., Ducrozet, G., Gentaz, L., Le Touzé, D., Ferrant, P., 2021a. Spectral wave explicit navier-stokes equations for wave-structure interactions using two-phase computational fluid dynamics solvers. Ocean Engineering 221, 108513.

Li, Z., Bouscasse, B., Ducrozet, G., Gentaz, L., Le Touzé, D., Ferrant, P., 2021b. Spectral wave explicit navier-stokes equations for wave-structure interactions using two-phase computational fluid dynamics solvers. Ocean Engineering 221, 108513. doi:10.1016/j.oceaneng.2020.108513.

Li, Z., Bouscasse, B., Gentaz, L., Ducrozet, G., Ferrant, P., 2018. Progress in Coupling Potential Wave Models and Two-Phase Solvers With the SWENSE Methodology. URL: https://doi.org/10.1115/OMAE2018-77466, doi:10.1115/OMAE2018-77466. v009T13A027.

Lin, Z., Qian, L., Bai, W., Ma, Z., Chen, H., Zhou, J.G., Gu, H., 2021. A finite volume based fully nonlinear potential flow model for water wave problems. Applied Ocean Research 106, 102445.

Lind, S.J., Xu, R., Stansby, P.K., Rogers, B.D., 2012. Incompressible smoothed particle hydrodynamics for free-surface flows: A generalised diffusion-based algorithm for stability and validations for impulsive flows and propagating waves. Journal of Computational Physics 231, 1499–1523.

Löhner, R., Yang, C., 1996. Improved ale mesh velocities for moving bodies. Communications in numerical methods in engineering 12, 599–608.

Lu, X., Chen, Y., John Chandar, D.D., Lou, J., 2016. Coupling of viscous and potential flow models with free surface: Implementation and application to offshore engineering. International Journal of Computational Methods and Experimental Measurements 4, 413–423. doi:10.2495/CMEM-V4-N4-413-423.

Luquet, R., Alessandrini, B., Ferrant, P., Gentaz, L., 2003. using explicit incident wave models .

Luquet, R., Ferrant, P., Alessandrini, B., Ducrozet, G., Gentaz, L., 2007. Simulation of a TLP in waves using the SWENSE scheme. Proceedings of the International Offshore and Polar Engineering Conference , 1916–1922.

Make, M., 2014. Predicting scale effects on floating offshore wind turbines .

Marshall, J., Adcroft, A., Hill, C., Perelman, L., Heisey, C., 1997. A finite-volume, incompressible navier stokes model for studies of the ocean on parallel computers. Journal of Geophysical Research: Oceans 102, 5753–5766.

Masciola, M., 2018. Map++ documentation. NREL: Golden, CO, USA .

Masciola, M., Jonkman, J., Robertson, A., 2013. Implementation of a multisegmented, quasi-static cable model, in: The Twenty-third International Offshore and Polar Engineering Conference, OnePetro.

Masciola, M., Jonkman, J., Robertson, A., 2014. Extending the capabilities of the mooring analysis program: A survey of dynamic mooring line theories for integration into fast, in: International Conference on Offshore Mechanics and Arctic Engineering, American Society of Mechanical Engineers. p. V09AT09A032.

Mayer, S., Garapon, A., Sørensen, L., 1998. A fractional step method for unsteady free-surface flow with applications to non-linear wave dynamics. International Journal for Numerical Methods in Fluids - INT J NUMER METHOD FLUID 28, 293–315. doi:10.1002/(SICI)1097-0363(19980815)28:23.0.CO;2-1.

Michel, G., Bonnefoy, F., Ducrozet, G., Prabhudesai, G., Cazaubiel, A., Copie, F., Tikan, A., Suret, P., Randoux, S., Falcon, E., 2020. Emergence of peregrine solitons in integrable turbulence of deep water gravity waves. Physical Review Fluids 5, 082801.

Monroy, C., Ducrozet, G., Bonnefoy, F., Babarit, A., Gentaz, L., Ferrant, P., 2010. RANS simulations of a CALM buoy in regular and irregular seas using the SWENSE method. Proceedings of the International Offshore and Polar Engineering Conference 3, 678–685.

Monroy, C., Seng, S., Sime, M., 2016. foamStar. 15Èmes Journées De L'Hydrodynamique .

Morison, J., Johnson, J., Schaaf, S., 1950. The force exerted by surface waves on piles. Journal of Petroleum Technology 2, 149–154.

Musial, W., Ram, B., 2010. Large-scale offshore wind power in the United States: Assessment of opportunities and barriers. Technical Report. National Renewable Energy Lab.(NREL), Golden, CO (United States).

Nematbakhsh, A., Bachynski, E.E., Gao, Z., Moan, T., 2015. Comparison of wave load effects on a tlp wind turbine by using computational fluid dynamics and potential flow theory approaches. Applied Ocean Research 53, 142–154.

NetZero, 2021. Special report, net zero by 2050: A roadmap for the global energy sector, international energy agency. URL: https://iea.blob.core.windows.net/assets/deebef5d-0c34-4539-9d0c-10b13d840027/NetZeroby2050-ARoadmapfortheGlobalEnergySector_CORR.pdf.

NUMECA, . Numeca, theoretical manual FINEMarine v3.1. NUMECA .

Oberhagemann, J., 2017. On prediction of wave-induced loads and vibration of ship structures with finite volume fluid dynamic methods. Ph.D. thesis. Universitätsbibliothek Duisburg-Essen.

OpenFOAM, 2009. Openfoam—the open source cfd toolbox—user guide.

ORCINA, . OrcaFlex—Documentation. URL: https://www.orcina.com/releases/orcaflex-101/.

Orcina, L., 2018. Orcaflex user manual: Orcaflex version 10.2 c. Daltongate Ulverston Cumbria, UK .

Osher, S., Fedkiw, R.P., 2001. Level set methods: an overview and some recent results. Journal of Computational physics 169, 463–502.

Paduano, B., Giorgi, G., Gomes, R.P., Pasta, E., Henriques, J.C., Gato, L., Mattiazzo, G., 2020. Experimental validation and comparison of numerical models for the mooring system of a floating wave energy converter. Journal of Marine Science and Engineering 8, 565.

Palm, J., Eskilsson, C., Paredes, G.M., Bergdahl, L., 2016. Coupled mooring analysis for floating wave energy converters using cfd: Formulation and validation. International Journal of Marine Energy 16, 83–99.

Patankar, S.V., 1980. Numerical heat transfer and fluid flow. Series on Computational Methods in Mechanics and Thermal Science, Hemisphere Publishing Corporation (CRC Press, Taylor & Francis Group). URL: http://www.crcpress.com/product/isbn/9780891165224.

Patankar, S.V., Spalding, D.B., 1983. A calculation procedure for heat, mass and momentum transfer in three-dimensional parabolic flows, in: Numerical prediction of flow, heat transfer, turbulence and combustion. Elsevier, pp. 54–73.

Paulsen, B.T., Bredmose, H., Bingham, H.B., 2014a. An efficient domain decomposition strategy for wave loads on surface piercing circular cylinders. Coastal Engineering 86, 57–76. URL: http://dx.doi.org/10.1016/j.coastaleng.2014.01.006, doi:10.1016/j.coastaleng.2014.01.006.

Paulsen, B.T., Bredmose, H., Bingham, H.B., 2014b. An efficient domain decomposition strategy for wave loads on surface piercing circular cylinders. Coastal Engineering 86, 57–76.

Pinguet, R., 2021. Hydrodynamics of semi-submersible floater for offshore wind turbines in highly nonlinear waves using Computational Fluid Dynamics (CFD), and validation of overset meshing technique in a numerical wave tank. Ph.D. thesis. Ecole Centrale Marseille.

Quallen, S., Xing, T., 2016. Cfd simulation of a floating offshore wind turbine system using a variable-speed generator-torque controller. Renewable Energy 97, 230–242.

Quallen, S., Xing, T., Carrica, P., Li, Y., Xu, J., 2013. Cfd simulation of a floating offshore wind turbine system using a quasi-static crowfoot mooring-line model, in: The twenty-third international offshore and polar engineering conference, OnePetro.

Randolph, M., Quiggin, P., 2009. Non-linear hysteretic seabed model for catenary pipeline contact, in: International Conference on Offshore Mechanics and Arctic Engineering, pp. 145–154.

Ransley, E., Yan, S., Brown, S., Hann, M., Graham, D., Windt, C., Schmitt, P., Davidson, J., Ringwood, J., Musiedlak, P.H., et al., 2020. A blind comparative study of focused wave interactions with floating structures (ccp-wsi blind test series 3). International Journal of Offshore and Polar Engineering 30, 1–10.

Ribes, A., Caremoli, C., 2007. Salome platform component model for numerical simulation, in: 31st annual international computer software and applications conference (COMPSAC 2007), IEEE. pp. 553–564.

Richardson, L.F., Gaunt, J.A., 1927. The deferred approach to the limit. Transactions of the Royal Society of London Ser. A, 299 – 361.

Rienecker, M.M., Fenton, J.D., 1981. A fourier approximation method for steady water waves. Journal of fluid mechanics 104, 119–137.

Rijas, A., Sriram, V., Yan, S., 2019. Variable spaced particle in mesh-free method to handle wave-floating body interactions. International Journal for Numerical Methods in Fluids 91, 263–286.

Rivera Arreba, I., 2017. Computation of nonlinear wave loads on floating structures. Master's thesis. NTNU.

Roache, P., 1997. Quantification of uncertainty in computational fluid dynamics. Annual Review of Fluid Mechanics 29, 123–160.

Robaux, F., 2020. Numerical simulation of wave-body interaction: development of a fully non-linear potential flow solver and assessment of two local coupling strategies with a CFD solver. Ph.D. thesis. Université Aix Marseille.

Robaux, F., Benoit, M., 2021. Development and validation of a numerical wave tank based on the harmonic polynomial cell and immersed boundary methods to model nonlinear wave-structure interaction. Journal of Computational Physics 446, 110560.

Robertson, A., Jonkman, J., Masciola, M., Song, H., Goupee, A., Coulling, A., Luan, C., 2014. Definition of the semisubmersible floating system for phase II of OC4. Technical Report. National Renewable Energy Lab.(NREL), Golden, CO (United States).

Rosemurgy, W.J., Beck, R.F., Maki, K.J., 2016. A velocity decomposition formulation for 2D steady incompressible lifting problems. European Journal of Mechanics, B/Fluids 58, 70–84. URL: http://dx.doi.org/10.1016/j.euromechflu.2016.03.007, doi:10.1016/j.euromechflu.2016.03.007.

Rusche, H., 2003. Computational fluid dynamics of dispersed two-phase flows at high phase fractions. Ph.D. thesis. Imperial College London (University of London).

Saincher, S., Sriram, V., Agarwal, S., Schlurmann, T., 2022. Experimental investigation of hydrodynamic loading induced by regular, steep non-breaking and breaking focused waves on a moving cylinder. European Journal of Mechanics .

Sarpkaya, T., Storm, M., 1985. In-line force on a cylinder translating in oscillatory flow. Applied Ocean Research 7, 188–196. doi:'10.1016/0141-1187(85)90025-2'.

Seiffert, B.R., Ducrozet, G., 2018. Simulation of breaking waves using the high-order spectral method with laboratory experiments: wave-breaking energy dissipation. Ocean Dynamics 68, 65–89.

Seiffert, B.R., Ducrozet, G., Bonnefoy, F., 2017. Simulation of breaking waves using the high-order spectral method with laboratory experiments: Wave-breaking onset. Ocean Modelling 119, 94–104.

Seng, S., 2012. Slamming and whipping analysis of ships. DTU Mechanical Engineering.

Siddiqui, 2017. Validation of damaged ship hydrodynamics by a domain decomposition approach using the Harmonic Polynomial Cell method and OpenFOAM , 2–5.

Siemens, P., 2019. Star-ccm+ user guide version 13.04. Siemens PLM Software Inc: Munich, Germany .

Simonsen, C.D., Otzen, J.F., Joncquez, S., Stern, F., 2013. Efd and cfd for kcs heaving and pitching in regular head waves. Journal of Marine Science and Technology 18, 435–459.

Skaare, B., Nielsen, F.G., Hanson, T.D., Yttervik, R., Havmøller, O., Rekdal, A., 2015. Analysis of measurements and simulations from the hywind demo floating wind turbine. Wind Energy 18, 1105–1122.

SNAME, T., 1950. Nomenclature for treating the motion of a submerged body through a fluid. The Society of Naval Architects and Marine Engineers, Technical and Research Bulletin , 1–5.

Sriram, V., Agarwal, S., Schlurmann, T., 2021a. Laboratory study on steep wave interactions with fixed and moving cylinder. International Journal of Offshore and Polar Engineering 31, 19–26.

Sriram, V., Agarwal, S., Yan, S., Xie, Z., Saincher, S., Schlurmann, T., Ma, Q., Stoesser, T., Zhuang, Y., Han, B., Zhao, W., Yang, X., Li, Z., Wan, D., Zhang, Y., Teng, B., Ning, D., Zhang, N., Zheng, X., Xu, G., Gong, J., Li, Y., Liao, K., Duan, W., Han, R., Asnim, W., Sulaiman, Z., Zhou, Z., Qin, J., Li, Y., Song, Z., Lou, X., Lu, L., Yuan, C., Ma, Y., Ai, C., Dong, G., Sun, H., Wang, Q., Zhai, Z.T., Shao, Y.L., Lin, Z., Qian, L., Bai, W., Ma, Z., Higuera, P., Buldakov, E., Stagonas, D., Lopez, S.M., Christou, A., Lin, P., Li, Y., Lu, J., Hong, S.Y., Ha, Y.J., Kim, K.H., Cho, S.K., Park, D.M., Laskowski, W., Eskilsson, C., Ricchiuto, M., Engsig-Karup, A.P., Cheng, L., Zheng, J., Gu, H., Li, G., 2021b. A Comparative Study on the Nonlinear Interaction Between a Focusing Wave and Cylinder Using State-of-the-art Solvers: Part A. International Journal of Offshore and Polar Engineering 31, 1–10. URL: https://doi.org/10.17736/ijope.2021.jc820, doi:10.17736/ijope.2021.jc820.

Sriram, V., Agarwal, S., Yan, S., Xie, Z., Saincher, S., Schlurmann, T., Ma, Q., Stoesser, T., Zhuang, Y., Han, B., et al., 2021c. A comparative study on the nonlinear interaction between a focusing wave and cylinder using state-of-the-art solvers: Part a. International Journal of Offshore and Polar Engineering 31, 1–10.

Sriram, V., Ma, Q., 2021. Review on the local weak form-based meshless method (mlpg): Developments and applications in ocean engineering. Applied Ocean Research 116, 102883.

Sriram, V., Ma, Q., Schlurmann, T., 2014a. A hybrid method for modelling two dimensional non-breaking and breaking waves. Journal of computational physics 272, 429–454.

Sriram, V., Ma, Q.W., Schlurmann, T., 2014b. A hybrid method for modelling two dimensional non-breaking and breaking waves. Journal of Computational Physics 272, 429–454. doi:10.1016/j.jcp.2014.04.030.

Sriram, V., Sannasiraj, S., Sundar, V., 2006. Simulation of 2-d nonlinear waves using finite element method with cubic spline approximation. Journal of Fluids and Structures 22, 663–681.

Sriram, V., Schlurmann, T., Schimmels, S., 2015. Focused wave evolution using linear and second order wavemaker theory. Applied Ocean Research 53, 279 – 296.

Sruthi, C., Sriram, V., 2017. Wave impact load on jacket structure in intermediate water depth. Ocean Engineering 140, 183–194.

Tahara, Y., Stern, F., Rosen, B., 1992. An interactive approach for calculating ship boundary layers and wakes for nonzero froude number. Journal of Computational Physics 98, 33 – 53. URL: http://www.sciencedirect.com/science/article/pii/002199919290171T, doi:https://doi.org/10.1016/0021-9991(92)90171-T.

Thomsen, J.B., Eskilsson, C., Ferri, F., 2017. Assessment of Available Numerical Tools for Dynamic Mooring Analysis. Technical Report. Tech. rep., Aalborg University.

Tian, Z., Perlin, M., Choi, W., 2012. An eddy viscosity model for two-dimensional breaking waves and its validation with laboratory experiments. Physics of Fluids 24, 036601.

Toedter, S., el Sheshtawy, H., Neugebauer, J., el Moctar, O., Schellin, T.E., 2021. Deformation measurement of a monopile subject to vortex-induced vibration using digital image correlation. Ocean Engineering 221, 108548.

UNFCCC, 2015. Paris agreement. URL: http://unfccc.int/files/essential_background/convention/application/pdf/english_paris_agreement.pdf.

Van Leer, B., 1979. Towards the ultimate conservative difference scheme. v. a second-order sequel to godunov's method. Journal of computational Physics 32, 101–136.

Vandebeek, I., Gruwez, V., Altomare, C., Suzuki, T., Vanneste, D., De Roo, S., Toorman, E., Troch, P., 2018. Towards an efficient and highly accurate coupled numerical modelling approach for wave interactions with a dike on a very shallow foreshore, in: Coastlab 2018, pp. 1–10.

Vaz, G., Jaouen, F., Hoekstra, M., 2009. Free-surface viscous flow computations: Validation of urans code fresco, in: International Conference on Offshore Mechanics and Arctic Engineering, pp. 425–437.

Vengatesan, V., Varyani, K., Barltrop, N., 1999. Wave-current forces on rectangular cylinder at low kc numbers, in: The Ninth International Offshore and Polar Engineering Conference, OnePetro.

Verbrugghe, T., Domínguez, J.M., Crespo, A.J., Altomare, C., Stratigaki, V., Troch, P., Kortenhaus, A., 2018. Coupling methodology for smoothed particle hydrodynamics modelling of non-linear wave-structure interactions. Coastal Engineering 138, 184–198. doi:10.1016/j.coastaleng.2018.04.021.

Veritas, D.N., 1994. Wadam—wave analysis by diffraction and morison theory. SESAM user's manual, Høvik .

Vickers, A., 2012. Improve the understanding of uncertainties in numerical analysis of moored floating wave energy converters. Ph.D. thesis. University of Exeter.

Van der Vorst, H.A., 1992. Bi-cgstab: A fast and smoothly converging variant of bi-cg for the solution of nonsymmetric linear systems. SIAM Journal on scientific and Statistical Computing 13, 631–644.

Vukčević, V., Jasak, H., Malenica, Š., 2016. Decomposition model for naval hydrodynamic applications, Part I: Computational method. Ocean Engineering 121, 37–46. doi:10.1016/j.oceaneng.2016.05.022.

Wang, J.h., Zhao, W.w., Wan, D.c., 2019a. Development of naoe-foam-sjtu solver based on openfoam for marine hydrodynamics. Journal of Hydrodynamics 31, 1–20.

Wang, Y., Chen, H.C., Vaz, G., Burmester, S., 2019b. Cfd simulation of semi-submersible floating offshore wind turbine under pitch decay motion, in: International Conference on Offshore Mechanics and Arctic Engineering, American Society of Mechanical Engineers. p. V001T01A002.

Welzel, M., Schendel, A., Hildebrandt, A., Schlurmann, T., 2019. Scour development around a jacket structure in combined waves and current conditions compared to monopile foundations. Coastal Engineering 152, 103515.

West, B.J., Brueckner, K.A., Janda, R.S., Milder, D.M., Milton, R.L., 1987. A new numerical method for surface hydrodynamics. Journal of Geophysical Research: Oceans 92, 11803–11824.

Wienke, J., Oumeraci, H., 2005. Breaking wave impact force on a vertical and inclined slender pile—theoretical and large-scale model investigations. Coastal engineering 52, 435–462.

WindEurope, 2020. Offshore wind in europe: Key trends and statistics 2019 URL: https://windeurope.org/wp-content/uploads/files/about-wind/statistics/WindEurope-Annual-Offshore-Statistics-2019.pdf.

Windt, C., Davidson, J., Akram, B., Ringwood, J.V., 2018. Performance assessment of the overset grid method for numerical wave tank experiments in the openfoam environment, in: International Conference on Offshore Mechanics and Arctic Engineering, American Society of Mechanical Engineers. p. V010T09A006.

Wu, G., Hu, Z., 2004. Simulation of nonlinear interactions between waves and floating bodies through a finite-element-based numerical tank. Proceedings of the Royal Society of London. Series A: Mathematical, Physical and Engineering Sciences 460, 2797–2817.

Xu, H., Zhang, Y., Santo, H., Chua, K.H., Law, Y.Z., Chan, E.S., 2021. Coupling of potential flow and cfd model for fluid and structure interactions, in: International Conference on Offshore Mechanics and Arctic Engineering, American Society of Mechanical Engineers. p. V008T08A009.

Yan, S., Li, Q., Wang, J., Ma, Q., Xie, Z., Stoesser, T., 2019. Comparative numerical study on focusing wave interaction with fpso-like structure. International Journal of Offshore and Polar Engineering 29, 149–157.

Yan, S., Ma, Q., 2007. Numerical simulation of fully nonlinear interaction between steep waves and 2d floating bodies using the qale-fem method. Journal of Computational physics 221, 666–692.

Yan, S., Ma, Q., 2017. A hybrid approach coupling mlpg-r with qale-fem for modelling fully nonlinear water waves, in: The 27th International Ocean and Polar Engineering Conference, OnePetro.

Yang, M., Teng, B., Ning, D., Shi, Z., 2012. Coupled dynamic analysis for wave interaction with a truss spar and its mooring line/riser system in time domain. Ocean Engineering 39, 72–87.

Zalesak, S.T., 1979. Fully multidimensional flux-corrected transport algorithms for fluids. Journal of computational physics 31, 335–362.

Zeng, X., Shi, W., Michailides, C., Zhang, S., Li, X., 2021. Numerical and experimental investigation of breaking wave forces on a monopile-type offshore wind turbine. Renewable Energy 175, 501–519.

Zhang, Y., Kim, B., 2018. A fully coupled computational fluid dynamics method for analysis of semi-submersible floating offshore wind turbines under wind-wave excitation conditions based on oc5 data. Applied sciences 8, 2314.

Zhou, Y., Xiao, Q., Liu, Y., Incecik, A., Peyrard, C., 2019. Investigation of focused wave impact on floating platform for offshore floating wind turbine: a cfd study, in: International Conference on Offshore Mechanics and Arctic Engineering, American Society of Mechanical Engineers. p. V010T09A071.

# List of Publications

Parts of this thesis work have been presented at international conferences and published in peer-reviewed journals. Below is the list of publications :

## REFEREED JOURNALS BASED ON THESIS

- **Aliyar Sithik**, Guillaume Ducrozet, Benjamin Bouscasse, Sriram Venkatachalam, and Pierre Ferrant. *"Numerical coupling strategy using HOS-OpenFOAM-MoorDyn for OC3 Hywind SPAR type platform"* Ocean Engineering, 263, 112206. 2022.
  doi: 10.1016/j.oceaneng.2022.112206
- **Aliyar Sithik**, Guillaume Ducrozet, Benjamin Bouscasse, Sriram Venkatachalam, and Pierre Ferrant. "*Efficiency and accuracy of domain and functional decomposition strategies for the wave-structure interaction problem*" Ocean Engineering, pp. 1-30. 2022. (*Revised version submitted*)
- Shagun Agarwal; Shaswat Saincher; V. Sriram; Shiqiang Yan; Zhihua Xie; Torsten Schlurmann; Qingwei Ma; Xiaotong Yang; Decheng Wan; Jiaye Gong; Yunbo Li; Yanyan Li; Jinshu Lu; Hanbing Sun; Yan Liu; Beilei Zou; Shuling Chen; Jing Lu; Jianguo Lin; Sa Young Hong; Yoon-Jin Ha; Kyong-Hwan Kim; Seok-Kyu Cho; Dong-Min Park; **Aliyar Sithik**; Benjamin Bouscasse; Guillaume Ducrozet; Pierre Ferrant . "*A Comparative Study on the Nonlinear Interaction Between a Focusing Wave and Cylinder Using State-of-the-art Solvers: Part B*" International Journal of Offshore and Polar Engineering. 31 (01): 11–18. doi : 10.17736/ijope.2021.jc832 Paper Number: IJOPE-21-31-1-011

## REFEREED JOURNALS (OTHERS)

- **Aliyar Sithik**, Jannik Meyer, V. Sriram and Arndt Hildebrandt (2021). Experimental investigation of offshore crane load during installation of a wind turbine jacket substructure in regular waves. Ocean Engineering, 241, 109979. ISSN 0029-8018. doi: 10.1016/j.oceaneng.2021.109979

## SCOPUS INDEXED CONFERENCE PROCEEDINGS

- **Aliyar Sithik**, Guillaume Ducrozet, Benjamin Bouscasse, Sriram Venkatachalam, and Pierre Ferrant. "*Breaking focused wave interaction with cylinder using HOS-OpenFOAM coupling*" In OCEANS 2022-Chennai, pp. 1-10. IEEE, 2022
  doi: 10.1109/OCEANSChennai45887.2022.9775539.

**Titre :** Interaction de vagues extrêmes avec des structures fixes ou flottantes par une approche numérique hybride

**Mot clés :** Couplage ; SWENSE ; OpenFOAM ; SPAR ; Amarres ; FOWT ; MoorDyn

**Résumé :** La thèse vise à étudier l'efficacité et la précision des solveurs NS et SWENSE pour simuler des structures fixes et flottantes. Les deux solveurs sont basés sur OpenFOAM et sont couplés indépendamment avec HOS pour la génération d'onde en termes de domaine et d'approche de décomposition fonctionnelle. Les solveurs sont testés pour trois applications. Les première et deuxième applications présentent l'interaction d'ondes de focalisation avec des cylindres fixes et mobiles et la troisième est l'interaction d'ondes régulières et irrégulières avec la sous-structure de type OC3 Hywind SPAR. Les méthodes et paramètres de génération d'ondes pour les solveurs NS et SWENSE sont discutés en détail pour les ondes régulières, irrégulières et focalisées. Pour vérification, l'incertitude du cas est quantifiée à l'aide de l'approche d'extrapolation de Richardson et validée avec les mesures expérimentales. Une réduction significative de la taille du maillage est prévue dans les deux approches. Pour l'étude de l'interaction des ondes de corps flottant, les amarres sont modélisées de deux façons : en considérant les lignes d'amarrage comme un ressort linéaire avec une raideur de ressort définie et un couplage avec un modèle d'amarrage dynamique (MoorDyn). Les résultats numériques de l'élévation de surface, des mouvements du corps et des tensions d'amarrage sont validés par rapport aux expériences menées dans le projet SOFTWIND, et l'efficacité et la précision des deux solveurs sont comparées.

**Title:** Extreme wave interaction with fixed and floating structures using hybrid coupling approach

**Keywords:** Coupling; SWENSE; OpenFOAM; focusing wave; SPAR; Moorings; FOWT; MoorDyn

**Abstract:** The thesis aims to study the effectiveness and accuracy of the NS and SWENSE-based solvers for simulating fixed and floating structures. Both solvers are OpenFOAM-based and are independently coupled with HOS for wave generation in terms of domain and functional decomposition approach. The solvers are tested for three applications. The first and second applications present the focusing wave interaction with fixed and moving cylinders and the third is the interaction of regular and irregular waves with the OC3 Hywind SPAR type substructure. The wave generating methods and parameters for NS and SWENSE solvers are discussed in detail for regular, irregular, and focused waves. For verification, the case's uncertainty is quantified using the Richardson extrapolation approach and validated with the experimental measurements. A significant reduction in the mesh size is predicted in both approaches. For the floating body wave interaction study, the moorings are modelled in two ways: by considering the mooring lines as a linear spring with defined spring stiffness and coupling with a dynamic mooring model (MoorDyn). The numerical results of surface elevation, body motions, and mooring tensions are validated against the experiments carried out in the SOFTWIND project, and the efficiency and accuracy of the two solvers are compared.